Investigation of Personalised Post-Reconstruction Positron Range Correction in ⁶⁸Ga Positron Emission Tomography Imaging

Rukiah A. Latiff

A thesis submitted to fulfilment of the requirements for the
degree of Doctor of Philosophy

Sydney School of Health Sciences
Faculty of Medicine and Health
The University of Sydney
2021

Abstract

Positron range limits the spatial resolution of Positron Emission Tomography, reducing image quality and accuracy. This thesis investigated factors affecting the magnitude of positron range, developed a personalised approach to range correction, and demonstrated the approach using simulated, phantom and patient data. The Geant4 Application for Emission Tomography software was utilised to model positron range when emitted by radionuclides, namely ^{18}F and ^{68}Ga, in water, bone and lung. The impact of range blurring in lungs was found to be ten times larger than in bone and four times larger than in water or soft tissue, regardless of the positron energy. Range effects occurring with different isotopes (^{18}F and ^{68}Ga) were evaluated across measurement and reconstructed spatial resolutions. It was found that range correction was not necessary when using ^{18}F for voxel sizes larger than 4 mm. In contrast, range correction was required for images generated using ^{68}Ga, particularly within or adjacent to the lung. An iterative, post-reconstruction range correction method was developed which relied only on the measured data. The correction method was validated in both simulation and phantom studies. Image quality and quantification accuracy of corrected images was shown to be superior when imaging with ^{68}Ga. Importantly, the range correction suppressed and controlled image noise at high iteration numbers. Finally, in a patient study, image noise in regions of uniform uptake was significantly increased by ~2% ($p<0.05$), yet mean standardized uptake values remained unchanged after correction, showing the same uptake for normal radionuclide distributions. The lesion contrast and maximum uptake values were improved by 20% and 45%, respectively with statistical significance ($p<0.05$). Although these promising results show that the proposed method of range correction can be generalized to reconstructed images regardless of measurement system, acquisition parameters and radionuclides used, further research is

warranted to improve the method, particularly with respect to removing or reducing the artefacts which were shown to impacted reader preference.

Acknowledgements

encouragement, patience, faith and scarificed. May Allah reward you for all the good deeds and kindness you have done for me.

Statement of Originality

This is to certify that to the best of my knowledge, the content of this thesis is my own work. This thesis has not been submitted for any degree or other purposes.

I certify that the intellectual content of this thesis is the product of my own work and that all the assistance received in preparing this thesis and sources have been acknowledged.

Signature:

Name: Rukiah A. Latiff
Sydney School of Health Sciences
Faculty of Medical and Health
The University of Sydney

Date: 15th June 2021

Table of contents

List of Figures

List of Tables

List of Abbreviations

^{64}Cu	Copper-64
^{18}F	Flourine-18
1D	One-dimensional
2D	Two-dimensional
3D	Three-dimensional
3DRP	Three-dimensional reprojection algorithm
^{68}Ge	Germanium-68
^{68}Ga	Gallium-68
^{177}Lu	Lutetium-177
^{82}Rb	Rubidium-82
^{89}Zr	Zirconium-89
ACFs	Attenuation correction factors
AMIDE	A Medical Image Data Examiner
aPSF	Annihilation point spread function
ASIRT	Additive simultaneous iterative reconstruction technique
BGO	Bismuth-germanate-oxide
CNR	Contrast noise ratio
CT	Computed Tomography
CTW	Coincidence time window
CZT	Cadmium–zinc-telluride
DATA	Diazepine-triacetate
DEW	Dual-energy-windows
DOI	Depth of interaction
DOTA	Dodecane tetraacetic
DOTANOC	DOTA-NaI^3-Octreotide
DOTATATE	DOTA-DPhe1-Tyr3-octreotate
DOTATOC	DOTA-d-Phe1-Tyr3-octreotide
ET	Estimation of trues
FBP	Filtered-backprojection

FDG	Fluorodeoxyglucose
FDOPA	Fluoro-dihydroxyphenylalanine
FORE	Fourier rebinning
FOV	Field of view
FT	Fourier transform
FWHM	Full-width-half maximum
FWTM	Full-width-tenth maximum
FWTMr	Full-width-tenth maximum residual
GATE	Geant4 Application for Emission Tomography
GSO	Gadolinium oxyorthosilicate
HU	Hounsfield unit
ICRP	International Commission on Radiological Protection
ISRA	Iterative image space reconstruction algorithm
IQ	Image quality
LOR	Line of response
LS	Least-squares
LSO	Lutetium oxyorthosilicate
LYSO	Lutetium yttrium oxyorthosilicate
MAP	Maximum a posteriori
MC	Monte Carlo
MDCT	Multi-detector CT
MEW	Multiple-energy-windows
MIBG	Metaiodobenzylguanidine
MLEM	Maximum likelihood expectation maximisation
MRI	Magnetic resonance imaging
MTC	Medullary thyroid carcinoma
NEMA	National Electrical Manufacturers Association
NETs	Neuroendocrine tumours
OSEM	Ordered-subset expectation maximization
PDE	Photon detection efficiency
PET	Positron Emission Tomography
PHA	Pulse-height analyzer

PINV	Pseudoinverse rebinning
PSMA	Prostate-specific membrane antigen
PMT	Photomultiplier tube
PR	Positron range
PRC	Positron range correction
RMS	Root-mean-squared
RMSD	Root-mean-squared deviation
SiPM	Silicon photomultipliers
SNR	Signal-noise ratio
SRAD	Speckle reducing anisotropic diffusion
SSRB	Single slice rebinning
SSTRs	Somatostatin receptors
TDSV	Tissue-dependent spatially-variant
TOF	Time-of-flight
WLS	Weighted least-squares

Glossary

PET_0 PET measured annihilation image obtained directly from the scanner.

PET_k Simulated annihilation image at k^{th} iteration.

PRC_{nrp} PRC image without relaxation parameter.

$PRC\gamma$ PRC image with relaxation parameter, $\gamma = 0$, 0.5 or 1.

PRC_k PRC image at k^{th} iteration.

R_{max} Maximum positron range.

R_{mean} Mean positron range.

Chapter 1

Introduction

1.1 Motivation

Positron Emission Tomography (PET) is a functional imaging technique that allows the quantification and 3-dimensional (3D) visualization based on the radiation intensity produced by the injection of radiotracers labelled with a positron-emitting radionuclide. The technique is widely used in cancer diagnosis and staging, assessing neurological diseases, for example; Alzheimer's disease and dementia, evaluation in cardiology such as myocardium blood flow and viability, as well as a potential increasing role in radiotherapy treatment planning and monitoring (Peng and Levin, 2010). The ability of PET to accurately and precisely map the concentration of the radiopharmaceuticals in the body is important as it is to be interpreted as a true reflection of the underlying physiology. Hence accurate quantification of the PET data is required. Factors that reduce image quality in PET scans include attenuation, scatter and random coincidences, as well as the variation of the detector response and dead time. However, those effects are often corrected during image reconstruction in a clinical scanner system. Other remaining challenges are positron range and the non-collinearity effect, which are independent of the PET scanner system and acquisition parameters (Blanco, 2006, Kemerink et al., 2011).

During positron radionuclide decay, the positron particles are emitted from the atom and travel a finite distance, known as the positron range, before subsequent annihilation with an electron in the body. Positron annihilation results in two 511 keV photons travelling in opposite directions. The detection of two annihilation photons in coincidence infers a Line of Response

(LOR). Thus, the LOR refers to the location of annihilation but not that of positron emission, resulting in blurring effects in the reconstructed PET image. This blurring impacts the quantitative accuracy of PET images, e.g., the estimated radiotracer uptake in a lesion. The magnitude of the positron range is proportionally dependent on the energy of the emitted positron and inversely proportional to the electron density of the surrounding tissue. In other words, high energy positron emitters contribute more blurring effects as compared to low energy positron emitters.

Nevertheless, annihilations within a low-density medium will exhibit more blurring than those within a high-density medium. This effect can introduce a loss of accuracy in PET quantification and is particularly problematic for high energy positron emitters such as ^{68}Ga (maximum 1.89 MeV). Likewise, the positron range effect is also pronounced in the lung medium, which has a lower electron density (0.26 g/cm^3) than most other human tissues.

Until recently, the positron range effect has been accepted as a relatively minor concern in clinical PET. Two factors are identified for this: the type of radionuclide used and the performance of PET systems. The most widely used radionuclide in PET imaging is Fluorine-18 (^{18}F) which is often used to label the glucose analogue, fluorodeoxyglucose (FDG), for clinical applications in cancer staging and monitoring. Another example is ^{18}F-labelled fluoro-dihydroxyphenylalanine (FDOPA) for neuroendocrine tumours (NETs) (Santhanam and Taïeb, 2014). ^{18}F (maximum 0.66 MeV) possesses a mean positron range of approximately 0.2 mm, 0.5 mm and 2.0 mm in bone, water and lung medium, respectively, which are all much less than the spatial resolution of a standard clinical PET scanner, about 4 mm (Latiff et al., 2017). Thus, the blurring effect caused by positron range is negligible and is not corrected for in commercial scanners. More recently, Gallium-68 (^{68}Ga) has become more widely used in clinical PET due to

the availability of ^{68}Ga generators and the relative simplicity of preparing ^{68}Ga-labelled radiopharmaceuticals in the clinic compared to [18]F (Velikyan, 2015). However, the mean positron range of ^{68}Ga is much higher than ^{18}F, estimated to be 1 mm, 2 mm and 9 mm in bone, water and lung medium, respectively (Latiff et al., 2017). Therefore, it is important to correct for positron range for such a high energy radionuclide, especially when imaging in a lung medium.

The second factor that explains the general acceptance of positron range effects in clinical PET is the limit of spatial resolution achievable in PET detectors. At present, the spatial resolution of whole-body PET imaging is approximately 4 mm, and this is expected to continue improving in the coming years. PET imaging was first conceived as a medical imaging modality in the 1970s when the spatial resolution of PET detectors was approximately 10-20 mm. Therefore, positron range had a negligible impact on performance. However, there have been tremendous improvements in performance over the past 50 years (Jones and Townsend, 2017). From the early scanners to the newest model of clinical EXPLORER PET/CT (Badawi et al., 2019, Berg and Cherry, 2018), the ideal PET scanner to be achieved is always high sensitivity, to maximize the acquired counts for the lowest possible injected radiopharmaceutical and high spatial and temporal resolutions (Jones and Townsend, 2017, Cherry et al., 2018). In the future, the spatial resolution of clinical PET will continue to improve as technology evolves so that the positron range blurring effect will become a more important factor and could affect the diagnosis (Meikle et al., 2021). Hence, the correction of positron range blurring is becoming increasingly necessary.

Improvement in spatial resolution is achieved by designing a finer array of detector elements allowing finer spatial sampling during data acquisition. For example, the size of detector elements in clinical PET has evolved from $6.35×6.35$ (mm)^2 in the early 1990s

(Wienhard et al., 1994) to 4×4 (mm)^2 today, which makes it feasible to reach an isotropic spatial resolution close to 4 mm (Slomka et al., 2016). However, to achieve such a fine crystal pitch, one needs to choose a scintillation material with a high light output (luminosity) to identify the active detector element without mispositioning and photodetectors that are able to decode the light produced in these small crystal elements.

Scintillation crystal characteristics are among the most critical factors to achieve high spatial resolution in PET imaging. Besides lower cost, availability, mechanical strength and moisture resistance, other desirable characteristics of scintillation crystals are high luminosity, fast rise and decay times, greater stopping power, improved energy resolution and the linearity of response with energy (Vaquero and Kinahan, 2015). For several decades, significant progress has been achieved in the discovery of new scintillator materials. Table 1.1 shows the trend of PET scintillator developments, comparing the characteristics of earlier relevant PET scintillator materials available in the 1980s and 1990s, such as bismuth-germanate-oxide ($Bi_4Ge_3O_{12}$ or BGO) and cerium-doped gadolinium oxyorthosilicate ($Gd_2SiO_5(Ce)$, or GSO), with newer materials which became widely available in the late 1990s, such as cerium-doped lutetium oxyorthosilicate ($Lu_2SiO_5(Ce)$, or LSO) and cerium-doped lutetium yttrium oxyorthosilicate ($Lu_{1.8}Y_{.2}SiO_5(Ce)$, or LYSO) (Berg and Cherry, 2018, Slomka et al., 2016)

Table 1.1: Characteristics of scintillator materials used in clinical PET (Source:(Zaidi and Alavi, 2007))

Material	Density (g/cm³)	Effective Atomic number(Z)	Luminosity (photons/keV)	Decay (ns)	Energy resolution at 511 keV(%)
BGO	7.13	7	9	300	12
GSO	6.71	59	8	60	7.9
LSO	7.4	66	25	40	9.1
LYSO	7.1	54	32	53	7.1

It is noted that the lutetium-based scintillators have superior performance properties compared to BGO and GSO. For example, the higher luminosity of LSO compared with BGO enables better energy resolution and finer subdivisions in the detector block, which leads to better spatial resolution.

Combining faster scintillators and more compact photodetectors with faster response times is one of the innovations in PET detector technology that has resulted in improved spatial resolution and effective sensitivity. Silicon photomultipliers (SiPM) are now the photodetector of choice for PET since first being introduced in 2009 (Jones and Townsend, 2017). SiPMs replaced the conventional photomultiplier tube (PMT) due to the compact size, high photon detection efficiency (PDE) and excellent timing properties (Roncali and Cherry, 2011). The excellent SiPM timing resolution of 44 ps is well suited for use in time-of-flight (TOF) capable PET systems. Also, whole-body PET imaging spatial resolution has the potential to improve further, to close to 3 mm, when using SiPM technology, because of its ability to be fabricated to match the smaller size crystals with a pitch of less than 4×4 (mm)^2 (Slomka et al., 2016).

Alternatively, semiconductor materials such as cadmium–zinc-telluride (CZT) can potentially have high spatial resolution detection and the ability to function at room temperature

(Iniewski, 2014, Peng and Levin, 2010, Vaska et al., 2005, Zheng et al., 2014). Furthermore, the semiconductor technology bypasses the relatively inefficient process of converting the 511 keV photons to light in the scintillator, instead directly converting the 511 keV photon into a large number of electric charges (Slomka et al., 2016). However, due to the CZT cost and its lower density, it is unclear whether it will replace scintillators such as LSO in the future.

The relative thickness of detector elements used for PET imaging leads to another geometric effect that degrades spatial resolution, known as parallax error or depth of interaction (DOI) effects. This effect is related to the uncertainty of the DOI in the detector elements, especially if penetration of photons into the neighbouring detector elements has occurred. For example, when considering a point source at the centre of FOV of a ring geometry scanner, all the emitted photons will enter the detectors perpendicularly to the detector surface. However, as the source is radially off-set, photons are more likely to impinge on the detectors with an oblique angle with respect to its axis, travel some unknown distance in the detector elements and possibly penetrate adjacent detector elements before being completely absorbed. As a result, the location of interaction will not be the same as the entry into the detector elements. Without DOI information, the detection electronics will incorrectly assign the LOR based on the entrance location of the interaction detector rather than the exact interaction location inside the detector elements. This uncertainty produces asymmetric blurring, which depends on the location of the source, width and thickness of detector elements, the absorption efficiency of detector elements, and the diameter of the scanner (Cherry et al., 2012, Phelps, 2006).

Developments in detector technology by reducing the size of crystal elements and adding depth of interaction (DOI) information for better spatial resolution uniformity have been made (Wienhard et al., 1994). Progressively, these improvements have led to the development of

dedicated human brain PET scanners with approximately 2.5 mm spatial resolution (Wienhard et al., 2002). Furthermore, based on the trends of clinical PET detector developments and evolutions, it is expected that the performance of PET will continue to improve in the near future (Meikle et al., 2021). Therefore, the correction for positron range blurring has now become an important factor in determining the image quality in clinical PET, and it is necessary to develop methods that minimize the effect.

Another motivation for developing positron range correction techniques is the application of preclinical PET. Since the spatial resolution in preclinical PET achieves approximately 0.7-2.0 mm (Sanaat et al., 2020, Goertzen et al., 2012), as compared to clinical PET, positron range blurring is thought to be a significant problem. Positron range causes an obvious spatial resolution degradation even for low energy radioisotopes (Levin and Hoffman, 1999) with a notable loss of contrast in mouse and rat brains for ^{18}F, which becomes severe for ^{15}O (Palmer et al., 2005). Regarding this, positron range correction is crucial to avoid misinterpretation of the data. Developments in preclinical technology often translate to clinical devices, and so, while this investigation concentrates on clinically relevant systems, preclinical scanner parameters offer further motivation to address the issue of positron range in clinical studies.

Several methods have been proposed for positron range correction (PRC), including inverse filtering using the Fourier transform (Derenzo, 1986, Haber et al., 1990) and iterative deconvolution within the image reconstruction framework (Agbeko et al., 2010, Cal-Gonzalez et al., 2018b, Fraile et al., 2016, Harzmann et al., 2014). However, compensating for positron range using inverse filtering increases image noise, especially for high energy radioisotopes. Furthermore, inverse filtering does not take into account the underlying electron density along

the path of the emitted positron, which can cause spatial variation of the blurring effect. Given that the positron range is inversely proportional to the electron density during transit, it is important to consider this factor during range correction.

Correcting for positron range using iterative deconvolution during the image reconstruction process requires access to the raw data, accurate modelling of the positron range, and individual resolution to be modelled within the system (system matrix) (Agbeko et al., 2010, Bai et al., 2003, Bertolli et al., 2016, Cal-Gonzalez et al., 2015a, Fraile et al., 2016, Harzmann et al., 2014, Kotasidis et al., 2014, Rahmim et al., 2009). This approach has also shown that this approach causes unpredictable edge artefacts that are exaggerated when the system matrix is overestimated (Alessio et al., 2013).

Only one method has investigated the attempt to correct the positron range after image reconstruction to the author's knowledge. In a study including both phantom and patient data and by first modelling the tissue-dependent spatially variant PR kernels followed by deconvolution using the Richardson-Lucy algorithm (Cal-Gonzalez et al., 2018a, Berger et al., 2019), the authors showed that spatial resolution and contrast were slightly improved but compromised with moderate induced image noise.

The proposed simulated post-reconstruction PRC in this study uses the Geant4 Application for Tomographic Emission (GATE), a Monte-Carlo simulation tool. The PRC method is based on the reliance of PET imaging locating positron-electron annihilations instead of positron emission directly. A PET measured image was used as the initial emission distribution from which an estimation of positron-range image was generated by GATE. The discrepancy between these two distributions providing a correction factor which could then be applied to the current deblurred image estimate. This PRC process is repeated iteratively to reduce the positron

range effect, therefore reducing the blurring effect in the reconstructed image and leading to the accurate positron emission location. Second, due to the fact that the annihilation distribution causes blurring in the image space (Agbeko et al., 2010, Cal-Gonzalez et al., 2015a, Rahmim et al., 2013), the modelling of the annihilation distribution in image space better represents the effect of positron range and localization than if modelling in data (sinogram) space.

Difficulties exist in using the raw PET data for incorporating PRC into the reconstruction due to the proprietary file formats, unless the researcher has an agreement with the vendor and compatible software. Therefore, the approach proposed can be implemented for any PET image regardless of scanner geometry, measurement properties, acquisition parameters and type of radiopharmaceutical used. The technique can be applied to PET images retrospectively, even if the raw data are not accessible and requires no modification of routine image reconstruction algorithms.

1.2 Aims

The main aim of this thesis is to develop a method that corrects for the positron range effect on patient-specific reconstructed ^{68}Ga PET images. The research focuses on developing, optimising, and validating a post-reconstruction de-blurring method for ^{68}Ga PET positron range correction to improve image quality and quantitative accuracy.

13Specifically, the objectives of the thesis are to:

1. Characterize ^{68}Ga positron range distribution in different radioisotope-medium combinations such as in water, bone and lung.

2. Investigate the impact of positron range on PET imaging performance which comprises:

   a) Assessment of positron range blurring in different media, such as bone, water and lung.

   b) Assessment of positron range blurring as a function of reconstructed PET system resolution.

3. Development and implementation of post-reconstruction positron range correction on phantom data and personalised PRC using patient-specific images.

1.3 Structure of the thesis

The thesis is organised as follows: Chapter 2 provides an introduction and background of the PET system, image reconstruction, functional imaging using ^{68}Ga and reviews previous positron range correction methods.

The first experimental work in this thesis is outlined in chapter 3, with the characterization of positron range for low and high energy positron-emitting radioisotopes, ^{18}F and ^{68}Ga, respectively. This was followed by validating each positron range measurement and estimation in media with different electron densities. Next, the study was extended to investigate the impact of positron range blurring in imaging, particularly for ^{68}Ga. The influence of the electron density of the medium on various PET scanner resolutions was examined through simulation. This study aimed to determine which PET system spatial resolution the positron

range effect becomes dominant, such that correction for the blurring effect becomes advantageous.

Chapter 4 is the second experimental study that describes the development and implementation of iterative post-reconstruction positron range correction (PRC). The proposed PRC operated in image space and was first implemented using phantom data. In this chapter, a detailed evaluation of the results is presented. This chapter is the core of the thesis, and the findings form the basis for the implementations of all following experiments.

Chapter 5 focuses on the implementation of the proposed PRC method on patient images. The performance of the PRC method was investigated qualitatively and quantitatively, concentrating on heterogeneous media and boundaries between tissues, such as lung/diaphragm, trachea/soft-tissue and soft-tissue/bone (Baum and Kulkarni, 2012). Since positron range is inversely proportional to the electron density of the media traversed by the positron and proportional to the emission energy of the radionuclide used, at this stage, the proposed PRC is personalised and adaptive for each patient based on their body tissue composition.

A summary of this thesis's major findings and conclusions and recommendations for future work are provided in Chapter 6.

Chapter 2

Background and Literature Review

In this chapter, we review the background and literature related to the topic of the thesis. We start with a broad review in section 2.1, which introduces positron emission tomography (PET) imaging, the need for quantitative data, the scanner, corrections during data acquisition and a brief overview of tomographic image reconstruction. Section 2.2 discusses the benefit of ^{68}Ga in PET imaging. It will be argued that despite an ability to produce a good diagnostic image quality, as compared to ^{18}F, many studies have shown that using high energy radionuclides would suffer from positron range effects that cause image blur. The topic of positron range and its impact on the PET image is covered in section 2.3. Several approaches to positron range correction are reviewed in this section, and the advantages and disadvantages of each are discussed. The main foundation of the idea to develop a post-reconstructed PRC is explained in section 2.4. Finally, section 2.5 summarises the topic that leads to the research questions addressed by this thesis.

2.1 An Introduction to PET Imaging and Quantitative PET.

Positron emission tomography (PET) imaging involves administering a small amount of positron-emitting radiopharmaceuticals into the body, which is subsequently distributed in tissues in a manner determined by its biochemical properties. For example, cancer cells may have a higher uptake of fluorodeoxyglucose (^{18}F-FDG) because they are often more metabolically active than healthy cells. Qualitatively, the three-dimensional image produced provides localization of the radiopharmaceutical's distribution in the body's various tissues, providing

crucial information related to the physiological and metabolic process in both healthy and diseased tissue.

The reconstructed PET image can provide quantitative data of the underlying physiological structure and function. The voxel values of the image can be calibrated in absolute units of concentration with acceptable accuracy and precision. Hence, it can accurately map the radiotracer concentration in the body and provide a true reflection of the underlying physiology. Quantitative PET is very important in clinical use for the detection of disease at an early stage, such as in atherosclerosis (Mohy-Ud-Din et al., 2015, Cal-Gonzalez et al., 2015a), tumour uptake and staging (Bai et al., 2013, Wang et al., 2013), assessment of treatment response (Beichel et al., 2019, Cattaneo et al., 2016, Soydal et al., 2013), evaluation of the physiological function via pharmacokinetic properties – which mathematically describes the mechanism of transport and biochemical reactions of the radiotracer in tissue (Rusten et al., 2013, Jonasson et al., 2016, Ben Bouallègue et al., 2019) and radiation dosimetry for radiation protection purposes (Violet et al., 2019, Pimpinella et al., 2017). To achieve such precise quantitative data, several corrections need to be performed to restore the detected distribution. These corrections are explained in section 2.1.5.

In this section, the positron emission radioactive decay, basic features of PET detectors and detection, correction for quantitative PET and tomographic image reconstruction are briefly described.

2.1.1 Positron emission radioactive decay

Radioactive decay is the process when an unstable atomic nucleus transforms into a stable one by releasing energy in the form of emitted particles and photons. For example, decay by positron emission is when a proton, p, in an atomic nucleus is transformed into a neutron, n and a positive charged electron, e^+. The positive charged electron also is known as a positron or beta particle (β^+) and the electron neutrino, v are ejected from the nucleus. Schematically, the process is:

$$p \rightarrow n + \beta^+ + v + energy \tag{2.1}$$

During positron decay, the positron particles are emitted from the nucleus and travel a finite distance, known as the positron range, before annihilating with an electron in the medium of interaction. Specifically, after ejection from the nucleus, the positron loses its kinetic energy in collisions with orbital electrons of the atoms in surrounding matter. These collisions cause ionization of the atoms, where the electron is ejected and/or excitation occurs – in which an orbital electron is raised to a higher energy state. In general, the positron is largely deflected in collisions with the orbital electrons. Occasionally, the positron can also interact with the nucleus, subsequently deviated from its original path by the strong electrical forces of the nucleus, resulting in bremsstrahlung photons are emitted. For these reasons, the positron tracks are tortuous, and their exact shape and length are unpredictable.

The positrons lose energy during collisions with the atoms of the surrounding matter, usually a few millimetres from the site emission site. At this point, the positron and electron form a temporary atomic-like system called positronium. The lifetime of the positronium is very short of about 10^{-10} sec (Cherry et al., 2012). Then, the positron combines with a negative electron in a process known as annihilation. Because of the positronium formation, the annihilation occurs

almost at rest, a near-pure matter to energy conversion, which results in two 511 keV photons travelling at almost 180º to one another. These annihilation photons travel to form a line of response (LOR) when detected by a PET scanner. However, the PET scanner identifying the LOR of annihilation but not the LOR of emission, which is one of the factors that imposed blurring effects in the PET image (figure 2.1). The blurring magnitude depends on which isotope is used and the interaction medium in the proximity of the positron emission. The details of the blurring effect caused by the positron range and influencing factors are explained in section 2.3.
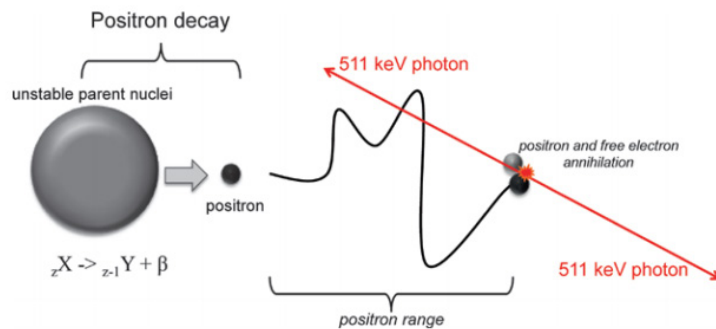
Figure 2.1: Illustration of the positron range between particle decay and annihilation process (Krishnamoorthy et al., 2017).

If positronium is formed and annihilation occurs before the positron loses all its kinetic energy or is not at rest, non-colinearity of the annihilation photons occur due to the small residual momentum. This effect describes the fact that the annihilation photons will not all be at exactly 180°, but will be emitted with uncertainties of around ± 0.25° with an overall effect of 0.5° full-width-half maximum (FWHM) (Cherry et al., 2012), as shown in figure 2.2. The non-collinearity results in positioning errors which contribute to the spatial blurring effect of PET imaging. The effect is linearly dependent on the diameter of the PET detectors, D;

$$R_{180^o} = 0.0022 \times D \qquad\qquad (2.2)$$

From eq. 2.2, one can conclude that non-collinearity can be an important limitation for clinical PET, which usually has a scanner bore of 80 cm diameter. However, the effect cannot be minimised by reducing the diameter because a bore size of 80-90 cm is required to accommodate the human body. Furthermore, the non-colinearity is independent of radioisotope used and medium of interaction, so it is best addressed during image reconstruction.
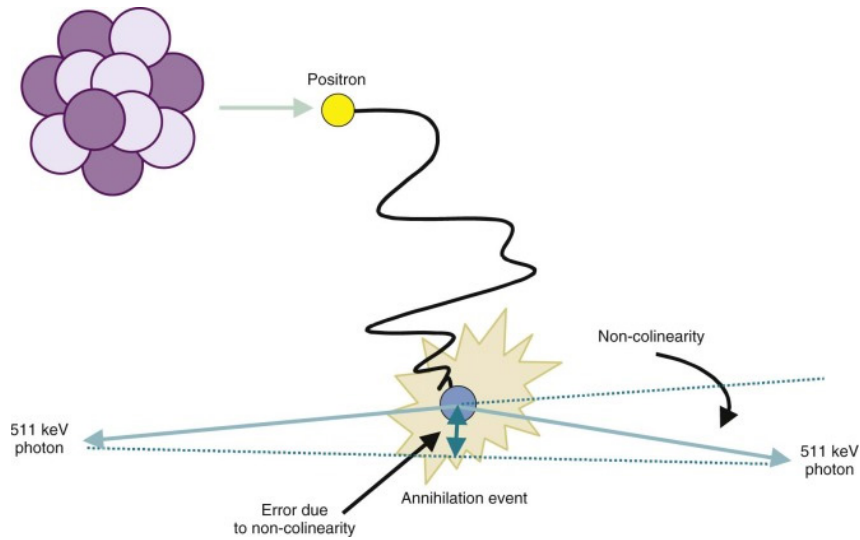
Figure 2.2: Non-collinearity event leads to positioning errors (Cherry et al., 2012).

2.1.2 PET detectors

Figure 2.3 shows an example of a bismuth germanate oxide ($Bi_4Ge_3O_{12}$ or BGO) crystal detector. When BGO crystals detect the LOR of annihilation photons, they converted the photons into scintillation lights where the amount of light produced is proportional to the energy deposited by the incident radiation in the crystals. The photomultiplier tube (PMT) is a photon sensor that triggers and amplifies photo-electron depending on the deposited energy of incoming scintillation photon and the number of dynodes in the PMT. Signals from the 4 PMTs are then

fed to electronic coincidence logic circuits to determine the location of the scintillation event by obtaining the total light emitted and calculating the local energy and local position centroid. Therefore, the event's location can be estimated based on the signal amplitudes distribution in the PMTs. This procedure to obtain the incident photon's location in the crystal is called Anger logic.

As mentioned in chapter 1, the ideal scintillation crystals for PET include its lower cost, availability, mechanical strength and moisture resistance. Other characteristics desired of scintillation crystal are high luminosity, faster rise and decay times, greater stopping power, improved energy resolution and the linearity of response with energy (Vaquero and Kinahan, 2015). The PET scanner consists of many block detectors of scintillation crystal coupled to photon detectors - a photomultiplier tube (PMT) and for newer systems, silicon PM (SiPM) – in a ring designed to detect both annihilations 511 keV gamma rays in coincidence.

Two conventional relevant PET scintillation crystals include bismuth germanate oxide ($Bi_4Ge_3O_{12}$ or BGO) and cerium-doped gadoliniumoxyorthosilicate ($Gd_2SiO_5(Ce)$, or GSO), and with a newer and widely used crystal, cerium-doped lutetium oxyorthosilicate ($Lu_2SiO_5(Ce)$ or LSO) (Slomka et al., 2016). The block detector was designed to allow small detector elements to be used by introducing light-sharing between PMTs. Therefore, Anger logic determines better localization of the incident photon and improving spatial resolution. A typical block detector commonly used in clinical PET scanners is shown in figure 2.3 (left and middle), where the small segmented crystals usually 8×8 arrays were cut with a fine saw. In the crystals, the incident annihilation photon is converted into light via the scintillation process. The slotted light guide then allows the scintillation light to be shared to varying degrees between the four PMTs. The amount of the shared light for each PMT is determined by the depth of the saw cuts in a fairly

linear pattern where the output from the block detectors reflect the coordinates of the crystal element (x,y).

Another method of light-sharing technique is a quadrant-sharing block design (figure 2.3, right), where each PMT monitors the corners of 4 different adjacent blocks. This approach also creates large area detector panels, reducing the number of PMTs required per detector element.
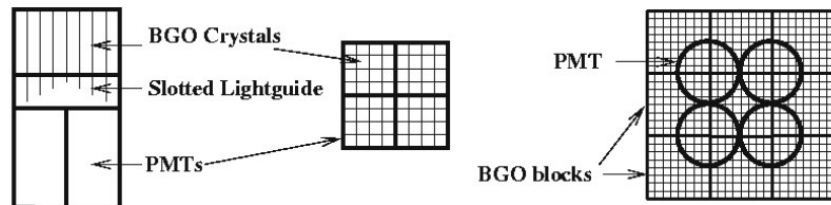
Figure 2.3: The standard detector design from the side (left) and looking down through the crystals (middle). The right picture shows the quad-sharing block design seen from the top through the crystals (Bailey et al., 2005a).

Silicon PM (SiPM) is another type of semiconductor photodetector that provides high photon detection efficiency (PDE) and magnetic insusceptibility, which is also suitable for PET/MR imaging. Moreover, the compact size of SiPM is beneficial to collect the scintillation light in a light-sharing detector with the light-sharing multiplexing is so much lower than PMT multiplexing for a block detector. For example, 4×9 arrays of LYSO crystals are multiplexed to 3 arrays of 3×2 pixels of SiPM, providing better crystal localisation than PMT (Hsu and Levin, 2020).

The block detectors are arranged in multiple rings or polygonal arrays around the subject. When annihilation photons interact with the crystal, the photon (gamma ray) is converted to light photons within the scintillation crystals, and it is the photomultiplier that detects these photons. Subsequently, detection of the pair of gamma rays from an annihilation

within a coincidence window, of width 2 nanoseconds in most PET scanners (Cherry et al., 2012), are registered as coincidence events. Localization of straight-line events between two opposite detectors can be identified using a line-of-response (LOR) (figure 2.4).

Coincidence events are only recorded if a pair of gamma rays are detected within the specified coincidence time window (CTW) and their deposited energy is within a predefined energy window. However, only true coincidence events originating from the same annihilation and are not scattered provide accurate information about the true radiotracer distribution and localization in the body, as shown in figure 2.4. Other coincidence events such as random and scattered coincidence, degrade qualitative and quantitative accuracy. Neither of these 2 coincidences is distinguishable from the true coincidence. Therefore, they contribute to the overall count rate and dead time losses. The random and scattered coincidence events are explained in the next subsection 2.1.5.2 and 2.1.5.3, respectively.
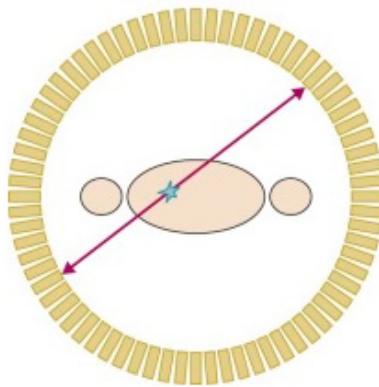
Figure 2.4: True coincidence events. Red arrows show 2 annihilation photons in a back-to-back direction. The red-dashed line shows a single LOR of true coincidence events (Cherry et al., 2012).

2.1.3 PET data acquisition

PET scanners were originally designed with axial collimators, or septa, between each ring of detectors. Two dimensional (2D) acquisition utilises the septa that allow the detection of photons emitted parallel to the plane of the detector ring only, known as direct coincidence. When performing fully three-dimensional (3D) acquisition, the septa are removed, and events that occur between detectors lying in any combination of rings can be recorded, which is called cross-plane (Cherry et al., 2012) or cross coincidence (Fahey, 2002) detection. The full 3D acquisition will improve the sensitivity of a scanner compared to 2D acquisition because of additional coincidence data from the oblique angle. However, random and scattered coincidence are increased in the 3D data, thus degrading the spatial resolution of the image. Coincidence events detected are stored in sinograms (two-dimensional histograms). In this format, possible LORs are ordered as a function of angular orientation versus displacement from the centre of the gantry, with each bin recording the number of LORs measured.

The sum of activity within the object and along a LOR is referred as the line-integral for that LOR. A full set of parallel line integrals recorded across a detector is called the projection. This is illustrated in figure 2.5. For a 2D object, at one angle, a projection (or projection profile) is a 1D projection. Thus, measuring projection profiles at equally spaced angular intervals, φ around the object along with offset, r, provides a 2D object matrix $P(r, \varphi)$ –the sinogram, where $P(r,\varphi)$ is a coordinate system in projection profile.
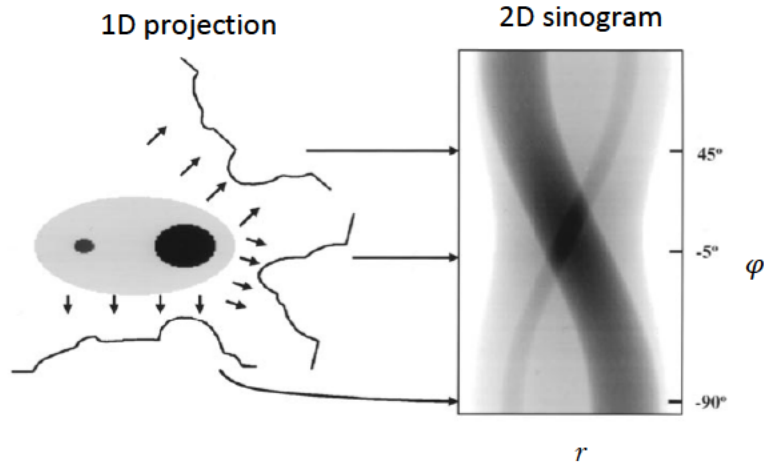
Figure 2.5: 1D projections of a 2D object and relation to its 2D sinogram at 3 different angles, φ and r is displacement from the centre of gantry. Each row in sinogram is a projection through an object at that specific angle, φ (Fahey, 2002).

2.1.4 Tomographic Image reconstruction

PET data can be acquired in a 2D or 3D mod in direct and cross-plane detection. For the 2D acquisition mode, the 3D volume of the data is reconstructed independently from $2l-1$ sinograms, where l is the number of detector rings. While for 3D acquisition mode, data is stored in l^2 sinograms for use with 3D reconstruction algorithm or rebinned to resemble 2D data before being reconstructed using 2D algorithms. The simplest method of rebinning is single slice rebinning (SSRB) (Daube-Witherspoon and Muehllehner, 1987). This method is fast but only accurate if the object being imaged is small, located in the centre of the transaxial plane with a small axial acceptance angle. The more sophisticated method was introduced as Fourier rebinning (FORE), which yields more accurate results, especially large objects and large acceptance angles (Defrise et al., 1997). The latest method, pseudoinverse rebinning (PINV) (Alejandro et al., 2020), also provide resulting image quality comparable with FORE. In addition,

PINV is faster than SSRB and FORE, making it possible to be implemented for real-time 3D PET image reconstruction.

Two general approaches of reconstruction are available: analytical and iterative algorithms, which are explained in the next subsection.

2.1.4.1 Analytical Image Reconstruction

Simple backprojection is the basic approach for reconstructing an image from the profiles. First, images are estimated using sinogram data – uniformly sampled projection profiles ordered by angle - where the information from each projection profile is uniformly re-distributed (backprojected) into the image space along the projection path. The backprojection of N profiles is described by:

$$f'(x,y) = \frac{1}{N}\sum_{i=1}^{N} P(r_i, \varphi_i) \qquad (2.3)$$

where $f'(x,y)$ is the estimated image and N is the number of projection angles acquired. However, simple backprojection suffers from a 'star pattern' artefact caused by the spillover of counts from high activity in pixels into neighbouring pixels, resulting in a blurring effect. The spillover decreased with distance, r from the region of interest and described by a $1/r$ function below where f is the reconstructed image and * is a convolution operation:

$$f'(x,y) = f(x,y) * \frac{1}{r} \qquad (2.4)$$

Methods to compensate for $1/r$ blurring are either using direct or filtered Fourier transform (FT) reconstruction (Saha, 2013). Direct FT represented the image profile in the frequency space rather than image space. As convolution in the image space is equivalent to multiplication in the frequency space, taking FT of both sides in equation 2.4;

$$F[f|'(x,y)] = F[f(x,y)] \times F\left[\tfrac{1}{r}\right] \tag{2.5}$$

$$F[f(x,y)] = \frac{F[f|'(x,y)]}{F\left[\tfrac{1}{r}\right]} \tag{2.6}$$

the image $f(x,y)$, can be estimated by calculating the inverse of $F[f(x,y)]$, $F^{-1}F[f(x,y)]$.

The next approach to eliminate the $1/r$ blurring effect is by using filtered FT. The central slice theorem in 2D, states that the FT of a projection profile, P(r,φ) is equal to the value of the FT of the object measured through the origin and along the same angle φ, in the frequency domain as below (Cherry et al., 2012):

$$F[P(r,\varphi)] = F(k_r,\varphi) \tag{2.7}$$

where $F(k_r,\varphi)$ denotes the value of FT measured at a radial distance k_r, along a line at angle φ in the frequency domain. The theorem provides a means to obtain 2D data from a series of 1D measurements in image space. Then, the ramp filter denoted as $H(k_r)$ is applied:

$$T'(k_r,\varphi) = |k_r| \times T(k_r,\varphi) \tag{2.8}$$

where $T(k_r,\varphi)$ is the unfiltered projection in the frequency space. Then, the inverse FT is performed following the backprojection as in eq. 2.3 but using the filtered profiles, T'. The filter suppresses the low-frequency information that contributes to a blurring effect and amplifies high-frequency data in the FT of the estimated image to yield fine details.

The application of the ramp filter before they are back-projected across the image results in the amplification of high-frequency noise. For this reason, images reconstructed by FBP are usually noisier than using simple backprojection itself. The ramp filter also leads to 'ringing' at sharp edges due to its properties that enhance high-frequency information to sharpen the images. However, a low pass filter can be used together with the ramp filter to preserve the low-frequency part of the image while suppressing noise at higher frequencies. The common type of such

combination filters are Shepp-Logan, Hamming, Hanning, Parzen and Butterworth filters. Those

filters are respectively expressed as (Saha, 2001):

$$\text{Shepp-Logan, } SL(v) = \frac{sin(\pi v)^{2n}}{\lfloor\frac{\pi v}{2n}\rfloor} \tag{2.9}$$

$$\text{Hamming, } Hm(v) = 0.54 + 0.46cos\lfloor\frac{\pi v}{2n}\rfloor \tag{2.10}$$

$$\text{Hanning, } Hn(v) = 0.5 + 0.5cos\lfloor\frac{\pi v}{2n}\rfloor \tag{2.11}$$

$$\text{Parzen., } Pv = v \tag{2.12}$$

$$\text{Butterworth,, } B(v) = \frac{1}{1+\left[\frac{f}{n}\right]^{2s}} \tag{2.13}$$

where v is frequency, n is selected cut-off frequency at which the frequency is accepted, and the

frequency above the band is eliminated, and s is the order that controls the filter's function slope.

The analytical method to reconstruct 3D data is the 3D reprojection algorithm (3DRP)

(Kinahan and Rogers, 1989), an extension of the FBP method to 3D. Since 2D data include noise,

acquiring 3D data is possible to improve the SNR of the reconstructed image because the scanner

sensitivity is improved. Furthermore, 3D data include oblique sinograms and hence provide

redundant information. However, the 3D dataset is incomplete because it is truncated in the axial

direction caused by the limited axial extent of the scanner. As the angle between detector rings

increases, the truncation become worse. Therefore, the 3D data is only complete if the scanner

had a sphere geometry and all axial angles projection ranging from 0º to 180º were included in

the measurement.

To compensate for the data from the truncation, data redundancy provided in 3D data

was utilised by first, extracting 2D sinograms from the 3D data at the axial angle of 0º. Then,

these sinograms were reconstructed using 2D FBP and stacked to form 3D volume. The

resulting image volume is now an initial image estimate, reprojected or forward-projected to estimate the missing LORs data to remove the truncation. Then, this complete 3D dataset is ready to be reconstructed using 3D FBP (Phelps, 2006).

The analytical reconstruction method is a linear process. For example, doubling the counts in each projection will result in a uniform doubling of intensity in the image. Thus, it is easy to implement and computationally fast. However, this method tends to produce streak artefacts if using data with poor counting statistics. It also does not consider various physical aspects of the imaging system and acquisition that degrade the data obtained, for example, the limited resolution of the detectors and scattered radiation.

2.1.4.2 Iterative image reconstruction

Iterative image reconstruction involves a repetitive cycle of image estimation until the current estimated image approximates the true image. Generally, the operation starts using a uniform image as the image estimate, which is forward projected to obtain the corresponding projection profile (estimated projection). This profile is compared to the measured image projection profile acquired by the imaging system. Then, correction factors are calculated from the ratio or the difference between these two profiles and applied to each voxel in the matrix to obtain an updated estimated projection. The method of correction using the ratio is called maximum likelihood expectation maximisation (MLEM) and the correction using the difference is called additive simultaneous iterative reconstruction technique (ASIRT) (Saha, 2016). Finally, the compare-and-update process is repeated until the satisfactory agreement between current estimated and true images are achieved. The general concept of iterative reconstruction is shown below (Cherry et al., 2012):
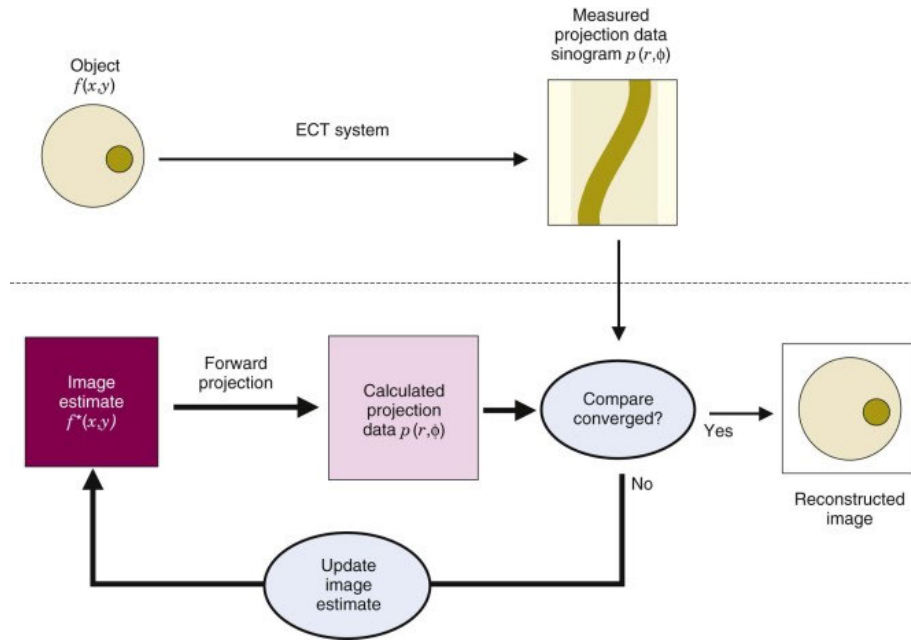
Figure 2. 6: A conceptual steps in iterative reconstruction.

The most widely used iterative reconstruction algorithms in PET are maximum likelihood expectation maximisation (MLEM) (Shepp and Vardi, 1982) and ordered-subset expectation maximization (OSEM) (Hudson and Larkin, 1994). MLEM is based on the maximum likelihood statistical criteria to measure the differences between the current image estimate and the true image. The algorithm involves 2 steps: first, the calculation of the expectation and second, the maximization of the expectation. Therefore, the new image estimate is generated when the current image estimate and the true image have the least differences and at the highest likelihood. Here, the estimated data is calculated based on the model of the acquisition and detection process (system matrix) and the source distribution estimated in the previous iteration. The ML criteria being evaluated within the EM reconstruction algorithm:

$$p_{j=\sum_i M_{i,j} a_i} \tag{2.14}$$

where p_j is the measured intensity or activity in the jth projection element, a_i is the intensity in an ith pixel in the image and $M_{i,j}$ is the probability that radiation emitted from the ith pixel will be detected in the jth projection element (Cherry et al., 2012).

OSEM is a modification of MLEM used to accelerate the reconstruction process by grouping projection data into an ordered sequence of subsets or blocks. The process includes 2 general steps. First, an initialization of image estimate at zero iteration. Second, the image update process. It uses only the subset of the projection data to estimate the image at each iteration rather than using the entire projection dataset. Each subset contains several projection views. During reconstruction, only one subset is used for the comparison and updating process. An update of this one subset is called a sub-iteration. The resulting reconstruction is then used as the starting value for the next different subset. Finally, one iteration is completed after all subsets are employed in the reconstruction algorithm (Saha, 2016).

Iterative reconstruction algorithms like MLEM and OSEM are nonlinear, but they can be modified by incorporating the physical factors that account for specific measurement characteristics such as object scatter and detector resolution. This capability leads to image estimates that are as accurate as possible given the accuracy of the system matrix. However, this algorithm increases noise with a high number of iterations or subsets. Hence, post-reconstruction filters can often be applied, or the iteration number needs to be set or controlled while observing the image convergence produced.

Point-spread function correction in reconstruction

An accurate system matrix was required during the reconstruction process so that the relationship between the projection and image space can correctly be modelled and leads to produce image estimates as close as possible to the true image. It is essentially a standard

correction reconstruction nowadays as it incorporates the PSFs of resolution degrading factors, particularly detector effects such as crystal widths, inter crystal scattering and penetration, positron range and non-collinearity (Rahmim et al., 2013).

Such resolution modelling can be carried out either in projection space such as in the MLEM approach or image space. Noted that when the positron range effect is negligible, such as PET imaging using ^{18}F, resolution modelling in projection space is appropriate. However, it is a problem when using high energy of positron emitter that contribute to the high positron range blurring as it cannot model a space-variant positron range effect. In contrast, resolution modelling in image space can model the space-variant blurring effect caused by the positron range (Rahmim et al., 2013).

Resolution modelling (RM) in the image space approach is simple to perform without a significant computational burden. Previous studies demonstrated that image-based RM improves the signal to noise ratio (SNR), spatial resolution and higher contrast recovery in the reconstructed image than projection-based modelling (Reader et al., 2003, Sureau et al., 2008, Rapisarda et al., 2010).

2.1.5 PET image correction

The main aim of tomographic imaging is to make sure the reconstructed image represents the object intensity and location accurately. For example, the intensity in the image should be exactly proportional to the radiopharmaceuticals concentration at the corresponding location in the object. This is because clinically, an accurate comparison of activity in different organs or diseased versus normal tissue is always made to make a diagnosis. Hence, several corrections need to be conducted in PET data, such as normalization, random coincidence correction,

scattered radiation correction, attenuation correction, dead time. In addition, the utilisation of time-of-flight (TOF) is necessary to improve PET quantification.

2.1.5.1 Normalisation

The typical PET scanner has more than 20,000 individual crystal detector elements. These crystals are precisely made but do vary slightly. There would also be a variation in the PMT or SiPM response to light that also needs to be corrected. Those differences contribute to different detector efficiencies. Correction for this variation is known as normalisation and is required to avoid rings and other artefacts caused by a non-uniform response in reconstructed images. The direct normalisation approach is performed by using a cylinder, plane or line uniform source of ^{68}Ge in the centre of the FOV (Phelps, 2006, Meikle and Badawi, 2005). ^{68}Ge is the parent nuclide that decays by electron capture to the short-lived positron emitter ^{68}Ga. Normalisation coefficient, $Norm_{(i,j)}$ for each pair of the detector (i,j) is computed from (Cherry et al., 2012):

$$Norm_{(i,j)} = \frac{N_{(i,j)}}{\overline{N}} \tag{2.15}$$

with $\overline{N}$ is the mean value of N(i,j) for all the coincidence detector pairs in the scanner. The normalisation coefficients then are used to correct the counts recorded in each detector pair during a patient scan, $C_{(i,j)}$ as follows:

$$C_{norm(i,j)} = \frac{C_{(i,j)}}{Norm_{(i,j)}} \tag{2.16}$$

where $C_{norm(i,j)}$ is the corrected counts. The correction is applied to the sinogram before image reconstruction. This method requires a very long acquisition time to avoid noise from the normalisation.

Another technique for determining normalisation is the component-based method. This is a factorized approach that separates the normalisation of true and scattered coincidence events and considers the variation normalisation effects with count rate (Badawi and Marsden, 1999). The component-based normalisation is measured from two separate scans, which first, scanning a rotating rod source with nothing in the FOV to calculate the geometric effects and second, scanning a uniform cylindrical source to calculate the detector efficiencies. In this case, the normalisation coefficients are the product of factors for all components representing the detector element intrinsic efficiency and variations of each LOR. The normalised-sinogram containing the normalisation factors for all LORs is then multiplied by the emission sonogram for normalisation.

2.1.5.2 Random coincidence correction

Random coincidence happens when 2 unrelated photons from different annihilation events are detected simultaneously as a single coincidence event and identified as a LOR (figure 2.7). Random events add to the background of the image, causing loss of image contrast. Random coincidence, R measured for each detector pair, is given by (Saha, 2015):

$$R = 2\tau . C_1 . C_2 \tag{2.17}$$

The 2τ is the coincidence timing window (CTW), where τ is the width of input pulses in nanoseconds for the system, typically 2-6 ns (Brasse et al., 2005), C_1 and C_2 are the count rate from a single channel of the pulse-height analyzer (PHA) of the two detectors along the LOR.

Generally, random coincidence can be corrected in two ways, including real-time subtraction of a delayed CTW and post-acquisition subtraction. For the first method, random coincidence is estimated using a delayed CTW. A delayed CTW needs to be set up by a much

greater time than its width of pulses. Thus, only events that arrive at the detector within the time of delay set-up are accepted and sent to the coincidence processing circuitry. Next, the events recorded in the delayed CTW are subtracted on-line from the total number of coincidence events for the detection pair. While for the second method, the subtraction is done in sinogram space where the delayed sinogram, which contains solely the random coincidence events, is subtracted from the prompt coincidence sinogram (Brasse et al., 2005).
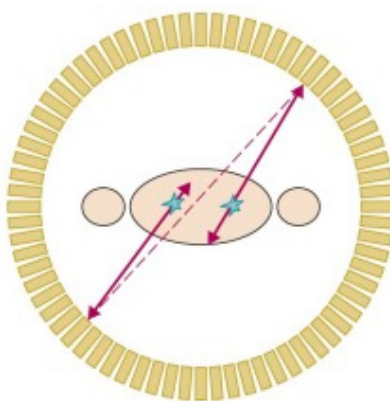
Figure 2.7: Random coincidence events. Red arrows show 2 annihilation photons in the back-to-back direction. The red dashed line shows the incorrect LOR from random coincidence events (Cherry et al., 2012).

2.1.5.3 Scattered radiation correction

Scattered radiation arises when one or both of the annihilation photons experience Compton scattering before detection. Compton scattering occurs when a photon transfers some of its energy to loosely bound electrons and deviates from its original path within the imaging field-of-view (FOV) before entering the PET detector. Scattered events increase the events detected in a LOR, which does not belong to the back-to-back emission direction of the two annihilation photons, as shown in figure 2.8. This leads to mispositioned LOR and therefore provide incorrect localization of the true event. Moreover, since the scattered coincidence causes

mispositioned events, it indirectly provides the addition of background events in the reconstructed images, thus decreasing image contrast.
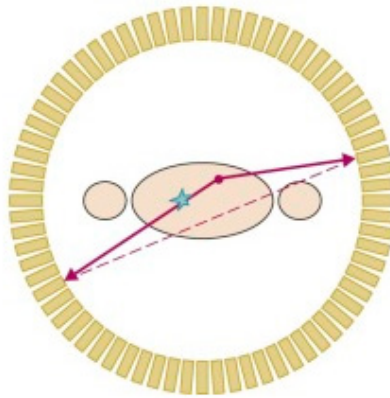
Figure 2.8: Scattered coincidence events. Red arrows show 2 annihilation photons where one of the photons is scatteredinside the body and deviate from their original path before being detected. The red dashed line shows the incorrect LOR from scattered coincidence events (Cherry et al., 2012).

The simplest approach for scatter correction is by fitting an analytical function to the scatter tails outside the object. The method is conducted in projection space, based on the assumption that after correcting for random coincidence, the events falling outside the object are mainly due to the scatter (Cherry and Sung-Cheng, 1995). First, the data from the tails of projection profiles are extrapolated using simple, smoothly varying functions across the entire projection. Then, the extrapolated data is subtracted from the projections prior to image reconstruction. The main disadvantage of this method is that scatter distribution is not always well approximated by a smooth analytical function, particularly in regions with heterogeneous tissue density like in the thorax, which may lead to over or under correction.

The second method is based on energy window approaches which can be divided into two: the 'dual-energy window' (DEW) (Grootoonk et al., 1991) or 'multiple energy windows' techniques (MEW) (Lingxiong et al., 1994) and 'estimation of trues' technique (ET) (Bendriem et al., 1993). Energy window approaches use the fact that Compton scattered photons can be

recorded at energies below the photopeak, with critical energy where only unscattered photons are recorded. The unscattered photons are assumed to deposit all energy within the detection system. Thus, the data recorded in energy windows set below or upper, or both, can be used to estimate the scatter contribution in the photopeak window.

The third approach is convolution subtraction (Bailey and Meikle, 1994). First, the scatter distribution is estimated by iteratively convolving the measured projection data with a mono-exponential kernel. Then, the resulting scatter estimation is subtracted from the data before reconstruction. It has been shown that this method is accurate in a simple object where the scattering medium is relatively homogenous but not in a complex object such as thorax.

The fourth approach uses a simulation-based algorithm. Using this method, the scatter estimation is simulated based on the physics interaction of photons with matter. The scatter contribution to a LOR is calculated from the initial emission distribution and attenuation map. This map is derived from the scatter probability estimation at a certain point through an angle towards one of the detectors using Klein-Nishina formula. The scatter estimation can be performed analytically (John, 1996) or tracking the photon using Monte-Carlo simulation (Levin et al., 1995)

2.1.5.4 Attenuation correction

Attenuation is the loss of true coincidence events detection due to their absorption in the body. It also depends on the thickness and density of the material that the gamma rays have to travel through before reaching the detectors. The attenuation process is outlined in figure 2.9, which exhibits the two annihilation photons originated from within the object of thickness, d. The μ is the linear attenuation coefficient (cm^{-1}) which describes the probability of interaction

per unit length in cm. Moreover, μ is dependent on the photon energy and the density of the medium that the photon passes through. From the figure, the first photon will have an attenuation of $e^{-\mu x}$, while attenuation of the second photon is $e^{-\mu(d-x)}$. Hence, the probability of attenuation for both photons is the multiplication of the two individual attenuations, resulting in $e^{-\mu d}$.
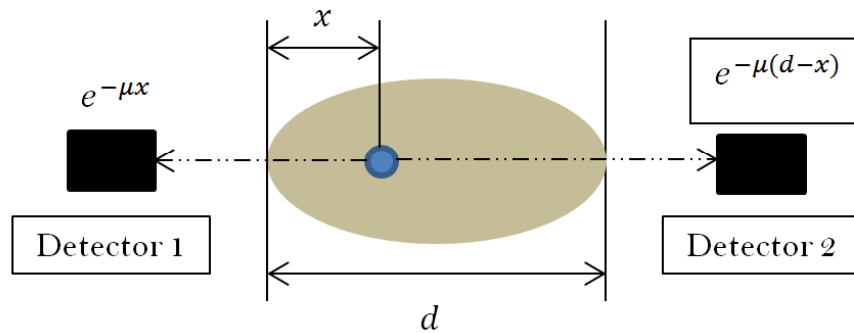
Figure 2.9: Photon attenuation in PET.

For a uniform density system, attenuation is much more likely in the centre of the body, and therefore, non-attenuation-corrected images will show lower levels of activity deep in the body compared to near the surface, as shown in figure 2.10(A) below.

(A)   (B)
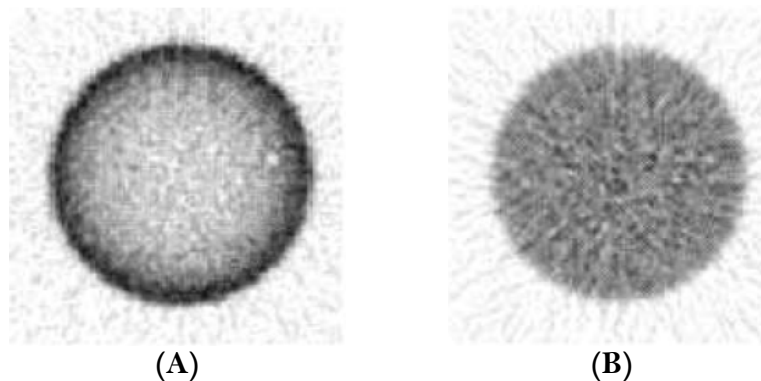
Figure 2.10: Reconstructed cylindrical phantom (A) before attenuation correction and (B) after attenuation correction (Phelps, 2006).

In general, the attenuation correction essentially adds counts back into more attenuated areas due to their being deeper or being surrounded by relatively dense structures. Similarly, it essentially subtracts counts from less attenuated areas than all other tissues (e.g. lungs and body surfaces). Figure 2.11(A) shows that attenuation causes incorrect radioactivity distribution in the lungs, liver, and skin.
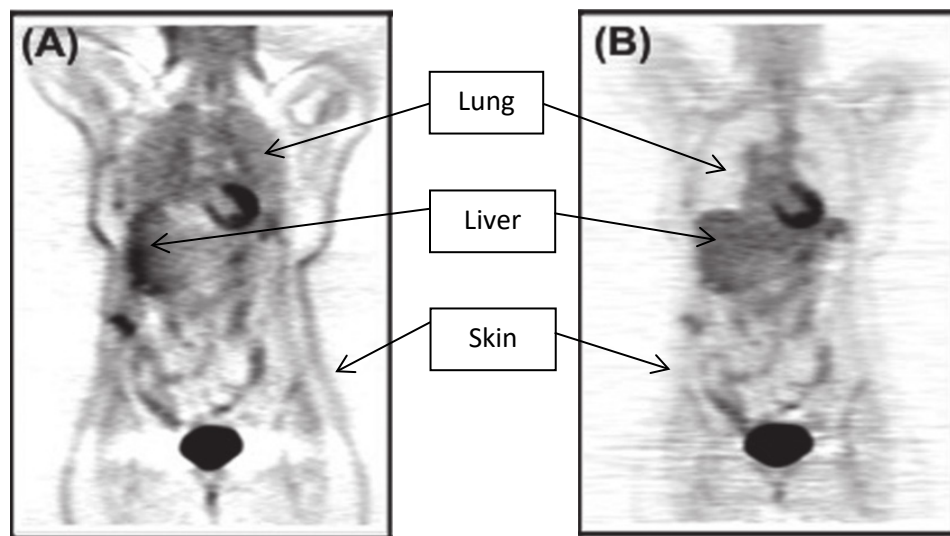
Figure 2.11: PET image (A) without attenuation correction and (B) with attenuation correction where it shows the true distribution in the lung, liver and skin (Lee et al., 2016).

Several approaches for attenuation correction exists, including calculated attenuation correction, transmission scanning, segmented attenuation correction, computed tomography (CT) based attenuation correction, and magnetic resonance imaging (MRI) based attenuation correction. The simplest method is the calculated attenuation correction implemented for a homogenous structure with a constant attenuation coefficient, such as in brain studies. For this case, integration of the exponential attenuation, $e^{\mu d}$ applied along the each LOR and generate the sinogram of attenuation factors (ACFs) (Phelps, 2006).

The second approach is transmission scanning using a radioactive source. For this method, typically, a thin rod source of germanium-68 (^{68}Ge) (t $_{1/2}$ = 273 days) is attached to the PET scanner gantry and rotated by an electric motor around the scanner to expose all detectors to radiation uniformly. Two types of scans are required for this method. The first type is a blank scan without patient in the scanner, and the second type is a transmission scan with patient in the scanner. First, the sinogram of attenuation correction factors (ACFs) for each LOR are computed by taking the ratio between the blank sinogram and the transmission sinogram. After that, the PET emission sinogram is multiplied on every element by the ACFs.

Initially, the transmission scan was performed prior to the radioisotope injection to the patient and required a long time to acquire enough counts for good accuracy of attenuation correction factors. An alternative approach to this method was introduced called post-injection transmission scanning, which performs the transmission scan immediately after the emission scan without moving the patient from the bed (Carson et al., 1988). This approach significantly shortens the time between transmission and emission scans, reducing the likelihood of patient motion and increasing scanning throughput.

A further reduction of transmission scan time has been possible by introducing the third method, which is segmented attenuation correction from transmission image. The method was also introduced to achieve lower noise levels for short transmission scans. For this approach, body structures are segmented into several types of tissues based on pixel values with a priori known attenuation coefficients (Visvikis et al., 2001, Xu et al., 1996, Nai et al., 2017).

The fourth method, CT based attenuation correction, is the most common attenuation correction technique nowadays for hybrid PET/CT systems. It is one of the transmission scanning techniques using an x-ray beam instead of using a radioactive source. However, this

technique provides a very low noise of attenuation map due to higher photon flux (Saha, 2016). Similarly with transmission scanning using radioactive sources, blank and transmission scans data are required and the ACFs are generated. Since the ACF depends on the energy of the photons, they have to be scaled from typical CT x-ray energy, ~70 keV to the 511 keV in PET before being used to correct for PET data. Potential pitfalls of this technique include misalignment of the emission data and the ACF due to patient movement, cardiac contraction and respiratory motion, the use of contrast agents and metal implants causing bias in attenuation coefficients (Lee et al., 2016) and truncation of the FOV in the CT scan potentially generating incomplete attenuation maps (Meikle and Badawi, 2005).

The current development of PET/MRI scanners motivates MRI based attenuation correction methods. However, the major challenge is that the MR data are not related to electron densities of media which have different attenuation coefficients. Therefore, three main approaches have been developed to estimate the attenuation coefficient based on the MR image. The three approaches include MR image segmentation into several tissue types corresponding to μ assigned (Lillington et al., 2020), using an attenuation atlas templates from CT images and morphed onto the patient's MR image to obtain continuous attenuation maps from the MR data (Wang et al., 2020) and exploits TOF PET emission data to jointly estimate the emission activity and attenuation coefficients (Nuyts, 2020).

2.1.5.5 Deadtime correction

Performance of PET detectors reduces at high counting rates due to dead time and pulse pile-up effects. Dead-the time is related to the time required to process individual detected events.

During the dead-time, the additional photons cannot be detected and result in loss of counts. Hence, the amount or concentration of activity will be underestimated.

PET scanners use empirical dead time models for correction. First, the dead time and the observed count rate as a function of radioactivity concentration are measured for a range of object sizes and energy thresholds. The resulting data are then fit with dead time models that take into account the system behaviour (paralyzable or non-paralyzable) to extrapolate from measured counts (Cherry et al., 2012, Phelps, 2006).

2.1.5.6 Time-of-flight (TOF)

It is also possible to localize more accurately the annihilation location along each LOR using TOF information. TOF is based on determining the precise time each coincidence photons are detected and calculating the inferred spatial difference (figure 2.12).

(A)   **(B)**
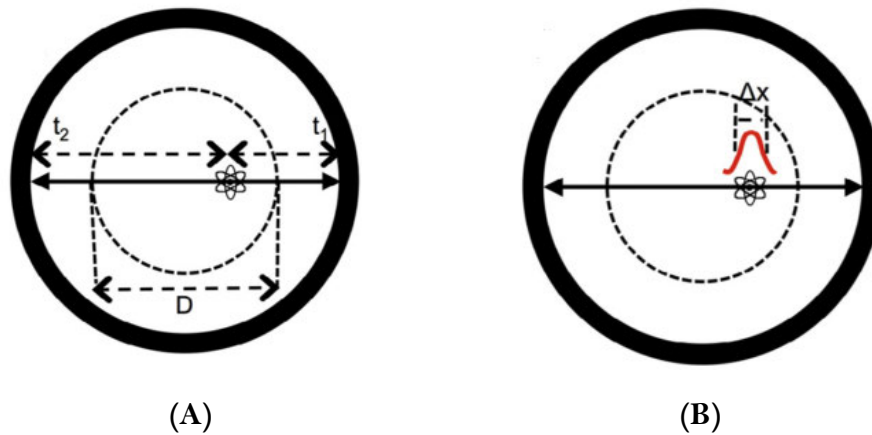
Figure 2.12: (A) Annihilation points at a distance from the centre of the detector within an object of diameter D. The coincident photons are detected at times t1 and t2 in the PET scanner. (B) With TOF, the position of annihilation points is localized along the LOR with a precision defined by a Gaussian distribution of width Δx (Surti and Karp, 2015).

If the difference of photon arrival times within defined CTW is Δt, the location of an annihilation event, with respect to the midpoint between the two detectors, Δx is given by:

$$\Delta x = \frac{\Delta t.c}{2} \tag{2.18}$$

where c is the velocity of light, 3×10^{10} cm/sec. TOF information helps reduce noise as long as the Δx is smaller than the size of the respective object diameter, D as shown in figure 2.12. This effect is measured in terms of signal-noise-ratio (SNR) and represented as:

$$SNR = \frac{D}{\Delta x} \tag{2.19}$$

The annihilation location estimates and SNR improve with better timing resolution, Δt which is proportional to eq. 2.18 (Saha, 2015). The timing resolution can be improved by using high luminosity scintillator materials and fast decay time such as LYSO; an effective photosensor which is SiPM, and choice of detector configuration to obtain good spatial resolution and sensitivity (Surti and Karp, 2015).

The benefit of TOF increases as the PET timing resolution improves, especially for heavy patients, which suffer from increased attenuation, leading to the loss of true counts and an increase of scattered counts. Hence, TOF imaging enhances data correction accuracy, therefore improving image quality and lesion detectability (Meikle et al., 2021).

2.2 Gallium-68 in PET Imaging

Gallium-68 (^{68}Ga), a daughter of germanium-68 (^{68}Ge), is a positron-emitting radioisotope with maximum positron energy of 1.89 MeV. Recently, ^{68}Ga has become more widely used in PET as compared to other cyclotron radiometal products such as copper-64 (^{64}Cu) and zirconium-89 (^{89}Zr) especially in cancer diagnosis imaging due to the availability of commercial ^{68}Ge generators (Velikyan, 2015) for the production of ^{68}Ga on-site, without the need for a cyclotron. The long half-life of ^{68}Ge (270.8 days) makes it possible to use the generator for approximately 9-12 months. Furthermore, ^{68}Ga yields higher positron per decay as compared to

[64]Cu and [89]Zr, reflecting more counts will be detected. Also, the cost of ^{68}Ga production and operation is reduced since the generator's cost is comparable with other radionuclides used for PET imaging. Another type of radiometal generator product is rubidium-82 ([82]Rb), which has higher beta energy than [68]Ga. Hence, high beta energy results in high positron range, which results in severe resolution degradation as opposed to [68]Ga.

The rapid utilisation of ^{68}Ga in nuclear imaging is also motivated by its chemical properties that allow simple radiopharmaceutical labelling with minimum loss of radioactivity (Shetty et al., 2010) as compared to other positron emitters such as [11]C (Meisenheimer et al., 2019). ^{68}Ga-labelling yields of more than 95% can be usually achieved within 15 min. It also has the potential to substitute ^{99m}Tc in imaging applications such as lung perfusion studies (Baum and Kulkarni, 2012), renal function, hepatobiliary, brain perfusion imaging (Kilian, 2014), bone metastases (Baum and Kulkarni, 2012, Fellner et al., 2012), cardiac function (Yang et al., 2010) and immune system (Choi et al., 2011). In addition, ^{68}Ga is possible to combine with lutetium-177 (^{177}Lu) as theranostic pair specifically for neuroendocrine tumours (NETs) (Werner et al., 2015).

In the past few years, extensive investigations of ^{68}Ga applications have been conducted to study its advantages in nuclear imaging. [68]Ga has been labelled with pharmaceuticals such as DOTA-d-Phe1-Tyr3-octreotide (DOTATOC), DOTA-DPhe1-Tyr3-octreotate (DOTATATE) or prostate-specific membrane antigen (PMSA) to form radiopharmaceuticals that have an affinity to specific targets. A particularly advantageous characteristic of ^{68}Ga radiopharmaceutical is that the uptake is not dependent on cell metabolism but provide relevant information based on somatostatin receptor expression. It has also been found that ^{68}Ga radiopharmaceuticals have higher detection accuracy in primary and metastatic NETs compared to using ^{18}F-FDG or ^{18}F-DOPA (Ambrosini et al., 2008, Chen et al., 2017, Kayani et al., 2008,

Janssen et al., 2016, Haug et al., 2012) and prostate cancer (Banerjee et al., 2010, Afshar-Oromieh et al., 2013). ^{68}Ga-labelled radiotracers are efficient in localizing metastases such as medullary thyroid carcinoma (MTC) (Ozkan et al., 2015, Tran et al., 2015) and osteomalacia (El-Maouche et al., 2016). Therefore ^{68}Ga-labelled radiopharmaceuticals are superior for cancer staging (Kroiss et al., 2013, Chang et al., 2016) and could change patient management as well as supported management decisions (Frilling et al., 2010, Naswa et al., 2011, Chen et al., 2017). Additionally, ^{68}Ga radiopharmaceuticals also play an important role in cancer monitoring because of the high sensitivity and specificity uptake in detecting recurrent cancers such as MTC (Ozkan et al., 2015, Tran et al., 2015) and NETs (Haug et al., 2013). Thus, ^{68}Ga radiopharmaceuticals could also be an alternative to the most widely used radionuclide in PET, ^{18}F compounds in imaging studies for tumour angiogenesis (Dijkgraaf et al., 2011), general oncology (Baum and Kulkarni, 2012, Persson et al., 2012), hypoxia(Fernández et al., 2013), tissue proliferation (Pellegrini et al., 2013) and brain tumours (Baum and Kulkarni, 2012, Kilian, 2014).

However, using ^{68}Ga alone in PET imaging does have a contrary effect on image quality compared to [18]F. Table 2.1 shows a comparison of physical properties for ^{68}Ga and [18]F. In most clinical applications, the time between administration and scanning is very important for the proper transfer and distribution of radioisotope from blood to tissues in the entire body and thus to produce a good diagnostic image. Being dependent on the radiopharmaceuticals kinetics and the organ pathology being imaged, is a limiting factor for ^{68}Ga because the half-life is shorter than [18]F. Furthermore, ^{68}Ga produces fewer positrons per disintegration than ^{18}F, meaning fewer annihilations and fewer gamma photons are produced. Therefore, the counts detected are lower than ^{18}F, resulting in relatively high noise and reduced image quality. However, this can be compensated for by either increasing the total scan period, using higher activity (Disselhorst et al., 2010) or using high specificity of pharmaceutical for ^{68}Ga-labeled uptake, for example,

DOTATOC (Sanchez-Crespo, 2013). Since the mean positron energy of ⁶⁸Ga is higher than ¹⁸F, the degradation of image quality is also contributed to by the positron range effect limiting the spatial image resolution explained in the next section.

Table 2.1: Physical properties of ¹⁸F and ⁶⁸Ga (Source: Laboratoire National Henri Becquerel, http://www.lnhb.fr/nuclear-data/).

Radionuclide	¹⁸F	⁶⁴Cu	⁸⁹Zr	⁶⁸Ga	⁸²Rb
Physical half-life (hours)	1.83	12.7	78.42	1.13	0.02
Maximum positron energy (MeV)	0.634	0.653	0.902	1.899	3.381
Probability of positron production per disintegrations	96.86%	17.52%	22.8%	87.68%	81.81%

2.3 Positron Range

2.3.1 Positron range effect

Positron range is defined as the distance between where the positron is emitted and annihilates with an electron. As it is the location of annihilation photon emission which is imaged by PET and not the origin of the decay, blurring effects appear in the reconstructed images (Agbeko et al., 2010), thus reduces image quality (Disselhorst et al., 2010, Park et al., 2007, Johnson et al., 2011) and leads to quantification inaccuracy (Johnson et al., 2011, Sanchez-Crespo et al., 2004). The effect of positron range is dependant on the energy of the positron emission, which is a property of the radioisotope (Cal-González et al., 2013) and the electron density of the medium that the positron travels through (Sanchez-Crespo et al., 2004) The higher the energy of the radioisotope, the longer is the range that contributes to reduced image quality. In addition, positron range contributes greater blur in low electron density media, such as lungs, compared

to the higher electron density media such as bone (Sanchez-Crespo et al., 2004). Moreover, the characteristic of blurring is independent of the system settings (Kemerink et al., 2011, Blanco, 2006), thus making it a critical factor of image quality degradation and leading to diagnostic misinterpretation. Therefore, the positron range effect must be corrected if accurate quantification in PET studies is desired.

2.3.2 A model of PET image formation

The PET image formation can be described as a convolution of the original image, $f(x)$ which contains the true activity distribution, with the system response function of the imaging system, $h(x)$ to produce a degraded PET image, $g(x)$. In the spatial domain, this can be represented as:

$$g(x) = f(x) * h(x) \tag{2.20}$$

The objective of image restoration is to obtain an improved estimate, $f'(x)$, of the original image, $f(x)$. Generally, the more detailed the information of $h(x)$ we have, the closer $f'(x)$ will be to $f(x)$, or that a more accurate restoration of $f(x)$ can be achieved. Hence, the, $h(x)$ can be modelled for a specific reconstructed image, system matrix and reconstruction algorithm. This system matrix includes various resolution degrading effects within the PET image reconstruction task to be addressed for. The system matrix is used to convert from measurement space to image space, so its dimensionality is the size of (measurement-space)*size of (image-space). Since it is impractical to calculate, it can be calculated on a LOR basis.

System matrix in image space in eq (2.20) is referred to as System-Transfer-Function, P is comprised of five components (Bai et al., 2003):

$$P = P_{norm}P_{blur}P_{attn}P_{geo}P_{range} \tag{2.21}$$

where P_{norm} is a matrix account for normalization factors for unscattered events; P_{blur} is an image space correction that accounts for: the non-collinearity of photons, the scattering of photons from one crystal to another and inter-crystal penetration before being stopped; P_{attn} is a matrix containing attenuation correction factors for each detector pair; P_{geo} is a matrix containing the geometrical mapping between the source and data to describe the probability that a photon pair reaches the front faces of a detector pair in the absence of attenuation and assuming perfect photon pair collinearity; and P_{range} is a local blurring operator applied in the image space that represents the positron range effect.

2.3.3 Positron range correction

The main goal of positron range correction (PRC) is to improve the PET image by restoring as accurate as possible the original image, $f(x)$. Two types of PRC are used for positron range correction strategies to improve PET image quality and quantification due to the positron range effect. The first type is direct Fourier deconvolution and the second is introducing the positron range effect into iterative image reconstruction algorithms. The second strategy is applied in the statistical iterative reconstruction algorithms such as maximum a posteriori (MAP) and MLEM.

2.3.3.1 Fourier deconvolution

The first type of PRC was first applied in a simulation study using a water medium (Derenzo, 1986), using inverse filtering in a Fourier deconvolution method. Thus, inverse operation or deconvolution can restore the true image by removing the positron range function

and can be achieved by dividing the Fourier transform of the recorded image with the Fourier transform of the positron range distributions.

The deconvolved projection data was computed as the inverse Fourier transform and assessment of the correction method was determined by calculating the root-mean-squared deviation (RMSD) between the initial projection data, T and the blurred projection data, B:

$$RMSD = \sqrt{\frac{1}{n}\sum_{i=1}^{n}[(B_i - T_i)/T_i]^2} \qquad (2.22)$$

The RMSD before and after correction were compared. It was found that this method significantly reduced systematic errors due to positron range, thus improving quantitative accuracy. However, the deconvolution process significantly increased the statistical noise, especially in radioisotopes emitting high energy positrons. Moreover, this study was limited to water only without considering other media with different densities such as bone and lung.

The application of Fourier deconvolution to remove positron range blurring was extended experimentally using a flood phantom and incorporating it into the filtered back-projection (FBP) reconstruction algorithm, hence without increasing computational time (Haber et al., 1990) and the improvement in image quality was assessed. This was achieved by computing a new filter, R' define as:

$$R' = R/D \qquad (2.23)$$

where R was the Fourier transform of the reconstruction filter, such as Shepp-Logan or Butterworth filters, and D was the Fourier transform of the positron range function. Therefore, the Fourier transform of the ideal projection data, S was obtained using:

$$S = P * R' \qquad (2.24)$$

At this stage, the result, S was then inverse-transformed and backprojected to form the corrected image. By including the reconstruction filter parameter, the noise amplification effect was reduced by adjusting the high-frequency response of the reconstruction filter to balance between the level of restoration and the noise in the reconstructed image.

The experimental study (Haber et al., 1990) shows promising positron range correction in water medium to simulate soft tissue. Using a ^{18}F phantom image as a gold standard, the range correction method reduced the full-width-half-maximum (FWHM) and full-width-tenth-maximum (FWTM) values ^{68}Ga and ^{82}Rb phantom images to close to the gold standard. However, reducing the statistical noise by adjusting the frequency response parameter was not practical because it could not recover the full resolution loss. Moreover, this method was based solely on estimation in a water medium representing the soft tissue, which is problematic as there is not much pure water in the body except in the bladder. Inverse filtering also disregards the type of tissue in which the positron travels, resulting in inaccuracies in non-soft tissue media such as lungs and bones.

2.3.3.2 Resolution modelling

The second approach to PRC was introducing the positron range effect into the process of iterative image reconstruction. It can be conducted in 2 different ways. First, introducing the positron range blurring into the factorized system matrix, eq 2.22, using a resolution modelling method (Rahmim et al., 2008, Bai et al., 2003, Kotasidis et al., 2014). The effect of positron range was represented as a discrete blurring kernel in homogeneous or heterogeneous medium and was directly incorporated into system matrix through the P_{range} factor (Bing et al., 2005) during the reconstruction. The second technique was to employ a positron range kernel as an additional

blurring to the object. The blurring was introduced in image reconstruction, particularly during the forward projection process (Cal-González et al., 2009, Bertolli et al., 2016, Fraile et al., 2016, Kraus et al., 2012). The summary of the process can be seen in figure 2.13. In this case, the system matrix should not incorporate the positron range effects.
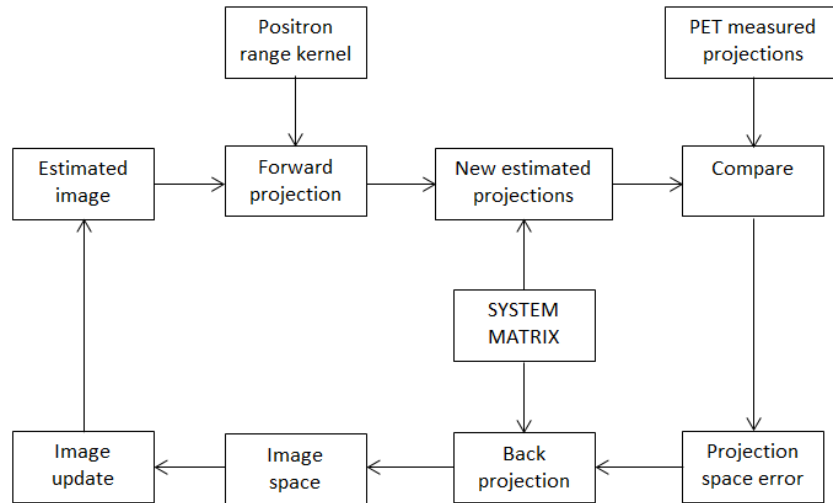
Figure 2.13: Flow diagram of iterative reconstruction algorithm and employment of positron range kernel during forward projection process.

Implementation of PRC during image reconstruction allows for adapting the local properties of the object, such as electron density, which influences the magnitude of blurring. Therefore, the blurring kernel calculated using MC simulation considering the density of the materials can be employed in this algorithm. The application of the technique significantly improved the contrast and resolution of the resulting PET image.

2.3.4 Positron range modelling in heterogeneous medium

Positron range shows a complex effect at the boundary of different tissues. For example, positrons emitted near the lung boundary can travel a longer distance than soft tissue and bone. Thus, using space-invariant deblurring kernels for heterogeneous objects is not sufficient and can result in artefacts, particularly at the boundaries of media (Bai et al., 2003). A similar artefact was also observed in PET imaging of thyroid glands near the trachea (Abdul-Fatah et al., 2009). Incorporating a heterogeneous positron range correction within the image reconstruction algorithm makes it possible to address this kind of artefact.

Space-variant analytical filtering approaches were proposed to correct positron range in heterogeneous media by performing successive convolution operations of tissue-dependent kernels to determine positron range models across boundaries (Bai et al., 2003). The shift-variant blurring model approximates the propagation and annihilation of positrons in the media. This was achieved by performing successive convolutions of tissue-dependent range kernels to model positron range across boundaries, where each convolution tracks the positrons annihilations and surviving positrons, respectively. Convolutions were repeated until all positrons are annihilated or escape the subject. At each convolution stage, the surviving positrons have lower energy than in the previous stage leading to the increased probability of annihilations within the next stage. Annihilation by positrons whose trajectories do not leave the region of interest was also recorded. These properties allowed for inhomogeneities within the subject to be modelled and employed in the system matrix. However, its accuracy deteriorates when approaching tissues boundaries.

An analytical method to generate a spatially-variant kernel for positron range correction in the heterogeneous medium was performed first by averaging the fitting parameters of the 1D annihilation distributions for originating and target voxels (Alessio and MacDonald, 2008). Then, the positron range kernel was derived according to:

$$\hat{P}_{ot} = \bar{C}_{ot}.e^{-\overline{k1}_{ot}d_{ot}(x)} + (1 - \bar{C}_{ot})e^{-\overline{k2}_{ot}d_{ot}(x)} \qquad (2.25)$$

where d_{ot} is the distance from originating voxel, x_o to a target voxel, x_t, $\bar{C}_{ot}$ is the average of C fitted parameters from voxels x_o and x_t and $\overline{k1,2}_{ot}$ is the average parameters from voxels x_o and x_t.. The 3D PR kernels are then generated and stored in a sparse matrix. Using information from CT images to provide an object attenuation map, the implementation of the positron range compensation was applied in a modified OSEM algorithm. In clinical PET, it was shown to produce sharper boundary definition with little to no tails at the water/lung boundary edge. This method was fast yet crude for implementing PR correction because they were averaging the fitted parameters to adjust variations across boundaries that do not accurately represent positron migration's complexity within different density media. In addition, the method does lead to hyper-resolved boundaries (Alessio and MacDonald, 2008). Figure 2.14 shows an example of 2D blurring kernels for ^{82}Rb derived from eq. 2.25.
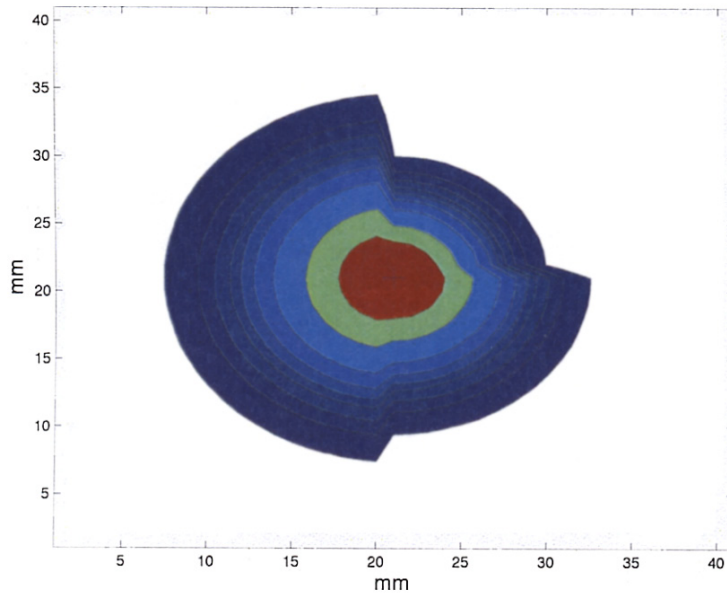
Figure 2. 14 : ^{82}Rb blurring kernel in the lung (left half of the plot), rib bone (upper right quadrant) and water (lower right quadrant). The FWTM is plotted in green and FW at 200th maximum is the most extreme contour plotted.

Finally, the spatially-variant positron range correction was efficiently implemented in resolution modelling, which yields artefact-free reconstructed images when the activity is placed close to tissue boundaries or in heterogeneous media (Cal-Gonzalez et al., 2015a, Cal-Gonzalez et al., 2018b). This was first achieved by generating the material-dependent profiles using MC simulation, which could model complex structures of biological tissues in a heterogeneous medium if sufficient details about the attenuation media are available. After that, the profile was scaled by the density of the material. The profiles also took into account the different materials that the positron travels through until it annihilates. This information was provided from the coregistered CT image, which was segmented to define 4 different tissues: air, lung, water, and bone. Finally, the knowledge of each profile was adapted to compute a universal positron range curve for each radionuclide, which was derived from simulations in water. With that, the authors avoid the need to compute positron range distributions for each tissue and increase computational speed during the correction of positron range during reconstruction.

2.4 Post-Reconstruction Positron Range Correction

As mentioned in the preceding paragraph, the method to model tissue-dependent and spatially-variant (TDSV) PR kernel and employed in resolution modelling (figure 2.13) results in an artefact-free image after PRC (Cal-Gonzalez et al., 2015a, Cal-Gonzalez et al., 2018b). The authors extended their study by developing the post-reconstruction PRC by using the Richardson-Lucy deconvolution algorithm (Cal-Gonzalez et al., 2018a):

$$u_j^{k+1} = u_j^k \times \Sigma_i \frac{x_i}{\Sigma_j P_{ij} * u_j^k} * P_{ij} \qquad (2.26)$$

where the division and multiplication are elementwise, u_j^{k+1} is an updated image at k+1 iteration, u_j^k is current image estimate at k[th] iteration, x_i is a reconstructed image, P_{ij} is PR kernel and * is a convolution. With the assumption of standard reconstruction image representing the positron annihilation points and hypothesis of the post-PRC method results in the image representing the positron emission points, no detailed explanation regarding results was reported. However, the authors claimed that the initial pre-clinical and phantom clinical studies conducted for validation provides accurate results and can be easily applied to any preclinical or clinical PET system. The methodology proposed was described below:
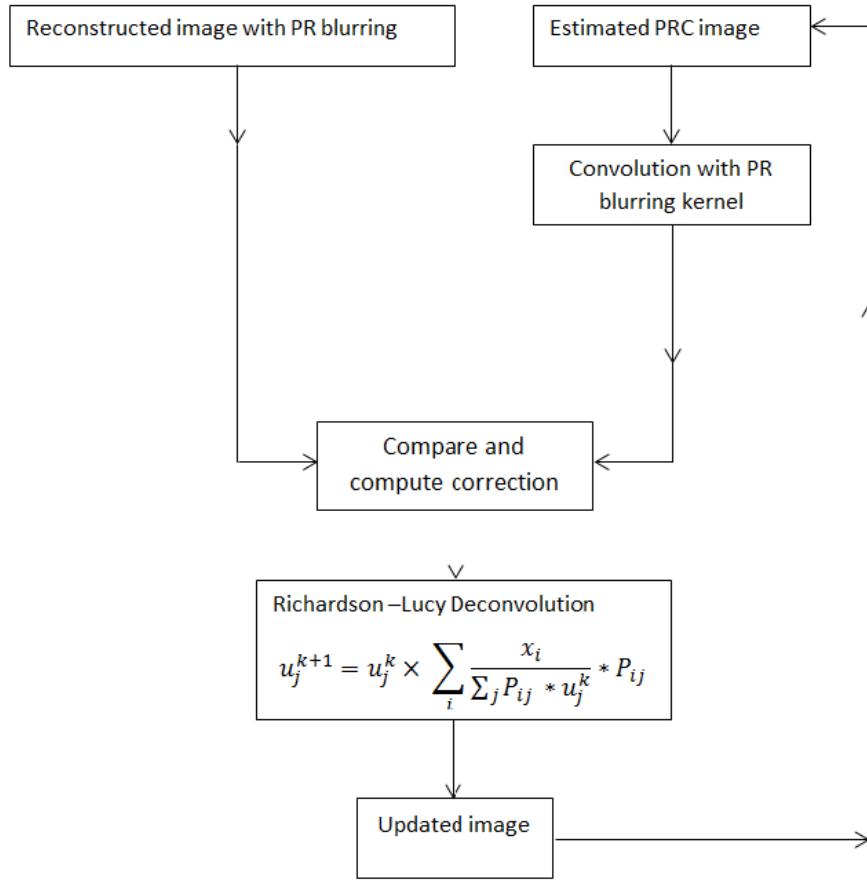
Figure 2.15:Schematic representation of the image-based positron range correction using iterative Richardson-Lucy algorithm with a spatially variant PR blurring kernel.

This approach was expanded into a patients study where the image quality of corrected and uncorrected was evaluated by 2 nuclear physicians (Berger et al., 2019). Although the attenuation map used only defined 4 different tissues, the implementation of this approach in patients study demonstrates an artefact-free of images, with mild improvement of contrast and spatial resolution but moderate degradation of noise.

2.5 Image Space Reconstruction Algorithm

This thesis was desired to explore and investigate a robust method of iterative PRC that can be applied after image reconstruction, without a need to model the PR kernel. So, the most

important aspect was to find the appropriate and reliable method of calculating the image error in the image space for updating and subsequently generate a sequence for iteration in the same space.

The initial theory of post-reconstructed PRC in this thesis was deduced from the idea of iterative image space reconstruction algorithm (ISRA) (Daube-Witherspoon and Muehllehner, 1986). Historically, the ISRA proposed to overcome the computer's memory capabilities during typical emission image reconstruction that need to handle excessive large arrays of data. The authors demonstrated that if the data are back-projected directly into 3D image volume, the computer memory requirement was greatly reduced due to compressing the large sparsely projection matrix into a compact data image matrix. Although the convergence speeds between EM and ISRA were comparable (Archer and Titterington, 1995), the latter algorithm requires less calculation per iteration than EM when the number of detector pairs is large (Daube-Witherspoon and Muehllehner, 1986). They also suggested that this approach was achievable when the sinogram was unavailable, or Fourier-based reconstruction was not applicable.

The ISRA was based on the modification of expectation maximization (EM) algorithm applied to the maximum likelihood algorithm (ML) and used back-projected of the measured projection data as input. The difference between the two algorithms relied on how the error image was calculated. While the image error of EM is determined in sinogram space, the image error of ISRA is determined in image space.

The notation is as follows with terminology as in eq. 2.14 in subsection 2.1.4.2. There are I source pixels, with the ith of which has emission density, a_i. Referring again to eq. 2.14, as $M_{i,j}$ is the probability that radiation emitted from the pixel i will be detected is assigned to projection j, with

$$\sum_i M_{i,j} = 1. \tag{2.27}$$

The inner product of the jth row of a matrix M_j and a vector a was denoted by

$$< M_j, a > = \sum_i M_{i,j} \, a_i \tag{2.28}$$

To estimate the emission density, a_i ($1 \le i \le I$) given the measured intensity in the jth projection element, p_j ($1 \le j \le J$), with the assumption that the $M_{i,j}$ are known, the EM algorithm generates a sequence of sets of estimates (a_i^k), according to the following iterative step. For each k=0,1,…., and for each $i = 1, \ldots.I$. Therefore, the iterative procedure derived by (Daube-Witherspoon and Muehllehner, 1986) for reconstructing the a_i, given the starting point $a_i^0 > 0$, is as follows (De Pierro, 1987):

$$a_i^{k+1} = a_i^k \times \frac{<M^i, p>}{<M^i, ma^k>} \tag{2.29}$$

where M^i is the columns of the matrix $m = \{M_{i,j}\}$ and p the measurement vector. The updating process was multiplying the original guess by an error image on a pixel basis, where it was defined by computing the ratio of back-projecting the measured data and back-projecting the calculated projections, denoted by $< M^i, p > / < M^i, ma^k >$. The flow diagram of ISRA algorithm implementation was shown in figure 2.16 (Daube-Witherspoon and Muehllehner, 1986), where the initial estimate is the image reconstructed by a simple, unfiltered backprojection to produce a 'raw' reconstructed image as explained in subsection 2.1.4.1. Hence, this initial estimate will not alter the result.
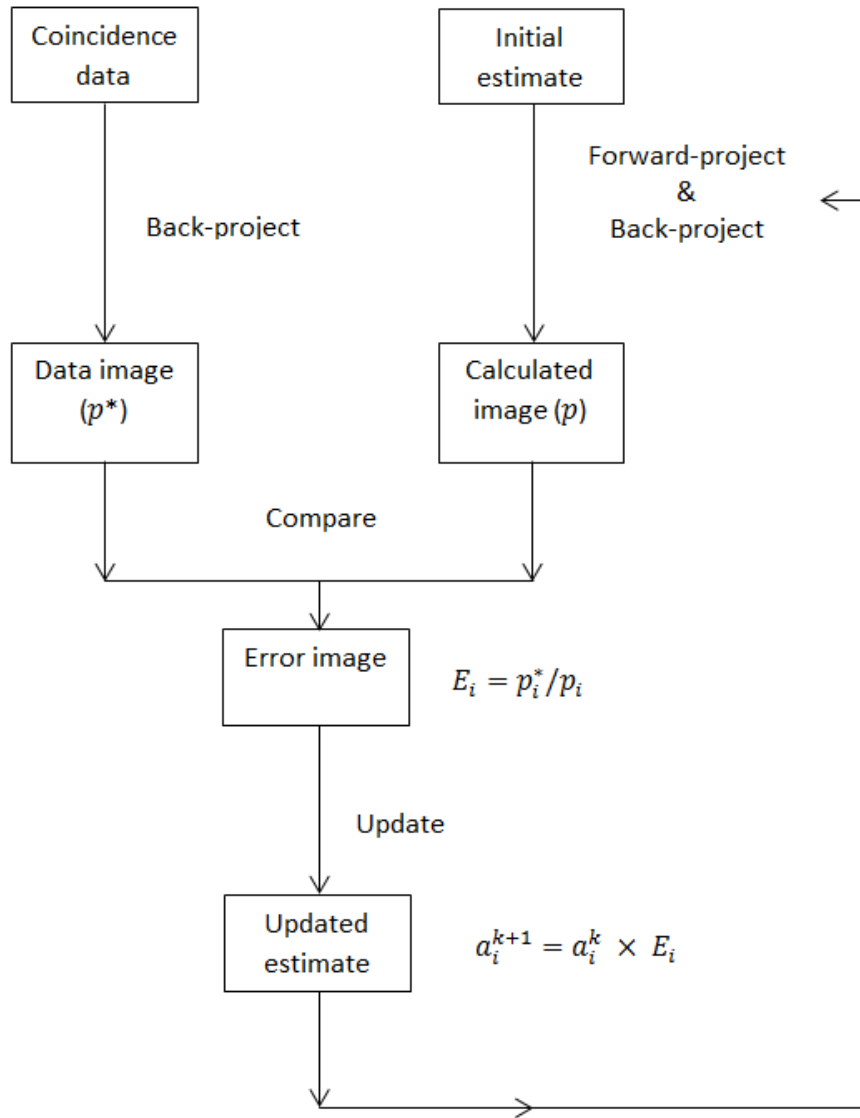
Figure 2.16: Schematic illustration of the steps in ISRA implementation.

The ISRA was proven to converge to non-negative least-squares (LS) (Titterington, 1987, Archer and Titterington, 1995, De Pierro, 1987). However, in terms of asymptotic theory, the resulting LS was inferior to the ML estimators, suggesting that using the weighted least-squares (WLS) criterion might improve the least-square procedure.

A study was conducted to investigate the use of WLS in ISRA, thus proposed a more general iterative reconstruction algorithm (Reader et al., 2011). Using a preceding notation, the WLS objective function, O_{WLS} which depended on the I-dimensional PET measured data vector, p_i and J-dimensional image estimate vector, a^k:

$$O_{WLS}(a^k) = \frac{1}{2}\sum_i^I \frac{\left(m_i - q_i^k\right)^2}{wls_i} \tag{2.30}$$

where wls is the weight and the expected data given image estimate, a^k are given by

$$q_i^k = \sum_{j=1}^J M_{ij}\, a_j^k + \cap \tag{2.31}$$

with M_{ij} is the probability that radiation emitted from the pixel i will be detected is assigned to projection j, the imaging system model was given by the matrix m= $\{M_{ij}\}_{I \times J}$ and $\cap$ accounts for the scatter and randoms event encountered in PET.

Reducing the O_{WLS} was performed for a better image estimate of a. This can be achieved by considering the gradient of the objective function:

$$\frac{\partial}{\partial a_j^k} O_{WLS}(a^k) = -\sum_{i=1}^I \frac{M_{ij}\left(p_i - q_i^k\right)}{wls_i} \tag{2.32}$$

$$= \sum_{i=1}^I \frac{M_{ij}q_i^k}{wls_i} - \sum_{i=1}^I \frac{M_{ij}p_i}{wls_i} \tag{2.33}$$

At this stage, the right-hand side of e.q 2.32 was the backprojection of weighted expected data minus the backprojection of the weighted measured data. A simple iterative algorithm can be derived to minimize the O_{WLS} by subtracting a variably-scaled amount of this gradient image:

$$a_j^{k+1} = a_j^k - \tau_j^k \left[\sum_{i=1}^I M_{ij}\frac{q_i^k}{wls_i} - \sum_{i=1}^I M_{ij}\frac{p_i}{wls_i}\right] \tag{2.34}$$

With τ_j^k is the scaling step size for each voxel for a given iteration, k, the following iterative update obtained below, just by using a ratio of weighted measured-backprojection and weighted expected-backprojection.

$$a_j^{k+1} = a_j^k \times \frac{\sum_{i=1}^{I} M_{ij}\frac{p_i}{wls_i}}{\sum_{i=1}^{I} M_{ij}\frac{q_i^k}{wls_i}} \tag{2.35}$$

If the weights are chosen to be $wls_i^k = 1$, then ISRA is obtained below and similar as e.q 2.28:

$$a_j^{k+1} = a_j^k \times \frac{\sum_{i=1}^{I} M_{ij}p_i}{\sum_{i=1}^{I} M_{ij}q_i^k} \tag{2.36}$$

Hence, the post-reconstructed iterative algorithm derived as eq. 2.29 and eq.2.36 was used as a foundation of the PRC developed in the next chapter.

2.6 Summary

From the review, it is noted that positron range imposes blurring, which occurs in image space. The blurring effect is independent of the tomographic imaging process or scanner setting and parameters. Hence, correction for positron range by modifying or adjusting the corresponding factors mentioned above is not feasible.

PRC methods have been developed to address the impact of the positron range. It can be concluded that all the correction methods reviewed were performed during the image reconstruction, given that the PET raw data and blurring kernel are available. Only one method so far has investigated the attempt to correct the positron range after image reconstruction. However, rigorous and detailed results have not yet been identified and published. To our knowledge, the method's potential has not yet been fully explored and it is of interest to know whether the post-reconstructed PRC without modelling the PR kernels can be implemented.

Therefore, this thesis will focus on developing the PRC implemented in reconstructed images and exploring its potential in clinical PET imaging.

Chapter *3*

Effect of Positron Range on Image Performance of ^{68}Ga PET

3.1 Introduction

Positron emission tomography (PET) spatial resolution and system sensitivity performance are important to accurately visualise and quantify the radiopharmaceutical distribution in biological systems. PET spatial resolution, which is the focus of this study, is influenced by factors including the physics of positron decay, photon interaction in the detectors and the detector material and geometry (Moses, 2011). After the decay of a positron-emitting nucleus, the positron travels a short distance via a tortuous path, depositing some of its energy along that path while approaching its resting energy of 0.511 MeV. When the positron particle is at or near its resting state, it annihilates with an electron, subsequently producing two back-to-back annihilation photons with 0.511 MeV each. The distance between the positron emission and annihilation locations is called the positron range. The 'effective positron range' is the average distance from the emitting point to the end of the positron track. In particular, due to the nature of the imaging geometry, the important distance is measured perpendicular to the direction of the annihilation photons (Cherry et al., 2012). The effective or mean positron range is always shorter than the exact range in the positron decay mechanism. The range is proportional to the positron energy and inversely proportional to the electron density of the medium in which it travels. As the PET scanner images the density of

annihilations rather than positron emissions, the effective positron range limits the achievable spatial resolution in PET (Alva-Sánchez et al., 2016).

Positron range is thought to be a significant problem in preclinical PET because it makes a significant contribution to the overall spatial resolution of approximately 1 mm FWHM (Goertzen et al., 2012, Yang et al., 2016). Furthermore, the blurring effect caused by positron range causes measurable spatial resolution degradation even for low energy radioisotopes (Levin and Hoffman, 1999) and loss of contrast in mouse and rat brains for ^{18}F and is more severe for more energetic positron emitters such as ^{15}O (Vázquez Canelas et al., 2016).

Historically, the positron range effect has been considered less relevant for clinical PET due to the relatively poorer spatial resolution of this system and almost exclusive use of ^{18}F. However, with progressive improvement of the PET scanner performance, as explained in chapter 1, section 1.1, the spatial resolution of current clinical scanners approaching 3 mm FWHM as results from smaller detector elements (Casey et al., 2017, Cherry et al., 2018). Hence, the positron range has become one of the important factors in image degradation that needs to be considered

Also, the clinical use of higher energy beta emitters such as ^{68}Ga (E_{max} 1.99 MeV), has grown rapidly in recent years, especially in cancer imaging as discussed in chapter 2, section 2.2. This is due to the availability of commercial ^{68}Ge generators that produce ^{68}Ga on-site and the ease with which important biomolecules can be labelled with ^{68}Ga directly (e.g. prostate-specific membrane antigen (PSMA) (Afshar-Oromieh et al., 2013), via chelating agents such as DOTA (Shetty et al., 2010). In addition, ^{68}Ga-labelled pharmaceuticals could be an alternative to ^{18}F-labelled pharmaceuticals due to their high performance in uptake (Dijkgraaf et al., 2011, Baum and Kulkarni, 2012, Persson et al., 2012, Fernández et al., 2013, Pellegrini et al., 2013). Its simple

radiopharmaceuticals labelling with minimum loss of activity also make ^{68}Ga-labelled pharmaceuticals a potential substitute to ^{99m}Tc-labelled pharmaceuticals in SPECT imaging (Kilian, 2014, Fellner et al., 2012, Yang et al., 2010, Choi et al., 2011). It has also been demonstrated that ^{68}Ga-labelled pharmaceuticals have superior sensitivity and specificity in NETs detection as compared to ^{111}In-labelled pharmaceuticals and ^{18}F-labelled PET/CT metaiodobenzylguanidine (MIBG) scintigraphy and magnetic resonance imaging (MRI) (Mojtahedi et al., 2014). ^{68}Ga-labelled pharmaceuticals also provide lower radiation exposure compared to ^{111}In-labelled pharmaceuticals and ^{18}F-labelled PET/CT (Walker et al., 2013) due to their higher affinity to the somatostatin receptor and shorter scan time (Sharma et al., 2014). Therefore, re-evaluation of the impact of positron range on clinical PET imaging performance is becoming essential.

Published experimental and simulation studies have focused on investigating positron range effects in air, water and other tissue-equivalent materials (Alva-Sánchez et al., 2016, Sanchez-Crespo et al., 2004, Kemerink et al., 2011, Disselhorst et al., 2010, Cal-González et al., 2011). However, these studies include PET scanner geometry and filtering, which are expected to further contribute to the blurring of the reconstructed image. The total system resolution of a PET scanner is obtained by the combination of these individual factors (Saha, 2016, Lecomte, 2009):

$$R_{sys} \approx k \sqrt{R_{det}^2 + R_{loc}^2 + R_{noncol}^2 + R_{pos}^2} \qquad (3.1)$$

where R_{sys} is system resolution, k is a factor accounting for the blurring that occurs during tomographic reconstruction ($1 \le k \le 1.3$); R_{det} is the intrinsic resolution of the detectors that considers the geometrical response midplane between coincident detector elements size; R_{loc} is

detector positioning accuracy resulting from crystal identification algorithm or depth-of-interaction (DOI) algorithm; R_{noncol} is the non-collinearity effect and R_{pos} is the mean positron range.

It is very challenging to conduct a physical experiment to measure the positron range alone as it is at sub-mm to mm. Moreover, the physical experiment will involve the detector system with limited spatial resolution, efficiency, attenuation, and noise. When these effects are included, the investigation of blurring caused by positron range only becomes impossible. However, the a simulation experiment can model the positron range effect without including any scanner and acquisition effect as stated in eq.3.1, thus providing a ground truth measurement for assessing quantitative accuracy.

Monte Carlo (MC) simulations are extensively used in nuclear medicine to develop, validate, and evaluate scanner devices, image reconstruction algorithms, or data correction techniques where the physical experiment study is not practical. The Geant4 Application for Tomographic Emission (GATE) toolkit used in this thesis is an advanced open-source MC simulation software for numerical simulations in medical imaging, such as PET and SPECT (Jan et al., 2004), radiotherapy and dosimetry (Sarrut et al., 2014). It is based on the complete range and advantages of Geant4 Monte-Carlo simulation libraries to produce simulations of nuclear imaging data through particle and photon tracking in various settings, including sophisticated detector geometries and well-validated physics models (Agostinelli et al., 2003). The architecture of GATE consists of four layers which are Geant4, core, application and user layers. The core layer defines the main tools and features of GATE using C++. The application layer is an extension of the core layer to handle more specific modelling. Finally, Geant4 provides a mechanism to run simulations interactively or batch-wise using scripts in the user layer. Hence, the GATE end-user does not require experience in programming; instead, dedicated scripting is

provided that extends the generic command interpreter of Geant4 to perform and control Monte-Carlo simulations.

This simulation study aimed to characterize ^{68}Ga positron range distribution in different radioisotope-medium combinations and investigate the impact of positron range blurring on spatial resolution, contrast recovery and quantitative accuracy of PET images. Results from ^{68}Ga were compared to ^{18}F, which have lower positron energy than ^{68}Ga. Investigation on how these metrics are impacted by sampling the reconstructed image (i.e. pixel size) was also conducted. The method to study the effect of positron range on image performance is fundamentally different from the approaches proposed in the literature. Since the effect of positron range blurring is independent of the PET scanner system, blurring effects other than those induced by the positron range effect, R_{pos} were omitted. Thus, blurring effects R_{noncol}, R_{det} and R_{loc}, were excluded from this study, as was the image reconstruction process and filtering effect, k. Due to that, the total PET spatial resolution in this phantom simulation study was only estimated by the mean positron range as below:

$$R_{sys} \approx \sqrt{R_{pos}^2} \qquad\qquad (3.2)$$

3.2 Methods

Monte-Carlo simulation was used in this study as it is a feasible approach to investigate the blurring effects induced by the positron range only. Simulations were performed of positron-emitting point sources in homogeneous media of bone, water and lung for ^{18}F and ^{68}Ga using GATE (Agostinelli et al., 2003). A one-dimensional (1D) annihilation point spread function (aPSF) was derived from three-dimensional (3D) annihilation coordinates and parameterized using functions with two exponential terms. The fitting parameters for each radionuclide-

medium combination were used to compute a two-dimensional (2D) blurring kernel. Then, the true simulated image was convolved with the positron range blurring kernel at high spatial sampling to emulate the positron range blurring occurs with infinite resolution in the physical world. This study design seems to provide a better understanding of how the positron range blurring induced impacted image performance. After that, images were down-sampled also to study the influence of reconstructed pixel images on image performance.

3.2.1 Positron range modelling in homogeneous media

A 0.01 mm radius spherical point source of ^{18}F and ^{68}Ga was simulated at the centre of a $30 \times 30 \times 30$ (cm)^3 of a homogeneous medium using GATE (Jan et al., 2004). Bone, water and lung were simulated separately to represent a range of electron densities present in human tissue. Densities were assigned according to the International Commission on Radiation Unit and Measurement (ICRU-44): 1.92 g/cm^3 (bone); 1.00 g/cm^3 (water); and 0.26 g/cm^3 (lung) (1989). During the GATE simulation, the following physical interaction processes were included: ionisation, Bremsstrahlung, positron annihilation, and multiple scattering. Approximately 5 million events were simulated for each radioisotope and medium combination, which took approximately 60 seconds per simulation to complete.

The mean and maximum positron range were obtained from the simulation and the annihilation coordinates in 3D were recorded and used to plot the 1D aPSF projected on the x, y and z, respectively, to show that the aPSFs are rotationally symmetric (Alva-Sánchez et al., 2016, Levin and Hoffman, 1999, Cal-González et al., 2013, Sanchez-Crespo et al., 2004). This distribution contributes directly to the spatial image resolution (Blanco, 2006). The 1D aPSF for different radioisotope-medium combinations were plotted using histograms (100 bins of 15 μm

except for ^{68}Ga in the lung for which the bin size was 35 µm). Each 1D aPSF was fitted using functions with two exponential terms:

$$P(x) = A \cdot e^{-Bx} + C \cdot e^{-Dx}, \; x \geq 0 \qquad (3.3)$$

where *P(x)* is the 1D distribution, while *A, B, C* and *D* are the fitting parameters. The 1st exponential coefficient (B) accounts for the fast decaying part of the aPSF, which has a low exponential constant. Hence, the B value is sensitive to the bin size chosen (Cal-González et al., 2013). Thus, it should not be compared to other values reported in the literature. The 2nd exponential coefficient (D) accounts for the tail of the aPSF, which is broader and a meaningful parameter to compare with other reported values (Cal-González et al., 2013).

3.2.2 Blurring kernel

The aPSF was obtained from the annihilation coordinate for each vector. Since the simulation of annihilation events was performed in a homogeneous medium, the 1D aPSF is isotropic and rotationally symmetric for each vector. The 1D aPSF was halved and the cusp-shaped distribution was fitted using a two-exponential function (Eq. 3.3). Fitting coefficients were used as input to generate a 2D blurring kernel at interval sampling of 0.1 mm. The blurring kernel is a 2D matrix whose elements have values according to the number of events within the corresponding area normalized by the total number of events. The goodness of the fitting was evaluated by R^2 (R=0 being the worst and R=1 being a perfect fit).

3.2.3 Simulation image

In order to measure the effect of positron range blurring in different materials, first, a noise-free 2D NEMA image quality phantom was simulated, based on a CT-segmented image, using a threshold of 1200 HU. The resulting simulated image spheres were 10.7, 12.4, 14.6, 18.5, 21.4 and 28.2 mm in diameter, with a target-background ratio of 8:1. Then, to emulate the positron range effect in different radioisotope-medium combinations, the image was convolved with the respective blurring kernel at a high spatial sampling of 0.1 mm, ensuring sub-pixel effects were considered. Subsequently, the image was down-sampled to pixel sizes of 0.5 mm, 1.0 mm, 2.0 mm and 4.0 mm. Finally, Poisson noise with a standard deviation of 10% of the mean counts was generated to replicate typical imaging conditions. The resulting images were zoomed by a factor of three for analysis.

3.2.4 Image analysis

The impact of positron range and image sampling (pixel size) was determined using measures of spatial resolution, contrast and activity loss for each simulated image. Since the positron range function is cusp-shaped, the long exponential tails affect edge sharpness and contrast in the PET image. Hence, Full-Width-Tenth-Maximum (FWTM) is the most appropriate metric to describe the impact of blurring on the image. A vertical line profile was drawn at the middle slice of the transverse plane sphere (figure 3.1) and fitted using a Gaussian fit. As a measure of the effect of positron range on the distortion of reconstructed lesions, we defined a metric called the spatial resolution residual as the difference between the actual diameter of a sphere and its measured FWTM. The Full-Width-Tenth-Maximum residual (FWTMr) was measured for the 10.7 mm sphere size, which is the smallest sphere. The contrast

and count loss measurements used an 8 mm diameter ROI, drawn at the centre of the sphere (figure 3.2). The FWTMr, contrast and activity loss were calculated as follows:

$$FWTMr\ (mm) = \left[\frac{FWTM - True\ size}{True\ size}\right] \qquad (3.4)$$

$$Contrast = \frac{C_t - C_b}{C_t + C_b} \qquad (3.5)$$

$$Activity\ loss(\%) = \frac{C_T - C_{T'}}{C_T} x100 \qquad (3.6)$$

where C_t is the count in the target, C_b is the count in the lesion background, C_T is count in the true image and $C_{T'}$ is the count in the convolved image.
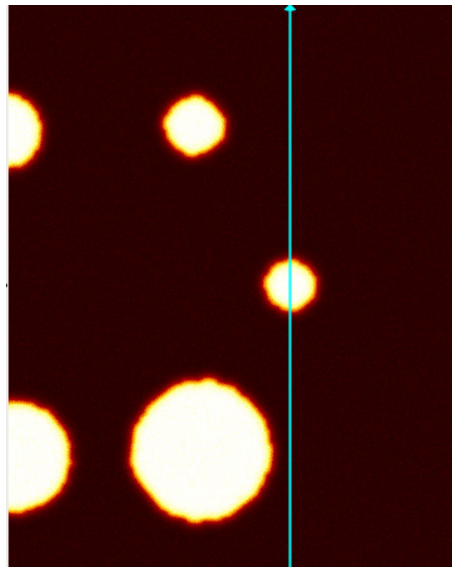
Figure 3. 1: Vertical line profile drawn at the middle slice of the transverse plane for 10 mm sphere.
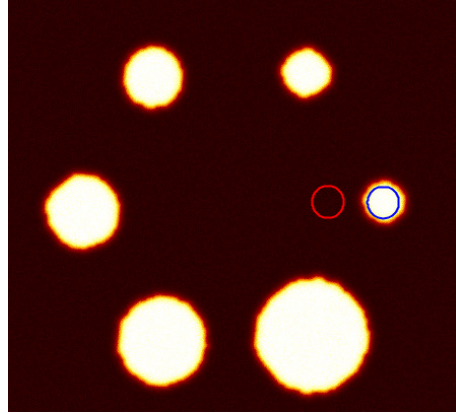
A) The blue and red circles in the convolved image, in this case in bone medium, indicate the ROIs placement for the count in the target, C_t and the count in the target, C_b , respectively.
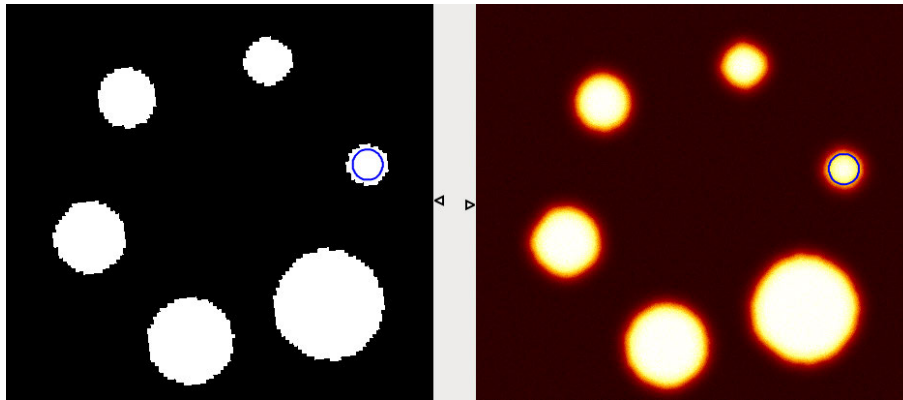
B) The left image indicates the ROI placement for the count in the true image, C_T and the right image for the count in the convolved image, $C_{T'}$, in this case in a bone medium.

Figure 3. 2: ROIs placement for the A) equation 3.5 and B) equation 3.6.

3.3 Results

3.3.1 Maximum and mean positron range

Figure 3.3 shows the simulated positron energy distribution of ^{18}F and [68]Ga. Figure 3.4 illustrates the radial positron range distribution in bone, water and lung for ^{18}F and [68]Ga. The distributions for these two radioisotopes are wider in the lung which has the lowest density

medium, followed by water, then compact in bone, which has the highest density. For ^{18}F, it can be seen that the maximum positron range is the highest in the lung with 8.22 mm, followed by 1.78 mm in water and 0.89 mm in the bone. The same trend results were obtained for ^{68}Ga where the highest maximum positron range occurs in the lung with 32.67 mm, followed by 8.44 mm in water and 3.70 mm in the bone. From these results, it is clear that ^{68}Ga has a substantially higher maximum positron range than ^{18}F in all media.
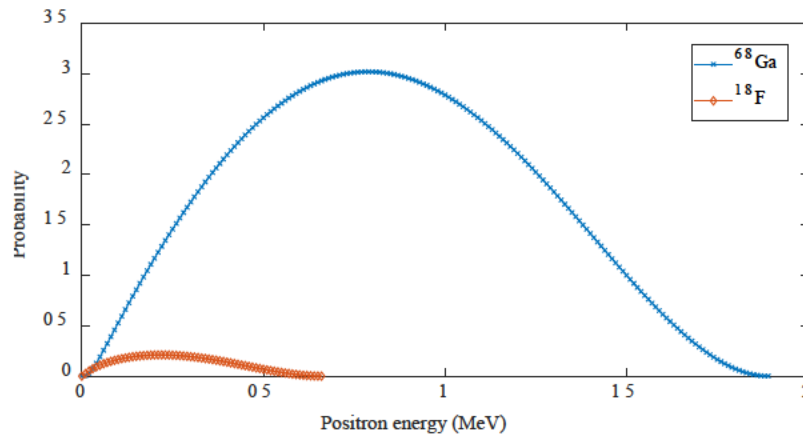
Figure 3.3: Positron energy distribution of ^{18}F at energy maximum of 0.66 MeV and ^{68}Ga at energy maximum of 1.89 MeV.
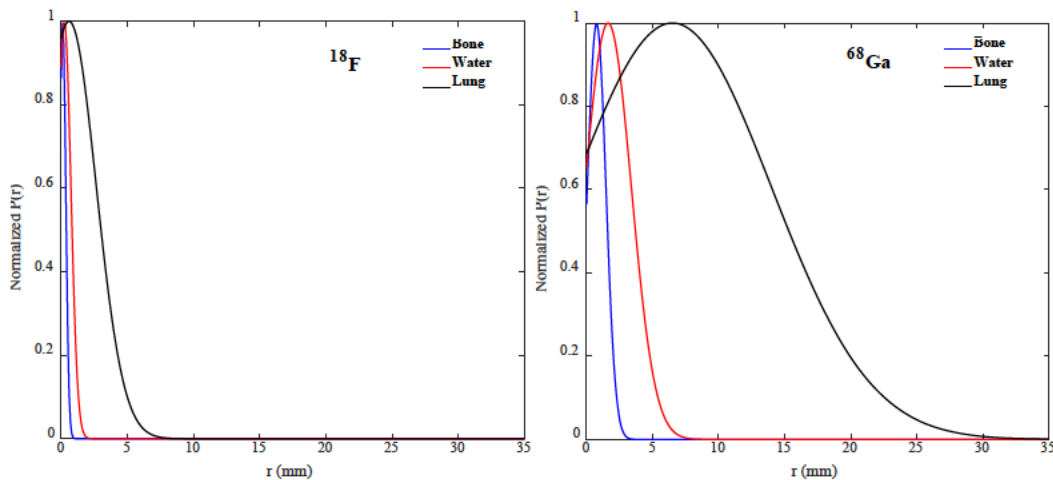
Figure 3.4: Radial positron range distribution for ^{18}F and ^{68}Ga simulated in the bone, water and lung, respectively.

Simulated mean positron ranges are shown in table 3.1, where they are also compared to values reported within the works of literature. The ^{18}F mean range (R_{mean}) is lower than ^{68}Ga in all media due to the lower energy of positrons emitted. As expected R_{mean} is the shortest in bone, followed by water and lung for both radionuclides due to the density differences of these media.

Table 3.1: Simulated R_{mean} (mm) of ^{18}F and ^{68}Ga in bone, water and lung, in bold, compared to published values. Relative percentage disagreement with our result is reported in parentheses.

Authors	^{18}F			^{68}Ga		
	Bone	Water	Lung	Bone	Water	Lung
	0.23	**0.48**	**1.91**	**1.01**	**2.22**	**9.04**
(Cho et al., 1975)		0.9 (87.5)*			1.79 (56.1)*	
(Bai et al., 2003)		0.51 (6 3)				
(Bailey et al., 2005b)		0.6 (25)			2.9 (30.6)	
(Partridge et al., 2006)		0.6 (25)			2.9 (30.6)	
(Champion and Le Loirec, 2007)		0.66 (37.5)†			3.56 (60.3)†	
(Alessio and MacDonald, 2008)		0.61 (27.1)				
(Cal-González et al., 2009)		0.61 (27.1)			2.21 (0.5)	
(Soultanidis et al., 2011)	0.33 (43.5)	0.56 (16.7)	2.23 (16.8)	2.62 (159.0)	2.62 (18.0)	9.94 (10.0)
(Lehnert et al., 2011)	0.25 (8.7)	0.48 (0)	1.86 (2.6)			
(Jodal et al., 2012)	0.37 (60.9)	0.62 (29.2)	2.44 (27.7)			
(Cherry et al., 2012)	0.33 (43.5)*	0.34 (33.3)*	2.47 (29.3)*	1.17 (15.8)*	2.24 (0.9)*	8.63 (4 5)*
(Cal-González et al., 2013)	0.32 (39.1)	0.57 (18.8)	1.85 (3.1)	1.44 (42.6)	2.69 (21.2)	8.86 (2.0)
(Bertolli et al., 2016)		0.55 (14.6)	2.14 (12.0)		2.54 (14.4)	9.69 (7.1)
(Fraile et al., 2016)					2.45 (10.4)	

* experimental study
† positronium formation

3.3.2 Annihilation point spread function

The 1D aPSF for different radioisotope-medium combinations were characterised by the sum of two exponential terms, as shown in equation 3.1. It is shown in table 3.2 that the D values which describe the tail of the distribution are consistently higher for ^{18}F as compared to ^{68}Ga. In addition, the D values are also at the highest in bone, followed by water and lung for both radioisotopes, as illustrated in figure 3.5. Thus, our results are consistent with previous studies, comparing the simulated distribution of positron annihilations, especially over different tissue types as considered in this study.

Looking across the two radioisotopes in figure 3.5, ^{68}Ga appears to produce wider kernels with longer tails in all media when compared to ^{18}F. Accordingly, the lung has the widest kernel, followed by water and bone. The magnitude of blurring imposed by each kernel was described by the FWTM, which was 0.63 mm, 1.39 mm and 5.88 mm, for ^{18}F in bone, water and lung, respectively. As for ^{68}Ga, the FWTM in bone was 2.77 mm, 5.97 mm in water and 24.34 in the lung. Therefore, the blurring imposed in the lungs was approximately ten times larger than in the bone and four times larger than in water or soft tissue, regardless of the energy of radioisotope used.

Table 3.2: Results of D (mm^{-1}) coefficient for different radioisotope-medium combinations, in bold, compared with published findings.

Authors	^{18}F			^{68}Ga		
	Bone	Water	Lung	Bone	Water	Lung
	7.78	**3.57**	**0.97**	**1.66**	**0.84**	**0.19**
(Derenzo, 1979)					0.87	
(Haber et al., 1990)		3.98				
(Levin and Hoffman, 1999)		3.22				
(Blanco, 2006)		3.38			0.87	
(Champion and Le Loirec, 2007)		2.79				
(Cal-González et al., 2013)	6.06	3.57	0.98	1.24	0.67	0.2
(Carter et al., 2019)	6.57	3.6	1.17	1.31	0.69	0.21
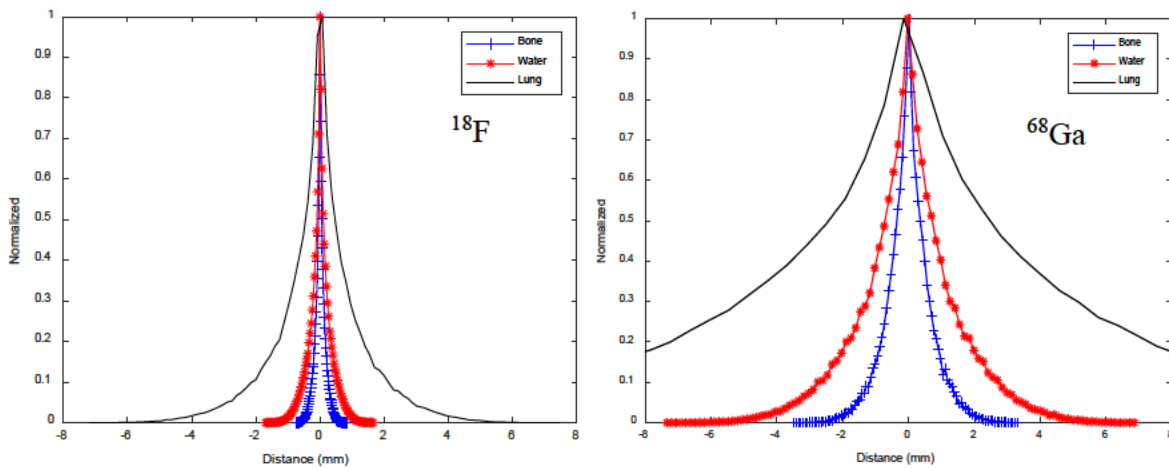
Figure 3.5: 1D aPSF for ^{18}F and ^{68}Ga in bone, water and lung, respectively. The distributions were normalized to 1.0 at zero distance.

Table 3.3: Fitting coefficients for ^{18}F and ^{68}Ga radioisotopes distribution in a different medium.

| Radioisotopes | Medium | Fitting coefficients | | | | R^2 |
		A	B	C	D	
^{18}F	Bone	0.41	61.10	0.71	7.78	0.99
	Water	0.47	31.91	0.66	3.57	0.99
	Lung	0.45	8.37	0.69	0.97	0.99
^{68}Ga	Bone	10080	1.66	0	1.66	0.99
	Water	6215	12.99	26040	0.84	0.99
	Lung	44240	0.20	0	0.20	0.99

3.3.3 Positron Range Blurring Kernels

The 2D blurring kernels for ^{18}F and ^{68}Ga in bone, water and lung medium were generated from profiles in figure 3.5, are shown in figure 3.6. For a 0.1 mm pixel, the the^{18}F kernel in bone appears the sharpest compared to other kernels where the kernel is fully contained within about 10 pixels. In water, the kernel is less sharp, with more activity spilling into the surrounding pixels. The lung kernel is the broadest as it has the lowest density among bone and water. Similar patterns are seen in the ^{68}Ga kernels but more diffused than the ^{18}F kernels in all media due to their higher positron energy.
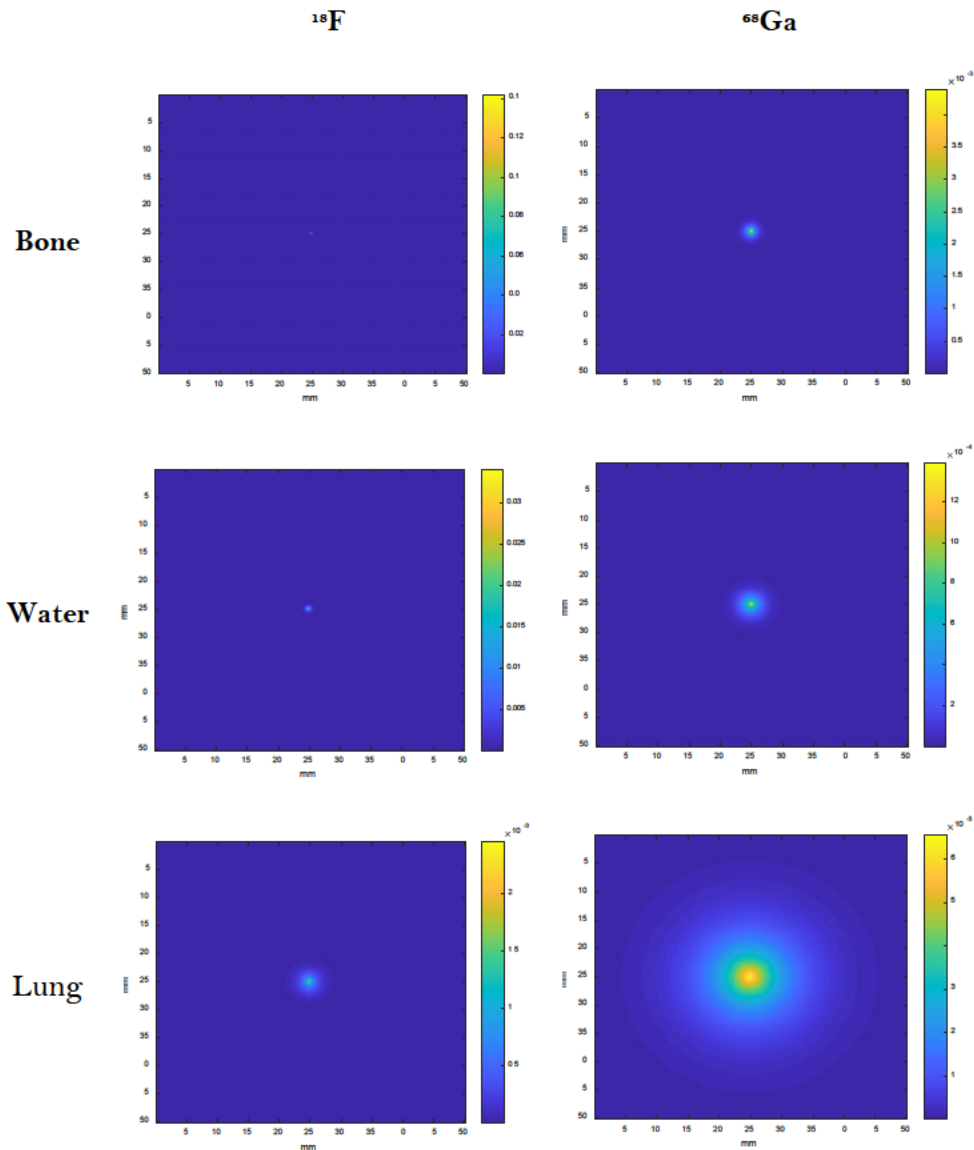
Figure 3.6: ¹⁸F and ⁶⁸Ga kernels in 0.1 mm pixel size for a different medium.

3.3.4 Positron range blurring effect

The 2D simulated true image convolved with combined isotope medium kernels across different pixel sizes are shown in figures 3.7 and 3.8, respectively. At this stage, the resulting images at the 0.1 mm pixel investigated were analogous to the image scanned directly from different PET spatial resolutions, corresponding to the mean positron range (Eq.3.2). The 0.1

mm pixel size was used to imitate the impact of positron range blurring in the infinite resolution in the physical world. Images were then down-sampled to investigate the impact of reconstructed pixel size on image performance.

From the visual assessment of the ^{18}F images and focusing on the smallest sphere (10.7 mm) at 0.1 mm pixel, the positron range blurring effect does not appear significant in the case of bone and water. In addition, images are more pixelated as the pixel size increases. However, at 0.1 mm pixel, a slight blurring occurs in lung medium, which becomes pixelated at 2 mm pixel-sized images. Meanwhile, at a 0.1 mm pixel, a blurring effect is apparent in bone for 68Ga image and the 10.7 mm sphere. However, pixelation of images at ≥ 2 mm pixels makes the blurring effect difficult to observe. At 0.1 mm for ^{68}Ga in lung medium, a clearly visible blurring effect was observed and severely degraded the image, even for the biggest sphere (28.2 mm) across all pixel sizes. Likewise, the 10.7 mm sphere is difficult to distinguish from the background. Overall, the 4.0 mm pixel-sized images of ^{18}F in all media and ^{68}Ga in bone and water suffer from aliasing that occurs when under-sampling a nearly continuous function, in this case, a very finely sampled function of 0.1 mm.
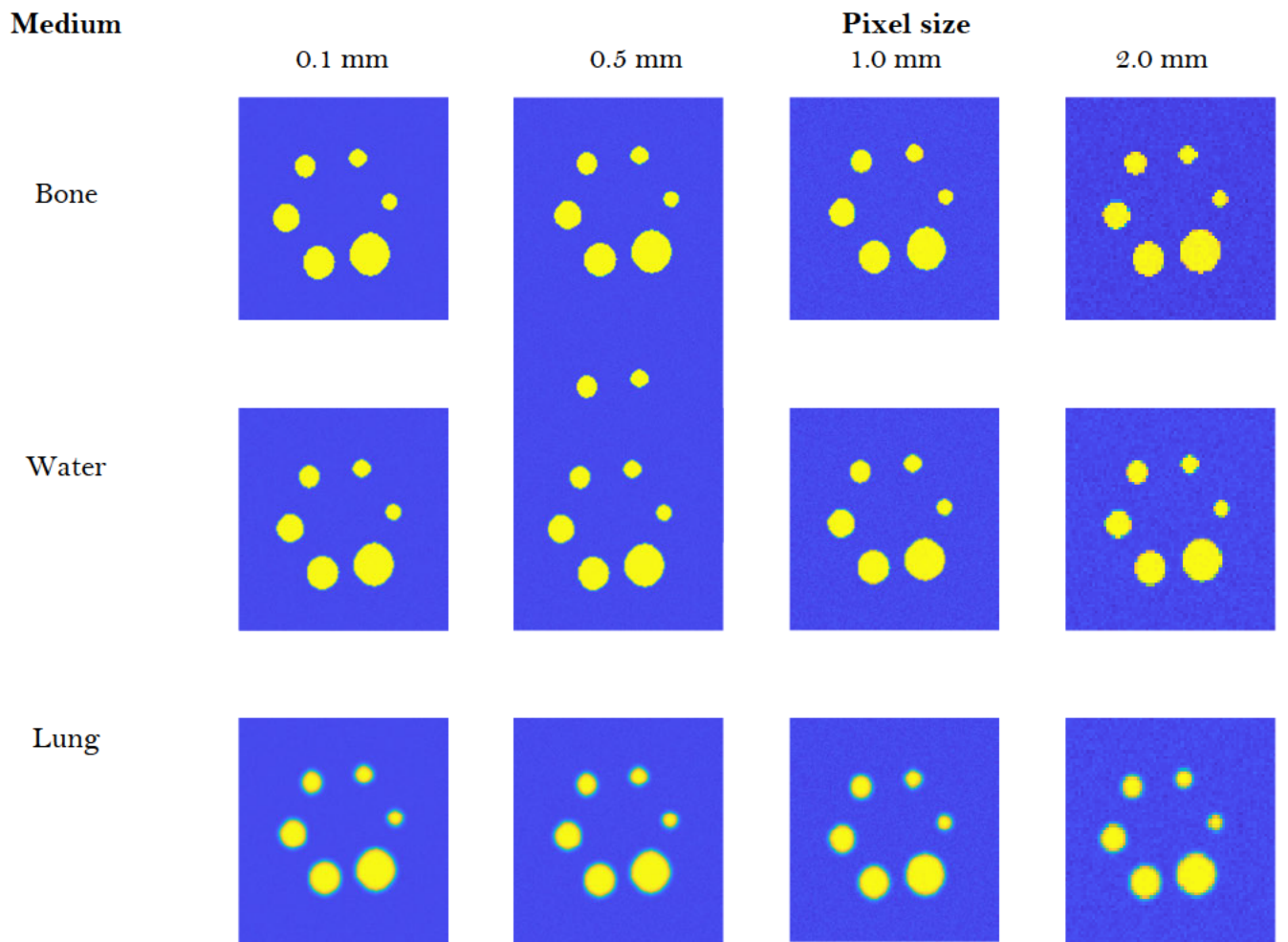
Figure 3.7: Simulated image convolved with respective ^{18}F kernel in each medium and pixel size. Each image is normalized into its respective maximum intensity.

Medium

0.1 mm   0.5 mm   1.0 mm   2.0 mm

Bone

Water

Lung
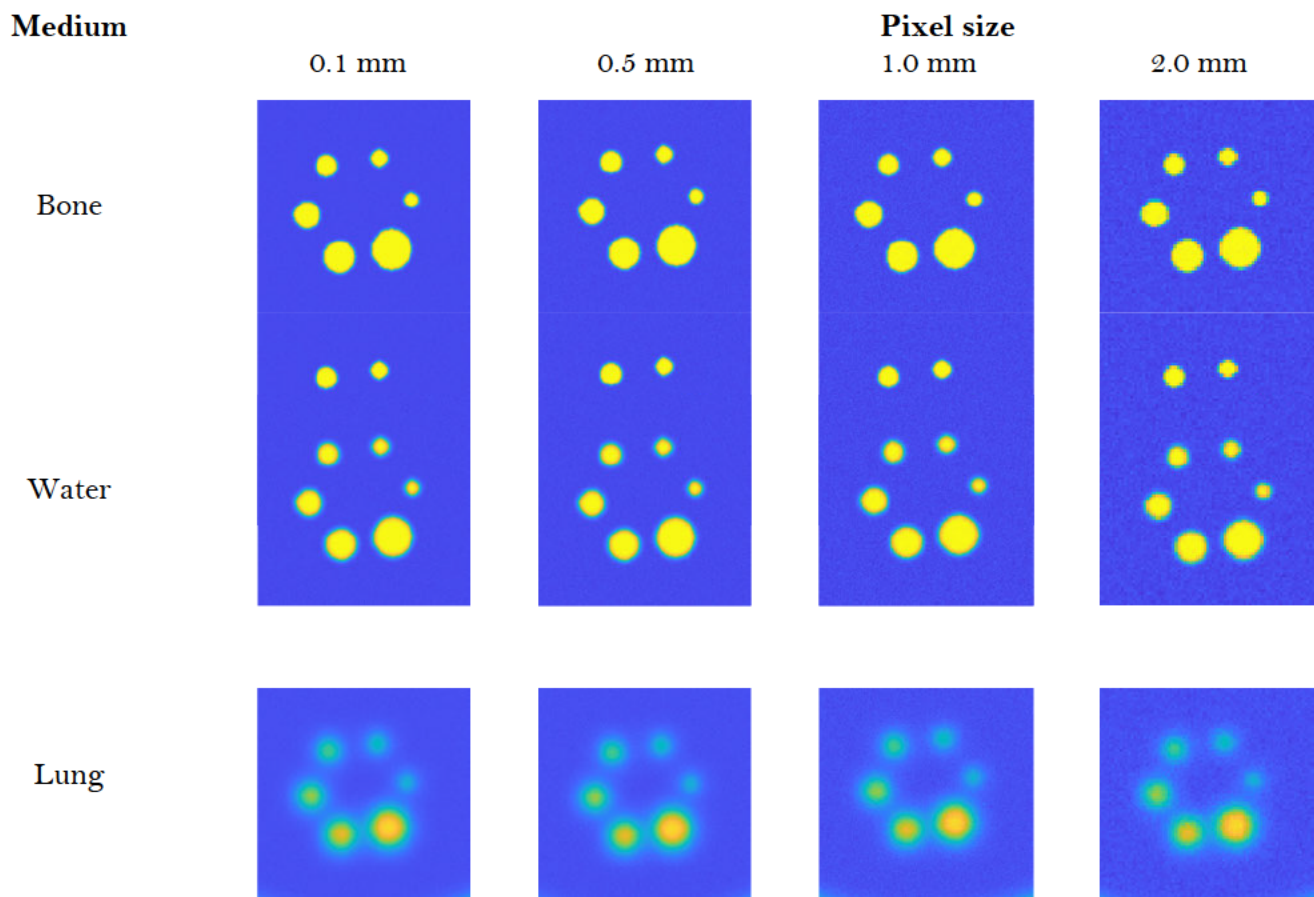
Figure 3.8: Simulated image convolved with respective ^{68}Ga kernel in each medium and pixel size. Each image is normalized to its respective maximum intensity.

Quantitative assessments of resolution, contrast and count loss are shown in figures 3.9, 3.10 and 3.11, respectively. From figure 3.9(A) for ^{18}F in bone and water, the blurring imposes about a 47% to 76% over-estimate of sphere size compared with the true size of 10.7 mm, as the pixel size increases. However, for ^{18}F in the lung, FWTMr is 54% to 60% for increasing pixel size. Considering ^{68}Ga in figure 3.9(B), the blurring effect observed in bone and water caused a 57% to 61% and 55% to 46% impact on FWTMr for increasing pixel size, respectively. For lung, the blurring is dominant with 122% to 158% FWTMr.

From figure 3.10(A), there was no difference in contrast of ^{18}F in bone, water and lung medium at up to 1 mm pixel size compared to the true image. However, differences are observed at 2 mm pixel size and greater. This indicates that positron range blurring does not affect contrast in bone, water and lung medium at 0.1 mm, 0.5 mm and 1 mm pixel size. For ^{68}Ga in figure 3.10(B), the contrast in bone and water is almost the same as the true image as the pixel size increases. However, the positron range in the lung reduces contrast by about 34% to 40% over all pixel sizes.

Figure 3.11 shows the effect of positron range blurring on count loss for ^{18}F and ^{68}Ga. ^{18}F in bone and water are not significantly affected by positron range blurring and, therefore, the count loss measured is less than 2% but increases rapidly at 4 mm pixel size. For ^{18}F in the lung, positron range blurring results in a 6-10% count loss as the pixel size increases. However, the count loss for ^{68}Ga in bone, water and lung were higher than ^{18}F with 2-6%, 9-13% and ~60% for increasing pixel size, respectively.

(A) **(B)**
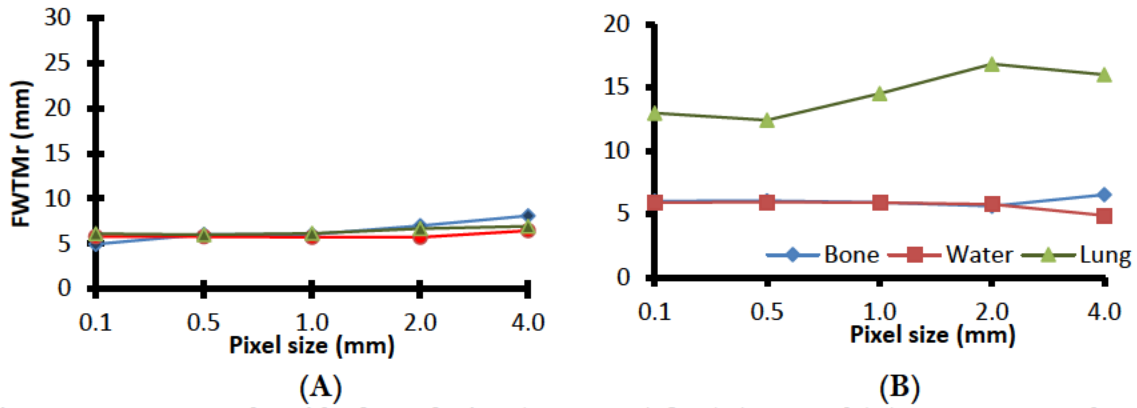
Figure 3.9: Measured residual resolution (FWTMr) for (A) ^{18}F and (B) ^{68}Ga measured at 10.7 mm sphere.

(A) **(B)**
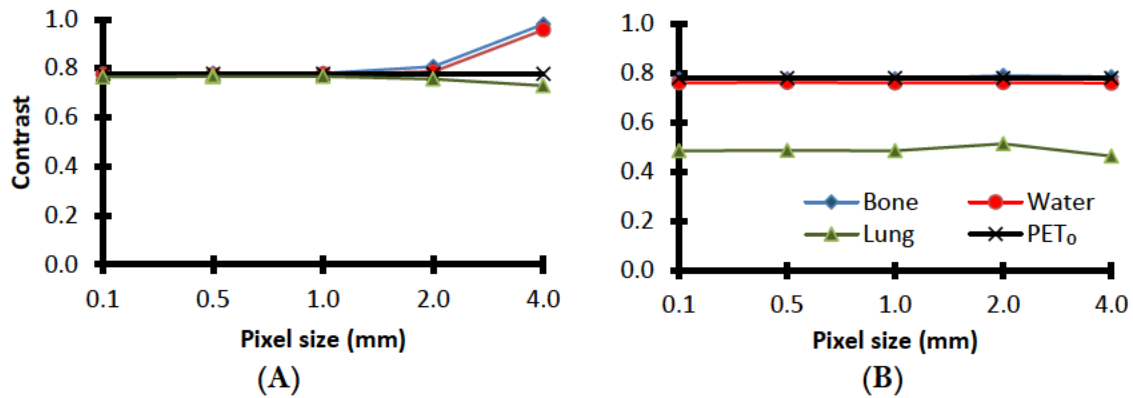
Figure 3.10: Contrast for (A) ^{18}F and (B) ^{68}Ga measured at 10.7 mm sphere. Noted in (A) that the blue, red and green lines which represent the contrast of ^{18}F in bone, water and lung medium are completely overlapped with the contrast of the true image (black line) at up to 1mm pixel size and start to differ at 2 mm pixel size onward.
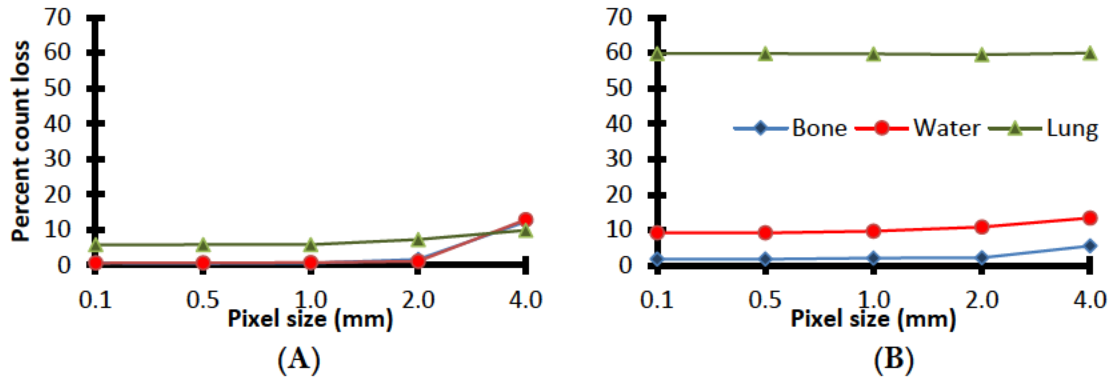
Figure 3.11: Count loss for (A) ^{18}F and (B) ^{68}Ga measured at 10.7 mm sphere.

3.4 Discussion

This study aimed to determine the mean, maximum and distribution of positron range for ^{18}F and ^{68}Ga in bone, water and lung media, and investigate the impact of positron range blurring on image performance at different reconstructed pixel sizes. This study excluded the blurring effect caused by non-collinearity, detector performance, image reconstruction, filtering and data correction, i.e., random coincidence, scattered radiation, attenuation and dead-time. Therefore, the PET spatial resolution was estimated by the mean positron range (R_{mean}) only, derived from eq.3.2. Then, the true simulated image was convolved with the positron range blurring kernel at a high spatial sampling of 0.1 mm to emulate the positron range blurring occurs with infinite resolution in the physical world. This enables the impact of the positron range blurring on image performance to be investigated in isolation from other effects.

This study confirmed that positron range is proportional to the energy of radioisotope and inversely proportional to the density of the medium the positron travels. Generally, our measurements agree well with previous studies. Differences in positron range measurements, compared to published simulation studies, are expected due to radioisotope spatial and energy binning effects and the different levels of physical interaction accuracy used during the simulation. For example, using a smaller binning interval results in a more precise estimation of

the radioisotope energy distribution. Moreover, factors relating to positron transport such as the medium description, the interaction cross-section, diffusion equation and energy threshold may differ between Monte-Carlo packages such as GATE, which was used in this study, EGS4 (Bai et al., 2003) and PeneloPET (Cal-González et al., 2010, Fraile et al., 2016). In fact, a thorough comparison cannot be made because prior studies do not provide sufficient details regarding all included physical interactions. Substantial discrepancies were observed between our results and a study by (Champion and Le Loirec, 2007) due to the use of a bespoke tracking code, which included positronium formation (Champion and Loirec, 2006), resulting in a longer positron range when compared to our study (See Table 1, Ref. 39). A detailed discussion about the influence of positronium formation on positron range can be found in (Lehnert et al., 2011).

The distribution of annihilations around the positron emission location was cusped-shaped, with long tails of relatively low intensity contributing to blurring. [18]F has the lowest FWTM and ^{68}Ga has the highest FWTM in each medium, as expected from the differences in the energy emission spectra. In general, higher FWTM leads to more severe blurring of images, which reduces detectability for small lesions and degrade quantitative accuracy, especially in preclinical PET applications since the resulting FWTM was greater than 2 mm FWTM (Levin and Hoffman, 1999). In contrast, except ^{68}Ga in the lung, all the measured FWTM of the blurring kernels were less than the spatial resolution in clinical PET systems of approximately 7 mm FWTM (Levin and Hoffman, 1999). The positron range blurring effect is dominant when higher energy radioisotopes are used, particularly in low-density tissue such as the lungs. From our results, the blurring imposed in the lungs was approximately ten times larger than in the bone and four times larger than in water or soft tissue, regardless of the energy of the radioisotope used. For this reason, the lung is the most problematic medium due to its low electron density with the highest mean positron range of up to 1 cm and FWTM up to 2 cm for ^{68}Ga, requiring

the most care when analysing image quality and tracer uptake in such studies.

Our approach of convolving the simulation image with positron range blurring kernel to study the real impact of positron range blurring to the reconstructed image was based on analytical work of Palmer and Brownell (Palmer and Brownell, 1992), who predicted the positron range effect as a function of different PET scanner spatial resolution of 1 mm, 2mm, 4 mm and 6 mm FWHM. First, they modelled the 4 different PET scanner resolution systems, including all systematic effects such as detector crystal size, bore size and positron range effect separately, followed by their combination to obtain the final spatial resolution. However, in our study, the image was directly simulated at 0.1 mm pixel size and convolved once with the positron range blurring kernel only before being down-sampled to the larger pixel size. Here, a 0.1 mm pixel size was sufficient to emulate the positron range blurring with infinite resolution in the physical world. Hence, the effect of positron range blurring can be investigated without blurring from other factors.

The findings of this study are important in determining at which reconstructed pixel size the positron range effect becomes dominant so that the correction is required and noteworthy corresponding to the type of radioisotopes used. Moreover, the impact of reconstructed pixel size on image performance was also investigated to distinguish between the blurring induced by the positron range and caused by the under-sampling of the image.

For ^{18}F, although the blurring is more apparent in the lung than water, both images give the same FWTMr at 0.1 mm to 1.0 mm pixel size, which is ~6 mm. This is because the FWTM for each image was determined by fitting the image aPSF curve using the Gaussian function. The aPSF of images are cusp-shaped with a sharp peak and broad tail. Hence, Gaussian fitting was not appropriate since it is underfitting the aPSF, especially at the tail region of the curve and

leads to the same approximation of FWTM. This also occurred for ^{68}Ga where the blurring effect is more apparent in water than in bone at 0.1 mm to 2.0 mm pixel size, but yielding the same FWTMr approximation of ~6 mm.

It was expected that the blurring effect due to the positron range to be clearly visible at 0.1 mm sampling for ^{18}F and ^{68}Ga since the R_{mean} for all radioisotope-medium combinations is greater than 0.1 mm. However, the positron range imposed a negligible blurring effect for ^{18}F in all media and moderate blurring for ^{68}Ga in bone and water. This could be explained by the smallest size of the sphere phantom that was still relatively bigger than the blurring magnitude corresponding to the R_{mean} for ^{18}F in all medium and ^{68}Ga in bone and water. Results inferred that the positron range blurring effect could not be observed clearly when the R_{mean} is within the PET spatial resolution limit, which is 3 mm -5 mm for clinical PET (Berg and Cherry, 2018) and 1.5 mm -2.5 mm for preclinical PET (Kuntner and Stout, 2014). Since the blurring magnitude for ^{68}Ga in the lung was two times larger than the smallest sphere, severe image degradation was observed.

Since the blurring effect in ^{18}F is negligible in bone and water, the contrast is predominantly influenced by the image space sampling rather than the positron range effects. In addition, the positron range does not impact contrast for ^{18}F at 0.1 mm to 2.0 mm pixel size in all media. However, the contrast increases at 4 mm pixel size in bone and water because the background count started to decrease due to reducing the capacity in each pixel to contain more count compared to in small pixel size. This also explains the count loss in ^{18}F. Although the count loss in the lung is higher than bone and water due to positron range, it is consistent at 0.1 mm to 1 mm pixel size, and the loss is higher at 4 mm pixel size. From this result, it can be concluded that the determination of contrast and count loss for ^{18}F PET in bone, soft tissue and lung are not affected by positron range at 4 mm image space sampling; hence no correction is required.

However, at sampling less than 4 mm, positron range correction is required to recover count losses due to positron range effects fully.

In contrast, ^{68}Ga imposed a noticeable degree of blurring to the image with the larger blurring kernel size in bone, water and lung than ^{18}F, as shown in figure 3.6. This is because tails of the kernels contain a large proportion of the total number of annihilations. Hence, for ^{68}Ga the contrast and count loss are dominant due to the positron range rather than image space sampling, as shown in figures 3.10(B) and 3.11(B). Therefore, the positron range correction necessary for ^{68}Ga in the lung due to 40% loss in contrast and 60% count loss. The correction may or may not be considered in bone and water because there is no contrast loss, and the count loss is only ~5% and ~15%, respectively.

The difference between results from this study of ^{18}F in water compared with those of (Palmer et al., 2005), which examined the model and simulated the positron range effect for high-resolution pre-clinical PET imaging, also can be highlighted. These authors used a simulated Nissl-stained coronal section of mouse and rat brain without stating the voxel size used to generate the simulation image. They first blurred these images with a 0.75 FWHM Gaussian simulating the PET scanner resolution and then blurred with a positron range kernel corresponding to ^{18}F. Their results indicate an important and clear resolution loss due to Gaussian blurring rather than positron range blurring. Hence the main factor contributing to blurring for ^{18}F appears to be the PET scanner itself and not the positron range. As brain tissue density is approximately equivalent to water, the results from Palmer et al. were contrasted with this current study. In our study, even at the finest pixel size (0.1 mm), the blurring due to positron range has only slightly appeared in the image of ^{18}F in the water medium.

3.5 Conclusion

The positron range distributions for ^{18}F and ^{68}Ga in bone, water and lung were characterized and the impact of positron range on image performance over different PET spatial resolutions and image space sampling were investigated. The findings in this study demonstrated that the positron range imposed a small impact on the image quality of ^{18}F in all media. However, the impact of positron range is significant when using radioisotopes with higher energy positrons, such as ^{68}Ga, especially in the lung, regardless of the image space sampling used. The positron range correction is not essential for ^{18}F at 4 mm image space sampling and can be considered for less than 4 mm voxel size. However, for ^{68}Ga, positron range correction should be considered in bone and water and is required in the lung, irrespective of the image sampling used. These findings form the basis for the next chapter, which developed positron range correction for ^{68}Ga-based for phantom and clinical PET.

Chapter 4

Development of Post-Reconstruction Positron Range Correction Method: A Phantom Study

4.1 Introduction

In the previous section, positron range resulted in image blurring with reduced contrast and quantitative accuracy for high energy radioisotopes, e.g. ^{68}Ga. The magnitude of blurring was proportional to the emission energy of each radioisotope and inversely proportional to the density of the medium traversed. In particular, blurring in the lung was up to ten times larger than in bone and four times larger than soft tissue (water) due to differences in density.

Positron range is independent of acquisition parameters (Kemerink et al., 2011, Blanco, 2006) and is not routinely corrected. With recent technologies developing a higher performance of clinical PET scanner with enhanced resolution and sensitivity (Jones and Townsend, 2017, Cherry et al., 2018, van Sluis et al., 2019), the positron range effect has become an increasingly crucial phenomenon to be considered. Several methods for positron range correction (PRC) have been reported in the literature. PRC was first applied in a phantom simulation study by (Derenzo, 1986), using a Fourier deconvolution method, but was limited to the correction of positron range in a water medium without considering any other types of materials such as bone and lung. Despite the success of (Derenzo, 1986) to improve quantitative accuracy, the method still suffered from noise amplification, especially with high energy radioisotopes. The method was extended in an experimental phantom study by incorporating the process into a filtered back-projection (FBP) reconstruction algorithm without increasing computational time (Haber et al., 1990). The noise amplification effect induced by direct Fourier deconvolution was reduced by adjusting the

high-frequency response of the reconstruction filter to balance between the level of restoration and the noise in the reconstructed image. Their experimental study showed an improved spatial resolution of ^{68}Ga and ^{82}Rb phantom images close to the gold standard, the ^{18}F phantom image. However, the attempt to reduce the statistical noise by adjusting the filter frequency response parameter was not practical for ^{82}Rb due to its highest blurring magnitude as compared to ^{68}Ga.

More sophisticated methods have been developed by several authors based on statistical iterative reconstruction. Iterative reconstruction methods provide an alternative to FBP that generally tends to be less noisy, have fewer streak artefacts, and allow for incorporating certain physical factors associated with the data acquisition into the reconstruction process, leading to more accurate results. Based on this concept, the algorithm is modified by incorporating the positron range function in the resolution modelling in two ways: i) introducing the positron range effect into the system matrix through a P_{range} factor (Agbeko et al., 2010, Bai et al., 2003, Rahmim et al., 2008, Kotasidis et al., 2014) or ii) employing positron range profiles as an additional blurring to the object, during forward projections (Bertolli et al., 2016, Cal-Gonzalez et al., 2015a, Fraile et al., 2016, Harzmann et al., 2014). The resulting algorithms for both methods attempted to recover the resolution loss from positron blurring and other system-related factors simultaneously. However, these methods require more accurate modelling of the system matrix, including positron range, which impacts the efficiency of the correction method.

A new approach to PRC using clinical PET data will be developed and investigated in the current work. Using the Geant4 Application for Tomographic Emission (GATE) Monte Carlo simulation package, the correction method was implemented using reconstructed PET images, making it applicable to any PET/CT scanner. Furthermore, the approach is more convenient than the previous since the scanner's raw data and reconstruction algorithm are not always accessible. Moreover, the method does not suffer drastically from enhanced noise; an issue raised

earlier. To our knowledge and at the time of writing, this is the second which developed the post-reconstructed PRC method after (Berger et al., 2019). In the next sections, we describe the method in detail, including implementation and validation using the NEMA image quality (IQ) phantom.

4.1.1 Positron range deblurring

The measured PET image is the distribution of the positron-electron annihilation sites from where back-to-back photons are generated. However, the true image we seek is the distribution of the positron emission locations. Hence, the measured PET image is a convolution of the true image and a blurring function which can be modelled as:

$$g(x,y,z) = \iiint h(x-x', y-y', z-z') f(x',y',z')dx'dy'dz' + n(x,y,z) \qquad (4.1)$$

where g is the observed image, the integral is a convolution, h is the blurring function, f is the true image and n is additive noise. In the Fourier domain, eq (4.1) becomes:

$$G(u,v,s) = H(u,v,s) \times F(u,v,s) + N(u,v,s) \qquad (4.2)$$

where $G(u,v,s), H(u,v,s), F(u,v,s)$ and $N(u,v,s)$ are the Fourier transforms of the observed image, blurring function, true image and noise, respectively.

The estimate of the true image, F', is computed by deconvolution for a given measured image, G and blurring function, H. Considering inverse filtering or direct deconvolution to restore the true image, F,

$$F'(u,v,s) = \frac{G(u,v,s)}{H(u,v,s)} = F(u,v,s) + \frac{N(u,v,s)}{H(u,v,s)} \qquad (4.3)$$

Eq.(4.3) is problematic because the blurring function, $H(u,v,s)$, has zeros in the Fourier domain. Division by zero or values approaching zero will severely amplify the noise.

One way to recover the true image, F, is to find an iterative algorithm where the iteration can be stopped to control the noise increase.

In practice, the image function estimated in PET image reconstruction is the positron annihilation distribution based on the annihilation point after the positron travels a finite distance, thus causing blur in the image. Thus, to avoid the blurring effect, the true image we wish to estimate, F, is the one that represents the positron emission points. Thus, our method aims to find the distribution of positron emissions given the distribution of positron annihilations obtained from the initial PET reconstruction.

The proposed deblurring method is an iterative algorithm that uses reconstructed images as input, specifically the PET measured image, the CT image and an image generated using GATE simulation, which provides an estimated positron-range image. In this study, the simulated annihilation image was an image distribution where the positrons annihilate with electrons. It was used as a 3D blurred image in a homogenous medium. It can be used in cases where the sinogram data and spatially variant point spread function are unavailable. The proposed PRC is implemented without the need to model the system response function of the imaging system, known as the system matrix. So it can be applied directly to the reconstructed image regardless of PET acquisition and reconstruction properties.

The proposed PRC method is inspired by PET tomography's image space reconstruction algorithm (ISRA) (Daube-Witherspoon and Muehllehner, 1986). The ISRA algorithm is a modification of the expectation maximization (EM) algorithm, which is based on a non-negative least-squares (NNLS) estimator rather than maximum likelihood (ML). The ISRA is computationally efficient to reduce the size of large and sparse data arrays by directly back-projecting the coincidence data during reconstruction (Daube-Witherspoon and Muehllehner, 1986). However, the disadvantage of this method is that it converges slower and provides less accurate estimates than MLEM. An alternative to NNLS that provides more accurate estimation in ISRA is weighted-least-squares (WLS) (Reader et al., 2011). The authors also used a special

scaled step size of the gradient of the WLS objective function to obtain a real multiplicative update in ISRA rather than a convolutional operation, as explained in chapter 2, section 2.5. Hence, the iteration update of ISRA is obtained by:

$$X_j^{(k+1)} = X_j^k \times \frac{\sum_{i=1}^{I} a_{ij}\frac{m_i}{w_i}}{\sum_{i=1}^{I} a_{ij}\frac{q_i^{(k)}}{w_i}} \tag{4.4}$$

where, $X_j^{(k+1)}$ is the updated image estimate at k+1 iterations, X_j^k is the current image estimate at the k$^{\text{th}}$ iteration, i is the sinogram bin index, j is the image voxel index, $\sum_{i=1}^{I} a_{ij}m_i$ is the backprojection of measured data, m_i, $\sum_{i=1}^{I} a_{ij}q_i^{(k)}$ is the backprojection of expected data, q_i, and w_i is the weighting factor. If $w_i = 1$, then, the de-blurring ISRA is summarized as:

$$X_j^{(k+1)} = X_j^k \times \frac{\sum_{i=1}^{I} a_{ij}m_i}{\sum_{i=1}^{I} a_{ij}q_i^{(k)}} \tag{4.5}$$

It was proven that eq. (4.5) converges to a non-negative least squares estimate (De Pierro, 1987, Titterington, 1987) for this particular chosen value of w_i. Hence, eq.(4.5) can be rewritten for the PRC case as:

$$PRC^{(k+1)} = PRC^k \times \frac{PET_0}{PET_k} \tag{4.6}$$

where $PRC^{(k+1)}$ is the updated deblurred image estimate at k+1 iterations, PRC^k is the current deblurred image estimate at the k$^{\text{th}}$ iteration , $\times$ is an element-wise multiplication operation, PET_0 is the PET measured annihilation image obtained directly from the scanner and PET_k is the simulated annihilation image from GATE output at the kth iteration, normalized to the total counts of PET_0.

In our proposed method, GATE is used to simulate the PET$_k$ given the PET$_0$ and CT images as input, which act as an emission source distribution and attenuation map. To start the process at zero iteration, the correction factor between PET$_k$ and PET$_0$ is determined and multiplied onto PET$_0$. However, this was only performed once, resulting deblurred image

estimate (PRC_k). Then, for the next iterations, the correction factor was multiplied by the current deblurred image estimate. A detailed explanation can be found in section 4.2.6. Finally, the iterative deblurring approach was utilised to minimize the image differences so that the image estimate, F' is close as possible to the true image, F.

4.2 Methods

In order to simulate the patient data to generate estimates of the annihilation locations in GATE, the positron emission location and material at which the positron will propagate must be known. Hence, a PET_0 image was used to create a voxelised emission map as one GATE input and a CT image was used to create a voxelised attenuation map as the other input. The main macro file for the simulation is attached as Appendix A.

4.2.1 Emission map

In this study, GATE version 7.2 was used. An emission map was provided in GATE by utilising the PET scan of the patient 3D image in Analyze image format (.hdr,.img). A linear translation description was used to convert the image into actual activity values in Bq (Appendix B).

4.2.2 Attenuation map

The CT image, acquired after the PET image, was used as an attenuation map input to GATE. It is easier to match the emission distribution/location and attenuation map if the CT image has the same dimension as the PET image. In this study, the original voxel size of the CT image was $0.98 \times 0.98 \times 3$ (mm)^3, while for PET image was $4.07 \times 4.07 \times 3$ (mm)^3. Here, the CT

image was resampled using MATLAB (R2017a, Mathworks, Massachusetts, United States) to have equivalent voxel size and thickness as the PET image before being imported into GATE. Resampling the CT image was done in such a way that it was easier to match the source locations in the PET image with the phantom geometry, in this study, the CT image.

Resampling the CT images in MATLAB results in misorientation, hence misalignment with PET image in the image viewer, A Medical Image Data Examiner (AMIDE) tools (Loening and Gambhir, 2003). The attenuation and emission images must align in transverse, coronal and sagittal views. The patient orientation also must be aligned between CT and PET images, i.e. whether it is supine-headfirst, etc. The patient orientation was set to supine-headfirst for both images. The orthogonal views between CT and PET images were aligned together by rotating the image 180o at y-direction and 90º at z-direction. All the image processing was done using MATLAB.

4.2.2.1 Mass density and attenuation map

GATE is able to generate a correspondence between HU (voxel values) and material by first, providing a calibration text file allowing to split the HU range into several materials and calibration text file to indicate the relation between HU and mass density (g/cm³). A macro file associated with this was attached in Appendix C. The stoichiometry calibration and correlation between CT numbers and tissue parameters have been studied by Schneider and colleagues for 71 human tissues regarding different elemental tissue compositions (Schneider et al., 2000). The results of the study are known as Schneider2000Materials (Appendix D) and Schneider2000Densities (Appendix E) tables, which are incorporated and utilised in GATE,

enabling automated HU to material density conversion and producing the materials database (Appendix F) and the resulting segmentation attenuation as shown in Appendix G.

For this is a phantom study, the density of the polymethyl methacrylate phantom wall material is equivalent to the bone marrow classes according to Appendix F. Therefore, the association between HU and NEMA mass density was correctly reflected by the relation of HU and bone marrow density.

4.2.3 Positioning the CT and PET images in GATE.

GATE uses two different origins for defining the CT image geometry as voxelised phantom and PET image as a source of emission distribution, respectively. Hence, both images must align together in GATE to ensure the simulation is based on correctly registered CT and PET voxel values. By default, the voxelised volumes in GATE, in this case, the CT image, are centred on their geometrical centre. However, the source (PET) image is placed in the 'first quarter', i.e. the image is placed starting at 0 0 0 mm (x, y, z). A simple translation of position is needed by shifting the PET image over half the size of the CT in all but negative directions to align the CT and PET images,

4.2.4 Production of simulated annihilation image

GATE can produce the simulated annihilation image, PET_k by utilising production and stopping particle position actors. The actor allows for collecting information during simulation, such as the number of particles created in a given volume, stores the position where particles are produced and where particles are stopped and modifying the simulation behaviour. In this study, we are interested only in positrons. Hence, the secondary particles are gamma radiation emission

from the annihilation point and the location where the annihilation gammas stop are not included. The exclusion can be achieved by adding a filter to refine the particle type criteria of the selected actor. Furthermore, the cut tool can also be used to avoid the production of gamma radiation which speed up the simulation. The output of this annihilation simulation was stored in a 3D image as analyze (.hdr/.img) image format. The overall flow for the generation of the simulated annihilation image is shown in figure 4.1.
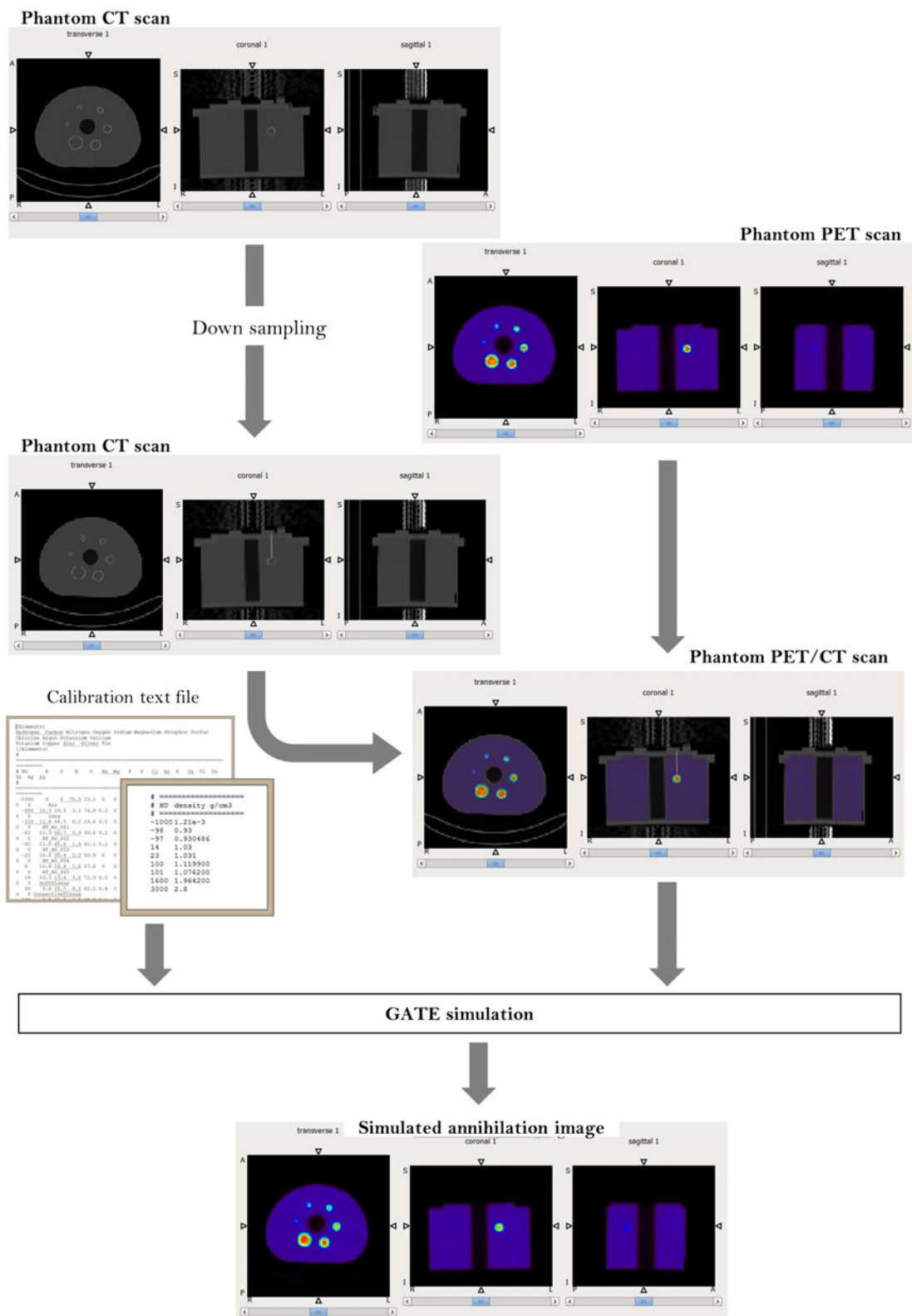
Figure 4.1: Flowchart for the generation of the simulated annihilation image.

4.2.5 Noise removal

The iterative deconvolution is expected to amplify the noise in the resulting image. Hence, to suppress noise during deblurring in this study, it is possible to introduce a relaxation parameter, W, to alter the progress of the deblurring on a pixel-by-pixel basis. The relaxation parameter reduces the amplitude of the correction for low-value pixels but allows the restoration to proceed at full strength for high pixel values. For example, for the NEMA phantom image, the relaxation function for the pixel at uniform background should be close to zero, while for pixels corresponding to hot spots, it should approach 1. Eq (4.6) was modified as (Berry, 2005):

$$X_j^{(k+1)} = X_j^k \times [W \times \left(\frac{PET_{measured}.img}{GATE_{anni_k}.img} - 1 \right) + 1] \tag{4.7}$$

By making the relaxation parameter a function of pixel value, $W_{X_j^k}$, the rate of convergence becomes different for different pixel values. The rate of convergence is slowed for noisy low pixel values but allowed at full speed for high pixel values or hot-spots in the image. As shown in (Berry, 2005), the first quarter of the sine function provides an excellent, non-linear function for the relaxation parameter. Here, as in (Berry, 2005), the following function is used to define the relaxation parameter.

$$W(p) = \begin{cases} p < p_{min} \rightarrow 0 \\ p_{min} \leq p \leq p_{max} \rightarrow \left(sin\left(\frac{\pi}{2}\right)\left(\frac{p-p_{min}}{p_{max}-p_{min}}\right) \right)^{\gamma} \\ p > p_{max} \rightarrow 1 \end{cases} \tag{4.8}$$

where p is the pixel value of the current pixel and γ is a noise reduction parameter that can be set between 0 and 1 to control the shape of the sine curve as well as the strength of noise suppression. The idea is that the sine function is scaled so that the $sin(0°)=0$ coincides with the p_{min} value and $sin(90°)=1$ coincides with the p_{max} value. If $\gamma=0$, then $W(p)$ is 1 for all values above p_{min}. However, if $\gamma > 0$, $W(p)$ rises continuously from 0 to 1. In this way, low γ values reduce the effect

of relaxation parameter and values approaching 1 increase the effect. Therefore, first, the effect of $\gamma=0$, $\gamma=0.5$ and $\gamma=1$ are examined in this study and evaluated to choose the optimal γ value before implementing PRC.

4.2.6 Iterative Positron Range Correction Deblurring Algorithm

Figure 4.2 shows the flowchart of the proposed iterative positron range correction (PRC) deblurring algorithm. The algorithm is initialized by simulation of the annihilation image, PET_1 in GATE based on the PET_0, which becomes the initial image estimate at zero iteration. The correction factors are then calculated between the PET_0 and the associated annihilation image, PET_1. Finally, the correction factors are applied to the PET_0, resulting in the first new image estimate (PRC_1) using MATLAB. The calculation of correction factors and updating images follows eq. (4.7). Step 1 was performed once at zeroth iteration, before proceeding to the first iteration.

Next, the first new image estimate (PRC_1) is simulated in GATE to obtain an updated simulated annihilation image, PET_1. Next, the correction factors between PET_0 and PET_1 are calculated. At this stage, the first new image estimate (PRC_1) becomes the old image estimate. Then, the correction factors are applied to the old image estimate (PRC_1), resulting in an updated image estimate (PRC_2). These steps above cover steps 2, 3 and 4 in figure 4.2, repeated iteratively until sufficient image quality is achieved. The MATLAB code to calculate the correction factors and perform image update is attached in Appendix H.
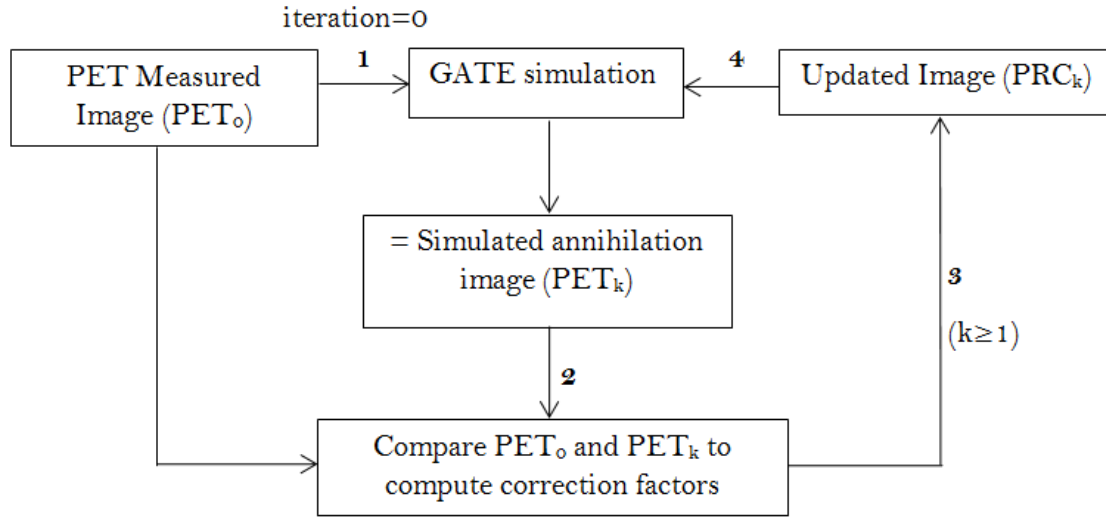
Figure 4.2: Flowchart for the Iterative Positron Range Correction Algorithm. Step 1 was performed once before proceeding to the first iteration. Then, steps 2 to 4 are repeated until the agreement is achieved.

4.2.7 NEMA Phantom study

The iterative PRC deblurring algorithm method was tested using images obtained with the National Electrical Manufacturers Association (NEMA) image-quality body phantom, as shown in figure 4.3. The NEMA phantom is built of acrylic glass material known as Poly(methyl methacrylate) (PMMA) with a density of 1.19 $g.cm^{-3}$. The phantom consists of a semi-anthropomorphic chamber and 6 internal fillable spheres with inner diameters of 37 mm, 28 mm, 22 mm, 17 mm, 13 mm, and 10 mm. These spheres are attached via capillary tubes of 1.5 mm diameter opening to the top lid of the phantom. The respective measured volume of each sphere in ml is 26.52, 11.49, 5.57, 2.57, 1.15, and 0.52 (Attarwala et al., 2014). A lung insert, which is a cylinder inserted in the centre of the phantom body, has an inner diameter of 44.5 mm and a volume of 194 ml. The phantom housing has a thickness of approximately 3 mm, and 10-20 mm lids of both ends of the phantom. Meanwhile, internal spheres have a wall thickness of

approximately 1 mm (Ziegler et al., 2015). Approximately 9.6 l of water was required for filling the phantom.
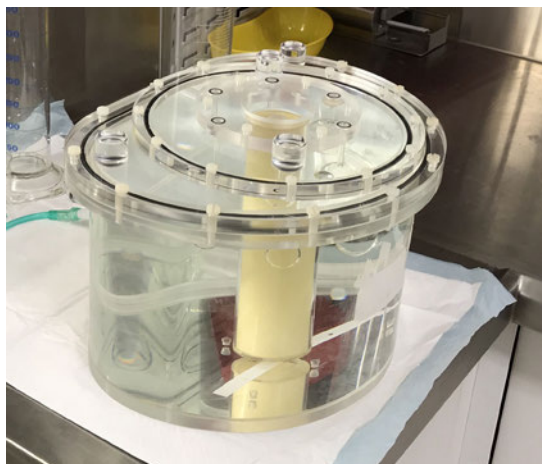
Figure 4. 3: NEMA Image Quality Body Phantom

The phantom was prepared following the ARTnet (Australasian Radiopharmaceuticals Trial network) site initiation preparation instructions (http://artnet.org.au/wp-content/uploads/2014/04/ARTnet-site-initiation-programme-FAQ-.pdf). ^{68}Ga activity was determined using the PTW Freiburg dose calibrator (Baden-Wuttermberg, Germany) to be 210 MBq with a residual of 1.03 MBq. Hence, the net activity was 208.97 MBq. The phantom was filled with this activity with a sphere to background ratio of ~8:1. Thus, the activity concentration in the spheres was 174.17 kBq/ml and in the phantom background, it was 21.77 kBq/ml.

The phantom was scanned using a Biograph mCT clinical PET system (Siemens Healthcare, Erlangen, Germany) by placing it in supine position securely on the scanner bed, in the centre of the field-of-view to make sure the entire phantom was included in the image.

Measurements of this phantom were collected and the raw data were normalised and corrected for dead time, attenuation, scatter, decay, and random coincidences prior to reconstruction. Images were reconstructed using the Royal North Shore Hospital's routine method of reconstruction: time-of-flight (TOF) OSEM (3 iterations, 21 subsets) with fully 3D

Point-Spread-Function (PSF), a zoom of 1 and post-reconstruction Gaussian filter of 5 mm full width at half maximum (FWHM). The image was reconstructed into 200×200 arrays of 4.07×4.07×2.027 (mm)^3 voxel size.

4.2.8 Performance evaluation of PRC

After the application of the proposed PRC method, the image was evaluated to determine target-to-background ratio (TBR), contrast recovery (CR), signal-to-noise ratio (SNR) and spatial resolution for each sphere. Contrast recovery is defined by the NEMA standard (2018) as:

$$CR_j = \frac{\frac{C_{H,c}}{C_{B,c}}-1}{\frac{a_H}{a_B}-1} \times 100\% \tag{4.9}$$

where $C_{H,c}$ is the average counts within a region of interest (ROI) drawn on each sphere, c on the central PET slice, $C_{B,c}$ the average background counts for ROIs of the same size, a_H the activity concentration in the hot spheres and a_B the activity concentration in the background. ROIs were defined as the same size of the sphere diameters, drawn over the spheres and in the background on the PET image, as shown in figure 4.4. In this study, the evaluation of the ROIs was performed using an open-source image analysis tool, A Medical Image Data Examiner (AMIDE) (Loening and Gambhir, 2003).

SNR was calculated as (Kertész et al., 2021):

$$SNR = \frac{\bar{s}}{\sigma_b} \tag{4.10}$$

with $\bar{s}$ is the mean signal, and σ_b is the standard deviation of background.
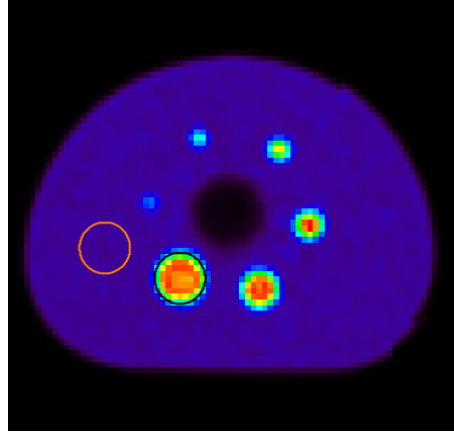
Figure 4. 4: A black circle indicates the ROI for the 37 mm sphere, and the orange circle indicates the background count for the corresponding sphere. The size of the ROI is similar to the dedicated sphere size, which is 37 mm.

Full-Width-Tenth-Maximum (FWTM) was used to evaluate the spatial resolution for each sphere. It is the most appropriate metric since the blurring distribution induced by the positron range is cusp-shape, with a broad tail. The metric was not a true measure of spatial resolution but, rather, an indication of relative spatial resolution to evaluate the effect of PRC updates. To determine the spatial resolution for each sphere volume, total slices in transverse, coronal and sagittal views were determined and summed to create a single slice of a certain thickness in each view. The vertical and horizontal FWTM for corresponding axial (x,y), coronal (y, z) and sagittal (x,z) directions were then calculated, resulting 6 resolution measurements for each sphere, as shown in figure 4.5. The mean for FWTM in this ^{68}Ga study was determined for each sphere volume and compared to ^{18}F spatial resolution for each sphere, which was considered the gold standard because of its negligible positron range effect, which was investigated in chapter 3.
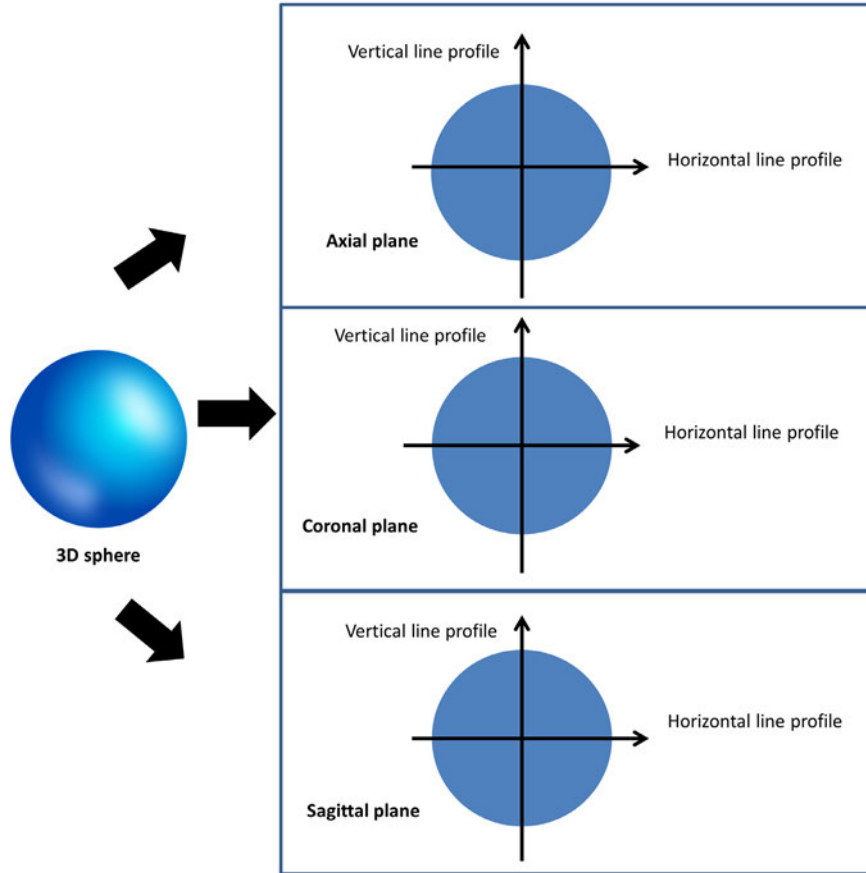
Figure 4. 5: Determination of FWTM for axial, coronal and transverse planes for each sphere.

4.3 Results

Parallel simulations were performed to model the phantom annihilation image. For one iteration in this study, the simulation was split into four independent 'sub-simulations', then summed together at the end to obtain approximately as similar counts detected as in the PET image obtained from the scanner. All the four sub-simulations finished within 5 hours when utilising four cores with 50 Gb RAM each. Hence for ten iterations, approximately 50 hours was required to complete the whole simulation.

Images of the NEMA IQ phantom from the PET scanner (PET_0), PET_0/CT image fusion and the simulated annihilation image, PET_1 is shown in figure 4.6. PET_1 (figure 4.6C), demonstrated that the ^{68}Ga is distributed more evenly in water than PET_0 (figure 4.6A). Furthermore, PET_0/CT image fusion accuracy was shown in profile figure 4.7(A), indicating perfect registration for both images. Additionally, a sharper transition was observed between the water and lung region, and the water and background boundary is more clearly seen in the PET_1, as indicated in profile figure 4.7(B)

It was found that the Gibbs artefact in PET_0 was reduced, especially in the largest sphere compared to PET_1. Figure 4.8 shows the profile comparison at the 37 mm sphere between PET_0 and PET_1. The Gibbs artefacts in PET_0 was due to PSF-based image reconstruction (Tsutsui et al., 2017). It is translated as a dense edge and decreases activity at the centre of the sphere for the 37 mm sphere, which is the largest sphere in the phantom. Also, for spheres less than 37 mm, Gibbs artefact was shown as a dense spot at the centre of the spheres.

(A) **(B)** **(C)**
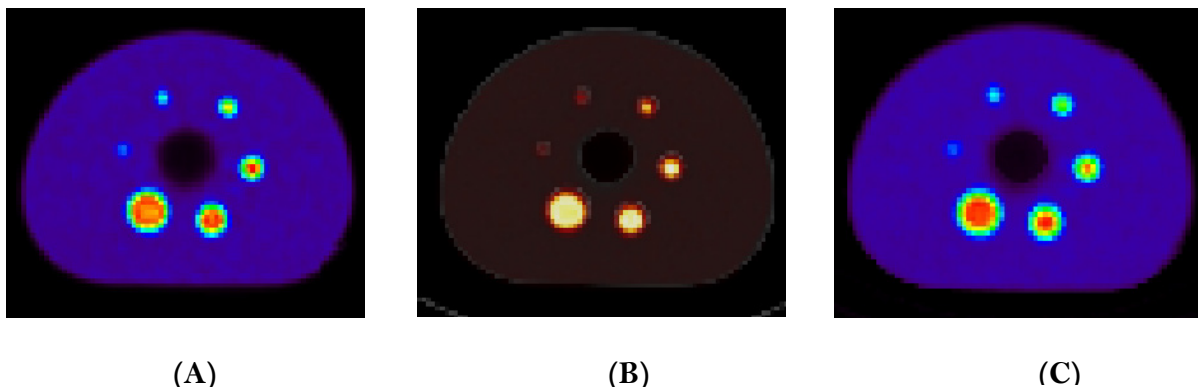
Figure 4.6: NEMA IQ phantom image A) PET_0, B) fused PET_0/resampled CT images and C) PET1.

Axial

Coronal

Sagittal

PET₀   CT_resampled
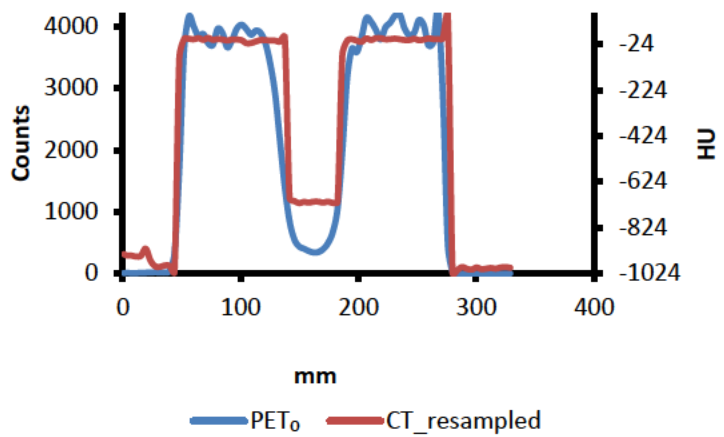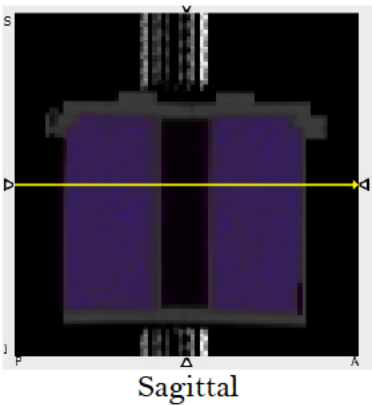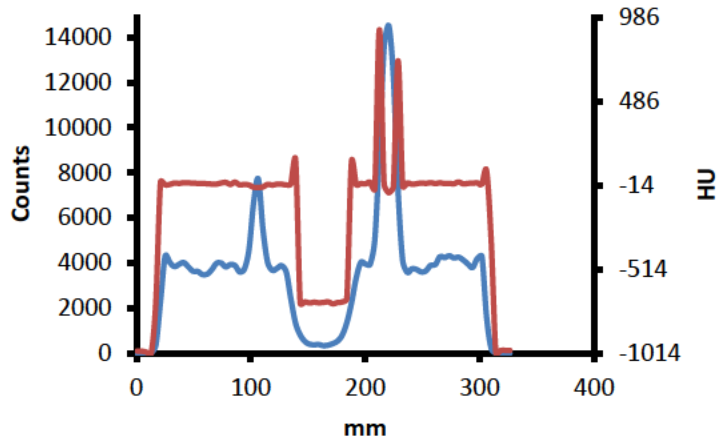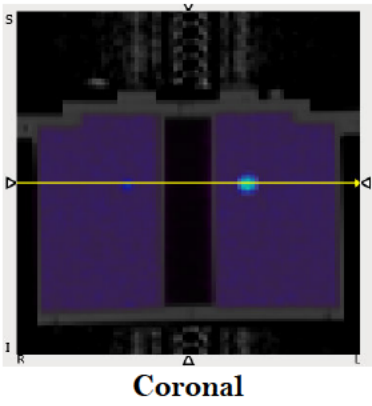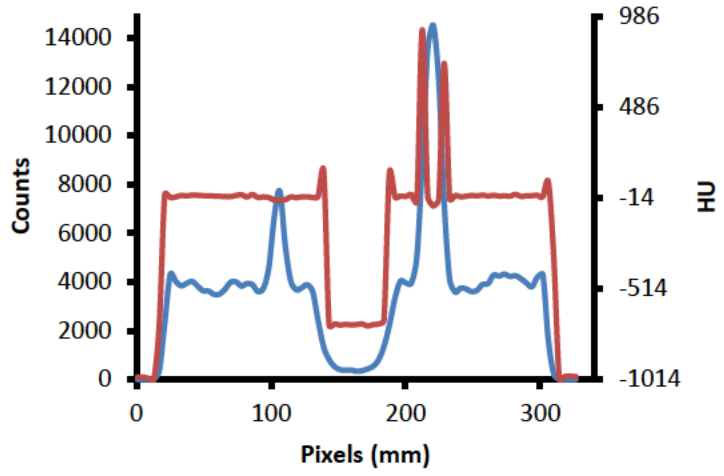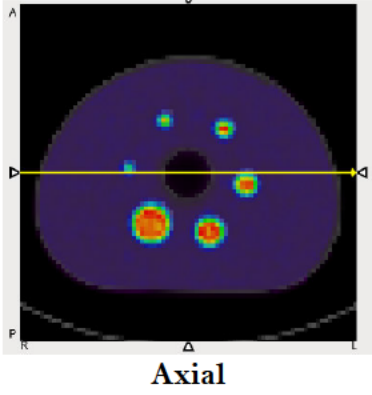
(A)
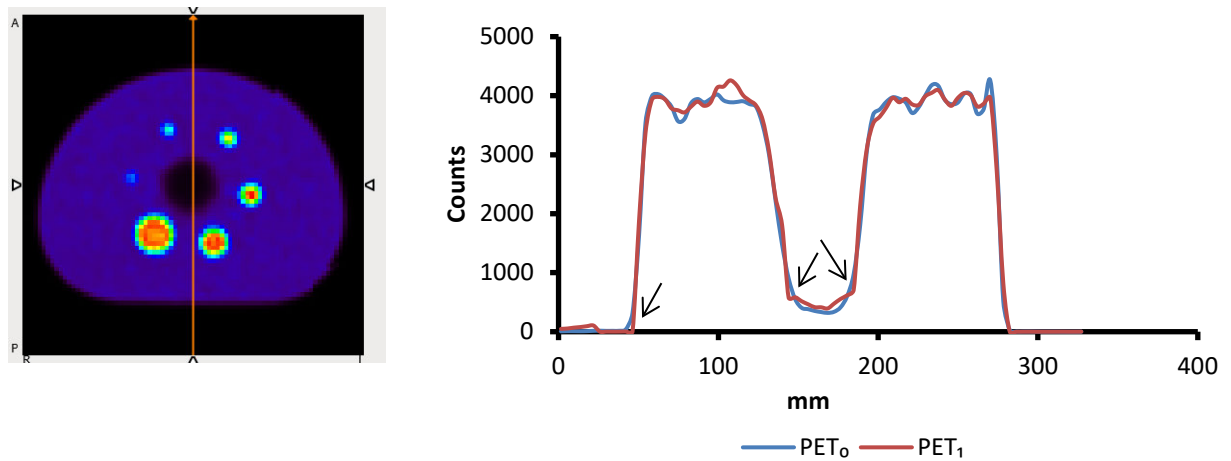
(B)

Figure 4. 7: (A) Profile figure for PET_0/CT image registration in axial, coronal and sagittal, respectively. (B) Profile comparison between PET_0 and PET_1. Arrows show a sharper transition between water/background and water/lung boundaries for PET_1.
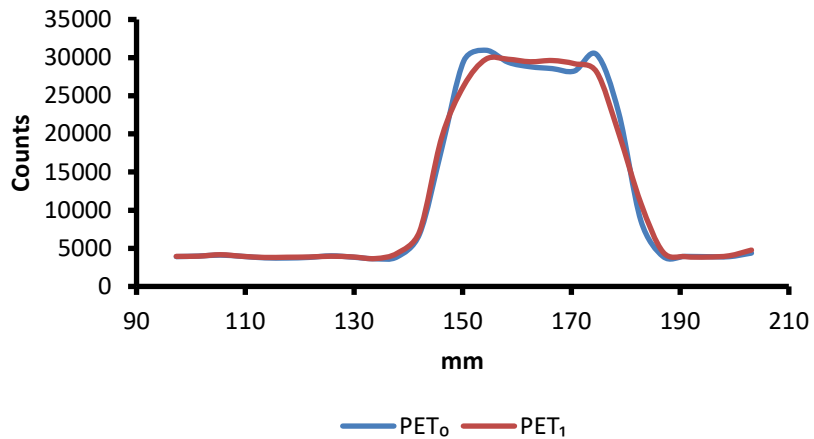
Figure 4. 8: Profile comparison at 37 mm sphere in PET_0 and PET_1 where the Gibbs artefact was reduced in PET_1.

4.3.1 Performance of PRC and relaxation parameter on ^{68}Ga NEMA IQ phantom

This section aims to identify a γ value that can yield an optimal diagnostic image before proceeding to performance analysis. Comparisons were made between PET_0 and PRC images after one iteration, but without the relaxation parameter (PRC_{nrp}); with the PRC and relaxation

parameter of γ=0 (PRCγ=0); with the PRC and relaxation parameter of γ=0.5 (PRCγ=0.5) ; and with the PRC and relaxation parameter of γ=1(PRCγ=1).

Figure 4.9 exhibited the first quarter of the sine function with different relaxation parameters, γ = 0, 0.5 and 1, respectively reflecting equation 4.8. With γ=0, the progress of deblurring is at maximum regardless of the intensity of voxels. However, with γ=0.5 and 1, the rate of convergence is modified corresponding to the voxels intensities.
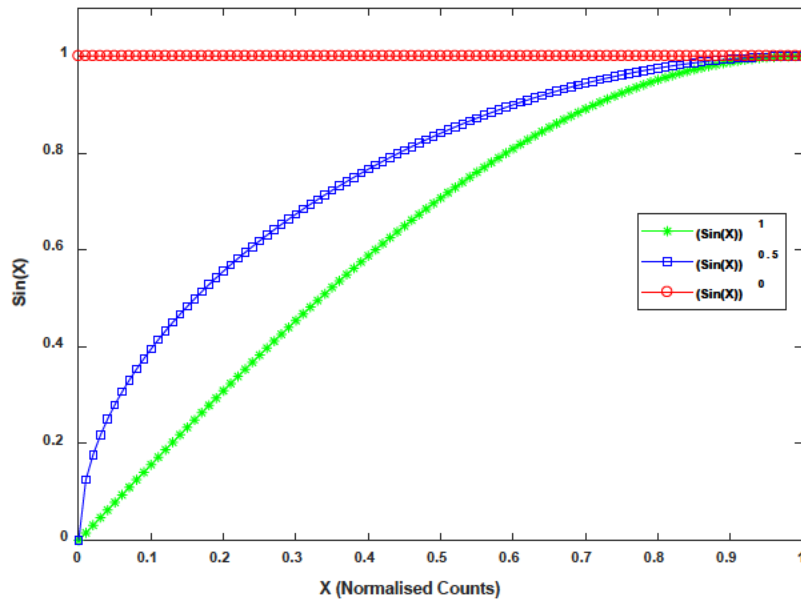
Figure 4. 9: The first quarter of sine graphs of equation 4.8 for γ=0, 0.5 and 1.

The results in table 4.1 show that the target-to-background ratio and the spatial resolution were slightly improved when a relaxation parameter was implemented. Also, it is indicated that the tail region of the FWTM was not affected by the relaxation parameter utilization. It is expected here that PRC_{rmp} and PRCγ=0 should yield the same results according to eq. 4.7. In addition, the noise enhancement during deblurring was suppressed as the γ increases. The root mean square error values (RMSE) reveals that utilising relaxation parameter

with γ=1 during PRC, results in a very small amount of count change per voxel as compared to PET$_0$, yet provides an improvement from the PRC deblurring process. As explained in 4.2.5, low γ values reduce the effect of relaxation parameter and values approaching 1 increase the effect.

Table 4.1: Performance of PRC without relaxation parameter and with relaxation parameter given different γ values, at one iteration. The resolution, noise and RMSE are the performance for 10 mm sphere only.

Image	Relaxation parameter	γ value	Target-to-background ratio		Resolution		Noise(σ)	RMSE
			10 mm	37 mm	FWHM (mm)	FWTM (mm)		
PET$_0$	-	-	3.5	7.3	9.6	19.0	188.7	
PRC$_{nrp}$	No	-	4.3	7.6	7.8	17.5	260.2	1.82e+03
PRCγ=0	Yes	0	4.3	7.6	7.8	17.5	260.2	1.82e+03
PRCγ=0.5	Yes	0.5	4.3	7.6	7.9	17.6	217.9	3.13e+02
PRCγ=1	Yes	1	4.1	7.6	7.9	17.6	200.9	68.63

4.3.1.1 Ring artefact and noise appearance

Figure 4.10 shows a ring artefact in the lung area and noise appearance at the periphery of the NEMA phantom for PRC$_{nrp}$ and PRCγ=0. The ring artefact diminished as the γ increases. On the other hand, the noise is still observed at γ=0.5. However, our most intriguing finding is that PRCγ=1 is able to eliminate the ring artefact in the lung area and at the same time effectively suppress noise, especially at the peripheral phantom.
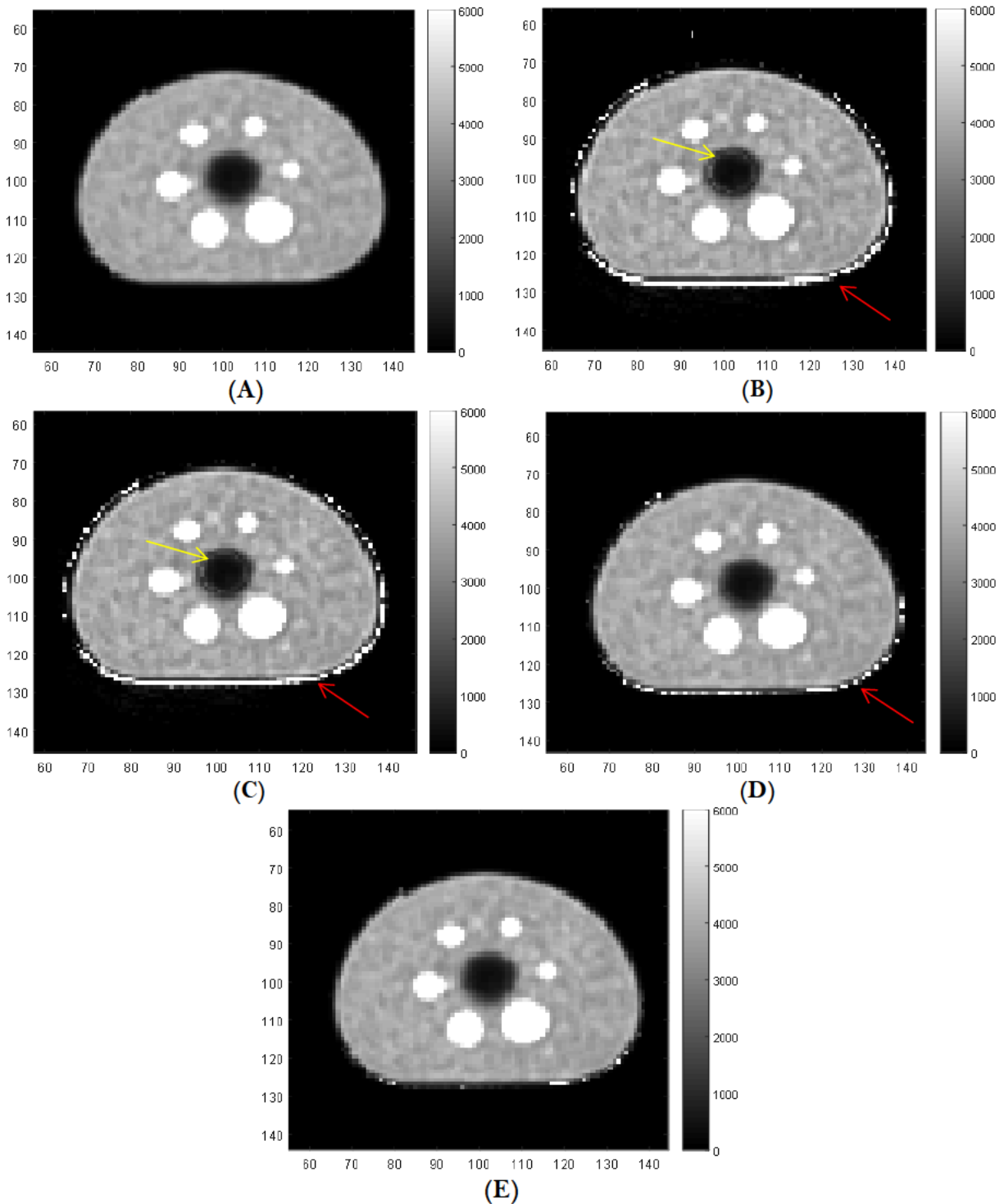
Figure 4.10: Figure (A) is the phantom image of ^{68}Ga PET$_0$, (B) ^{68}Ga PRC$_{nrp}$ (C) ^{68}Ga PRCγ=0, (D) ^{68}Ga PRCγ=0.5, (E) ^{68}Ga PRCγ=1. Images are normalized to the same maximum value to show the ring artefact and noise that occurred. The yellow arrow indicates a ring artefact in the lung area in (B) and (C), which diminished in (E). The red arrow indicates the noise appearance during deblurring which was suppressed at γ=1 (E).

As explained above, the line profiles comparison is also used to show the existence and elimination of the ring artefact and noise. Figure 4.11(A) shows an example of a vertical line profile drawn for the ^{68}Ga PET$_0$ NEMA phantom image. Figure 4.11(B) indicated that the ring artefact occurs in the lung area in PRC$_{nrp}$ and PRCγ =0. In addition, substantial peripheral noise appears for both images.

The ring or Gibbs artefacts in this study showed the edge-overshoot around the rapid changes in image contrast between lung area and the ^{68}Ga-filled phantom. During deblurring, the amplitudes of the detected frequencies were restored and the undetected frequencies were set to zero. Therefore, there was a truncation of a Fourier series of a discontinuous function and visually represented as a ringing.

Overall, it was found that increasing γ value to the maximum value of 1 drastically reduced or eliminated ring artefacts and noise, whilst retaining the signal enhancements of PRC.

(A)

(B)
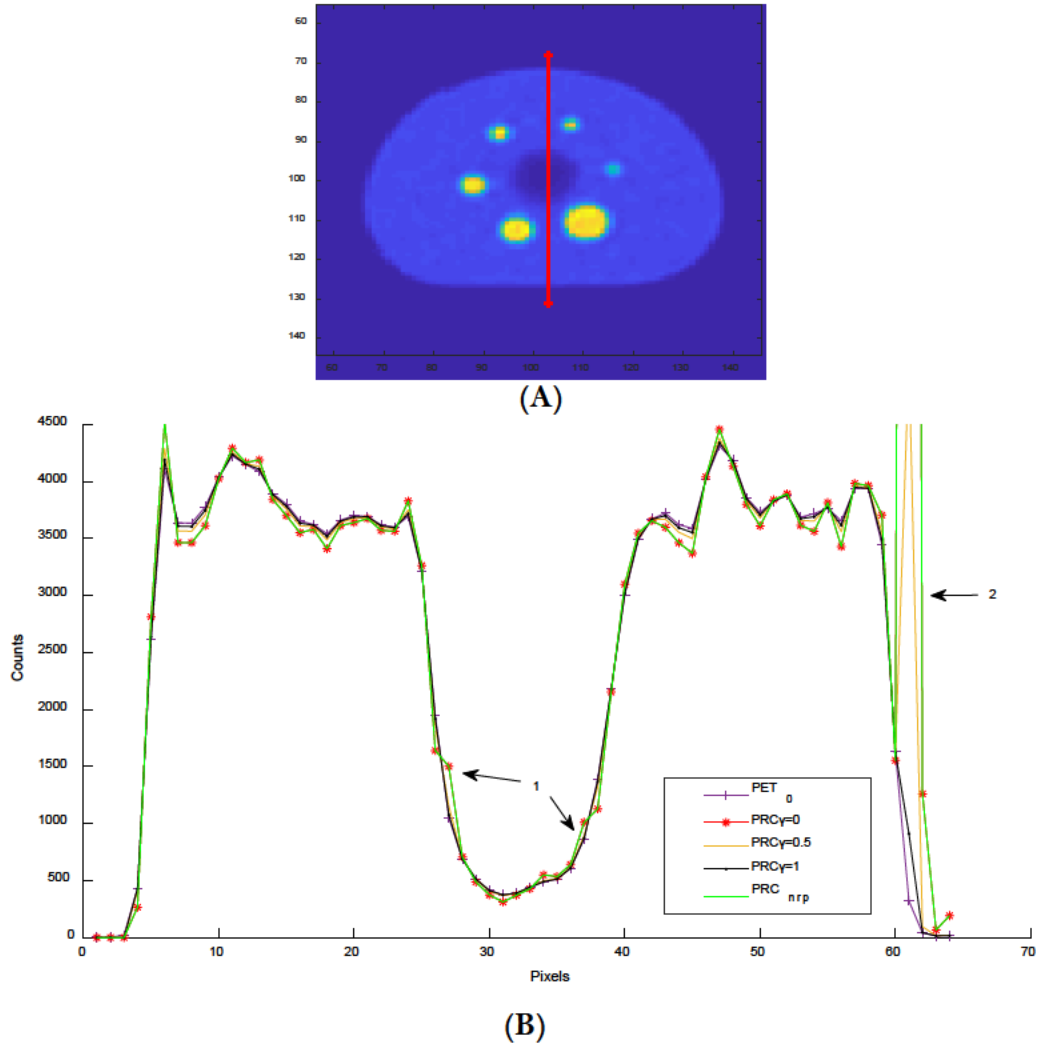
Figure 4.11: A) An example of a vertical line profile drawn in the axial phantom image. B) Comparison of vertical line profiles for PET_0, PRC_{nrp} and PRC with γ values. Arrow 1 shows the Gibbs artefact in the lung region, while arrow 2 shows the peripheral noise at the posterior of the phantom.

4.3.2 Image updates

After determining $\gamma=1$ yields images with much reduced artefacts without comprising signal recovery, the implementation of PRC was conducted over 10 iterations. PET_0 and PRC_k images, where k is the iteration numbers, are shown in figure 4.12. The contrast was visually improved as the iteration increases, especially for 10 mm, 13 mm and 17 mm spheres. Artefacts

were observed at the bottom boundary of the phantom after PRC and the intensity increased as

the iteration increases, as exhibited in figure 4.13
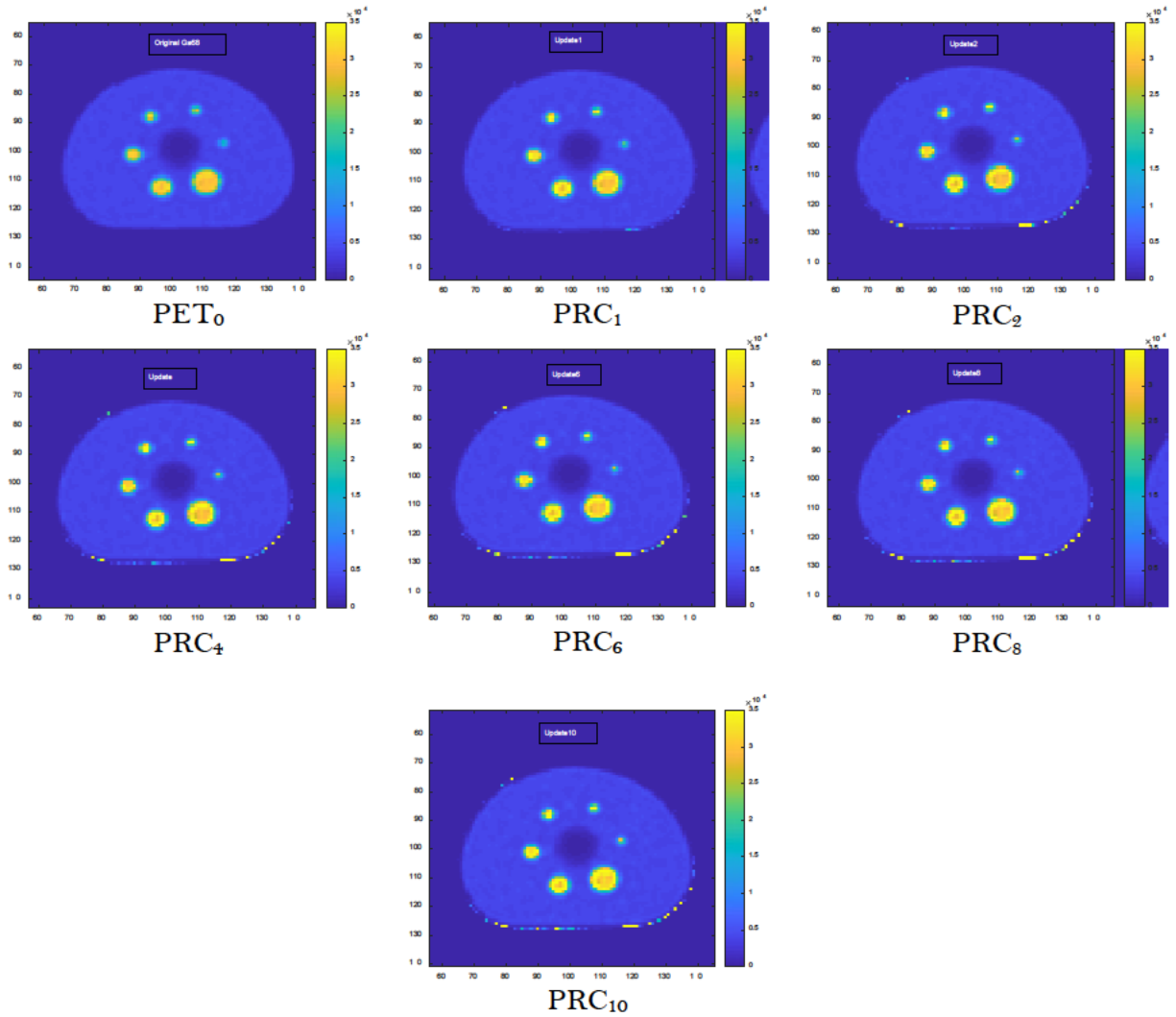
Figure 4.12: Comparison of NEMA IQ phantom for PET_0 and PRCk where k=1, 2, 4, 6, 8, 10. Images were normalized to the same maximum intensity.
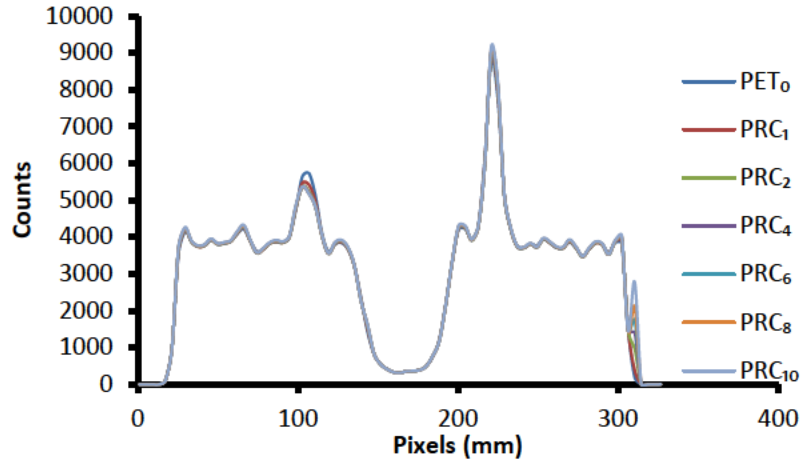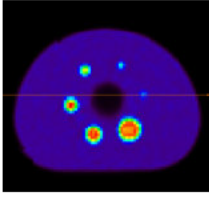
(A)
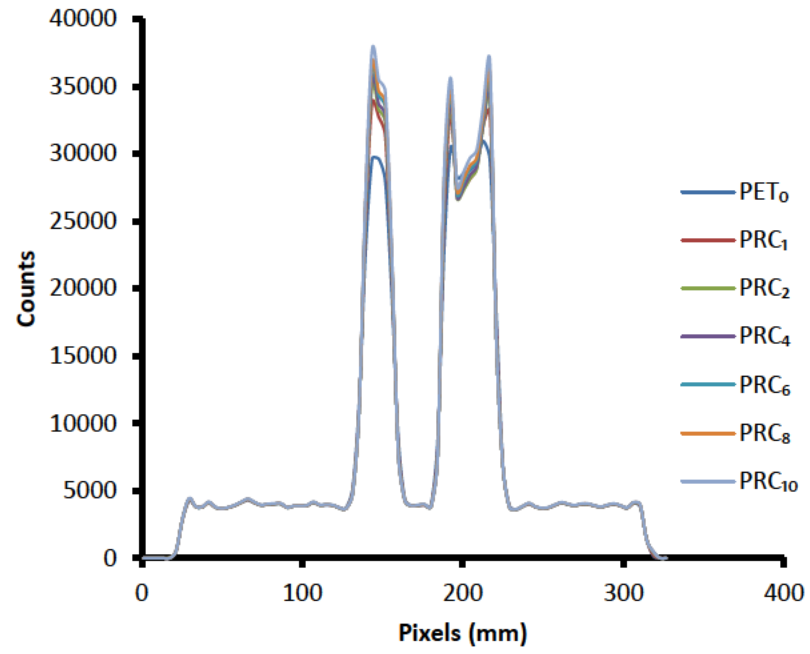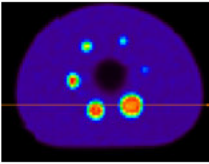
(B)

Figure 4. 13: Profiles comparison for (A) 10 mm and (B) 37 mm for PET_0 and PRC_k where k=1, 2, 4, 6, 8, 10.

4.3.3 Target to background ratio

The true concentration ratio of hot spheres to the background for the NEMA IQ phantom was 8:1. Results in table 4.2 show that after 10 updates, only the largest spheres, which are 28 mm and 37 mm, approaching full convergence and recovered the true target to background ratio (TBR), compared to other spheres size.

Table 4.2: Target to background ratio (TBR) for PET_0 and PRC_k, at k=1 to 10 updates

Image/Sphere size	10 mm	13 mm	17 mm	22 mm	28 mm	37 mm
PET_0	2.0	2.7	4.7	5.9	6.5	6.9
PRC_1	2.1	2.8	5.4	6.6	7.0	7.2
PRC_2	2.1	2.8	5.6	6.7	7.1	7.3
PRC_3	2.1	2.8	5.6	6.8	7.2	7.3
PRC_4	2.1	2.8	5.6	6.8	7.2	7.3
PRC_5	2.1	2.8	5.7	6.9	7.2	7.4
PRC_6	2.1	2.8	5.7	6.9	7.3	7.4
PRC_7	2.1	2.8	5.7	6.9	7.3	7.4
PRC_8	2.1	2.8	5.7	7.0	7.3	7.5
PRC_9	2.1	2.8	5.8	7.0	7.4	7.5
PRC_{10}	2.1	2.8	5.8	7.1	7.5	7.6

.

4.3.4 Contrast recovery coefficient

The contrast recovery coefficients (CRC) calculated for each sphere of the IQ phantom are presented in figure 4.14. Update 0 indicated the CRC of PET_0. In general, as the iterations increase, the CRC gradually increases. For the 10 mm sphere, although the CRC have notable increment at update 1, it remains relatively stable as the iteration increases from 1 to 10 (see figure 4.14B). After 10 updates, the rate of convergence looks about the same for all spheres. The highest CRC is achieved by the largest hot sphere, which is 37 mm with 94%, and the lowest is by the smallest sphere, which is 10 mm with 16%. This is because the larger spheres converge

quickly and the smaller spheres take more iterations to converge. The convergence rate depends on the sphere size due to the larger spheres suffer from a less partial volume effect compared with the smaller spheres.

(A)

(B)

Legends: ◆ 10 mm   ■ 13 mm   ▲ 17 mm   ✕ 22 mm   ✳ 28 mm   ● 37 mm
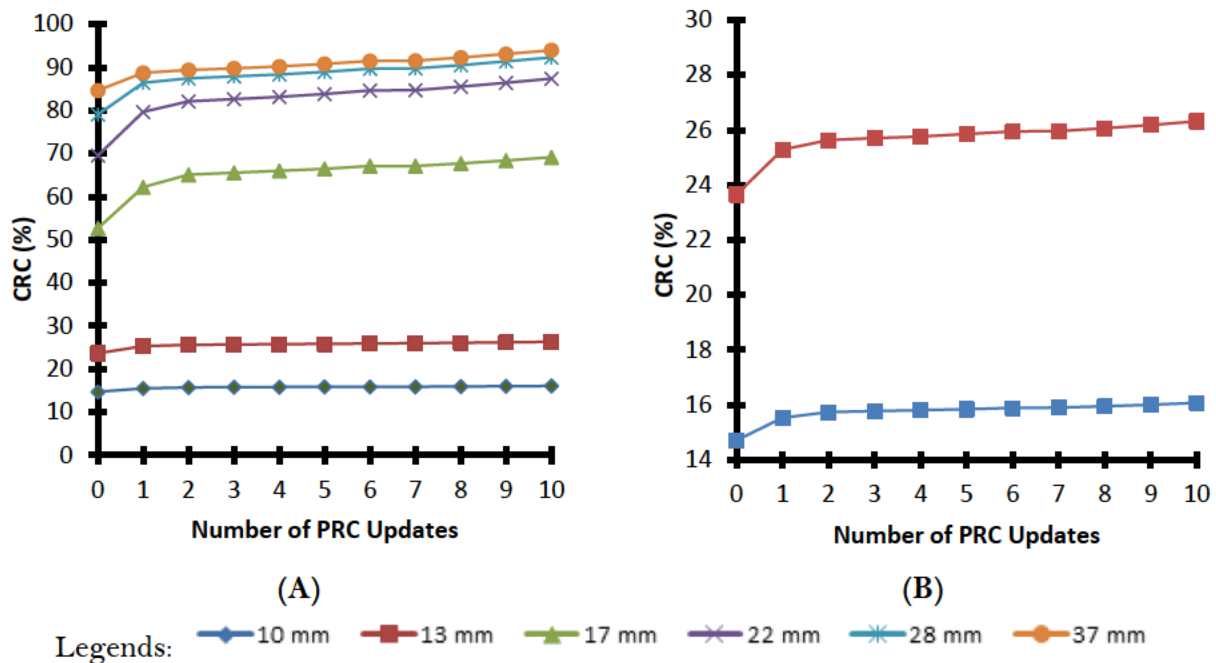
Figure 4.14: A) CRC for all spheres and B) magnification of the Y-axis for 10 mm and 13 mm spheres.

4.3.5 Signal-Noise Ratio

Figure 4.15 presents the SNR for each sphere as a function of the number of PRC iterations. Generally, the SNR decreases as the number of PRC updates increases at updates 1 and 2 due to moderate noise reduction. However, the SNR level is relatively constant from updates 3 to 10 because the noise reduction at associated updates was negligible. It can be observed that for a given PRC update, 10 mm sphere has the optimal SNR. Moreover, the level and rate of decrease in SNR were independent of the sphere size. This is because the SNR was calculated as the ratio of the mean ROI and standard deviation of the ROI itself, rather than the difference of mean ROI and standard deviation of the background, divided by the standard

114

deviation of the ROI. Hence in this study, the SNR value depended on the standard deviation of ROI in each sphere.
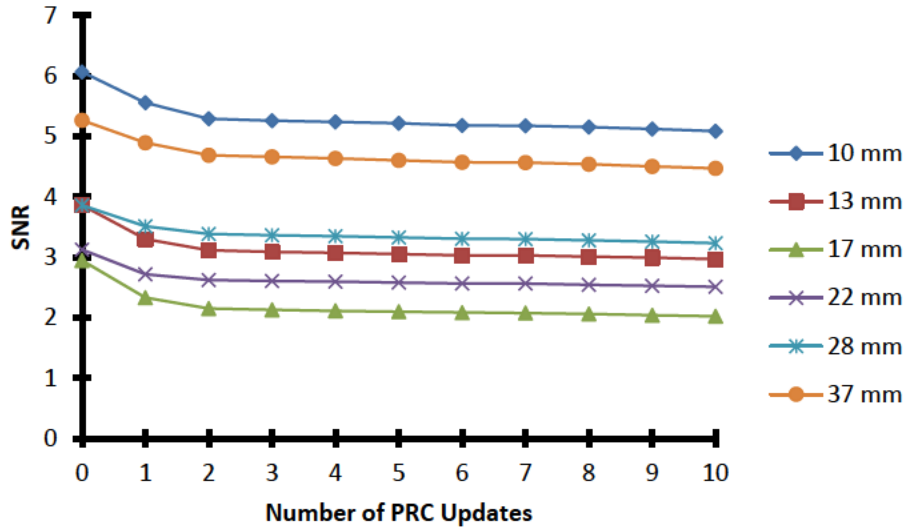
Figure 4.15: Spheres SNR vs the number of PRC updates.

4.3.6 Spatial Resolution

Analysis of FWTMr according to eq. 3.4 to measure the impact of PRC updates at all spheres was performed, as shown in 4.16. Update 0 indicated the FWTMr of ^{68}Ga NEMA IQ phantom for PET_0. It was found that the blurring effect was reduced rapidly at iteration 1 and almost consistent from iteration 2 to 10. The smallest sphere, 10 mm, results in the least blurring reduction as it suffers most from the partial volume effect. In this case, the measured counts in the sphere was preserved but they are smeared over a larger volume than the sphere. Meanwhile, the large spheres, 28 mm and 37 mm, have the least impact of partial volume effect. Hence the measured counts were not smeared and are within the corresponding sphere size.

The mean FWTM for each sphere of the ^{68}Ga PRC_k NEMA IQ phantom is compared to the ^{18}F PET_0 study in figure 4.17. This is not a direct measure of spatial resolution but an

indication of PRC impact between ^{18}F and PRC updates of ^{68}Ga. The blue-square line is the FWTM of ^{18}F PET$_0$, while the red-diamond line is the FWTM of ^{68}Ga with error bars represent the standard deviation.

These results provide useful information about how many iterations of PRC are required before the spatial resolution of the ^{68}Ga image approaches or exceed that of ^{18}F. Update 0 indicated the FWTM of ^{68}Ga NEMA IQ phantom for PET$_0$. For 10 mm and 13 mm spheres, the FWTM of ^{68}Ga study is better than ^{18}F after 1 iteration, while the other spheres achieved similar FWTM after approximately 6-10 iterations.
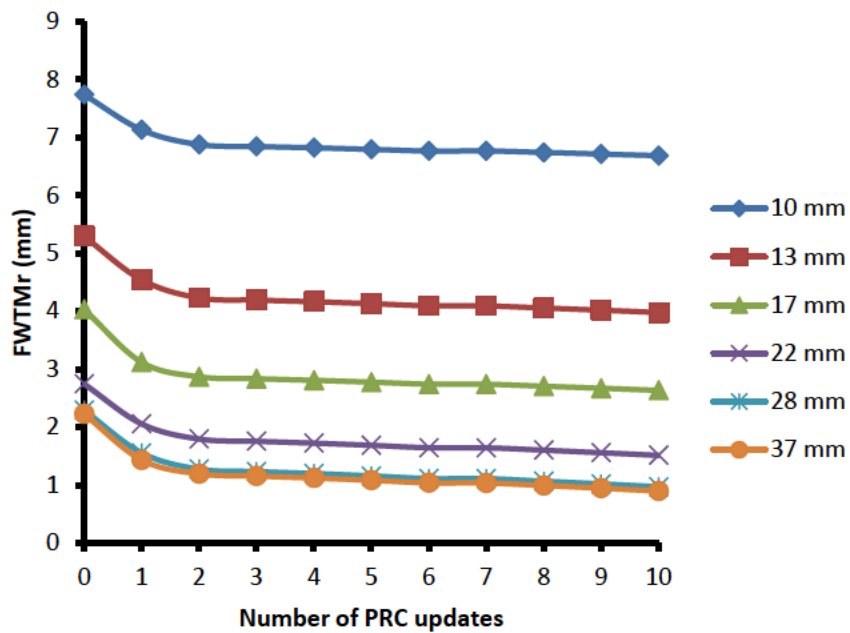
Figure 4. 16: Measured residual resolution (FWTMr) for ^{68}Ga measured at all spheres size.
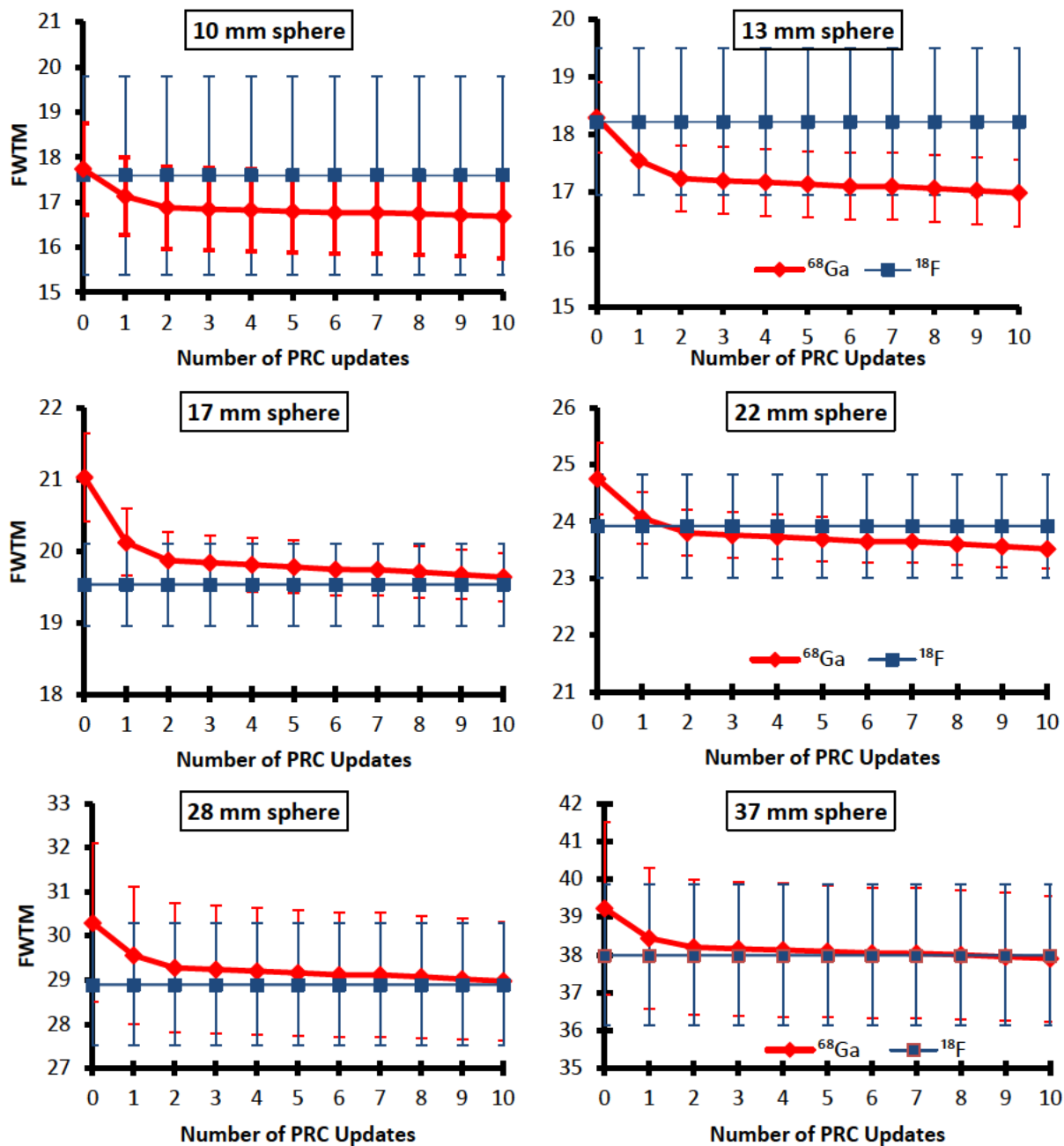
Figure 4.17: FWTM for each sphere for PET_0 (at 0 iteration) and PRCk images for 10 iterations.

4.4 Discussion

As the performance of clinical PET scanners improves and the use of isotopes with greater positron energies and, thus, larger positron range increases, the impact of positron range is becoming an important consideration. In this study, the post-reconstruction positron range correction (PRC) was developed and its performance was evaluated using a phantom study. It was demonstrated that the proposed method for post-reconstruction PRC improves certain metrics of image quality and quantification for ^{68}Ga compared to ^{18}F, such as FWTM and contrast recovery coefficient.

The proposed post-reconstruction PRC method is an iterative deblurring algorithm implemented directly within image space and performed using GATE and Matlab (see eq. 4.7). The method aims to estimate the distribution of positron emissions given the distribution of positron annihilations obtained from the PET scanner (PET$_0$), based on voxel-by-voxel PRC factors. The method presented in this work is sufficiently general to be applied to any reconstructed PET image, regardless of scanner geometry or radionuclide. Furthermore, it is suggested that a gamma hyperparameter equal to 1 effectively controls the image noise.

It is crucial to note that positron range distributions are difficult to model, as they may be generated by different ranges and directions within each voxel, depending on the materials that the positron traverses. Hence, generating an accurate attenuation map of the density of the underlying tissues to model the positron distribution is a key factor for the proposed method. GATE simulations were utilised to model the complex heterogeneous medium given sufficient attenuation details for each medium from co-registered CT images. The CT image was segmented according to (Schneider et al., 2000), generating a rigorous attenuation map including 71 types of tissues and interpolation for materials between two points to confirm the positron

characteristic for different tissues and boundaries. Moreover, this robust approach taken is to avoid an attenuation mapping discontinuity that may cause a voxel value in the image to be missed, if the segmentation was not thoroughly performed. Since this is a phantom study, an issue of segmentation discontinuity, especially at the complex and irregular tissue boundaries, cannot be explored. However, such physical complexities will be investigated in the next chapter by implementing PRC using real patient data.

Another important consideration in developing the post-reconstruction PRC method is the precise simulated annihilation image. This image acted as a spatially variant and tissue-dependent 3D blurring kernel performed according to the GATE simulations, which is a highly validated toolkit for such tasks. As we can see in figure 4.6, there is only a slight difference in the appearance of the spheres in PET_0 image compared to the simulated annihilation image, PET_1 visualization. Concerning PET_1, the boundary of the water/glass sphere is still not clear. However, the water/lung and water/background boundaries are clear compared to the PET_0 image. This is because, with the mean positron range in water for ^{68}Ga was ≈ 2 mm (as explained in chapter 3) and the thickness of glass spheres at only ≈ 1 mm, the positron could travel across the water/glass interface. In contrast, with the thickness of phantom housing and lung insert of 3 mm, the positron is attenuated at the water/lung and water/background interface, giving clear boundaries compared to the PET_0 image.

The first iteration of PRC deblurring method using eq. 4.6 introduces a noticeably high noise level in the corrected image, especially at the periphery of the phantom. Also, a Gibbs artefact manifests as a doughnut-shaped appearance around the lung region and within the largest sphere. This expected effect is related to the ill-posedness of the inverse deconvolution problem. The cause of the problem is the mismatch between the simulated blurring kernel and the true blurring kernel resulting in overshoot and ringing oscillations appearing at sharp edges.

If these are allowed, the artefact and noise are likely to increase with the iteration number. These Gibbs artefacts and excessive noise could be corrected by using a stopping rule (Almeida et al., 2015), performing a Gaussian post-filtering of the image and separating image reconstruction from PSF compensation strategy (Zeng, 2011). However, we preferred not to follow these approaches to conserve the high-resolution properties of the PRC_k images. Our aim to suppress noise and eliminate ring artefact and at the same time retain the high-resolution image was achieved by implementing relaxation using a hyper-parameter, γ (eq. 4.7). Consequently, we managed to control the noise magnitude and make it consistent as the iteration increases and this is where the strength of our approach lies. It is very important to control the image noise as it directly impacts the accuracy of the relative changes in standardized uptake value (SUV) (Boellaard et al., 2004). However, the application of a relaxation parameter reduced the Gibbs artefact in the lung area yet it failed to eliminate it within the largest sphere of the phantom.

Finally, we observed that the quantitative image performance measured by FWTMr, FWTM and CRC, improves after PRC with manageable noise as iterations increase. These results suggest that our approach is a promising alternative, although artefact appears, to previous PRC methods which use analytic system matrix resolution modelling. The techniques proposed can be generalised to different types of radionuclides and any other PET system regardless of geometrical specification without the need to provide accurate modelling of the system matrix, including positron range PSF. The system matrix allows modelling the individual resolution degrading effects shown in equation 2.21, including scattering, attenuation, non-collinearity, inter-crystal penetration, normalisation and positron range which are incorporated within the statistical reconstruction algorithm such as OSEM (Fraile et al., 2016, Cal-Gonzalez et al., 2018b, Bertolli et al., 2016), MLEM (Agbeko et al., 2010, Harzmann et al., 2014, Kraus et al., 2012) and MAP (Bing et al., 2005). However, the accuracy of the individual resolution

degrading effects modelled in the system matrix has a critical role in the quality of the reconstructed images. For example, different PET scanner has different specification and performance. Hence, the modelling for each factor in the system matrix for that corresponding PET scanner, except the positron range, need to be accurately estimated and modelled, respectively. Moreover, positron range PSF is proportional to the energy of the radioisotope and inversely proportional to the density of the media. Therefore, modelling the positron range PSF, especially in heterogeneous media, is difficult when considering the different media from the emission to the annihilation locations. Furthermore, it has been shown that resolution modelling can cause unpredictable edge artefacts (Alessio et al., 2013). These artefacts are generally exaggerated when the resolution model overestimates the degradation. However, it can be avoided by conservatively modelling the resolution effects.

4.5 Conclusion

A method of post-reconstruction PRC was developed, implemented and validated. The first part of this work involved simulating an accurate simulated annihilation image, PET_k, which acted as a 3D blurring kernel, based on a given PET_0 and a robust attenuation map that was acquired at the same time as the PET data. After that, the correction factor was determined iteratively and applied to the blurred image.

The proposed PRC method using iterative deblurring provides high-resolution and quantitative improvements in clinical PET phantom images. Furthermore, the relaxation parameter applied in the algorithm reduces Gibbs artefacts in the cold region and effectively controls the image noise. Thus, the method results in accurate images with stable noise performance. Since this is a phantom study, an issue of attenuation map discontinuity, especially

at the complex and irregular tissue boundaries, was not explored and will be investigated in the next chapter. Nevertheless, these promising results showed the feasibility of the PRC method and its potential for implementation in patient studies.

Chapter 5

Personalised Post-Reconstruction Positron Range Correction: Patient Study

5.1 Introduction

Neuroendocrine tumours (NETs) occur when the abnormal cells in the neuroendocrine system are rapidly growing in an uncontrolled manner. NETs are heterogeneous tumours comprised of 17 different neuroendocrine cell types originating in the skin, lung, hepatobiliary system, urogenital tract, thyroid and gastrointestinal tract (Schimmack et al., 2011, Maxwell and Howe, 2015). However, the most common primary regions are the small bowel, followed by the rectum, lung, colon, pancreas, stomach and appendix (Yao et al., 2008, Campana and Tomassetti, 2016).

According to the Australian Institute of Health and Welfare (AIHW) (aihw.gov.au/reports/cancer, accessed date: 19/10/2020), in 2016, there were 4108 new cases of NETs diagnosed in Australia with an incidence rate of 15 cases per 100,000 persons. In 2020, it was estimated that 4,972 new cases of NETs were diagnosed, including 2,629 males and 2,343 females, with an incidence rate of 17 cases per 100,000 persons.

Medical imaging is one of the techniques conducted to diagnose NETs, besides a blood test, urine test, endoscopy techniques and biopsy. Medical imaging is performed to identify the primary lesions, assess the staging and evaluate the treatment response for restaging (Serra and Andreone, 2016). Anatomic imaging such as multi-detector CT (MDCT) and magnetic resonance (MR) identify normal and abnormal organs or tissue with very high spatial resolution but with

limited functional information regarding the amount of viable and necrotic tumours. Meanwhile, functional imaging includes the use of ^{18}F-fluorodeoxyglucose (FDG) or ^{68}Ga-labeled PET compounds, which have a high affinity to NET cells. These new PET compounds demonstrate the NETs pathophysiological uptake, thus indicate their functionality.

NETs over synthesize and secrete peptide receptors such as somatostatin (SST) and/or amines that can be used as tumour markers and lead to clinical symptoms such as abdominal pain, bile duct obstruction, weight loss, jaundice and diarrhoea (Yalcin, 2015, Schimmack et al., 2011, Kaewput et al., 2018). Five subtypes of somatostatin receptors (SSTR) have been identified and named chronologically according to publication. These were SSTR type 1-5 (SSTR1-SSTR5) (Hoyer et al., 1995). Each of these SSTR subtypes has different receptor localizations within a chromosome (Patel, 1999). In NETs, the receptor with the most abundant secretion is SSTR2, followed by SSTR1 and SSTR5, lower amounts of SSTR3 are expressed and finally, SSTR4 was rarely detected (Reubi, 2004).

^{68}Ga-DOTA peptide is a somatostatin analogue that can be tagged to the positron emitter, ^{68}Ga, by the chelator, 1,4,7,10-tetraazacyclododecane-1,4,7,10-tetraacetic acid (DOTA) or the novel new chelator, 6-Amino-1,4-diazepine-triacetate (DATA) (Gaertner et al., 2019). This ^{68}Ga-compound has a high affinity for somatostatin receptors. Three major ^{68}Ga-compounds are currently available for PET imaging which include ^{68}Ga-DOTA-DPhe1-Tyr3-octreotate (DOTATATE), ^{68}Ga-DOTA-d-Phe1-Tyr3-octreotide (DOTATOC) and ^{68}Ga-DOTA-NaI[3]-Octreotide (DOTANOC). Since NETs overexpress SSTR2, ^{68}Ga-DOTATATE is a selective PET tracer for NET imaging due to its high binding affinity with SSTR2 (Shastry et al., 2010, Sharma et al., 2014, Johnbeck et al., 2014). However, the differences in SSTR binding affinity among the above PET tracers is not clinically significant (Levent et al., 2012, Johnbeck et al., 2014). Therefore, no preferential use of one compound over the others was advised. .

Functional imaging using ^{68}Ga-labeled PET has been widely performed due to the increased sensitivity and specificity of these new compounds. A meta-analysis regarding the performance of ^{68}Ga PET or PET/CT imaging in patients with NETs reported the pooled sensitivity and specificity of 91% and 94%, respectively, which was recommended for initial diagnosis of NETs (Singh et al., 2018). Excluding staging and restaging, the reported sensitivity for detecting primary and/or metastatic NET lesions was 78%-100%; meanwhile, a specificity of 83%-100% was reported. These enhancements have led to changes in the patient's management for 45% of the cases (Singh et al., 2018). Another systematic review and meta-analysis studied the changes to patient's management in NETs after ^{68}Ga PET scanning. The study involved 1500 patients and it was found that 44% of the cases changed in the type of therapy, for example, from surgery to chemotherapy; or changed in treatment strategy, for example, change in surgical strategy. It was found that the type of therapy changes occurred 3 times more frequently than changing the treatment strategy (Barrio et al., 2017).

In chapter 4, it was shown that the implementation of PRC for ^{68}Ga imaging was achievable and improved the image quality of PET phantom images and simultaneously controlled the image noise. However, noise or artefacts at the periphery phantom, within the air region, was seen as the number of iterations increased. In the application considered in chapter 4, the attenuation map was based on the comprehensive correlation between the CT numbers, tissue compositions and densities developed (Schneider et al., 2000). This chapter suggests that the density of the air needs to be modified, e.g. using a lung equivalent density, to reduce the noise and artefacts within the air region.

Post-reconstruction PRC is proposed to be applied to a patients' PET image, which contains various and heterogenous tissue compositions and densities, e.g., lung compared to soft-tissue has a longer positron range that can impact the ability to identify small lesions. In addition,

physiological motion, such as breathing and movement of air and material in the bowel, may cause differences between PET and CT images impacting the quality of PRC corrections. Therefore, as an extension of chapter 4, this chapter includes quantitative and qualitative image analysis to explore and investigate the PRC approach using patients PET/CT data with complex, irregular tissue boundaries that may potentially undergo motion.

5.2 Method

In this chapter, post-reconstruction PRC was implemented using patient data. Briefly, 17 of 20 patients were selected for the PRC implementation. The images before (PET_0) and after PRC (PRC_k) were then compared and analysed quantitatively. A reader study was also conducted to compare and assess the image quality qualitatively. A flow diagram of the study design is shown in figure 5.1. A detailed method is explained in the next sections.
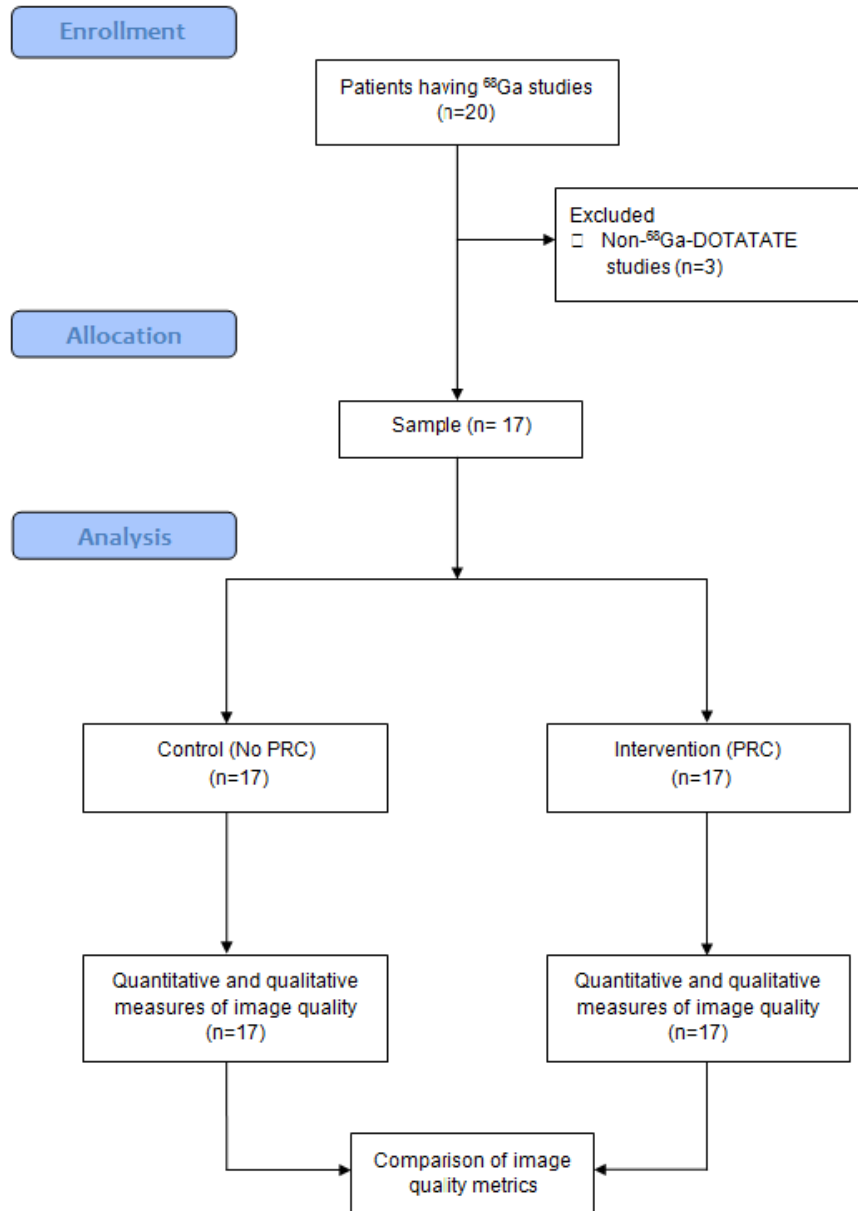
Figure 5.1: The flowchart of clinical PRC implementation. As PRC does not exclude analysis of the original image, the images from all selected subjects were passed through both the control and intervention arm for comparative analysis.

5.2.1 Ethics approval

The ethics approval was obtained from the University of Sydney Human Research Ethics Committee (HREC) Project no.:2017/854 (Appendix I).

5.2.2 Patients

First, twenty anonymized patient images from the Royal North Shore Hospital were assessed for eligibility. Patients were identified as 01 to 20 in this study. The first three patients were excluded, patients 01 to 03, because they were ^{68}Ga-PSMA studies for prostate cancer. Seventeen patients, patients 04 to 20, with clinical indications for NET imaging had undergone a ^{68}Ga-DOTATATE PET/CT scan and were included and evaluated. First, a CT topogram was acquired using 120kVp and 35mAs with a scan length of 1576 mm, which serves as an anatomic reference for the PET/CT scan. Next, the 64-slice CT scan was performed using 120 kVp and 80 mAs followed by a PET scan using a Biograph mCT clinical PET/CT system (Siemens Healthcare, Erlangen, Germany) from the top of the skull to mid-thigh, approximately 45 minutes after ^{68}Ga-DOTATATE administration, using 6 to 7 beds positions with 150 sec per position. The axial field of view of the PET scanner was 221 mm.

Images were reconstructed using the Royal North Shore Hospital's routine method of PET/CT reconstruction: fully 3D Point-Spread-Function (PSF) image reconstruction performed with time-of-flight (TOF), using an OSEM protocol (3 iterations, 21 subsets), and the subsequent application of a post-reconstruction Gaussian filter of 5 mm full width at half maximum (FWHM). The PET images have a 200×200 matrix, 4.07×4.07 ×3 (mm)^3 voxel size. Meanwhile, the CT images were reconstructed in a 512×512 matrix and voxel size of 0.98×0.98×3 (mm)^3.

5.2.3 Iterative Post-Reconstruction PRC

The details of the PRC algorithm and method are explained in chapter 4, subsection 4.2.1. To determine the number of iterations employed for the PRC algorithm, results from chapter 4 (section 4.3) was used as a guide. Chapter 4, figure 4.13 demonstrated that the artefacts intensity increases as iteration increased. Likewise, figures 4.14, 4.15 and 4.16 demonstrated that for small spheres, the image quality metrics, such as contrast recovery, SNR and spatial resolution, drastically improved within the first and second iterations. However, the measurements were consistent from third to tenth iterations. Therefore, five iterations were chosen for the patients' study as this provided equivalent image quality results to 10 iterations but with fewer artefacts. The algorithm of the proposed PRC developed in chapter 4 can be found in figure 4.2.

The developed post-reconstruction positron range correction algorithm relies on the discrepancies between the PET measured annihilation image (PET_0) from the scanner and the simulated annihilation image (PET_k) generated by GATE, based on the corresponding PET_0 that acted as positron-emission image input to GATE at zero iteration. Therefore first, the PET_k image needs to be examined whether GATE can model positron range distribution within different types of tissue density in the body composition and complexity of different tissue boundaries.

5.2.4 Modification of the CT number

As explained in chapter 4, section 4.2.2.1, the attenuation map requires calibration of Hounsfield units (HU) and tissue density. In the previous phantom study, CT numbers ranging from -1050 HU to -950 HU were used for air and from -950 HU to -120 HU for lung. In this patient study, initially, the same range of CT numbers was implemented to represent air and lung tissue. However, the resulting PRC image resulted in noise or artefacts in the air regions

There were two attempts to remove the introduced artefact. First, using a masking approach where the minimum and maximum values in the air region were determined and then subtracted. However, the approach was rigid and fragile as the range values within the air regions were varied at different locations, such as in the abdominal area, trachea and nasopharynx. Consequently, the method can under or over remove the false uptake and was considered inefficient.

Therefore, a second approach involved modifying the CT number to eliminate the observed false uptake in air regions, such as background, trachea, oesophagus and bowel. The method to remove false uptake in the regions of air was deduced from eq. 4.6 in subsection 4.1.2 of chapter 4, where the image error was calculated by determining the ratio of the PET_0 and the simulated annihilation image, PET_k. From the equation, the image error increases when the value in the annihilation image is low, resulting in unreasonably high values after the updating process. Therefore, the CT number for air was modified to be equivalent to the lung, ranging from -800 HU to -120 HU. This range was chosen to yield a density from $\sim 0.26 g/cm^3$, equivalent to the lung during inflation, to ~ 1 g/cm^3 during deflation, according to ICRU report 44 (1989). By implementing this method, the false uptake in the air region was successfully removed. The adjustment of the CT number results in an attenuation map as in Appendix J.

5.2.5 Image analysis

Image analysis was performed using AMIDE software (Loening and Gambhir, 2003). For the uniform region, the figures of merit used for quantitative image analysis were noise, contrast, signal-to-noise ratio (SNR) and the mean and maximum standardized uptake values

(SUV). The image noise was defined as the standard deviation of counts in the region of interest (ROI) (Lois et al., 2010). The ROI delineated for noise analysis was estimated from a 2D box drawn on organs with physiological uptake of ^{68}Ga-DOTATATE. Regions included the liver with a size of 50×40 (mm)^2, lung with a size of 30×70 (mm)^2, muscle with a size of 80×70 (mm)^2, and the spleen and kidney cortex with a size of 30×30 (mm)^2. The selection of ROI sizes covered the organs as widely as possible to reduce bias in the calculation.

Standardized uptake values are a semiquantitative measure commonly used to quantify tracer accumulation in PET studies. The value has been used for diagnostic evaluation, assessing response to therapy and prognostic prediction. Generally, the SUV assesses the radioactivity concentration in the region of interest (ROI) normalized to the radioactivity concentration in the body (equation 5.1); where the body size is based on the patient's body weight, lean body mass or body surface area (Adams et al., 2010).

$$SUV = \frac{activity\ concentration\ in\ ROI}{injected\ activity / body\ size} \tag{5.1}$$

The radiopharmaceutical uptake of these organs was evaluated using SUV$_{mean}$ and SUV$_{max}$. In addition, the SUV$_{mean}$ and SUV$_{max}$ for pituitary were also determined using ROI drawn around the whole organ (Kunikowska et al., 2012). All ROIs were drawn using AMIDE software and all the SUVs were calculated using the equations 5.2 and 5.3:

$$SUV_{mean} = \frac{mean\ activity\ concentration}{injected\ dose / body\ weight} \tag{5.2}$$

$$SUV_{max} = \frac{maximum\ activity\ concentration}{injected\ dose / body\ weight} \tag{5.3}$$

The relative changes of noise for each organ were compared between PET$_0$, which were the original PET images before PRC, and PRC$_5$, image after PRC after 5 iterations:

$$Relative\ noise\ changes = \frac{Noise\ PET_0 -\ Noise\ PRC_5}{Noise\ PET_0} \times 100 \qquad (5.4)$$

The SUVmean and SUVmax of the pathological uptake were determined by drawing a spherical ROI for lesions analysis. The identified lesions were less than 2 cm in diameter (Lois et al., 2010).

The lesion contrast and SNR were calculated as follows (Yan et al., 2016):

$$Contrast = \frac{Mean\ Lesion}{Mean\ Liver} \qquad (5.5)$$

$$SNR = \frac{Mean\ lesion}{SD\ background} \qquad (5.6)$$

Relative contrast changes between PET_0 and PRC_5 image were computed as below to determine the contrast performance (Cal-Gonzalez et al., 2018b, Lois et al., 2010):

$$Relative\ contrast\ changes = \frac{Contrast\ PRC_k - Contrast\ PET_0}{Contrast\ PET_0} \times 100 \qquad (5.7)$$

Violin plots were used to display noise, uptakes, contrast and SNR distributions (Weissgerber et al., 2017). The descriptive and inferential statistics of the data were described and analysed using SPSS Statistics (IBM Corp. Released 2017. IBM SPSS Statistics for Windows, Version 25.0. Armonk, NY: IBM Corp). The noise difference, contrast difference, SNR difference and uptake difference between corrected and uncorrected images were not normally distributed. Therefore, the Wilcoxon Signed-Ranked test was used to compare the measurement metrics between PET_0 and PRC_5 images. A $p<0.05$ is considered to indicate that a significant difference was observed between the two images.

5.2.6 Reader study

Seventeen pairs of PET_0 and PRC_5 images were compared side-by-side and reviewed independently by two experienced nuclear medicine physicians. The image quality assessment was performed in MIM software, which those readers routinely use for clinical reporting at Royal North Shore Hospital. The readers were blinded to the patient's identity and which of the images were positron range corrected. However, a brief clinical history was provided. Not all scans showed active disease, i.e., the test was negative for the disease. Readers scored the images according to the questionnaire in Appendix K. The questionnaire was designed to gather information about the overall image quality, artefacts and image preference for lesions presentation in PET_0 and PRC_5 images. The flowchart of the study is shown in figure 5.2.
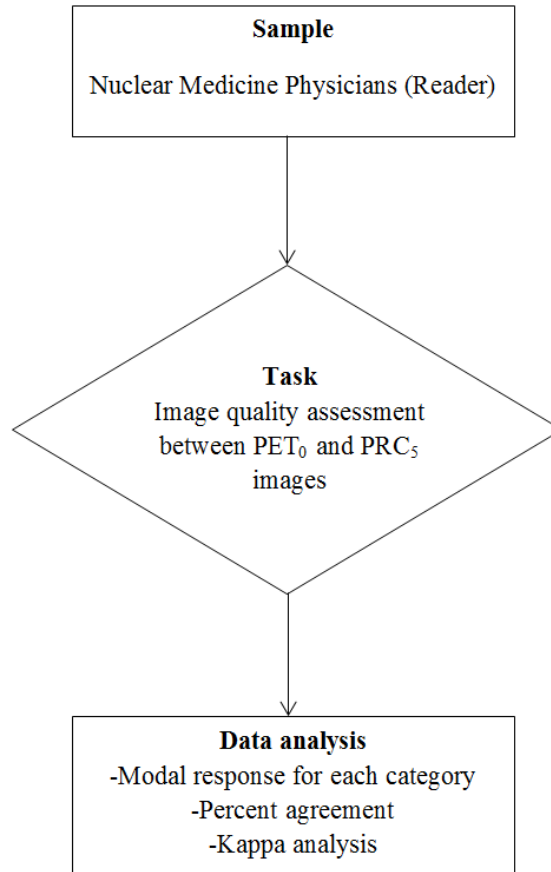
Figure 5.2: Flowchart for reader study to assess image quality.

The percentage agreement among readers was calculated below (McHugh, 2012):

$$Percent\ agreement = \frac{Frequency\ of\ agreement\ between\ reader\ 1\ and\ 2}{Total\ images,17} \times 100 \qquad (5.8)$$

The observed agreement was also determined using Cohen's kappa statistic, κ which was given by (Watson and Petrie, 2010) to correct for random chance effects:

$$\kappa = \frac{P_0 - P_E}{1 - P_E} \qquad (5.9)$$

where P_0 is the observed agreement, 1 is the perfect agreement and P_E is the expected agreement. The following table shows κ values and their interpretation, respectively (Watson and Petrie,

2010). P <0.05 was considered to indicate that the agreement between readers was significant and beyond chance.

Table 5. 1: Cohen's kappa, κ and degree of agreement

κ	Interpretation
<0.00	Poor
$0.00 \leq κ \leq 0.20$	Slight
$0.21 \leq κ \leq 0.40$	Fair
$0.41 \leq κ \leq 0.60$	Moderate
$0.61 \leq κ \leq 0.80$	Substantial
>0.80	Almost perfect

The kappa value is influenced by 3 factors which were prevalence of the attributed variables (prevalence index), bias to what extent the readers disagree on the proportion of each variable (bias index) and independent ratings (Julius and Chris, 2005). If the prevalence index is high, the probability of an agreement achieved due to chance is also high and reduced the kappa accordingly. In contrast, if the bias index is large, the kappa value is higher than when bias is low or absent. Therefore, independent ratings in this study were the reader should perform the image quality assessment without knowledge and influence of the other reader's assessment.

Referring to cell notation of 3×3 crosstabulation table in table 5.7, prevalence index and bias index were calculated as below:

$$Prevalence\ index = \frac{|a-e-i|}{Total\ image,17} \tag{5.10}$$

$$Bias\ index = \frac{|c-g|}{Total\ image,17} \tag{5.11}$$

For image quality data, the frequency for each selected category was calculated. The image quality for PET_0 and PRC_k was determined based on the most frequently selected image

quality category. The modal response was chosen to summarize the outcome by finding the most selected category (Keeble et al., 2016).

5.3 Results

In this section, the performance of the post-reconstruction PRC algorithm on PET image quality was assessed quantitatively and qualitatively. The hypothesis was that the PRC implementation would not change the normal physiological distribution and uptake in the body and improve the lesion contrast and sharpness.

5.3.1 Demographic

Seventeen patients were included in this retrospective study, with 12 females and 5 males. The mean age was 54.6 ± 16.6 years, ranging from 23-82 years, the mean weight was 69.5 ± 20.2 kg, ranging from 44-128 kg and the mean injected dose was 150.5 ± 23.4 MBq, ranging from 130.9-194.3 MBq. One patient underwent splenectomy. Patients were referred for either staging or restaging/follow-up of various malignant tumours indicated for the ^{68}Ga-DOTATATE scan. The detailed demographics can be found in Appendix L.

Parallel simulations were performed to model the patient's annihilation image. For each patient image and one iteration in this study, simulation was split into 8 independent 'sub-simulations', which then summed together at the end to obtain approximately similar counts detected as in the image from the PET scanner. All the 8 sub-simulations were completed within 30 minutes to 2 hours, depending on the complexity of radioisotope distribution in the body, when using 8 cores with 20 Gb RAM each. Hence for 5 iterations, approximately 2.5 hours to 10 hours were required to complete the whole simulation. The resulting updated image was normalised to the total number of the PET measured image.

5.3.2 PET measured annihilation image vs simulated annihilation image

In this thesis, PET measured annihilation image was represented as the PET_0 while simulated annihilation image was represented as PET_k. At this stage, to simulate PET_k, the original CT number of air was used, ranging from -1050 HU to -950 HU. Figure 5.3 below exhibited the resulting attenuation map according to chapter 4, section 4.2.2.1 and Appendix G.

Axial   **Coronal**   **Sagittal**
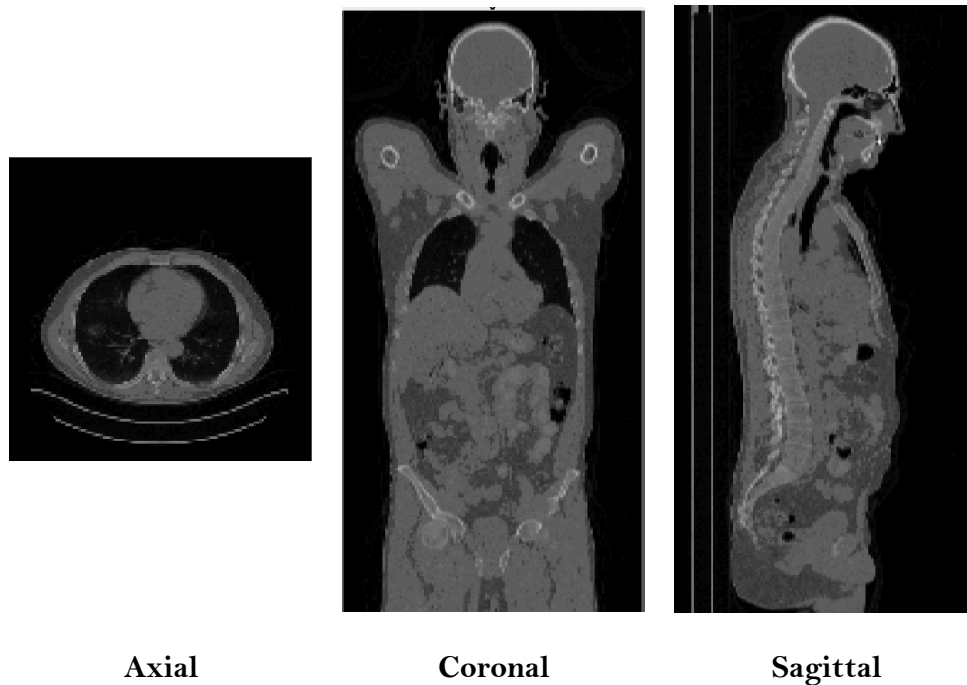
Figure 5. 3: An example of a segmented attenuation map for a patient's PET image according to the values listed in Appendix G.

While figure 5.4 demonstrated the resulting simulated annihilation image at zero iteration, PET_1 given PET_0. Images in figure 5.4 were displayed using the same maximum threshold to exaggerate the contrast and appreciate the air regions. Compared to PET_0, PET_1 agrees with the expected theoretical positron-annihilation image. Which is, in the low-density area, such as in the lung, the positron range is longer than in the high-density areas, such as bone. Hence, the boundaries of lung and bone, as well as air and soft tissue were distinguishable in simulated annihilation image. Moreover, the air regions were clearly seen as expected because

there is no uptakes in these areas and matched with the air area in the CT image. The appearance of bronchioles in the lung also indicates that the tissue composition and density definition utilised in this simulation were sufficient. Thus, it was interesting to find that GATE demonstrated a thorough simulated annihilation image that matches the expected theoretical image.
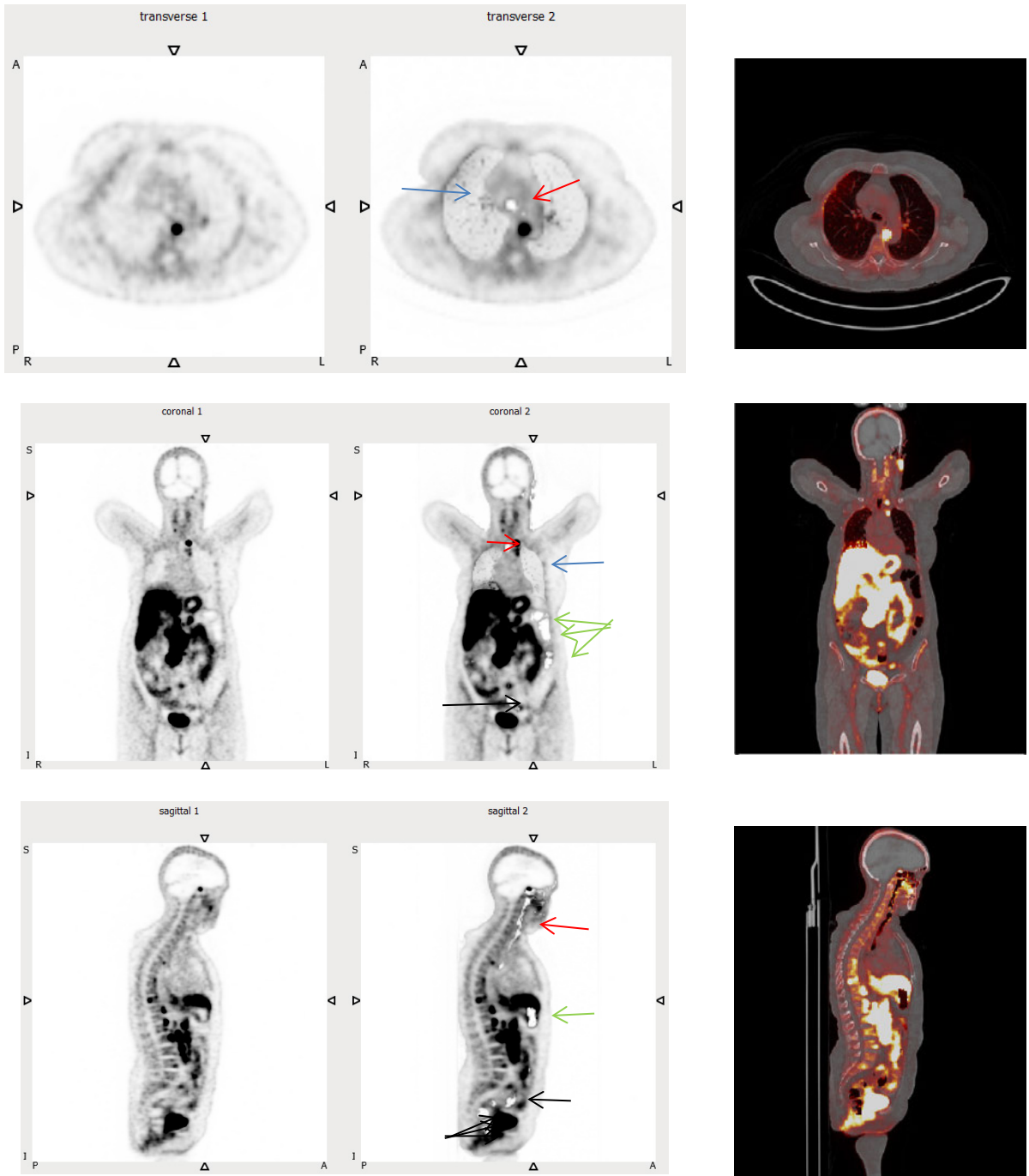
Figure 5.4: The first row is transverse, the second row is coronal and the third row is sagittal views of patient 04. The first column from the left is the PET_0 image, the second column is the PET_1 image and the third column is the PET_1/CT fused image. Red arrows indicate the trachea, blue arrows indicate the lung, green arrows indicate the air region in the abdominal area and black arrows indicate the air region in the pelvis area. The PET_1/CT image demonstrated that both images were aligned and the air regions were matched.

Band artefact observed between upper liver and lung diaphragm in PET_1 image as shown in figure 5.5. The artefact was resulting from under correction of attenuation around the diaphragm in CT derived attenuation image due to the mismatch between CT and PET_0 image due to respiration.
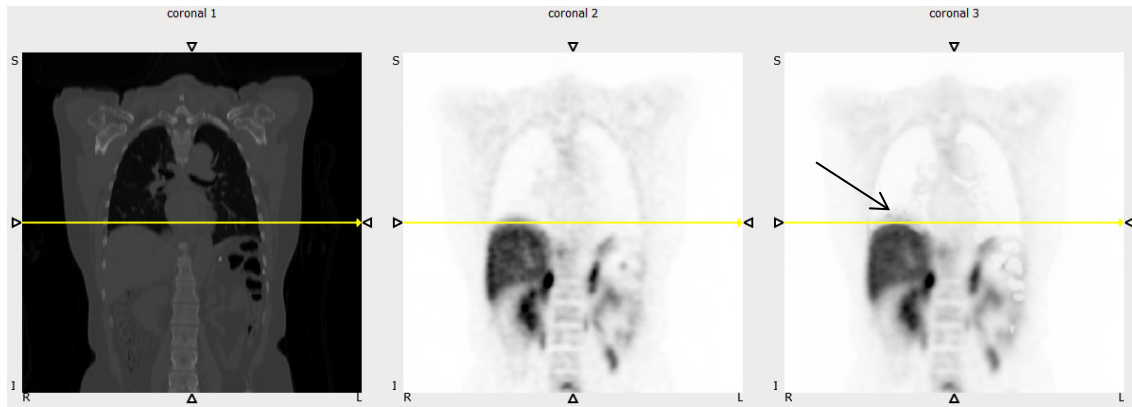
Figure 5. 5: Patient 11: Respiratory motion produces misalignment between CT image (left) and PET measured image, PET_0 (middle), results band artefact in simulated annihilation image, PET_1 (right).

5.3.3 Modification of CT number

Figures 5.6 to 5.8 show a comparison of PRC_5 images for patient 14 in transverse, coronal and sagittal views before and after CT number modification for air medium (subsection 5.2.4).

Before CT number modification for air medium, it was obvious that artefacts occur as false uptake in air regions such as the trachea, oesophagus and in abdomen. Therefore, a modification of CT number for air was performed by choosing a range of -800 HU to -120 HU, which was equivalent to the CT number of the lung. This method provided a solution to eliminating the observable false uptake as demonstrated from the line profiles.
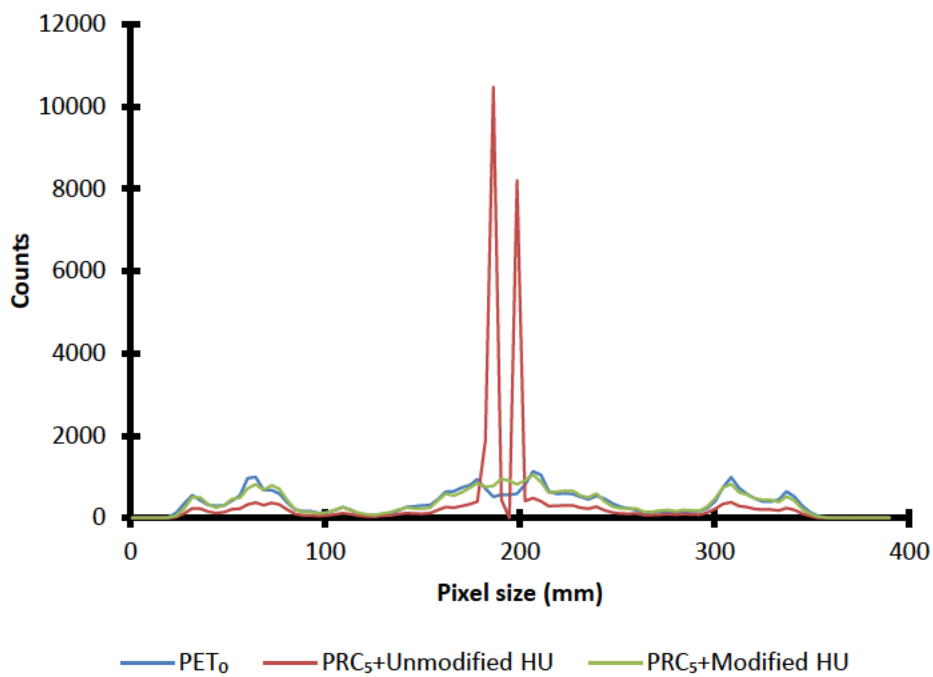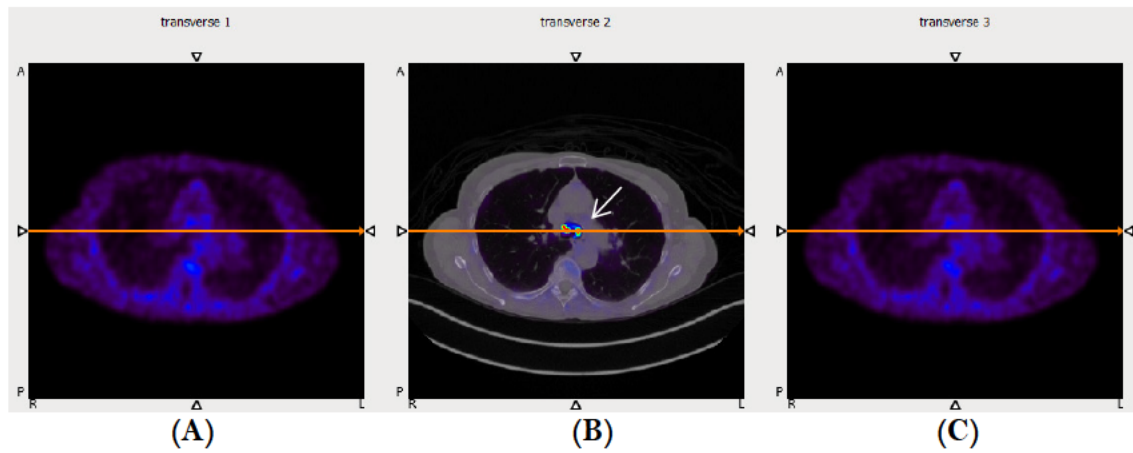
Figure 5.6: Patient 14: Comparison of transverse view images before and after modification of CT number during PRC implementation. (A) The PET_0 image, (B) is the fused PRC_5/CT image with unmodified CT number and (C) is the PRC_5 image with modified CT number. The white arrows show the location of artefacts diminished after CT number of air is modified to be equivalent to lung as demonstrated in (C) and the line profile in (D).
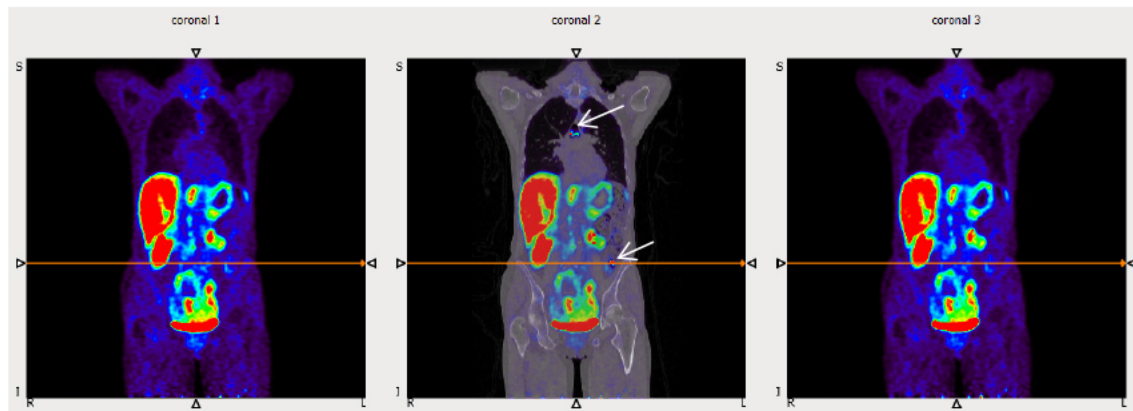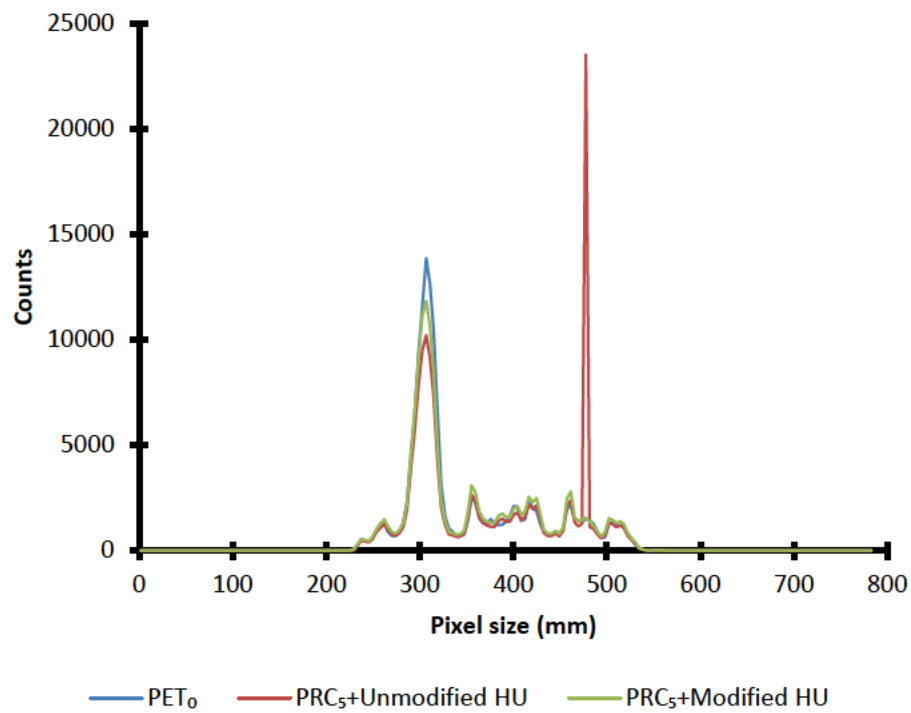
Figure 5.7: Comparison of coronal view images before and after modification of CT number during PRC implementation. (A) The PET_0 image, (B) is the fused PRC_5/CT image with unmodified CT number and (C) is the PRC_5 image with modified CT number. The white arrows show the location of artefacts diminished after CT number of air is modified to be equivalent to lung as demonstrated in (C) and the line profile in (D).

(D)
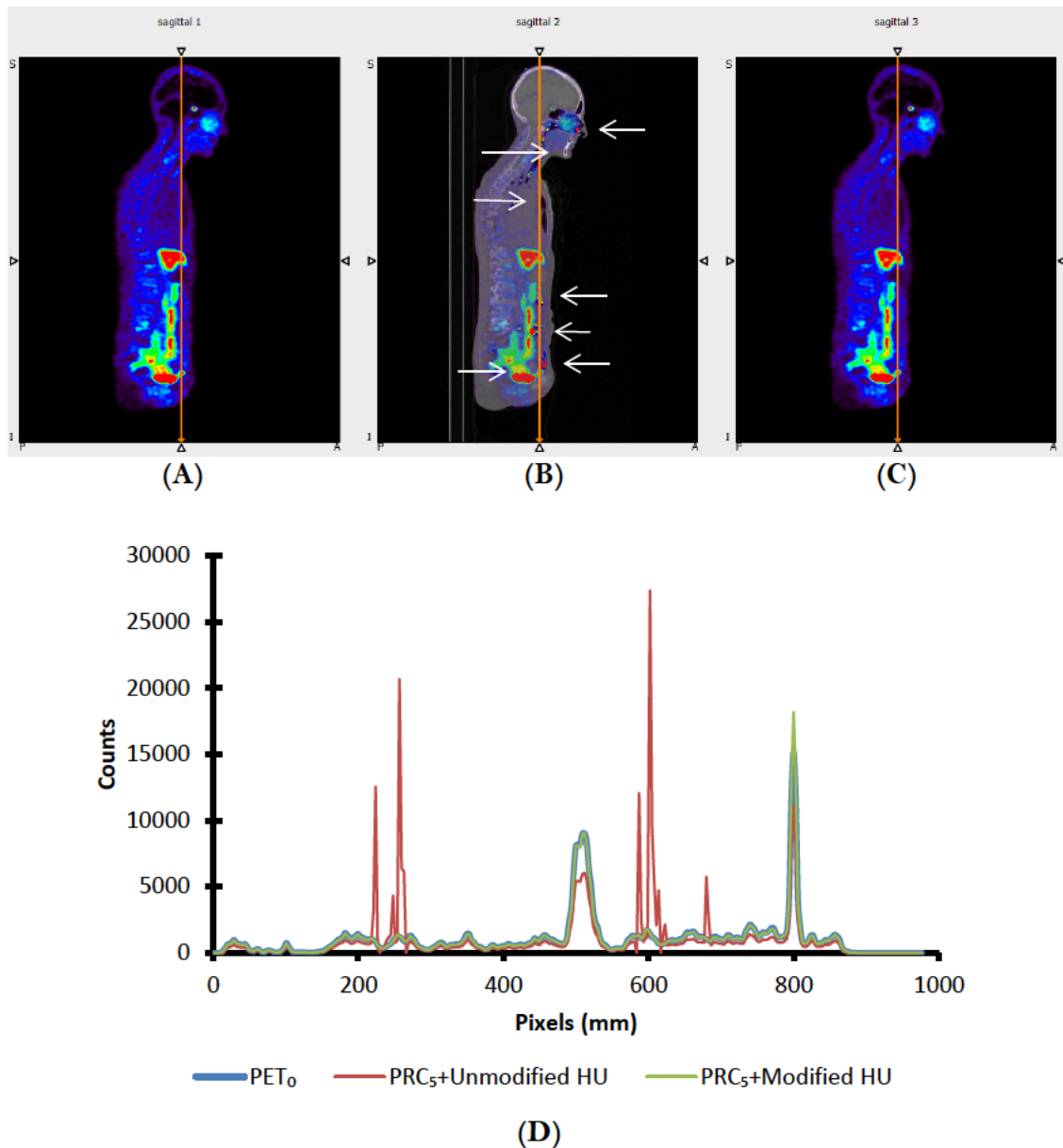
Figure 5.8: Comparison of sagittal view images before and after modification of CT number during PRC implementation. (A) The PET_0 image, (B) is the fused PRC_5/CT image with unmodified CT number and (C) is the PRC_5 image with modified CT number. The white arrows show the location of artefacts diminished after CT number of air is modified to be equivalent to lung as demonstrated in (C) and the line profile in (D).

It was evident that the proposed post-reconstructed PRC method works well between soft-tissue/lung boundaries demonstrated in figure 5.9, even when a lesion was close to a tissue-boundary shown by the white circle (figure 5.10). With 5 iterations, the PRC_5 image shows no

artefact in the lung or/and trachea, thus demonstrating that the original uptake was correctly co-registered with its respective tissues. These images were displayed using nearest neighbour interpolation using the same maximum threshold to increase the contrast of boundaries.
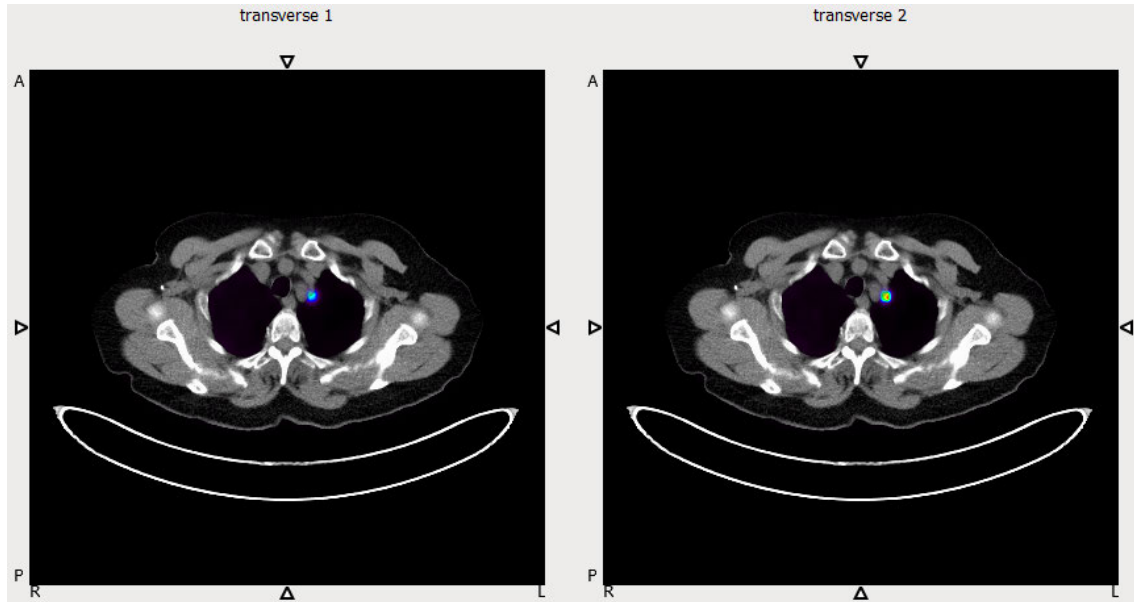
Figure 5.9: Patient 04: Fused PET_0/CT image (left) and PRC_5/CT image (right) where lesion located between soft-tissue and lung.
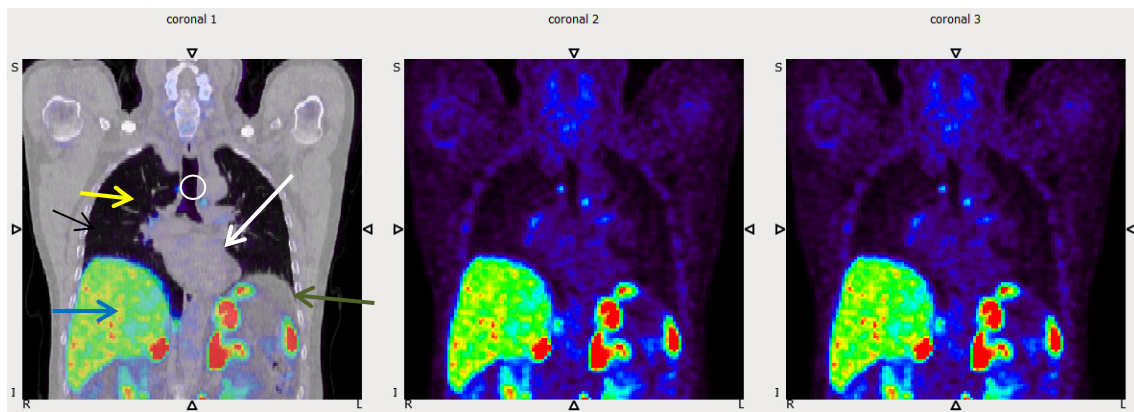
Figure 5.10: Patient 07: Fused PET_0/CT image (left) to locate the lung, rib bone, liver, heart, and spleen indicated by yellow, black, blue, white and green arrows, respectively. The white circle indicates the location of a lesion between lung, soft-tissue and trachea. The PET_0 (centre) and PRC_5 (right) images.

5.3.4 Noise and uptake of uniform region

For quantitative analysis, PRC_5 images were normalized to have the same total counts as PET_0. Of 17 patients, one underwent splenectomy, one patient did not have uniform uptake in the spleen, and 2 patients did not have uniform uptake in the liver. Thus, we obtained 81 ROIs, which comprised 15 liver, 17 lungs, 17 muscle, 15 spleens and 17 kidneys. These ROIs were analysed for image noise. In addition, the pituitary gland was evaluated only for uptake and not image noise. Therefore, a total of 98 ROIs were analysed for radiopharmaceuticals uptake, i.e., SUV_{mean} and $SUV_{max.}$

The distribution of image noise and uptake of PET_0 and PRC_5 were displayed as violin plots with bandwith 1, shown in figure 5.11. The shape of the plot displays the frequencies of data with the tails of the violin trimmed to show the exact range of data. Each cluster indicates the data contributed from the respective organs. The data was not normally distributed. It was skewed and contained outliers. The kidneys and spleens have the highest noise compared to other organs (figure 5.11A). Meanwhile, for uptake, the lung and muscle are the lowest, followed by liver, kidney, pituitary and spleen, accordingly (figure 5.11 B & C).

(A) **(B)** **(C)**
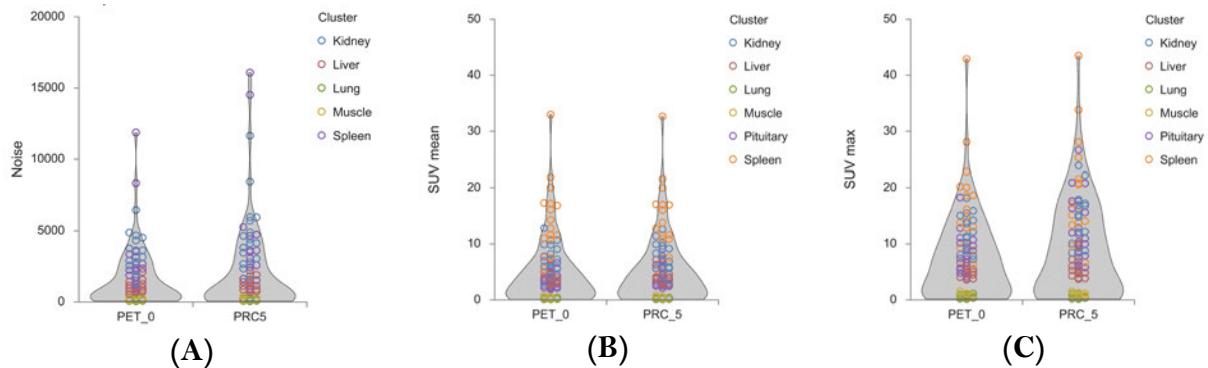
Figure 5.11: Data distribution for (A) noise, (B) SUV mean uptake and (C) SUV maximum uptake of PET_0 and PRC_5 images for the uniform region.

Table 5.2 shows the analysis of image noise and uptake for PET_0 and PRC_5 images. Median image noise significantly increased ~2% after PRC implementation compared to PET_0 (p<0.05). There was a slight increment ~6% of SUV_{mean} for PRC_5 images. However, the increment was not significant (p=0.667). The SUV_{max} was significantly increased ~25% for PRC_5 images (p<0.05).

SUV_{mean} was considered for uptake in the uniform region because the drawn ROIs were relatively large. It averages the values from multiple voxels, therefore reducing count bias (Kinahan and Fletcher, 2010). Although it is sensitive to ROI definition by the observer, most importantly, it is relatively independent of image noise. The SUV_{mean} thus suitable to quantify normal physiological uptake and in this study demonstrated that normal uptake was retained after PRC implementation (Adams et al., 2010). In contrast, SUV_{max} includes only the highest voxel intensity. Therefore it is biased to quantify uptake in uniform regions. Furthermore, it is relatively independent of ROI delineation but sensitive to image noise (Adams et al., 2010). Consequently, when the image noise significantly increases after PRC, it influences the maximum uptake values in the region.

Table 5.2: Noise and uptake for uniform regions

Image Quality Metrics	N	Image	Mean	Median (IQR)	Min	Max	Std. Dev	P value
Noise	81	PET_0	1,609	921 (186-247)	59	11,867	2,008	0.000
		PRC_5	2,157	938 (186-326)	58	16,076	3,026	
SUV_{mean}	98	PET_0	5.0	3.4 (0.3-7.0)	0.07	33.0	5.8	0.667
		PRC_5	5.1	3.6 (0.3-7.2)	0.07	32.6	5.8	
SUV_{max}	98	PET_0	7.3	5.6 (0.7-11.1)	0.13	42.9	7.3	0.000
		PRC_5	9.0	7.0 (0.7-15.1)	0.13	43.5	8.7	

The results in table 5.2 show that images obtained using the PRC algorithm retain the normal distribution and average uptake of ^{68}Ga-DOTATATE when compared to PET_0 images. The maximum-intensity projection (MIP) images of two patients, patient 13 and patient 16, are shown in figure 5.12. Patient 13 reported a stable scan appearance where no new avid lesions were found. Meanwhile, patient 16 was reported as normal scan appearance with no lesions observed. Here, the performance of the post-reconstructed PRC to retain the similar distributional uptake for organs that have normal physiological uptake of ^{68}Ga-DOTATATE was compared to PET_0, used as a reference. Although speckles artefacts were seen in the abdominal area in PRC_5 images, normal physiological uptake of ^{68}Ga-DOTATATE for PET_0 and PRC_5 images were clearly observed in the pituitary, spleen, liver, adrenals and kidneys. In addition, a low, diffused and uniform uptake was seen in the salivary glands, thyroid gland, bones, lungs, and muscles. These visual appearances in figure 5.12 aligned with the data distribution demonstrated in figures 5.11B and C.
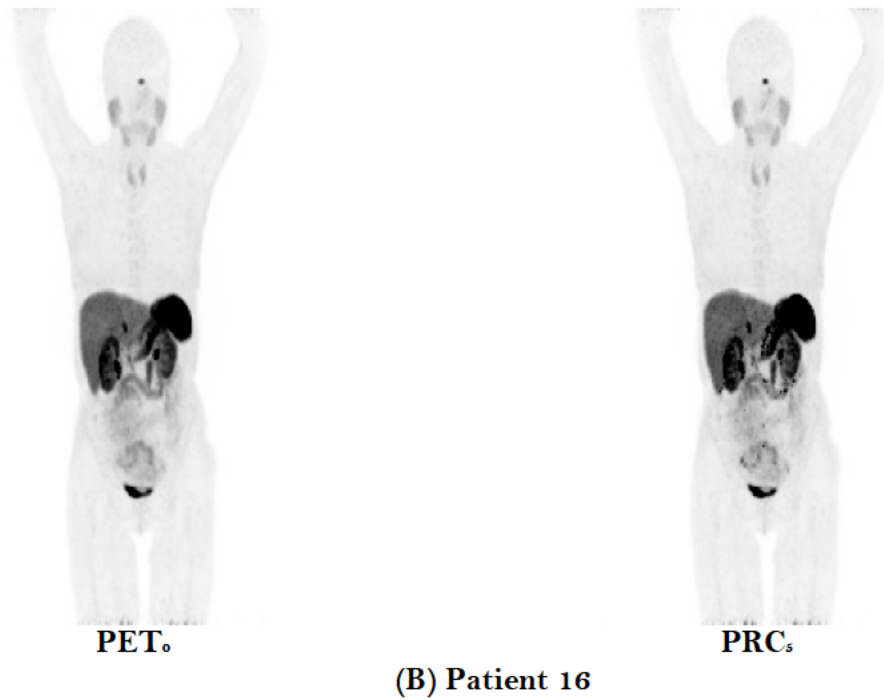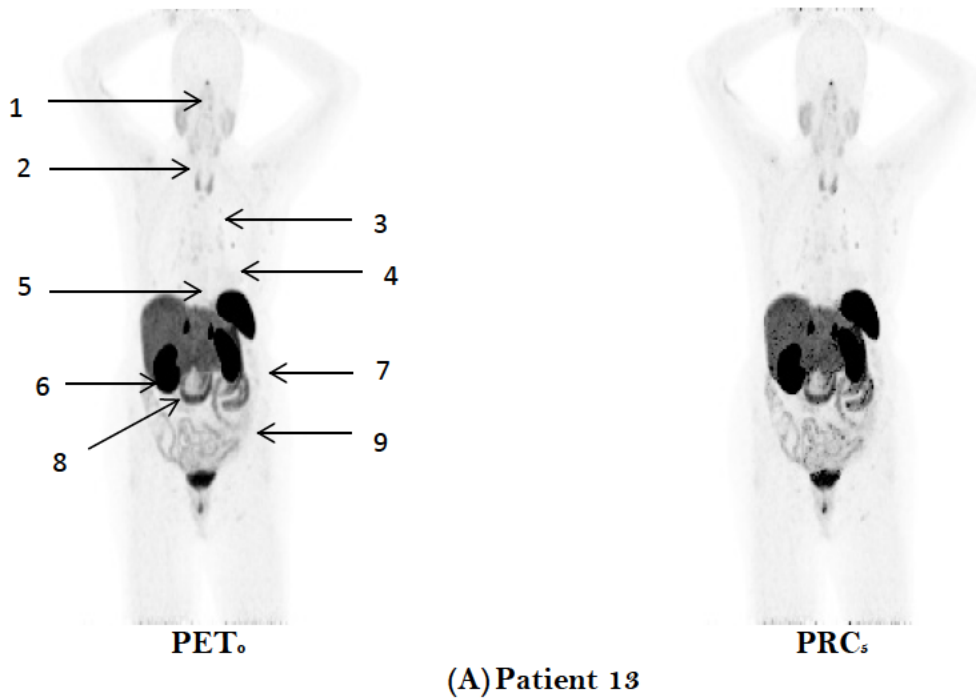
Figure 5.12: Maximum intensity projection image showing the physiological distribution of 68Ga-DOTATATE. Organs with a normal distribution of the radiopharmaceutical are highlighted with numbered arrows: 1) pituitary gland; 2)salivary gland; 3) thyroid; 4) lung; 5) spine bone; 6) liver; 7) spleen; 8) adrenal; and 9) kidney.

5.3.5 Lesion contrast, uptake and signal–noise ratio

Figure 5.13 shows the distribution of contrast, SNR and uptakes of lesions. Meanwhile, table 5.3 provides a detailed statistical analysis. A total of 59 lesions were identified and analysed for contrast, SNR and uptake (SUVs). The tails of the violin plot were trimmed to exhibit the exact range of data. All data were not normally distributed and skewed. The contrast was the only metric that has the outliers. Overall, the lesion contrast was significantly improved ~20% after PRC. The SNR was also significantly improved ~6% and the mean and maximum uptakes were significantly increased ~21% and ~45%, respectively. SUV_{max} was considered for lesions uptake due to accurate estimation of the true SUV within the 2 cm lesions (Kinahan and Fletcher, 2010).
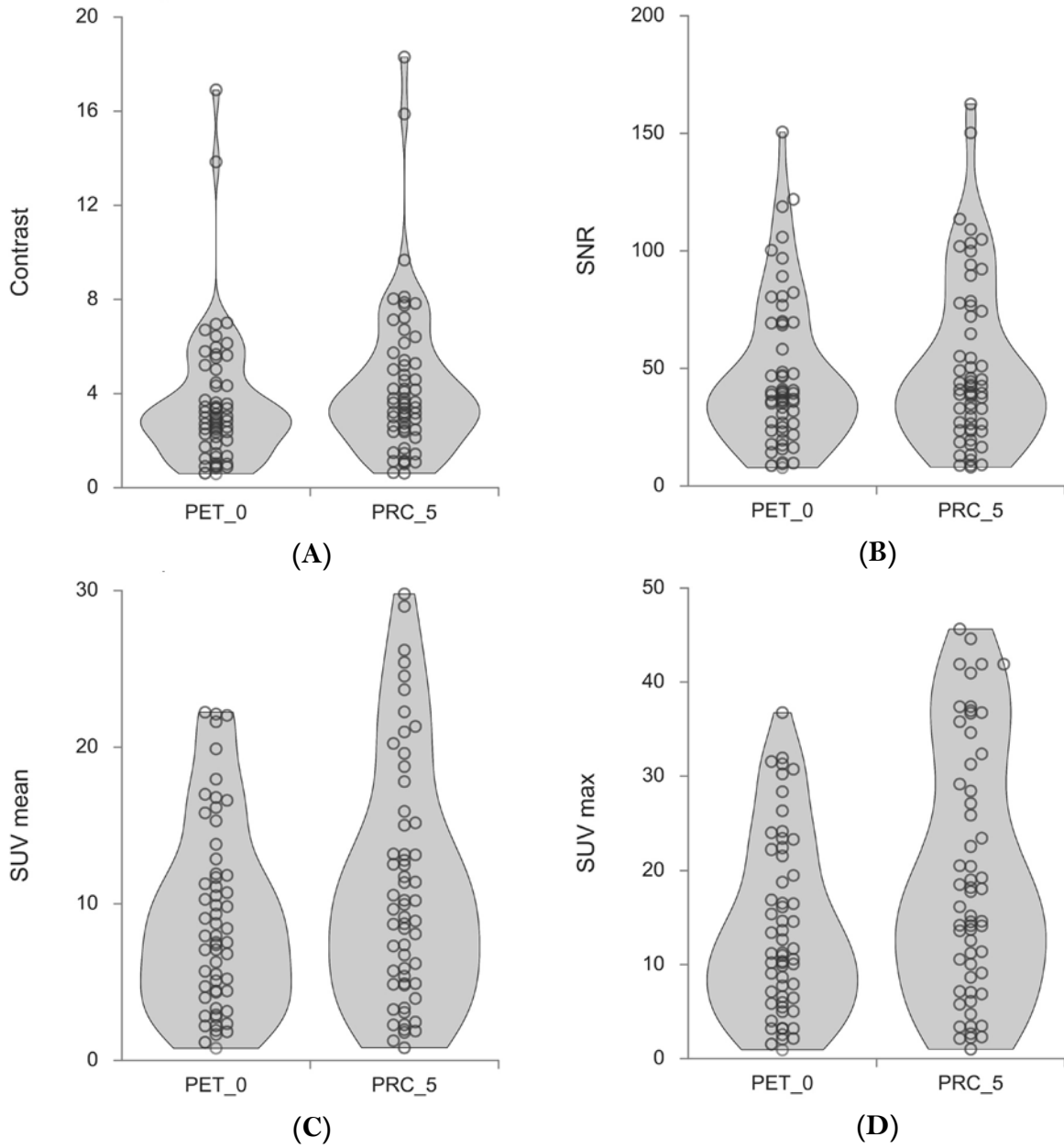
Figure 5.13: Data distributions for (A) contrast, (B) SNR, (C) mean standardised uptake value and (D) maximum standardised uptake value for lesions.

Table 5.3: Lesions contrast, SNR and uptakes before and after PRC.

Image Quality Metric	N	Image	Mean	Median (IQR)	Min	Max	Std. Dev	P value
Contrast	59	PET_0	3.6	3.0 (1.9-4.5)	0.6	16.9	2.8	0.000
		PRC_5	4.4	3.6 (2.4-5.4)	0.6	18.3	3.2	
SNR	59	PET_0	47.0	38.8 (25.0-69.3)	7.8	150.6	31.4	0.001
		PRC_5	50.7	41.0 (24.2-74.3)	8.0	162.5	35.3	
SUV_{mean}	59	PET_0	9.0	8.0 (4.4-11.9)	0.8	22.2	6.0	0.000
		PRC_5	11.1	9.7 (4.9-15.2)	0.8	29.8	7.6	
SUV_{max}	59	PET_0	13.7	11.2 (6.0-21.6)	0.9	36.8	9.3	0.000
		PRC_5	19.4	16.2 (8.7-31.3)	1.0	45.6	13.2	

5.3.6 Reader study assessment

5.3.6.1 Overall image quality

Readers were asked to assess the overall relative image quality of PET_0 and PRC images based on 4 categories provided in a questionnaire (Appendix K). Overall, for PET_0 images, excellent was the most frequently selected category and for PRC_5 images, it was satisfactory (figure 5.14). Hence, results suggest that PET_0 has better image quality than PRC_5 images. Examples of images are shown in figures 5.15 to 5.17. Figures 5.15 and 5.16 demonstrate the

relative excellent and satisfactory image quality of PRC_5 images compared to PET_0, respectively. Also, figure 5.17 shows the satisfactory image quality observed by reader 1 but non-diagnostic by reader 2.
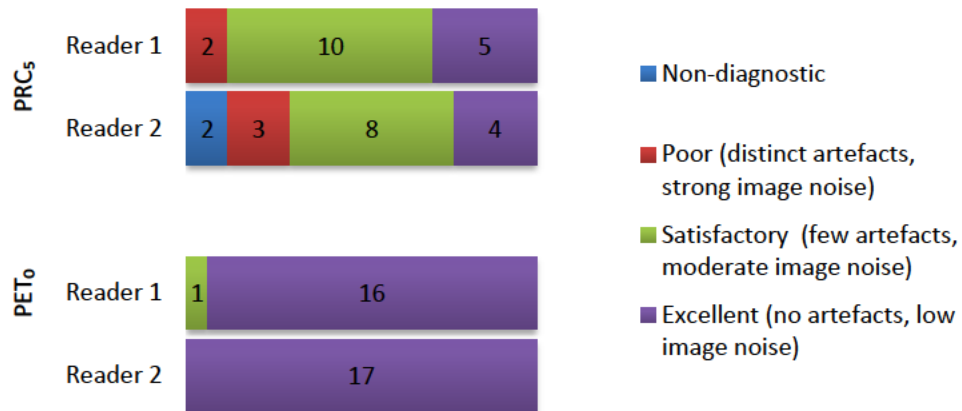
Figure 5.14: Number of cases for each image quality category for PET_0 and PRC images regarding readers 1 and 2, respectively.
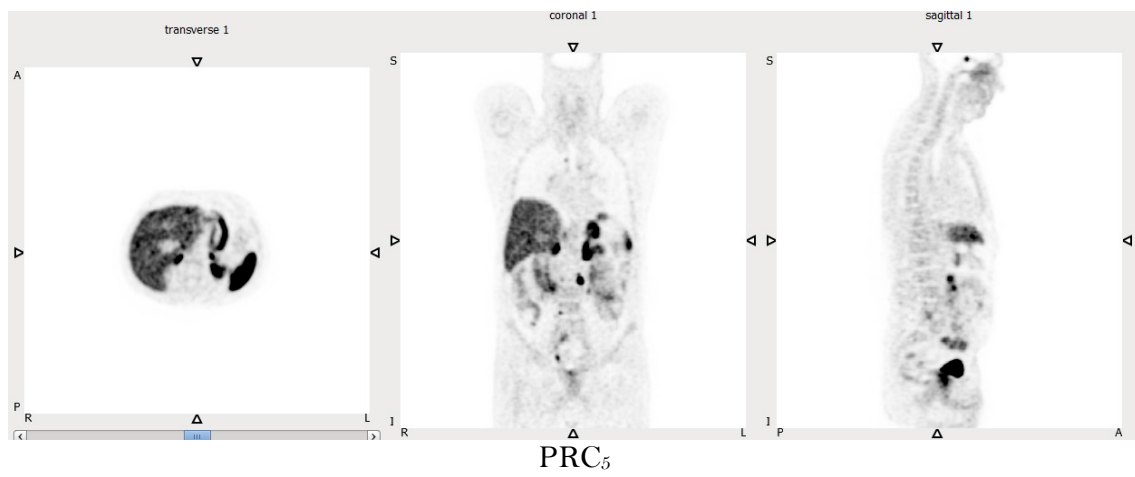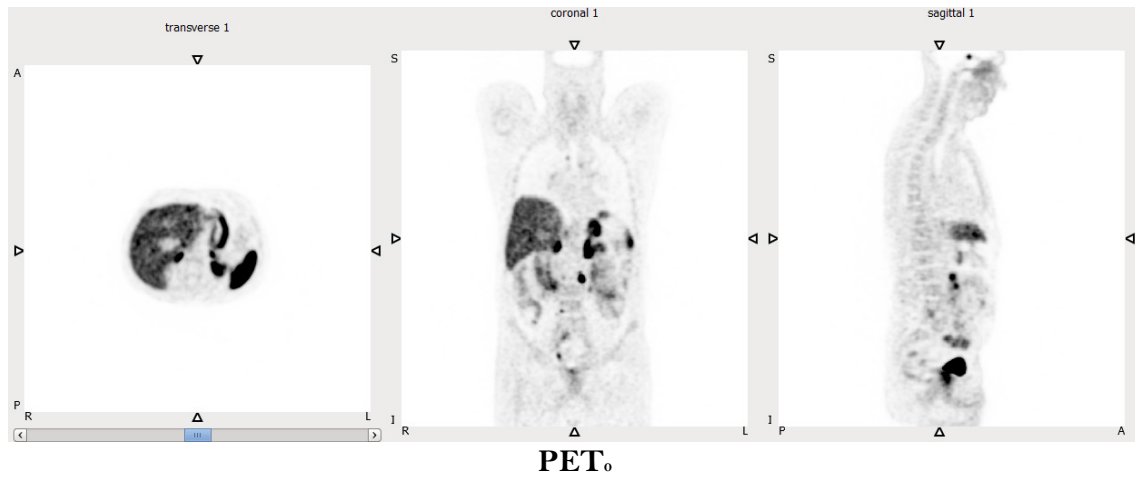
PET$_0$

PRC$_5$

Figure 5.15: Patient 07: Both readers observed that PET$_0$ and PRC$_5$ images have relatively excellent image quality.
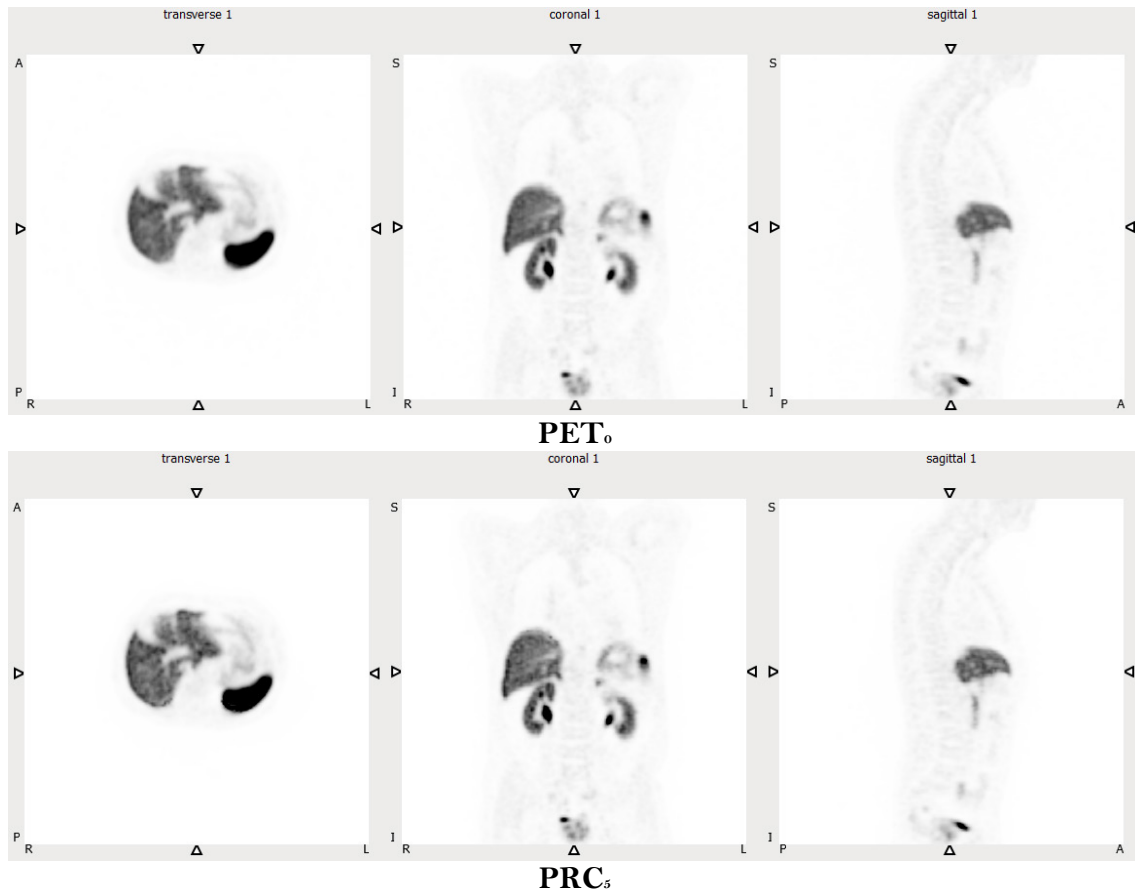
PET₀

PRC₅

Figure 5.16: Patient 09: Both readers observed that the PET_0 image has relatively excellent image quality than the PRC_5 image, which has relatively satisfactory image quality.
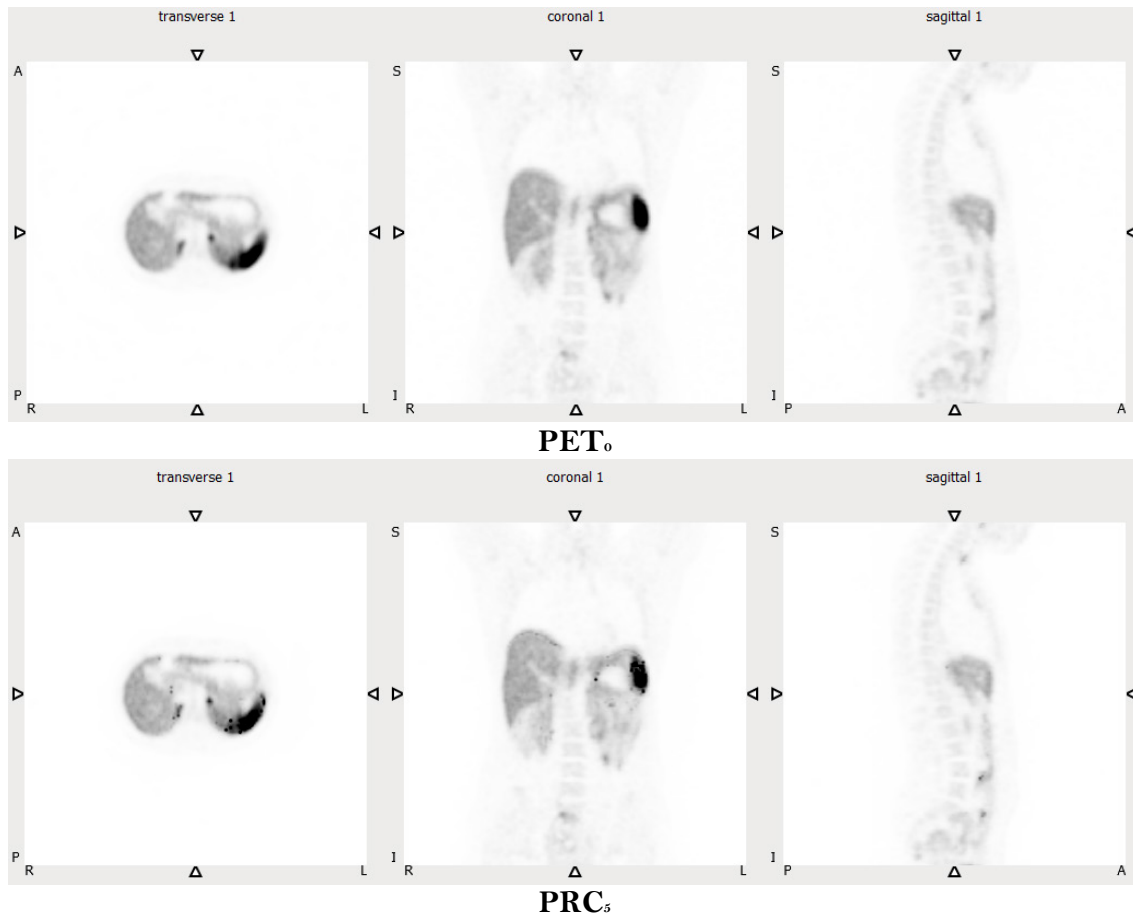
PET$_0$

PRC$_5$

Figure 5.17: Patient 19: Both readers observed that the PET$_0$ image has relatively excellent image quality than the PRC$_5$ images. However, one reader evaluated the PRC$_5$ images as relatively poor and the other reader scored as satisfactorily.

The generated attenuation map vary between patient according to the HU for each tissue for each patient. Figures 5.18 and 5.19 show generated attenuation maps after CT number modification according to Appendix J, resulting in an artefact-free PRC$_5$ for patient 12 and PRC$_5$ with artefact for patient 20 (figure 5.21), respectively. Both attenuation maps have a similar range of windowing, 0 to 39 but resulting a different grey level at the same particular region, for example the liver. It was noted that the tissue boundaries in the attenuation map image for patient 12 are less rigid and continuity observed compared to the attenuation map image for patient 20. It was evident that patient 20 has more variation in the HU map, leading to the artefacts observed

in the PRC image. The high intensity at the tissue boundaries in the attenuation map for patient 20 was seen as similar as rigid/discrete tissue classification was performed. This is due to variation of tissue composition in patient 20 that reflected as non-uniform intensity distribution. Any misregistration between PET_0 and attenuation map, particularly in the abdominal area, was difficult to detect for both patients. This is because organs in the abdominal area were clustered into two classes only: soft-tissue and connective tissue, according to their CT numbers.
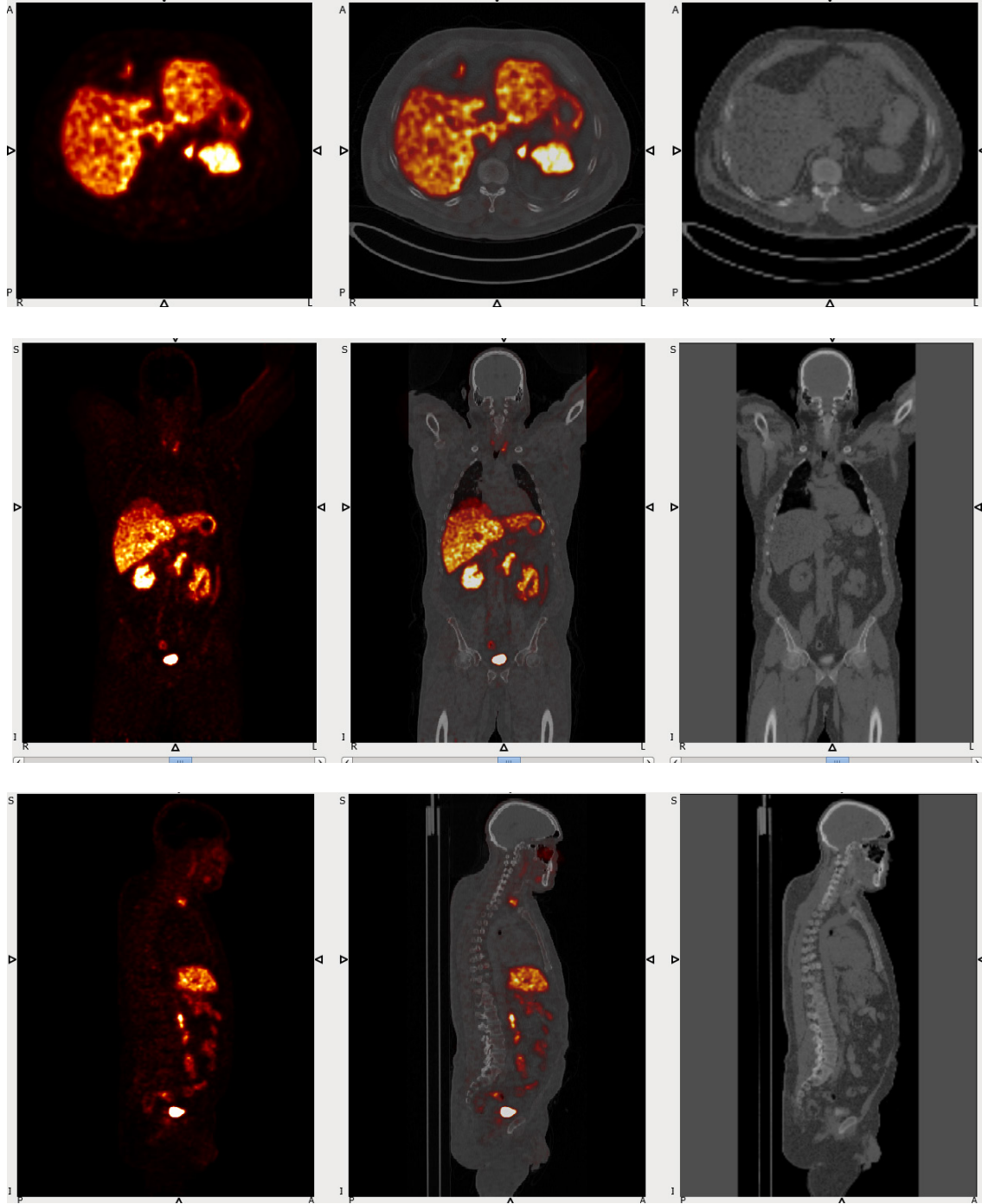
Figure 5. 18: PET_0 (first column), PET_0/CT (second column) and generated attenuation map (third column) according to Appendix J. The first row is axial, the second row is coronal, and the third row is sagittal views for patient 12, where the PRC_5 was free from artefacts.
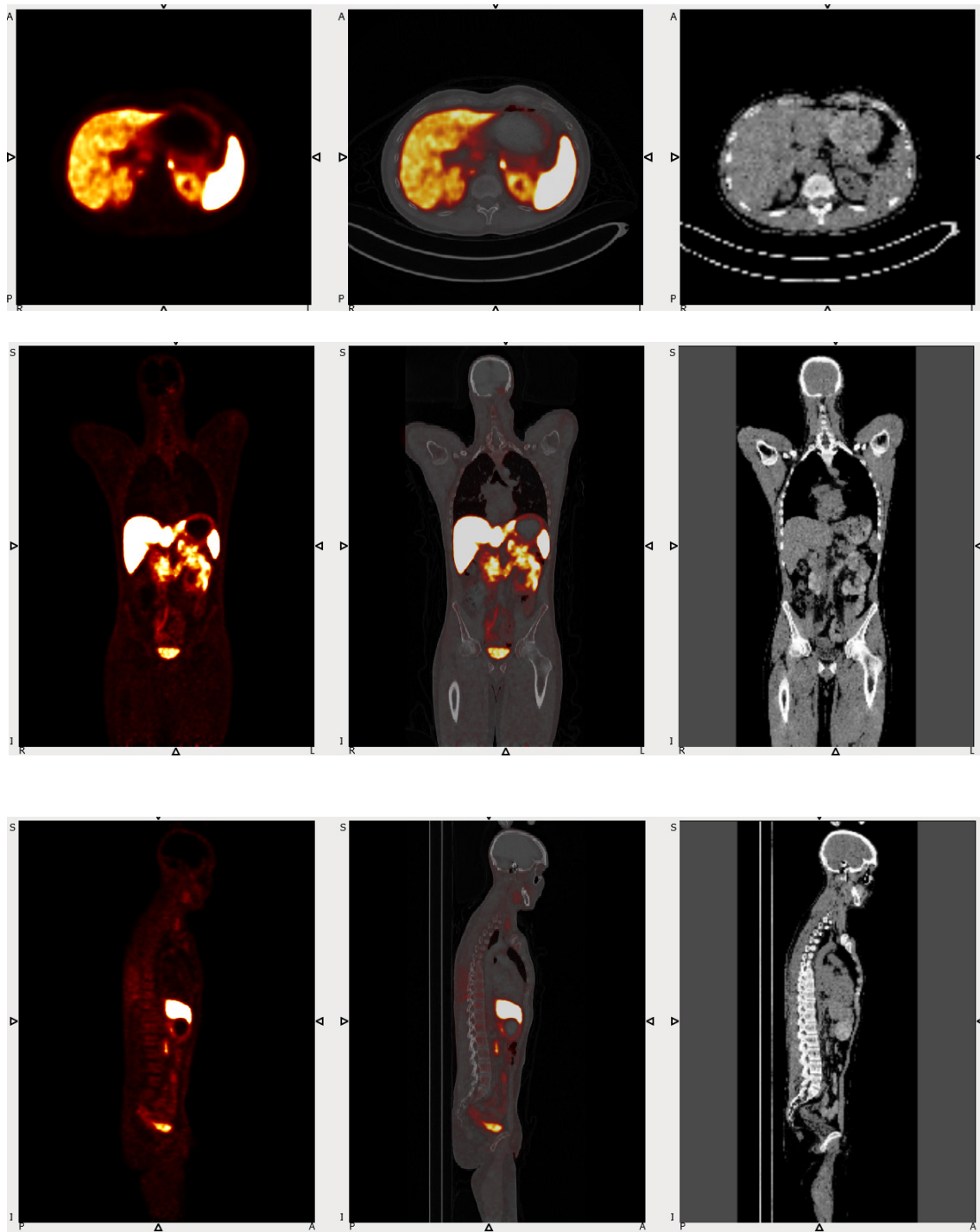
Figure 5. 19: PET$_0$ (first column), PET$_0$/CT (second column) and generated attenuation map (third column) according to Appendix J. The first row is axial, the second row is coronal, and the third row is sagittal views for patient 20, where PRC$_5$ was suffered from artefacts.

Percentage agreement was calculated according to e.q 5.8 and shown in table 5.4. Also, table 5.4 provides frequencies of cases that have agreement or disagreement of scoring. Agreement meaning both readers provide similar image quality assessment and disagreement occurred when readers rated different image quality on the same selected image. Readers reached 94% agreement, which was 16/17 cases of PET_0 images have excellent image quality and disagreed in 1 case. There was also reader agreement of 59% that 4 cases of PRC images have excellent image quality and 6 cases were satisfactory.

Table 5. 4: Frequency of image quality agreement between two readers.

Images	Agreement				Disagree-ment	Total Image	Percent-age agreement (%)
	Non-diagnostic	Poor	Satisfac-tory	Excellent			
PET_0	0	0	0	16	1	17	94.1
PRC_5	0	0	6	4	7	17	58.8

5.3.6.2 Artefact presentation

Here, readers evaluated whether there were obvious artefacts within particular regions in the body for PET_0 and PRC_5 images. Body regions included liver, pancreas, peritoneum, bowel, bones, nodes, lung and others. Readers found that all PET_0 and 8/17 PRC_5 images did not have obvious artefacts. Speckle artefacts were observed as pronounced in PRC_5 images, particularly in the liver, bowel and other regions including stomach, spleen, kidneys and adrenals, followed by pancreas, peritoneum and one case in the lung, which is between the lung diaphragm and the upper right lobe of the liver. However, no artefacts were seen in bones and nodes. The data for artefact presentation assessment is shown in figure 5.20.

Figure 5.21 shows an image from patient 20, which demonstrates evident artefacts after

PRC. The PRC_5 image was evaluated as poor image quality by both readers.
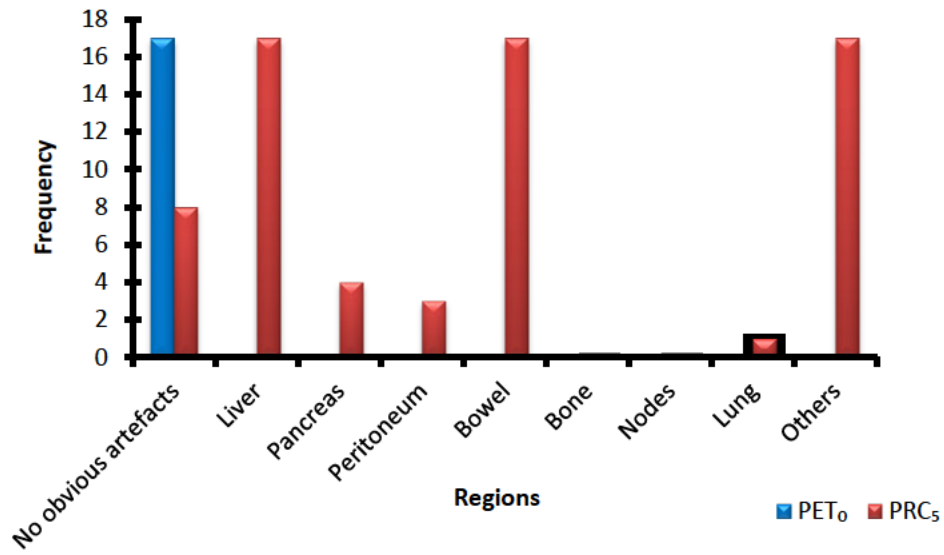
Figure 5.20: Frequency of artefacts presentation in each region for PET_0 and PRC_5 images, where 'others' included stomach, spleen, kidneys and adrenals.

PET$_0$
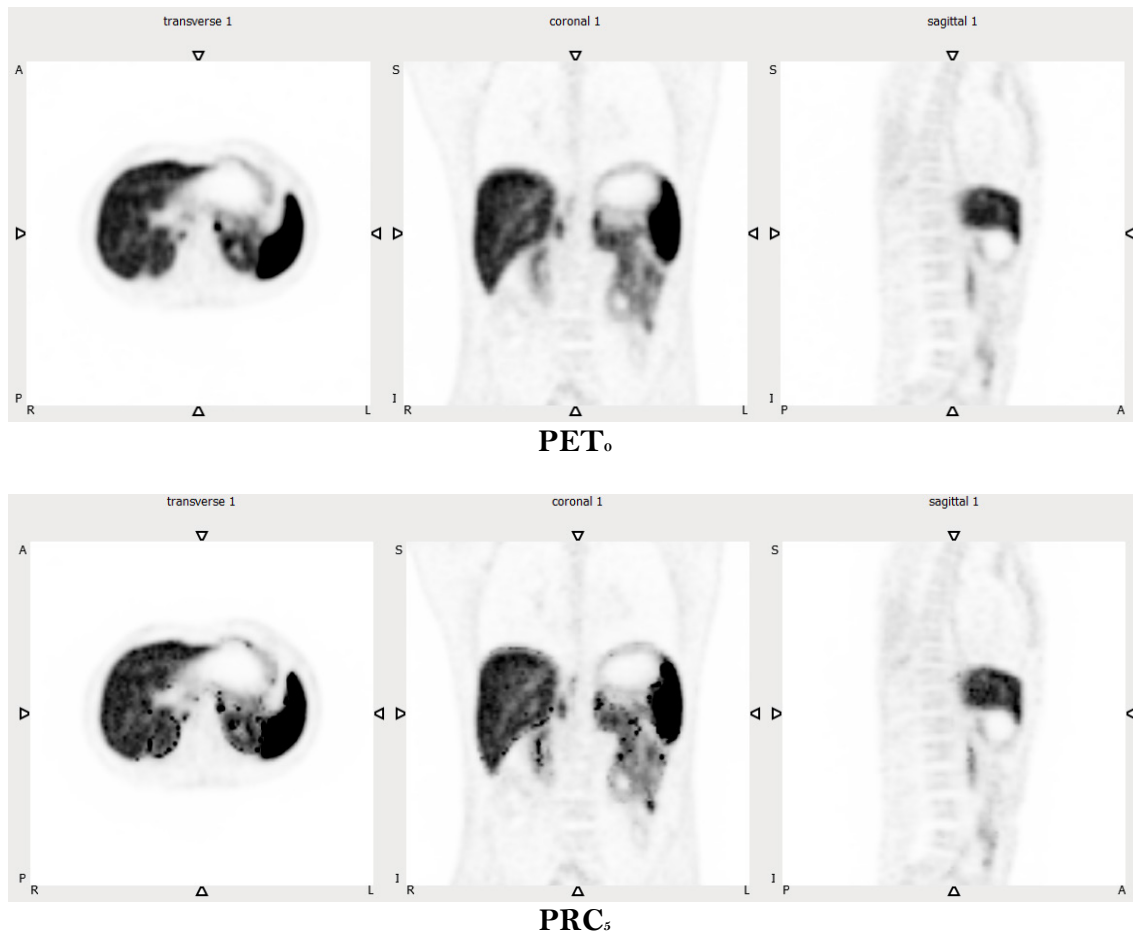
PRC$_5$

Figure 5.21: Patient 20: Image comparison of artefacts presents in liver, kidneys and spleen in PRC$_5$ image.

5.3.6.3 Reader preference based on lesion appearance

For this task, readers were asked to indicate their preferred image based on lesion appearance within different body regions. The frequency of their preferences is shown in figure 5.22 and the reason for preference in table 5.5. In most cases, readers had no preference for lesions found in the pancreas, peritoneum, bone, lymph nodes, lung and others that include stomach, spleen, kidneys, and adrenal regions due to similar lesions appearance between PET$_0$ and PRC$_5$ images. The preference for PET$_0$ images only occurred because they were free from artefacts when compared to PRC$_5$ images. Moreover, preference for PRC$_5$ images in liver, pancreas, bone

and lymph nodes were due to improvements in image quality, as measured by increased contrast and sharpness. Examples of image quality improvement are shown in figures 5.23 and 5.24.
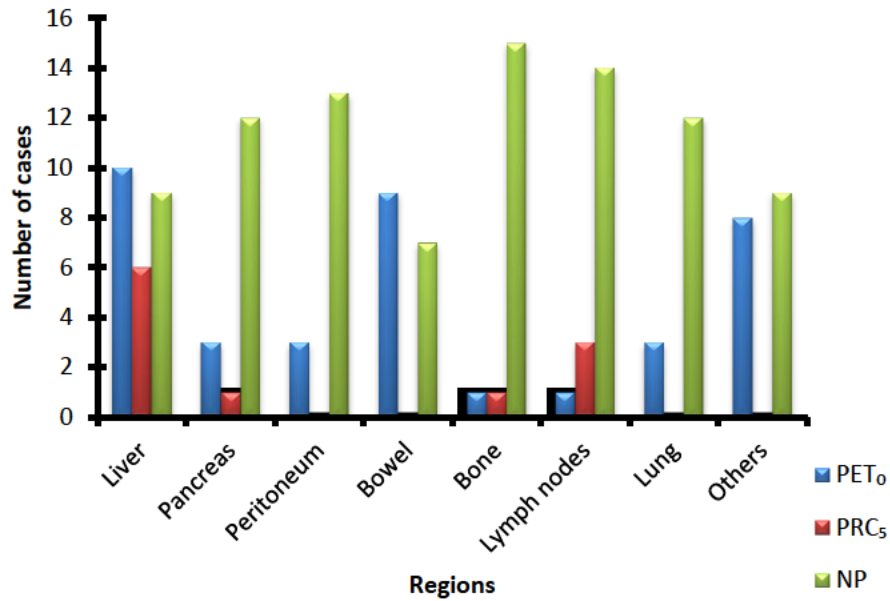
Figure 5.22: Number of cases for any lesion presentation preferred in each region.

Table 5. 5: Frequency of reasons for reader preference

More lesions	Increased contrast in PRC$_5$ images	Increased sharpness in PRC$_5$ images	Artefact free in PET$_0$ images
0	11	4	32

PET₀   **PRC₅**
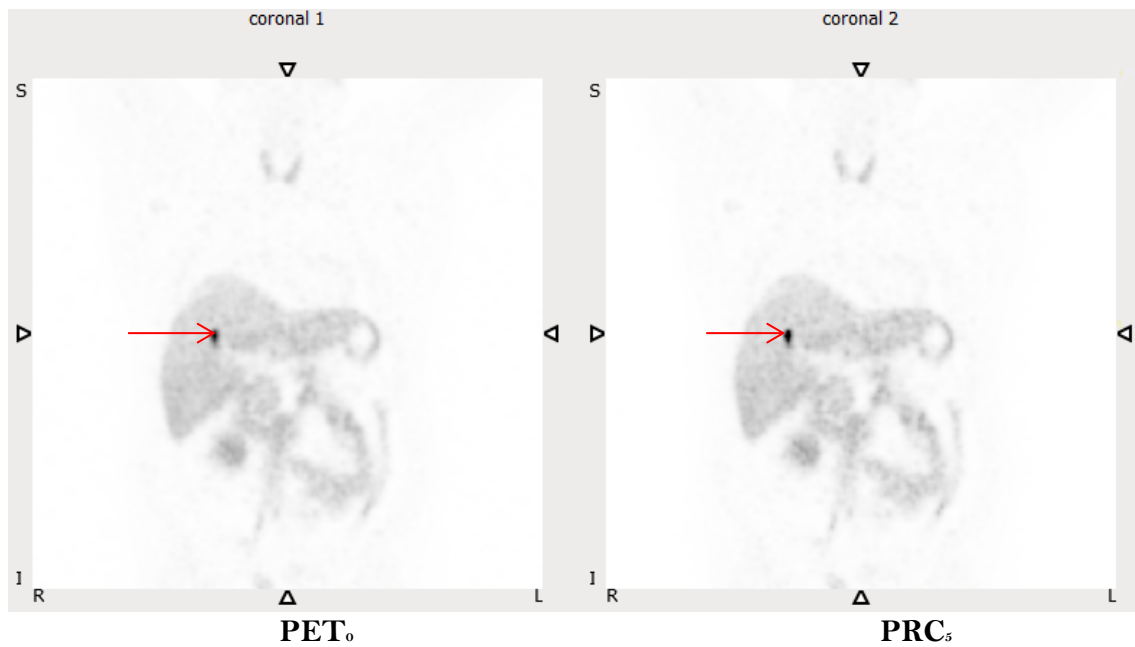
Figure 5.23: Patient 12: Red arrows indicate the lesion in the liver, where the contrast improves after PRC.

PET₀   **PRC₅**
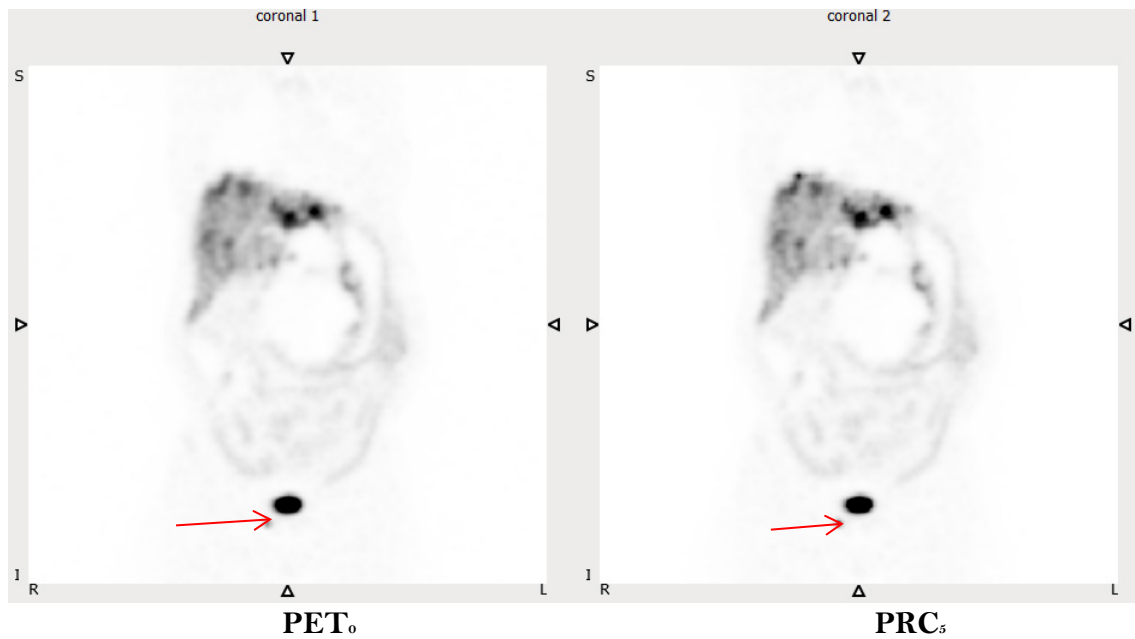
Figure 5.24: Patient 15: Red arrows indicate the lesion in the pubis bone where the sharpness improves after PRC.

The percentage preference agreement among the two readers based on lesions appearance in given regions was calculated according to e.q 5.8. Table 5.6 shows the frequency of cases that have agreement or disagreement of scoring among two readers. For example, given one particular region in one image, the agreement means both readers agree that no lesions (NL) appear in that region or if lesions are observed, they provided similar image preference either PET_0, PRC_5 or no preference (NP). On the other hand, disagreement meaning there were different decisions of lesions existence or different preferences either PET_0, PRC_5, or NP image occurred among two readers.

It was found that the highest agreement of 29.4 % was achieved for lesions presentation in the peritoneum. Readers have the same observations in 5/17 images where both found no lesions observed in 3 cases and no preference image for 2 cases.

The second highest agreement reached 23.5% for lesions appearance in bone, lungs and other categories, respectively. For lesions presentation in bone, both readers observed no lesions for 3 cases and chose no preference image in one case. Meanwhile, readers found that lesions did not exist for 3 cases and preferred PET0 in 1 case for lesions in the lungs. Also, for lesions in others, readers agreed that no lesions appeared in 2 cases, preferred one PET_0 image and one no preference image.

Readers have a similar agreement of 17.6% for lesions appearance in liver, pancreas and lymph nodes categories, respectively. Given lesions appearance in the liver, readers preferred one PET_0, one PRC_5 and one no preference image. The PRC_5 image was preferred because the contrast and sharpness were improved. Meanwhile, readers agreed that no lesions were found in 2 images and no preference image in 1 case for lesions in the pancreas and lymph nodes, respectively.

Finally, the lowest agreement was achieved for lesions presentation in the bowel. The percentage agreement was 11.8%, where both readers agreed that lesions were not present in the bowel.

Table 5.6: Frequency of agreement regarding image preference by lesions in body regions and percentage agreement. NL was chosen if readers found no lesions in that region.

Regions		Agreement			Disagreement	Total Image	Percent-age agreement (%)
	NL	Image preference					
		PET_0	PRC_5	NP			
Liver	0	1	1	1	14	17	17.6
Pancreas	2	0	0	1	14	17	17.6
Peritoneum	3	0	0	2	12	17	29.4
Bowel	2	0	0	0	15	17	11.8
Bone	3	0	0	1	13	17	23.5
Lymph nodes	2	0	0	1	14	17	17.6
Lungs	3	1	0	0	13	17	23.5
Others	2	1	0	1	13	17	23.5

NP = No preference   NL= No lesions

5.3.6.4 Overall image preference

Figure 5.25 gathers information on the overall PET image preference for readers 1 and 2, respectively. It is shown that readers preferred PET_0 over PRC images. Table 5.7 is the data tabulation to explain whether their preference was similar or different for the same selected image. It is observed that readers have a similar preference on 12/17 images, including 11 of PET_0 and one of PRC images. This results in percentage agreement of preference by approximately 71%. Cohen's kappa analysis produces κ =0.309 (95% CI, -0.032 to 0.650), which

showed fair agreement among the two readers and above the agreement expected by chance. However, the value of kappa is not significantly different (p<0.05) from zero with p=0.088.

In this study, the prevalence index is 0.59; the bias index is equal to zero and readers have assessed the image independently without any discussion with each other. It was found that the prevalence index is high and reduced the kappa value (Julius and Chris, 2005) in which there were image preference categories that were likely to be chosen due to chance. Hence in this study, readers obviously preferred PET_0 due to artefacts free than PRC images.

In conclusion, the fair agreement of preference was found but likely due to chance. However, because readers are well trained, the percentage agreement of preference which is 71%, can be safely relied upon to determine interrater reliability (McHugh, 2012).
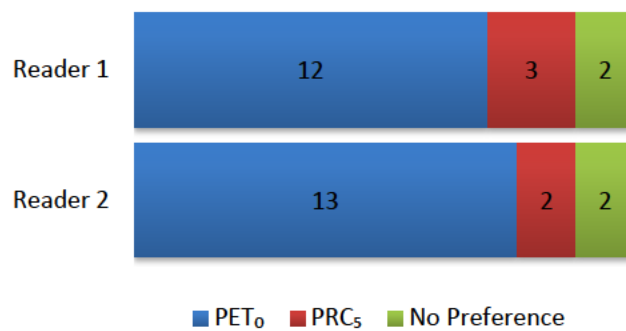
Figure 5.25: Total number of overall image preferences for readers 1 and 2.

Table 5.7: Cross-tabulation of image preference between readers 1 and 2. Superscript letters are used to indicate the cell notation used for the 3x3 contingency table. The main diagonal cells (a, e and i) represent agreement and the off-diagonal cells (c and g) represent disagreement.

Reader		Reader 2			Total
	Image	PET_0	PRC_5	NP	
	PET_0	11^a	0^b	1^c	12
Reader 1	PRC_5	1^d	1^e	1^f	3
	NP	1^g	1^h	0^i	2
Total		13	2	2	17

5.4 Discussion

The implementation of PRC developed in chapter 4 was applied to patient ^{68}Ga-DOTATE PET/CT images to investigate and explore its performance within different noise levels, biological tissue compositions and densities, and difficult and non-uniform tissue boundaries.

The PRC proposed an iterative post-reconstruction deblurring method where the correction factors were determined from the discrepancies between PET_0 from the scanner and simulated annihilation image, PET_k. PET_0 was an estimate of emission source image input in GATE to simulate the annihilation image, PET_k. Again, as discussed in chapter 4, it was vital to produce an accurate and precise simulated annihilation image that can deal with the physical complexities of densities and tissue boundaries. Accordingly, this only can be achieved with a rigorous calibration method utilised in this study (Schneider et al., 2000) to obtain an accurate attenuation map. As opposed to previous studies that segmented the CT image into only 4 different tissues, which were air, lung, water-like tissue and bone to generate an attenuation map (Cal-Gonzalez et al., 2018b), our study utilised the calibration of CT numbers correlated with 71

types of tissue with different elemental composition. This method can resolve the small difference of media densities with an accuracy better than 0.04 g/cm³. For example, the lung can be classed into 9 with range densities of 0.10 g/cm³ to 8.8 g/cm³ to indicate normal to abnormal, accordingly (Emond et al., 2019); 5 classes of adipose tissue within the range of 0.93 g/cm³ to 1.03 g/cm³ and 13 classes of skeletal tissue such as sternum (1.25 g/cm³), femur (1.33 g/cm³) and clavicle (1.46 g/cm³). Hence, confirmed positron range distributions in different materials with almost similar densities, that the positron travels through until it annihilates; and at non-uniform tissue-boundaries within simulated annihilation images.

In general, the post-reconstructed PRC developed managed to retain the normal distribution and uptake of ^{68}Ga in the body where the most intense uptake is found in the spleen, followed by kidneys and pituitary with moderate and homogenous uptake in the liver and the lowest uptake in lungs and muscle (Moradi et al., 2016, Hofman et al., 2015, Watts et al., 2014, Kunikowska et al., 2012, Kuyumcu et al., 2013), although artefacts were induced, commonly in the abdominal region. The result verified that the algorithm would not change normal physiological distribution and uptake in the organ of interest but did induce artefacts.

The problem of noise enhancement during PRC (Cal-Gonzalez et al., 2018b, Bertolli et al., 2016, Harzmann et al., 2014, Bing et al., 2005) was still not sufficiently addressed by the implementation of a relaxation, parameter W, in PRC algorithm used in this study as explained in chapter 4. It was demonstrated by a quantitative and qualitative study where the noise increment in PRC_k was ~2%. However, readers still categorised the PRC_k images as satisfactory, with few artefacts and moderate image noise.

PRC using space-invariant deblurring kernels in heterogenous media results in artefacts at the boundaries of the media (Bai et al., 2003). For example, when performing the Richardson-

Lucy deconvolution with 5 iterations, which is a similar number of iterations used in this study, the lung kernel overcorrected the soft tissue compared to PRC_5 (Appendix M). Also, it produced Gibbs artefacts in the lung/liver boundary. Besides, the bone and water kernels did not impact the image because the positron ranges are smaller than the PET scanner spatial resolution.

However, this problem was addressed by implementing a spatially variant deblurring kernel in resolution modelling (Cal-Gonzalez et al., 2015b) and works well for lesions between heart and lung (Cal-Gonzalez et al., 2018b). The post-reconstruction PRC proposed in this study should also work well if there is lesion uptake between different tissue densities and boundaries, without a need to compute any blurring kernels or recompute the system matrix with resolution modelling as exhibited in figures 5.9 and 5.10. The figures indicate that the original uptake image was correctly co-registered with its respective tissues; and that the PRC proposed in this study did not over-correct voxels in soft tissues close to lung or air in the trachea. This was evident in PRC_5 image in this study, where no artefact or false uptake appears, even though at a more complicated location where a lesion was observed in soft tissue, located between lung and trachea as shown in figure 5.10.

Quantitatively, in this study, lesion contrast and SNR were significantly improved after PRC (Cal-Gonzalez et al., 2018b, Rahmim et al., 2009, Bing et al., 2005) and significant changes in uptake occurred (Berger et al., 2019). However, the quantitative result did not influence the readers sufficiently to cause them to prefer PRC images over PET_0 images. The preference was because the appearance of artefacts, found mostly in the liver, bowel, stomach, spleen, kidneys, and adrenals, give suspicious or doubt to the readers whether the lesions were real or false, leading to incorrect diagnosis. Some PRC images in this study visually improve lesion contrast and sharpness such as in liver, bones, and lymph nodes (Alessio and MacDonald, 2008). Nevertheless, again, the appearance of artefacts influenced the readers' preference.

Artefacts were observed in PRC images but not in CT images verifying that they were induced due to inaccurate attenuation maps during the PRC deblurring process. There was a variation in the attenuation map generated according to each patient's CT number in each tissue. It was evident that patient with more variation in the attenuation map leads to assemble artefacts. It was obvious in the abdominal region and can result in a false positive. For example, a bowel region is a common place of the lymph nodes. Hence, artefacts appear as increased uptake leading to an incorrect diagnosis. The artefacts were also due to discrepancies between bowel position in CT and PET_0. The discrepancies exist because of physiological motion such as peristalsis and respiratory. Other considered artefacts were also found between the upper liver and lung diaphragm created deviation of location in CT and PET_0 images as indicated in figure 5.5. In the CT image, the lungs have a low attenuation value. , However, in PET_0, the lungs move in and out at their base due to respiratory. As the CT was a snapshot of the respiratory cycle and physiological motion whereas PET_0 image averaged all the motions within 15-18 minutes scan, this also allows movement of gas through the gastrointestinal and bladder filling; and possible patient movement on the scanning bed that contributed to the PET_0 and CT images misalignment. Therefore, the CT derived attenuation map produced was inaccurate and greatly affected the simulated positron-range image as it depends on the attenuation map to calculate the density of the tissue for simulating the range.

A possible solution to eliminate speckle-like artefacts in abdominal regions in the PET images might be to use a post-reconstruction speckle reducing anisotropic diffusion (SRAD) (Alrefaya, 2018). SRAD considered computing the edge stopping function based on the PET/CT image registration as a guideline of smoothing and sharpening filters applied to the image. The author demonstrated that SRAD was able to reduce speckle and enhances edges in simulated PET images and so may be helpful to reduce such artefacts during PRC.

Another potential approach to correct for misalignment between PET and CT images to produce an accurate attenuation map were first, acquiring PET images in gated mode and extract patient-specific motion from gated PET using a deformable registration model (Dawood et al., 2008, Bai and Brady, 2009, Lu et al., 2018); or ungated mode and utilised wavelet-denoising modified Richardson-Lucy (WRL) deconvolution to reduce the motion blur (Xu et al., 2011).

To this author's knowledge, there has been only a single prior study involving qualitative image assessment after PRC by two readers using patient data of ^{68}Ga PET imaging (Berger et al., 2019). In that study, results showed that their PRC method moderately improved contrast, spatial resolution, increased noise and changed of uptake. However, a direct comparison of PRC performance on contrast, spatial resolution and noise cannot be made between the current investigation and that previous study. This is due to different image quality metrics, scoring and analysis, and differences in how the readers perceive the image.

5.5 Conclusion

Post-reconstruction PRC was implemented on patient images and demonstrated significant but small increases in image noise. It also improved lesion contrast, SNR and increased uptake. However, the PRC images were not preferred by readers when artefacts were present. In artefact free images, PRC images are preferred due to improvement in image contrast and SNR. Further research is warranted to improve the method, particularly regarding removing or reducing the artefacts that impacted reader preference.

Chapter 6

Summary, future directions and conclusions

6.1 Summary

Positron range is an important factor in PET image degradation due to increased image blurring. The blurring due to positron range effects is associated with events recorded by the detectors, which do not directly reflect the positron emission location but the annihilation events that occur after the radioactive decay. Therefore, the effects limit PET spatial resolution and lead to reduced image quality and quantification accuracy (Sanchez-Crespo et al., 2004, Cal-Gonzalez et al., 2015b, Disselhorst et al., 2010, Alva-Sánchez et al., 2016, Kemerink et al., 2011, Emond et al., 2019).

This thesis aimed to improve PET image quality and quantification by investigating the methods used to correct for the effects of positron range, specifically for high energy positron emitters such as ^{68}Ga. The investigation included the factors affecting the magnitude of the positron range and developed a personalised approach to positron range correction (PRC) based on the image space reconstruction algorithm. The proposed approach was implemented using simulations, phantom and patient data, and the impact of the correction on image quality performance was examined.

While the impact of PRC on image quality and quantification in pre-clinical PET data were expected and acknowledged in many studies (Bertolli et al., 2016, Fraile et al., 2016, Cal-Gonzalez et al., 2018b, Harzmann et al., 2014, Agbeko et al., 2010), only a small number of studies have investigated its role in clinical PET (Kraus et al., 2012, Rahmim et al., 2009). Until now,

PRC in clinical PET has not been routinely applied. This is because high energy betas that produce a greater blurring effect, on the scale of clinical studies, have not been commonly used in PET imaging. So the limit of spatial resolution achievable by the PET detectors makes the positron range blurring effect relatively negligible. However, this is no longer the case due to the increasing use of more energetic positron emitters in clinical studies, such as ^{68}Ga (Velikyan, 2015) and improvements in PET scanner performance (Jones and Townsend, 2017).

The focus of this work was to examine the positron range effect in clinical PET and develop a suitable method that could be implemented with reconstructed PET images for a variety of high energy positron emitters, regardless of PET scanner geometry or acquisition parameters. Furthermore, the PRC developed also employed noise regularization in image space to control noise amplification during deblurring.

A discussion and summary of the major findings arising from each of the experimental chapters are provided.

Chapter 3: Effect of ^{68}Ga on PET image performance

The simulation study aimed to investigate the impact of ^{68}Ga positron range blurring across image sampling, feature contrast and count losses by utilising Monte Carlo (MC) simulation. Monte Carlo simulation is used extensively in nuclear medicine for development, validation and evaluation of scanner devices, image reconstruction algorithms and data correction techniques where the physical experiment or study is either not possible or not practical. For example, it is challenging to conduct a physical experiment to measure the positron range in isolation, as the range is typically at the sub-mm scale. Moreover, physical experiments

will involve the scanner and acquisition parameters, including the corresponding effects such as limited spatial resolution, detector efficiency, attenuation, and noise. When these effects are included, the investigation of blurring caused by positron range alone is often not possible. Utilising MC simulation, it was possible to model the blurring due solely to positron range in different media such as bone and lung without including any scanner and acquisition effects, thus providing a ground truth measurement for quantitative accuracy assessment.

The GATE toolkit is an advanced open-source MC simulation software used for numerical simulations in medical imaging, such as PET and SPECT (Jan et al., 2004), radiotherapy and dosimetry (Sarrut et al., 2014). GATE is based on extensive libraries of well-validated physics models that provide particle tracking and interaction records that can be used to simulate nuclear imaging with sophisticated detector geometries in different scenarios (Agostinelli et al., 2003). As well as EGS4, GATE could be used to determine annihilation locations and allows processes to be tracked. Also, unnecessary tracking can be terminated to reduce the computational burden.

To achieve the first objective of the thesis, investigation of positron range effects from ^{68}Ga in water, bone and lung, the simulation study was carried out using GATE. Although GATE provides positron energy spectrum models for different radioactive source properties, ^{68}Ga is not yet available. Therefore, an accurate energy spectrum for positron emission from ^{68}Ga was required to be defined in the database, whether using a discrete, histogram or linear interpolated spectrum (http://www.opengatecollaboration.org/). In this study, the histogram mode was utilised based on an analytical model to calculate the positron emission energy probability density (Levin and Hoffman, 1999). As expected, the results confirmed that the positron range was greatest in the lung, followed by water and bone.

Positron range is independent of the scanner system and acquisition parameters (Kemerink et al., 2011, Blanco, 2006). Given this fact, it was of interest to investigate the exclusive impact of positron range on PET image performance as the second objective of the thesis. Therefore, the positron range distributions for ^{18}F and ^{68}Ga in bone, water and lung were characterized, again using Monte-Carlo simulation software GATE (Agostinelli et al., 2003) and the impact of positron range blurring on imaging performance over different levels of image sampling was investigated. The method used was fundamentally different from alternative approaches proposed in the literature (Palmer et al., 2005). Hence, blurring effects other than those induced by positron range, such as non-collinearity, the intrinsic resolution of the detectors, and detector positioning accuracy, the image reconstruction process and filtering effects, were excluded from this study. Thus, the degree of blurring was only due to the mean positron range.

In this study, blurring caused by the positron range was estimated to be tenfold in the lung compared to bones and four times compared to water, regardless of radioisotope used. The ^{18}F results demonstrated that the positron range imposed a negligible blurring impact in all media. However, when using radioisotopes that emit higher energy positrons, such as ^{68}Ga, the impact of the positron range was substantial, especially in the lung, regardless of the image sampling used in this study. Overall, positron range correction was not required for ^{18}F clinical PET when using a 4 mm image sampling, which is a typical voxel size of reconstructed clinical PET images, but would be appropriate for images with finer sampling. However, positron range correction for ^{68}Ga should be considered in bone and water where the effect is on the same scale as standard voxel sizes and is required in lungs irrespective of the image sampling used.

The findings in this study confirmed that PRC is necessary for lung medium regardless of the type of radioactive source used. Furthermore, it was also shown that high spatial resolution PET scanners would be sensitive to positron range blurring. Hence, PRC is vital in preclinical

PET and PET brain imaging when the spatial resolution of the PET scanner is on the order of approximately 1.5 mm (Goertzen et al., 2012, Frost, 2020).

Chapter 4: Development of post-reconstructed positron range correction method: A phantom study.

In the second study, a new method of PRC was proposed, explored and validated in a phantom study to achieve the third objective of this thesis. Rather than using PRC implemented during image reconstruction, either in projection space (Derenzo, 1979, Haber et al., 1990, Agbeko et al., 2010, Bai et al., 2003, Rahmim et al., 2009, Kotasidis et al., 2014, Bertolli et al., 2016, Cal-Gonzalez et al., 2015a, Fraile et al., 2016, Harzmann et al., 2014) or image space (Cal-Gonzalez et al., 2018a), a post-reconstruction iterative PRC method was developed based on the image space reconstruction algorithm (ISRA) (Daube-Witherspoon and Muehllehner, 1986). The method exploited the ability of GATE to simulate an annihilation image given an estimate of the positron emission image and a map of the annihilation media from the segmented CT image. The first part of this work simulated an annihilation image, using the PET measured image (PET_0) as an initial estimate of the positron emission location. Then, based on a robust CT segmentation for the attenuation map (Schneider et al., 2000), GATE converts the emission estimate to an expected distribution of the annihilation locations, corresponding to the locations where the positrons come to a halt. Subsequently, positron range correction factors were determined and applied to PET_0, resulting in a deblurred image (PRC_1) used as an estimate of the positron range free image for the next iteration. This post-reconstruction PRC approach yielded an improvement in contrast and spatial resolution in clinical PET phantom images. The advantages of this approach were that it was easy to adapt to different types of high energy positron emitters and it did not require the raw data and/or manipulation of the reconstruction algorithm.

Moreover, the method also managed to control noise enhancement during the deblurring process. However, the disadvantage of this method was it required a GATE positron-range simulation at each iteration which computationally burdensome.

A crucial part of this method was to make sure the simulated annihilation image was accurate. Theoretically, following positron decay, the positron travels a finite distance until it loses its kinetic energy before it annihilates with an electron in the medium of interaction. Subsequently, two 511 keV photons are produced and travel in opposite directions to each other. Therefore, to produce an accurate simulated annihilation image, photons produced during annihilations must be filtered out.

Chapter 5: Personalised post-reconstruction positron range correction: Patient study.

The third and final objective of the thesis was extended to an investigation of post-reconstruction PRC applied to a study of 17 patients. The study was conducted in order to test whether the proposed approach to PRC works well with real data, which includes various tissue densities, irregular boundaries, physiological uptake and patient motion such as respiration, cardiac motion, movement of the stomach and bowel due to peristalsis and changes in the size of the bladder. The reader study also qualitatively compared the image quality performance before and after PRC.

Preliminary results demonstrated that false uptake, or artefacts, occurred within areas filled with air, such as in the trachea and abdomen. To eliminate this effect, a modification of the air CT number was made, increasing it to be equivalent to that of the lung. From the reader study, although PRC images had satisfactory image quality with few artefacts and moderate

image noise, the noise was significantly higher than PET_0 images. However, the PRC images retained the physiological uptake and distribution after deburring.

It was found that the proposed post-reconstruction PRC method produced significantly improved lesion contrast, SNR, quantification of radionuclide uptake and definition of image boundaries. Interestingly, no artificial uptake or artefact was observed if lesions were located between tissue boundaries, such as between lung/soft tissue and soft tissue/trachea. Furthermore, results from the reader study confirmed that lesion contrast and sharpness were improved in the liver, lymph nodes, pancreas and bone images without inducing artefacts. However, the spatial resolution improvement demonstrated in the phantom study was not translated into patient study outcomes.

Artefacts induced were evident in the liver and the abdominal area, including bowel, stomach, spleen, adrenals and kidneys, and were present as a speckle-like artefact. These artefacts could be confused with nodule uptake in lymph nodes in the abdominal region or possibly confused with a tumour.

6.2 Limitations and future directions

Findings arising from this research lead to new questions that need to be investigated. Recommendations for future work based on findings from chapters 3, 4 and 5 are presented here.

Effect of positronium formation on positron range

Positron range measurement conducted in this study neglected the influence of positronium formation. In contrast, a study investigating the properties of positron annihilation through positronium formation showed that it increases in the positron range of approximately

38% for ^{18}F and 60% for [68]Ga (Champion and Le Loirec, 2007). Moreover, without considering positronium formation, the positron range was underestimated by more than a factor of two (Robson et al., 2015). The effects arising from positronium formation would be a general limitation for Monte-Carlo code used in PET imaging, for instance, GATE (Jan et al., 2004), EGS4 (Kawrakow, 2000) and PeneloPET (España et al., 2009). Currently available tools do not take into account positronium formation and only apply cross-sections for free positron annihilation. However, studying the positronium formation cross sections for different tissues is feasible, similar to those performed previously (Makochekanwa et al., 2009). These cross-sections obtained could then eventually be included in Monte Carlo simulation models to allow for more accurate simulation.

Computational considerations

Theoretically, there is a potential to use GATE to simulate the entire measurement process then iteratively compare with the measured PET data to update an initial GATE image space estimate. However currently, it is computationally impractical in a clinical setting where the high-performance computer is not provided.

GATE is a particle-tracking based simulation and was computationally intensive (Gillam and Rafecas, 2016) and slow to produce statistically useful results (Kawrakow et al., 2008a). In this study, GATE was performed on a high-performance computer at the University of Sydney. The simulation based on real patient data, with image matrix of 200×200, (4.07×4.07 ×3) mm³ voxel size and 368 slices, was not able to complete within 36 hours using 300 Gb RAM and a single core.

One of the strategies to reduce the computing time is an acceleration approach based on parallel simulations (Gillam and Rafecas, 2016). The simulation algorithm was adapted to a

distributed architecture where the simulation was split into several independent 'sub-simulations', which were merged together at the end. For each iteration for one patient study, using 8 cores with 20 Gb RAM each and the simulation split into 8, all sub-simulations were completed within 30 minutes to 2 hours, depending on the complexity of radioisotope distribution in the body.

During simulation, by default, GATE produces two images simultaneously, the positron-emission image and the positron-annihilation image based on a given PET emission estimate. As the simulation was split into 8, there were 16 images produced which contains 8 images for positron-emission and positron-annihilation images, respectively. The image size was 59 Mb each resulting in a total 944 Mb image size. However, the main interest in this study was the positron-annihilation image, which indicated the location of positron annihilations. Therefore, it could be beneficial if the GATE simulation package can simulate only positron-annihilation images in the future to speed up the time of computing.

Another potential strategy to accelerate the simulation is combining GATE with EGSnrc, where the time simulation of particle transport in the phantom was reduced by a factor of 4 (Kawrakow et al., 2008b). Another approach would be to adapt the simulation code to a graphics processing unit (GPU) with significant simulation acceleration (Herraiz et al., 2011). It would be worth devoting effort to adapting the post-reconstruction PRC simulation code to GPU since performing clinically realistic simulations in GPU have been shown to speed up the computing time by a factor of 400-800 (Bert et al., 2013).

Although programming the PRC algorithm to take full advantage of GPU features is not a trivial task, GATE v7.2 already incorporates the possibility of using GPUs for PET applications. Technically, conducting GATE simulation in GPU was 12 times faster than in CPU

(Elmoujarkach, 2018). However, the GPU support was discontinued in the newer release of GATE8.0 (Boersma, 2017).

Application of personalised post-reconstruction PRC

The PRC method in this study improved contrast and sharpness during deblurring for ^{68}Ga PET images. As such, it would be important to investigate the performance of the PRC algorithm using higher energy positron radioisotopes such as [82]Rb used for cardiac imaging. Rb-82 has a short half-life of 1.3 minutes and maximum positron energy of 3.4 MeV, which leads to longer positron ranges and contributes to poor image resolution properties (Conti and Eriksson, 2016, Rahmim et al., 2008). In addition, since the cardiac region is located between the lungs, it would be interesting to investigate the effectiveness of the PRC in improving contrast between the myocardium and other organs or between myocardial defects and the left ventricle.

Another potential application is in lung imaging which uses ^{68}Ga to characterise lung cancer or [15]O to evaluate perfusion. The proposed PRC method developed artefacts in the lung/diaphragm. However, no artefacts were observed in the rest of the lung area, which exhibits the greatest positron range blurring effects compared to other tissues. The study conducted could not provide conclusive results regarding lesion appearance in the lung due to limited cases available in the patient study. In this study, positron range contributed substantial blurring in the lung and demonstrated quantification bias (Emond et al., 2019). Therefore, it would be of interest to examine the performance of image quality and quantification and patient management of lung cancer staging after PRC implementation with large samples of cases involving lung area.

The post-reconstruction PRC algorithm developed in this study could also be implemented for prostate imaging, which uses ^{68}Ga-labelled prostate-specific membrane antigen (^{68}Ga-PSMA). As ^{68}Ga-PSMA is effective in diagnosing and staging patients with newly

diagnosed prostate cancer (Basha et al., 2019), it is important to investigate whether the implementation of PRC may improve initial cancer staging.

Finally, the post-reconstruction PRC algorithm could also be used to deblur positron-range effects in whole-body or brain PET/MR. The magnetic field is known to shape the positron-range blurring kernel resulting in reduced mean positron range in the transaxial plane or perpendicular to the magnetic field when strong (>3T) magnetic fields are employed (Kraus et al., 2012, Bertolli et al., 2016, Soultanidis et al., 2011). However, most PET/MR systems have a field strength of 3T or less and the mean positron range still contributes significantly to the blurring effect (Bertolli et al., 2016). Hence, post-reconstruction PRC could be implemented to remove positron-range blurring as it only requires the reconstructed PET image and an attenuation map. Furthermore, the MR-based attenuation map could be used as an attenuation lookup table for input to GATE for positron-range image simulation.

Artefacts

Speckle-like and pixelated artefacts were observed in the liver and abdominal areas such as in the bowel, stomach, spleen, adrenals and kidneys. The artefacts were induced due to a mismatch between PET and CT images used as input to GATE and more variation in the CT-number, resulting in the inaccurate CT-derived attenuation map. Respiratory motion was the largest contributor to PET image and CT derived attenuation misalignment, particularly in liver/lung diaphragm and the bowel, leading to visible artefacts. Besides respiratory motion, gas movement and peristalsis of the bowel also contributed to the mismatch. Moreover, the CT image is only a snapshot at a single-respiratory phase, but the PET image includes a multi-respiratory phase over time. Hence, the registration of PET and CT images was not fully aligned due to differences in time frame and phase.

Many studies have reported methods for correcting respiratory motion in PET/CT to avoid the artefacts and this topic was thoroughly reviewed in (Pepin et al., 2014). Another potential strategy is acquiring the attenuation map derived from transmission scan using radioactive sources, as explained in chapter 2, section 2.1.5.4. This results in an attenuation map within the same time frame as the PET image, resulting in a more accurate simulated annihilation image. Also, to avoid misalignment of PET image and attenuation map, MR-based attenuation map is possible to be implemented as it is based on MRI data acquired simultaneously as the PET image (Lillington et al., 2020, Wang et al., 2020). Therefore, the PET image and attenuation map are matched and avoid the occurrence of artefacts. There is a potential that the method to correct for the misalignment can be included in this post-reconstruction PRC framework.

Deep learning for post-reconstruction PRC

Deep learning is a subset of machine learning based on artificial neural networks that contain multiple layers in the network architecture to extract features from the raw input. Due to recent advancements in computing power, including graphics processing units, and the availability of large volumes of labelled data for training, deep learning methods have attracted much attention to solving a variety of problems in the medical imaging field, including computer-aided diagnosis, disease prediction and image segmentation (Kim et al., 2019). Deep learning has also been recently applied to positron range correction in simulated preclinical studies (Joaquín et al., 2021). The study utilised convolutional neural networks to learn from the example training dataset that requires PET and CT images. This study may provide insights on how the post-reconstruction PRC method could also be developed further based on a deep-learning architecture. There is a potential that the post-reconstruction PRC method can be improved in

speed as the simulation in GATE is not necessary, providing sufficient data for training. Additionally, deep learning may have the ability to estimate CT-derived attenuation maps from PET images (Joaquín et al., 2021). Hence, using only PET images as input may be enough to develop deep learning for PRC.

6.3 Conclusion

This thesis investigated the impact of positron range on PET images in different tissues, explored the development of a personalised post-reconstruction PRC method, and investigated the benefits and limitations of the approach using simulated phantom and patient data. The study demonstrated that PRC is necessary for high energy beta emitters such as ^{68}Ga compared to ^{18}F, especially in the lung region due to its lower density. An iterative, post-reconstruction, positron range correction method was developed, which relied only on the PET measured data and associated CT information, and operated in image space. A correction factor was determined by the ratio of PET measured data and GATE-simulated annihilation data. Moreover, a regularization in image space was implemented to control noise amplification during deblurring. As a result, PRC in this study improved contrast and sharpness at different noise levels in a patient study. Although the proposed PRC method induced artefacts in the liver and abdominal areas in patient images, there are potential benefits in other applications such as in cardiac, lung and prostate imaging. Furthermore, the post-reconstruction PRC method developed in this study can be implemented on any PET scanner, independent of scanner geometry or acquisition parameters, regardless of the type of radionuclide used for imaging.

References

1989. *Tissue substitutes in radiation dosimetry and measurement*, Bethesda, Md., U.S.A, International Commission on Radiation Units and Measurements.

2018. *Performance Measurements of Positron Emission Tomographs*, Rosslyn, Va, National Electrical Manufacturers Association.

Abdul-Fatah, S. B., Zamburlini, M., Halders, S. G. E. A., Brans, B., Teule, G. J. J. & Kemerink, G. J. 2009. Identification of a Shine-Through Artifact in the Trachea with [124]I PET/CT. *Journal of Nuclear Medicine*, 50(6)**,** 909-911.

Adams, M. C., Turkington, T. G., Wilson, J. M. & Wong, T. Z. 2010. A systematic review of the factors affecting accuracy of SUV measurements. *AJR. American journal of roentgenology*, 195(2)**,** 310-320.

Afshar-Oromieh, A., Malcher, A., Eder, M., Eisenhut, M., Linhart, H. G., Hadaschik, B. A., Holland-Letz, T., Giesel, F. L., Kratochwil, C., Haufe, S., Haberkorn, U. & Zechmann, C. M. 2013. PET imaging with a [^{68}Ga]gallium-labelled PSMA ligand for the diagnosis of prostate cancer: biodistribution in humans and first evaluation of tumour lesions. *European Journal of Nuclear Medicine and Molecular Imaging*, 40(4)**,** 486-495.

Agbeko, N. N., Cheng, J. C., Laforest, R. & O'sullivan, J. A. Positron range correction in PET using an alternating EM algorithm. IEEE Nuclear Science Symposium Conference Record, 2010. 2875-2878.

Agostinelli, S., Allison, J., Amako, K., Apostolakis, J., Araujo, H., Arce, P., Asai, M., Axen, D., Banerjee, S., Barrand, G., Behner, F., Bellagamba, L., Boudreau, J., Broglia, L., Brunengo, A., Burkhardt, H., Chauvie, S., Chuma, J., Chytracek, R., Cooperman, G., Cosmo, G., Degtyarenko, P., Dell'acqua, A., Depaola, G., Dietrich, D., Enami, R., Feliciello, A., Ferguson, C., Fesefeldt, H., Folger, G., Foppiano, F., Forti, A., Garelli, S., Giani, S., Giannitrapani, R., Gibin, D., Gómez Cadenas, J. J., González, I., Gracia Abril, G., Greeniaus, G., Greiner, W., Grichine, V., Grossheim, A., Guatelli, S., Gumplinger, P., Hamatsu, R., Hashimoto, K., Hasui, H., Heikkinen, A., Howard, A., Ivanchenko, V., Johnson, A., Jones, F. W., Kallenbach, J., Kanaya, N., Kawabata, M., Kawabata, Y., Kawaguti, M., Kelner, S., Kent, P., Kimura, A., Kodama, T., Kokoulin, R., Kossov, M., Kurashige, H., Lamanna, E., Lampén, T., Lara, V., Lefebure, V., Lei, F., Liendl, M., Lockman, W., Longo, F., Magni, S., Maire, M., Medernach, E., Minamimoto, K., Mora

De Freitas, P., Morita, Y., Murakami, K., Nagamatu, M., Nartallo, R., Nieminen, P., Nishimura, T., Ohtsubo, K., Okamura, M., O'neale, S., Oohata, Y., Paech, K., Perl, J., Pfeiffer, A., Pia, M. G., Ranjard, F., Rybin, A., Sadilov, S., Di Salvo, E., Santin, G., Sasaki, T., Savvas, N., Sawada, Y., et al. 2003. Geant4—a simulation toolkit. *Nuclear Instruments and Methods in Physics Research Section A: Accelerators, Spectrometers, Detectors and Associated Equipment,* 506(3)*,* 250-303.

Alejandro, L.-M., Pablo, G., José Manuel, U., Jacobo, C.-G., Juan José, V., Manuel, D. & Joaquín, L. H. 2020. Real-Time 3D PET Image with Pseudoinverse Reconstruction. *Applied sciences,* 10(2829)*,* 2829.

Alessio, A. & Macdonald, L. Spatially variant positron range modeling derived from CT for PET image reconstruction. IEEE Nuclear Science Symposium Conference Record, 19-25 Oct. 2008. 3637-3640.

Alessio, A. M., Rahmim, A. & Orton, C. G. 2013. Resolution modeling enhances PET imaging. *Medical Physics,* 40(12)*,* 120601.

Almeida, G. L., Silvani, M. I., Souza, E. S. & Lopes, R. T. A stopping criterion to halt iterations at the Richardson-Lucy deconvolution of radiographic images. Journal of Physics: Conference Series, 2015. 012003.

Alrefaya, M. Adaptive speckle reducing anisotropic diffusion filter for positron emission tomography images based on anatomical prior. 4th International Conference on Computer and Technology Applications (ICCTA), 3-5 May 2018. 194-201.

Alva-Sánchez, H., Quintana-Bautista, C., Martínez-Dávalos, A., Ávila-Rodríguez, M. A. & Rodríguez-Villafuerte, M. 2016. Positron range in tissue-equivalent materials: experimental microPET studies. *Physics in Medicine and Biology,* 61(17)*,* 6307.

Ambrosini, V., Tomassetti, P., Castellucci, P., Campana, D., Montini, G., Rubello, D., Nanni, C., Rizzello, A., Franchi, R. & Fanti, S. 2008. Comparison between ^{68}Ga-DOTA-NOC and ^{18}F-DOPA PET for the detection of gastro-entero-pancreatic and lung neuro-endocrine tumours. *European Journal of Nuclear Medicine and Molecular Imaging,* 35(8)*,* 1431-1438.

Archer, G. E. B. & Titterington, D. M. 1995. The Iterative Image Space Reconstruction Algorithm (ISRA) as An Alternative To The EM Algorithm For Solving Positive Linear Inverse Problems. *Statistica Sinica,* 5(1)*,* 77-96.

Attarwala, A. A., Molina-Duran, F., Büsing, K.-A., Schönberg, S. O., Bailey, D. L., Willowson, K. & Glatting, G. 2014. Quantitative and Qualitative Assessment of Yttrium-90 PET/CT Imaging. *PLOS ONE*, 9(11), e110401.

Badawi, R. D. & Marsden, P. K. 1999. Developments in component-based normalization for 3D PET. *Physics in medicine & biology*, 44(2), 571-594.

Badawi, R. D., Shi, H., Hu, P., Chen, S., Xu, T., Price, P. M., Ding, Y., Spencer, B. A., Nardo, L., Liu, W., Bao, J., Jones, T., Li, H. & Cherry, S. R. 2019. First Human Imaging Studies with the EXPLORER Total-Body PET Scanner. *J Nucl Med*, 60(3), 299-303.

Bai, B., Bading, J. & Conti, P. S. 2013. Tumor quantification in clinical positron emission tomography. *Theranostics*, 3(10), 787-801.

Bai, B., Ruangma, A., Laforest, R., Tai, Y. C. & Leahy, R. M. Positron range modeling for statistical PET image reconstruction. IEEE Nuclear Science Symposium Conference Record, 2003. 2501-2505.

Bai, W. & Brady, M. 2009. Regularized B-spline deformable registration for respiratory motion correction in PET images. *Physics in Medicine and Biology*, 54(9), 2719-2736.

Bailey, D. L., Karp, J. S. & Surti, S. 2005a. Physics and Instrumentation in PET. *In:* BAILEY, D. L., TOWNSEND, D. W., VALK, P. E. & MAISEY, M. N. (eds.) *Positron Emission Tomography: Basic Sciences.* London: Springer London.

Bailey, D. L. & Meikle, S. R. 1994. A convolution-subtraction scatter correction method for 3D PET. *Physics in Medicine & Biology*, 39(3), 411.

Bailey, D. L., Townsend, D. W., Valk, P. E. & Maisey, M. N. 2005b. *Positron Emission Tomography: Basic Sciences*, London, Springer London, Limited.

Banerjee, S. R., Pullambhatla, M., Byun, Y., Nimmagadda, S., Green, G., Fox, J. J., Horti, A., Mease, R. C. & Pomper, M. G. 2010. ^{68}Ga-Labeled Inhibitors of Prostate-Specific Membrane antigen (PSMA) for Imaging Prostate Cancer. *Journal of Medicinal Chemistry*, 53(14), 5333-5341.

Barrio, M., Czernin, J., Fanti, S., Ambrosini, V., Binse, I., Du, L., Eiber, M., Herrmann, K. & Fendler, W. P. 2017. The Impact of Somatostatin Receptor–Directed PET/CT on the Management of Patients with Neuroendocrine Tumor: A Systematic Review and Meta-Analysis. *Journal of Nuclear Medicine*, 58(5), 756.

Baum, R. P. & Kulkarni, H. R. 2012. THERANOSTICS: From Molecular Imaging Using Ga-68 Labeled Tracers and PET/CT to Personalized Radionuclide Therapy - The Bad Berka Experience. *Theranostics*, 2(5), 437-447.

Beichel, R. R., Ulrich, E. J., Smith, B. J., Bauer, C., Brown, B., Casavant, T., Sunderland, J. J., Graham, M. M. & Buatti, J. M. 2019. FDG PET based prediction of response in head and neck cancer treatment: Assessment of new quantitative imaging features.(Research Article). *PLoS ONE*, 14(4), e0215465.

Ben Bouallègue, F., Vauchot, F. & Mariano-Goulart, D. 2019. Comparative assessment of linear least-squares, nonlinear least-squares, and Patlak graphical method for regional and local quantitative tracer kinetic modeling in cerebral dynamic ^{18}F-FDG PET. *Medical Physics*, 46(3), 1260-1271.

Bendriem, B., Trebossen, R., Frouin, V. & Syrota, A. A PET scatter correction using simultaneous acquisitions with low and high lower energy thresholds. IEEE Conference Record Nuclear Science Symposium and Medical Imaging Conference, 31 Oct-6 Nov 1993. 1779-1783

Berg, E. & Cherry, S. R. 2018. Innovations in Instrumentation for Positron Emission Tomography. *Seminars in Nuclear Medicine*, 48(4), 311-331.

Berger, A., Cal-Gonzalez, J., Rasul, S., Hacker, M., Grahovac, M., Schembri, G., Latiff, R., Rausch, I., Beyer, T. & Kench, P. Clinical impact of Spatially Variant Positron Range Correction for ^{68}Ga-DOTATATE and ^{68}Ga-PSMA PET/CT. Annual Congress of the European Association of Nuclear Medicine, 1 Oct 2019 Barcelona, Spain. 61-62.

Berry, R. 2005. *The handbook of astronomical image processing*, Richmond, VA, Willmann-Bell.

Bert, J., Perez-Ponce, H., Bitar, Z., Jan, S., Boursier, Y., Vintache, D., Bonissent, A., Morel, C., Brasse, D. & Visvikis, D. 2013. Geant4-based Monte Carlo simulations on GPU for medical applications. *Physics in Medicine and Biology*, 58(16), 5593-5611.

Bertolli, O., Eleftheriou, A., Cecchetti, M., Camarlinghi, N., Belcari, N. & Tsoumpas, C. 2016. PET iterative reconstruction incorporating an efficient positron range correction method. *Physica Medica*, 32(2), 323-330.

Bing, B., Laforest, R., Smith, A. M. & Leahy, R. M. Evaluation of MAP image reconstruction with positron range modeling for 3D PET. IEEE Nuclear Science Symposium Conference Record, 23-29 Oct 2005. 2686-2689.

Blanco, A. Positron Range Effects on the Spatial Resolution of RPC-PET. IEEE Nuclear Science Symposium Conference Record, Vol 1-6, 2006. 2570-2573.

Boellaard, R., Krak, N. C., Hoekstra, O. S. & Lammertsma, A. A. 2004. Effects of Noise, Image Resolution, and ROI Definition on the Accuracy of Standard Uptake Values: A Simulation Study. *Journal of Nuclear Medicine*, 45(9), 1519-1527.

Boersma, D. 2017. Segmentation violation with GPU. *gate-users@list.opencollaboration.org*.

Brasse, D., Kinahan, P. E., Lartizien, C., Comtat, C., Casey, M. & Michel, C. 2005. Correction Methods for Random Coincidences in Fully 3D Whole-Body PET: Impact on Data and Image Quality. *Journal of Nuclear Medicine*, 46(5), 859-867.

Cal-González, J., Herraiz, J. L., España, S., Corzo, P. M. G., Vaquero, J. J., Desco, M. & Udias, J. M. 2013. Positron range estimations with PeneloPET. *Physics in Medicine and Biology*, 58(15), 5127-5152.

Cal-González, J., Herraiz, J. L., España, S., Desco, M., Vaquero, J. J. & Udías, J. M. Positron range effects in high resolution 3D pet imaging. IEEE Nuclear Science Symposium Conference Record, 2009. 2788-2791.

Cal-González, J., Herraiz, J. L., España, S., Desco, M., Vaquero, J. J. & Udías, J. M. Validation of PeneloPET positron range estimations. IEEE Nuclear Science Symposium & Medical Imaging Conference, Oct. 30 -Nov. 6 2010. 2396-2399.

Cal-González, J., Herraiz, J. L., España, S., Vicente, E., Herranz, E., Desco, M., Vaquero, J. J. & Udías, J. M. 2011. Study of CT-based positron range correction in high resolution 3D PET imaging. *Nuclear Instruments and Methods in Physics Research, Section A: Accelerators, Spectrometers, Detectors and Associated Equipment*, 648(SUPPL. 1), S172-S175.

Cal-Gonzalez, J., Herraiz, J. L., Udias, J. M., Conti, M., Kuntner, C., Blaickner, M. & Beyer, T. 2018a. Post-Reconstruction Positron Range Correction for Preclinical and Clinical PET Imaging. *Nuclear Science Symposium (NSS) and Medical Imaging Conference (MIC)*. Sydney, Australia.

Cal-Gonzalez, J., M, P., Liva, Herraiz, J. L., Vaquero, J. J., Desco, M. & Udias, J. M. 2015a. Tissue-Dependent and Spatially-Variant Positron Range Correction in 3D PET. *IEEE Transactions on Medical Imaging*, 34(11), 2394-2403.

Cal-Gonzalez, J., Moore, S. C., Park, M. A., Herraiz, J. L., Vaquero, J. J., Desco, M. & Udias, J. M. 2015b. Improved quantification for local regions of interest in preclinical PET imaging. *Physics in Medicine and Biology*, 60(18), 7127-7149.

Cal-Gonzalez, J., Vaquero, J. J., Herraiz, J. L., Pérez-Liva, M., Soto-Montenegro, M. L., Peña-Zalbidea, S., Desco, M. & Udías, J. M. 2018b. Improving PET Quantification of Small Animal [⁶⁸Ga]DOTA-Labeled PET/CT Studies by Using a CT-Based Positron Range Correction. *Molecular Imaging and Biology,* 20(4)**,** 584-593.

Campana, D. & Tomassetti, P. 2016. Incidence, Epidemiology, Aetiology and Staging, Classification, Clinical Presentation/Signs and Symptoms, Diagnosis, Staging Procedures/Investigation. *In:* AMBROSINI, V. & FANTI, S. (eds.) *PET/CT in Neuroendocrine Tumors.* Cham: Springer International Publishing.

Carson, R. E., Daube-Witherspoon, M. E. & Green, M. V. 1988. A method for postinjection PET transmission measurements with a rotating source. *Journal of Nuclear Medicine,* 29(9)**,** 1558-1567.

Carter, L., Pratt, E., Sanders, V., Massicano, A., Cutler, C., Lapi, S. & Lewis, J. 2019. The Impact of Positron Range on PET Resolution, Evaluated with Phantoms and PHITS Monte Carlo Simulations for Conventional and Non-conventional Radionuclides. *Molecular Imaging and Biology* 22(1)**,** 1-12.

Casey, M., Burbar, Z., Rothfuss, H., Panin, V. & Bharkhada, D. 2017. A next generation SiPM based PET/CT system with improved time and spatial resolution. *The Journal of Nuclear Medicine,* 58(1332.

Cattaneo, G. M., Bettinardi, V., Mapelli, P. & Picchio, M. 2016. PET guidance in prostate cancer radiotherapy: Quantitative imaging to predict response and guide treatment. *Physica Medica,* 32(3)**,** 452-458.

Champion, C. & Le Loirec, C. 2007. Positron follow-up in liquid water: II. Spatial and energetic study for the most important radioisotopes used in PET. *Physics in Medicine and Biology,* 52(22)**,** 6605-25.

Champion, C. & Loirec, C. L. 2006. Positron follow-up in liquid water: I. A new Monte Carlo track-structure code. *Physics in Medicine and Biology,* 51(7)**,** 1707.

Chang, C. A., Pattison, D. A., Tothill, R. W., Kong, G., Akhurst, T. J., Hicks, R. J. & Hofman, M. S. 2016. ⁶⁸Ga-DOTATATE and ¹⁸F-FDG PET/CT in Paraganglioma and Pheochromocytoma: utility, patterns and heterogeneity. *Cancer Imaging (BioMed),* 16(1).

Chen, S.-H., Chang, Y.-C., Hwang, T.-L., Chen, J.-S., Chou, W.-C., Hsieh, C.-H., Yeh, T.-S., Hsu, J.-T., Yeh, C.-N., Tseng, J.-H., Chen, T.-C. & Yen, T.-C. 2017. ⁶⁸Ga-DOTATOC and ¹⁸F-FDG PET/CT for identifying the primary lesions of suspected and metastatic

neuroendocrine tumors: A prospective study in Taiwan. *Journal of the Formosan Medical Association.*

Cherry, S. R., Jones, T., Karp, J. S., Qi, J., Moses, W. W. & Badawi, R. D. 2018. Total-Body PET: Maximizing Sensitivity to Create New Opportunities for Clinical Research and Patient Care. *Journal of Nuclear Medicine,* 59(1)**,** 3-12.

Cherry, S. R., Sorenson, J. A. & Phelps, M. E. 2012. Physics in Nuclear Medicine. Philadelphia: Elsevier/Saunders.

Cherry, S. R. & Sung-Cheng, H. 1995. Effects of scatter on model parameter estimates in 3D PET studies of the human brain. *IEEE Transactions on Nuclear Science,* 42(4)**,** 1174-1179.

Cho, Z. H., Chan, J. K., Ericksson, L., Singh, M., Graham, S., Macdonald, N. S. & Yano, Y. 1975. Positron ranges obtained from biomedically important positron-emitting radionuclides. *Journal Of Nuclear Medicine: Official Publication, Society Of Nuclear Medicine,* 16(12)**,** 1174-1176.

Choi, J. Y., Jeong, J. M., Yoo, B. C., Kim, K., Kim, Y., Yang, B. Y., Lee, Y.-S., Lee, D. S., Chung, J.-K. & Lee, M. C. 2011. Development of ^{68}Ga-labeled mannosylated human serum albumin (MSA) as a lymph node imaging agent for positron emission tomography. *Nuclear Medicine and Biology,* 38(3)**,** 371-379.

Conti, M. & Eriksson, L. 2016. Physics of pure and non-pure positron emitters for PET: a review and a discussion. *EJNMMI physics,* 3(1)**,** 8-8.

Daube-Witherspoon, M. E. & Muehllehner, G. 1986. An Iterative Image Space Reconstruction Algorthm Suitable for Volume ECT. *IEEE Transactions on Medical Imaging,* 5(2)**,** 61-66.

Daube-Witherspoon, M. E. & Muehllehner, G. 1987. Treatment of axial data in three-dimensional PET. *Journal of nuclear medicine : official publication, Society of Nuclear Medicine,* 28(11)**,** 1717-1724.

Dawood, M., Buther, F., Xiaoyi, J. & Schafers, K. P. 2008. Respiratory Motion Correction in 3-D PET Data With Advanced Optical Flow Algorithms. *IEEE Transactions on Medical Imaging,* 27(8)**,** 1164-1175.

De Pierro, A. R. 1987. On the Convergence of the Iterative Image Space Reconstruction Algorithm for Volume ECT. *IEEE Transactions on Medical Imaging,* 6(2)**,** 174-175.

Defrise, M., Kinahan, P. E., Townsend, D. W., Michel, C., Sibomana, M. & Newport, D. F. 1997. Exact and approximate rebinning algorithms for 3-D PET data. *IEEE Transactions on Medical Imaging,* 16(2)**,** 145-158.

Derenzo, S. E. 1979. *Precision measurement of annihilation point spread distributions for medically important positron emitters,* ; California Univ., Berkeley (USA). Lawrence Berkeley Lab.

Derenzo, S. E. 1986. Mathematical Removal of Positron Range Blurring in High Resolution Tomography. *IEEE Transactions on Nuclear Science,* 33(1)**,** 565-569.

Dijkgraaf, I., Yim, C.-B., Franssen, G. M., Schuit, R. C., Luurtsema, G., Liu, S., Oyen, W. J. G. & Boerman, O. C. 2011. PET imaging of α(v)β(3) integrin expression in tumours with ^{68}Ga-labelled mono-, di- and tetrameric RGD peptides. *European Journal of Nuclear Medicine and Molecular Imaging,* 38(1)**,** 128-137.

Disselhorst, J. A., Brom, M., Laverman, P., Slump, C. H., Boerman, O. C., Oyen, W. J. G., Gotthardt, M. & Visser, E. P. 2010. Image-Quality Assessment for Several Positron Emitters Using the NEMA NU 4-2008 Standards in the Siemens Inveon Small-Animal PET Scanner. *Journal of Nuclear Medicine,* 51(4)**,** 610-617.

El-Maouche, D., Sadowski, S. M., Papadakis, G. Z., Guthrie, L., Cottle-Delisle, C., Merkel, R., Millo, C., Chen, C. C., Kebebew, E. & Collins, M. T. 2016. ^{68}Ga-DOTATATE for Tumor Localization in Tumor-Induced Osteomalacia. *The Journal of Clinical Endocrinology & Metabolism,* 101(10)**,** 3575-3581.

Elmoujarkach, E. 2018. GATE on GPU. *gate-users@lists.opencollaboration.org.*

Emond, E. C., Groves, A. M., Hutton, B. F. & Thielemans, K. 2019. Effect of positron range on PET quantification in diseased and normal lungs. *Physics in Medicine and Biology,* 64(20)**,** 205010-205010.

España, S., Herraiz, J. L., Vicente, E., Vaquero, J. J., Desco, M. & Udias, J. M. 2009. PeneloPET, a Monte Carlo PET simulation tool based on PENELOPE: features and validation. *Physics in Medicine and Biology,* 54(6)**,** 1723-1742.

Fahey, F. H. 2002. Data acquisition in PET imaging. *Journal of Nuclear Medicine Technology,* 30(2)**,** 39-49.

Fellner, M., Biesalski, B., Bausbacher, N., Kubícek, V., Hermann, P., Rösch, F. & Thews, O. 2012. ^{68}Ga-BPAMD: PET-imaging of bone metastases with a generator based positron emitter. *Nuclear Medicine and Biology,* 39(7)**,** 993-999.

Fernández, S., Dematteis, S., Giglio, J., Cerecetto, H. & Rey, A. 2013. Synthesis, in vitro and in vivo characterization of two novel ^{68}Ga-labelled 5-nitroimidazole derivatives as potential agents for imaging hypoxia. *Nuclear Medicine and Biology,* 40(2)**,** 273-279.

Fraile, L. M., Herraiz, J. L., Udías, J. M., Cal-González, J., Corzo, P. M. G., España, S., Herranz, E., Pérez-Liva, M., Picado, E., Vicente, E., Muñoz-Martín, A. & Vaquero, J. J. 2016. Experimental validation of gallium production and isotope-dependent positron range correction in PET. *Nuclear Instruments and Methods in Physics Research Section A: Accelerators, Spectrometers, Detectors and Associated Equipment,* 814(110-116.

Frilling, A., Sotiropoulos, G. C., Radtke, A., Malago, M., Bockisch, A., Kuehl, H., Li, J. & Broelsch, C. E. 2010. The Impact of ^{68}Ga-DOTATOC Positron Emission Tomography/Computed Tomography on the Multimodal Management of Patients With Neuroendocrine Tumors. *Annals of Surgery,* 252(5)**,** 850-856.

Frost, G. R. 2020. Hybrid PET/MRI enables high-spatial resolution, quantitative imaging of amyloid plaques in an Alzheimer's disease mouse model. *Scientific reports.,* 10(1).

Gaertner, F. C., Plum, T., Kreppel, B., Eppard, E., Meisenheimer, M., Strunk, H., Bundschuh, R. A., Sinnes, J. P., Rösch, F. & Essler, M. 2019. Clinical evaluation of [^{68}Ga]Ga-DATA-TOC in comparison to [^{68}Ga]Ga-DOTA-TOC in patients with neuroendocrine tumours. *Nuclear Medicine and Biology,* 76-77(1-9.

Gillam, J. E. & Rafecas, M. 2016. Monte-Carlo simulations and image reconstruction for novel imaging scenarios in emission tomography. *Nuclear Instruments & Methods in Physics Research Section a–Accelerators Spectrometers Detectors and Associated Equipment,* 809(76-88.

Goertzen, A. L., Bao, Q., Bergeron, M., Blankemeyer, E., Blinder, S., Cañadas, M., Chatziioannou, A. F., Dinelle, K., Elhami, E., Jans, H.-S., Lage, E., Lecomte, R., Sossi, V., Surti, S., Tai, Y.-C., Vaquero, J. J., Vicente, E., Williams, D. A. & Laforest, R. 2012. NEMA NU 4-2008 Comparison of Preclinical PET Imaging Systems. *Journal of Nuclear Medicine,* 53(8)**,** 1300-1309.

Grootoonk, S., Spinks, T. J., Jones, T., Michel, C. & Bol, A. Correction for scatter using a dual energy window technique with a tomograph operated without septa. Conference Record of the 1991 IEEE Nuclear Science Symposium and Medical Imaging Conference, 2-9 Nov. 1991 1991. 1569-1573 vol.3.

Haber, S. F., Derenzo, S. E. & Uber, D. 1990. Application of mathematical removal of positron range blurring in positron emission tomography. *IEEE Transactions on Nuclear Science,* 37(3)**,** 1293-1299.

Harzmann, S., Braun, F., Zakhnini, A., Weber, W. A., Pietrzyk, U. & Mix, M. 2014. Implementation of Cascade Gamma and Positron Range Corrections for I-124 Small Animal PET. *IEEE Transactions on Nuclear Science*, 61(1)**,** 142-153.

Haug, A. R., Cindea-Drimus, R., Auernhammer, C. J., Reincke, M., Beuschlein, F., Wängler, B., Uebleis, C., Schmidt, G. P., Spitzweg, C., Bartenstein, P. & Hacker, M. 2013. Neuroendocrine Tumor Recurrence: Diagnosis with ^{68}Ga-DOTATATE PET/CT. *Radiology*, 270(2)**,** 517-525.

Haug, A. R., Cindea-Drimus, R., Auernhammer, C. J., Reincke, M., Wängler, B., Uebleis, C., Schmidt, G. P., Göke, B., Bartenstein, P. & Hacker, M. 2012. The Role of ^{68}Ga-DOTATATE PET/CT in Suspected Neuroendocrine Tumors. *Journal of Nuclear Medicine*, 53(11)**,** 1686-1692.

Herraiz, J. L., España, S., Cal-González, J., Vaquero, J. J., Desco, M. & Udías, J. M. 2011. Fully 3D GPU PET reconstruction. *Nuclear instruments & methods in physics research. Section A, Accelerators, spectrometers, detectors and associated equipment*, 648(S169-S171.

Hofman, M. S., Lau, W. F. E. & Hicks, R. J. 2015. Somatostatin Receptor Imaging with ^{68}Ga DOTATATE PET/CT: Clinical Utility, Normal Patterns, Pearls, and Pitfalls in Interpretation. *RadioGraphics*, 35(2)**,** 500-516.

Hoyer, D., Bell, G. I., Berelowitz, M., Epelbaum, J., Feniuk, W., Humphrey, P. P. A., O'carroll, A. M., Patel, Y. C., Schonbrunn, A., Taylor, J. E. & Reisine, T. 1995. Classification and nomenclature of somatostatin receptors. *Trends in Pharmacological Sciences*, 16(3)**,** 86-88.

Hsu, D. F. C. & Levin, C. S. 2020. New-Generation Silicon Photomultiplier-Based Clinical PET/CT and PET/MR Systems. *In:* ZHANG, J. & KNOPP, M. V. (eds.) *Advances in PET: The Latest in Instrumentation, Technology, and Clinical Practice*. Cham: Springer International Publishing.

Hudson, H. & Larkin, R. 1994. Accelerated image reconstruction using ordered subsets of projection data. *IEEE Transactions on Medical Imaging*, 13(4)**,** 601-609.

Iniewski, K. 2014. CZT detector technology for medical imaging. *Journal of Instrumentation*, 9(11)**,** C11001-C11001.

Jan, S., Santin, G., Strul, D., Staelens, S., Assié, K., Autret, D., Avner, S., Barbier, R., Bardiès, M., Bloomfield, P. M., Brasse, D., Breton, V., Bruyndonckx, P., Buvat, I., Chatziioannou, A. F., Choi, Y., Chung, Y. H., Comtat, C., Donnarieix, D., Ferrer, L., Glick, S. J., Groiselle, C. J., Guez, D., Honore, P. F., Kerhoas-Cavata, S., Kirov, A. S., Kohli, V., Koole, M.,

Krieguer, M., Laan, D. J. V. D., Lamare, F., Largeron, G., Lartizien, C., Lazaro, D., Maas, M. C., Maigne, L., Mayet, F., Melot, F., Merheb, C., Pennacchio, E., Perez, J., Pietrzyk, U., Rannou, F. R., Rey, M., Schaart, D. R., Schmidtlein, C. R., Simon, L., Song, T. Y., Vieira, J. M., Visvikis, D., Walle, R. V. D., Wieërs, E. & Morel, C. 2004. GATE: a simulation toolkit for PET and SPECT. *Physics in Medicine and Biology*, 49(19)*,* 4543.

Janssen, I., Chen, C. C., Millo, C. M., Ling, A., Taieb, D., Lin, F. I., Adams, K. T., Wolf, K. I., Herscovitch, P., Fojo, A. T., Buchmann, I., Kebebew, E. & Pacak, K. 2016. PET/CT comparing ^{68}Ga-DOTATATE and other radiopharmaceuticals and in comparison with CT/MRI for the localization of sporadic metastatic pheochromocytoma and paraganglioma. *European Journal of Nuclear Medicine and Molecular Imaging*, 43(10)*,* 1784-1791.

Joaquín, L. H., Adrián, B. & Alejandro, L.-M. 2021. Deep-Learning Based Positron Range Correction of PET Images. *Applied sciences*, 11(1)*,* 266.

Jodal, L., Le Loirec, C. & Champion, C. 2012. Positron range in PET imaging: an alternative approach for assessing and correcting the blurring. *Physics in Medicine and Biology*, 57(12)*,* 3931-43.

John, M. O. 1996. Model-based scatter correction for fully 3D PET. *Physics in Medicine and Biology*, 41(1)*,* 153.

Johnbeck, C. B., Knigge, U. & Kjær, A. 2014. PET tracers for somatostatin receptor imaging of neuroendocrine tumors: current status and review of the literature. *Future oncology.*, 10(14)*,* 2259-2277.

Johnson, N. P., Sdringola, S. & Gould, K. L. 2011. Partial volume correction incorporating Rb-82 positron range for quantitative myocardial perfusion PET based on systolic-diastolic activity ratios and phantom measurements. *Journal of Nuclear Cardiology*, 18(2)*,* 247-258.

Jonasson, M., Wall, A., Chiotis, K., Saint-Aubert, L., Wilking, H., Sprycha, M., Borg, B., Thibblin, A., Eriksson, J., Sörensen, J., Antoni, G., Nordberg, A. & Lubberink, M. 2016. Tracer Kinetic Analysis of (S)-^{18}F-THK5117 as a PET Tracer for Assessing Tau Pathology. *The Journal of Nuclear Medicine*, 57(4)*,* 574.

Jones, T. & Townsend, D. 2017. History and future technical innovation in positron emission tomography. *J Med Imaging (Bellingham)*, 4(1)*,* 011013.

Julius, S. & Chris, C. W. 2005. The Kappa Statistic in Reliability Studies: Use, Interpretation, and Sample Size Requirements. *Physical Therapy*, 85(3)*,* 257-268.

Kaewput, C., Suppiah, S. & Vinjamuri, S. 2018. Correlation between standardized uptake value of ^{68}Ga-DOTA-NOC positron emission tomography/computed tomography and pathological classification of neuroendocrine tumors. *World Journal of Nuclear Medicine*, 17(1)**,** 34-40.

Kawrakow, I. 2000. Accurate condensed history Monte Carlo simulation of electron transport. I. EGSnrc, the new EGS4 version. *Medical Physics*, 27(3)**,** 485-498.

Kawrakow, I., Mitev, K., Gerganov, G., Madzhunkov, J. & Kirov, A. Efficient photon transport in positron emission tomography simulations using VMC++. Journal of Physics. Conference Series, 2008a. IOP Publishing, 012014.

Kawrakow, I., Mitev, K., Gerganov, G., Madzhunkov, J. & Kirov, A. 2008b. SU-GG-I-109: Using EGSnrc Within GATE to Improve the Efficiency Of positron Emission Tomography Simulations. *Medical Physics*, 35(6)**,** 2667-2667.

Kayani, I., Bomanji, J. B., Groves, A., Conway, G., Gacinovic, S., Win, T., Dickson, J., Caplin, M. & Ell, P. J. 2008. Functional imaging of neuroendocrine tumors with combined PET/CT using ^{68}Ga-DOTATATE (DOTA-DPhe1,Tyr3-octreotate) and ^{18}F-FDG. *Cancer*, 112(11)**,** 2447-2455.

Keeble, C., Baxter, P. D., Gislason-Lee, A. J., Treadgold, L. A. & Davies, A. G. 2016. Methods for the analysis of ordinal response data in medical image quality assessment. *The British Journal of Radiology*, 89(1063)**,** 20160094-20160094.

Kemerink, G. J., Visser, M. G. W., Franssen, R., Beijer, E., Zamburlini, M., Halders, S. G. E. A., Brans, B., Mottaghy, F. M. & Teule, G. J. J. 2011. Effect of the positron range of ^{18}F, ^{68}Ga and [124]I on PET/CT in lung-equivalent materials. *European Journal of Nuclear Medicine and Molecular Imaging*, 38(5)**,** 940-948.

Kertész, H., Beyer, T., London, K., Saleh, H., Chung, D., Rausch, I., Cal-Gonzalez, J., Kitsos, T. & Kench, P. L. 2021. Reducing Radiation Exposure to Paediatric Patients Undergoing [18F]FDG-PET/CT Imaging. *Molecular Imaging and Biology*.

Kilian, K. 2014. ^{68}Ga-DOTA and analogs: Current status and future perspectives. *Reports of Practical Oncology & Radiotherapy*, 19(S13-S21).

Kim, M., Yun, J., Cho, Y., Shin, K., Jang, R., Bae, H.-J. & Kim, N. 2019. Deep Learning in Medical Imaging. *Neurospine*, 16(4)**,** 657-668.

Kinahan, P. E. & Fletcher, J. W. 2010. Positron Emission Tomography-Computed Tomography Standardized Uptake Values in Clinical Practice and Assessing Response to Therapy. *Seminars in Ultrasound, CT, and MRI*, 31(6)**,** 496-505.

Kinahan, P. E. & Rogers, J. G. 1989. Analytic 3D image reconstruction using all detected events. *IEEE Transactions on Nuclear Science*, 36(1)**,** 964-968.

Kotasidis, F. A., Angelis, G. I., Anton-Rodriguez, J., Matthews, J. C., Reader, A. J. & Zaidi, H. 2014. Isotope specific resolution recovery image reconstruction in high resolution PET imaging. *Medical Physics*, 41(5)**,** 052503.

Kraus, R., Delso, G. & Ziegler, S. I. 2012. Simulation Study of Tissue-Specific Positron Range Correction for the New Biograph mMR Whole-Body PET/MR System. *IEEE Transactions on Nuclear Science*, 59(5)**,** 1900-1909.

Krishnamoorthy, S., Schmall, J. P. & Surti, S. 2017. PET Physics and Instrumentation. *In:* KHALIL, M. M. (ed.) *Basic Science of PET Imaging*. Cham: Springer International Publishing.

Kroiss, A., Putzer, D., Frech, A., Decristoforo, C., Uprimny, C., Gasser, R. W., Shulkin, B. L., Url, C., Widmann, G., Prommegger, R., Sprinzl, G. M., Fraedrich, G. & Virgolini, I. J. 2013. A retrospective comparison between ^{68}Ga-DOTA-TOC PET/CT and ^{18}F-DOPA PET/CT in patients with extra-adrenal paraganglioma. *European Journal of Nuclear Medicine and Molecular Imaging*, 40(12)**,** 1800-1808.

Kunikowska, J., Królicki, L., Pawlak, D., Zerizer, I. & Mikołajczak, R. 2012. Semiquantitative Analysis and Characterization of Physiological Biodistribution of 68Ga-DOTA-TATE PET/CT. *Clinical Nuclear Medicine*, 37(11)**,** 1052-1057.

Kuntner, C. & Stout, D. 2014. Quantitative preclinical PET imaging: opportunities and challenges. *Frontiers in Physics*, 2(12).

Kuyumcu, S., Özkan, Z. G., Sanli, Y., Yilmaz, E., Mudun, A., Adalet, I. & Unal, S. 2013. Physiological and tumoral uptake of 68Ga-DOTATATE: standardized uptake values and challenges in interpretation. *Annals of nuclear medicine*, 27(6)**,** 538-545.

Latiff, R. A., Meikle, S. R., Gillam, J. E. & Kench, P. L. Positron range estimation using Geant4 Application for Tomography Emission (GATE) Australasian Physical & Engineering Sciences in Medicine, March 01 2017. 245-355.

Lecomte, R. 2009. Novel detector technology for clinical PET. *European Journal of Nuclear Medicine and Molecular Imaging*, 36(1)**,** 69-85.

Lee, T. C., Alessio, A. M., Miyaoka, R. M. & Kinahan, P. E. 2016. Morphology supporting function: Attenuation correction for SPECT/CT, PET/CT, and PET/MR imaging. *Quarterly Journal of Nuclear Medicine and Molecular Imaging*, 60(1), 25-39.

Lehnert, W., Gregoire, M. C., Reilhac, A. & Meikle, S. R. 2011. Analytical positron range modelling in heterogeneous media for PET Monte Carlo simulation. *Phys Med Biol*, 56(11), 3313-35.

Levent, K., Emre, D., Meltem, O., Clemens, D., Ahmet, A., Yildiz, O., Ilhami, U. & Bedii, K. 2012. Comparison of ^{68}Ga-DOTATATE and ^{68}Ga-DOTANOC PET/CT imaging in the same patient group with neuroendocrine tumours. *European Journal of Nuclear Medicine and Molecular Imaging*, 39(8), 1271.

Levin, C. S., Dahlbom, M. & Hoffman, E. J. 1995. A Monte Carlo correction for the effect of Compton scattering in 3-D PET brain imaging. *IEEE Transactions on Nuclear Science*, 42(4), 1181-1185.

Levin, C. S. & Hoffman, E. J. 1999. Calculation of positron range and its effect on the fundamental limit of positron emission tomography system spatial resolution. *Physics in Medicine and Biology*, 44(3), 781-799.

Lillington, J., Brusaferri, L., Kläser, K., Shmueli, K., Neji, R., Hutton, B. F., Fraioli, F., Arridge, S., Cardoso, M. J., Ourselin, S., Thielemans, K. & Atkinson, D. 2020. PET/MRI attenuation estimation in the lung: A review of past, present, and potential techniques. *Medical Physics*, 47(2), 790-811.

Lingxiong, S., Freifelder, R. & Karp, J. S. 1994. Triple energy window scatter correction technique in PET. *IEEE Transactions on Medical Imaging*, 13(4), 641-648.

Loening, A. M. & Gambhir, S. S. 2003. AMIDE: A Free Software Tool for Multimodality Medical Image Analysis. *Molecular Imaging*, 2(3), 131-7.

Lois, C., Jakoby, B., Long, M., Hubner, K., Barker, D., Casey, M., Conti, M., Panin, V., Kadrmas, D. & Townsend, D. 2010. An Assessment of the Impact of Incorporating Time-of-Flight Information into Clinical PET/CT Imaging. *The Journal of Nuclear Medicine*, 51(2), 237-45.

Lu, Y., Fontaine, K., Mulnix, T., Onofrey, J. A., Ren, S., Panin, V., Jones, J., Casey, M. E., Barnett, R., Kench, P., Fulton, R., Carson, R. E. & Liu, C. 2018. Respiratory Motion Compensation for PET/CT with Motion Information Derived from Matched Attenuation-Corrected Gated PET Data. *Journal of Nuclear Medicine*, 59(9), 1480.

Makochekanwa, C., Bankovic, A., Tattersall, W., Jones, A., Caradonna, P., Slaughter, D. S., Nixon, K., Brunger, M. J., Petrovic, Z., Sullivan, J. P. & Buckman, S. J. 2009. Total and positronium formation cross sections for positron scattering from H_2O and HCOOH. *New Journal of Physics*, 11(10), 103036.

Maxwell, J. E. & Howe, J. R. 2015. Imaging in neuroendocrine tumors: an update for the clinician. *International Journal of Endocrine Oncology*, 2(2), 159-168.

Mchugh, M. L. 2012. Interrater reliability: the kappa statistic. *Biochemia medica*, 22(3), 276-282.

Meikle, S. R. & Badawi, R. D. 2005. Quantitative Techniques in PET. *In:* BAILEY, D. L., TOWNSEND, D. W., VALK, P. E. & MAISEY, M. N. (eds.) *Positron Emission Tomography: Basic Sciences.* London: Springer London.

Meikle, S. R., Sossi, V., Roncali, E., Cherry, S. R., Banati, R., Mankoff, D., Jones, T., James, M., Sutcliffe, J., Ouyang, J., Petibon, Y., Ma, C., El Fakhri, G., Surti, S., Karp, J. S., Badawi, R. D., Yamaya, T., Akamatsu, G., Schramm, G., Rezaei, A., Nuyts, J., Fulton, R., Kyme, A., Lois, C., Sari, H., Price, J., Boellaard, R., Jeraj, R., Bailey, D. L., Eslick, E., Willowson, K. P. & Dutta, J. 2021. Quantitative PET in the 2020s: a roadmap. *Physics in Medicine and Biology*, 66(6), 06RM01.

Meisenheimer, M., Saenko, Y. & Eppard, E. 2019. Gallium-68: Radiolabeling of Radiopharmaceuticals for PET Imaging - A Lot to Consider. *In:* NAQVI, S. A. R. & IMRANI, M. B. (eds.) *Medical Isotopes.* United Kingdom: IntechOpen Limited.

Mohy-Ud-Din, H., Lodge, M. A. & Rahmim, A. 2015. Quantitative myocardial perfusion PET parametric imaging at the voxel-level. *Physics in medicine and biology*, 60(15), 6013.

Mojtahedi, A., Thamake, S., Tworowska, I., Ranganathan, D. & Delpassand, E. S. 2014. The value of ^{68}Ga-DOTATATE PET/CT in diagnosis and management of neuroendocrine tumors compared to current FDA approved imaging modalities: a review of literature. *American Journal of Nuclear Medicine and Molecular Imaging*, 4(5), 426-434.

Moradi, F., Jamali, M., Barkhodari, A., Schneider, B., Chin, F., Quon, A., Mittra, E. S. & Iagaru, A. 2016. Spectrum of 68Ga-DOTA TATE Uptake in Patients With Neuroendocrine Tumors. *Clinical Nuclear Medicine*, 41(6), e281-e287.

Moses, W. W. 2011. Fundamental Limits of Spatial Resolution in PET. *Nuclear instruments & methods in physics research. Section A, Accelerators, spectrometers, detectors and associated equipment*, 648 Supplement 1(S236-S240.

Nai, Y.-H., Ose, T., Shidahara, M. & Watabe, H. 2017. ^{137}Cs transmission imaging and segmented attenuation corrections in a small animal PET scanner. *Radiological Physics and Technology*, 10(3)**,** 321-330.

Naswa, N., Sharma, P., Kumar, A., Nazar, A. H., Kumar, R., Chumber, S. & Bal, C. 2011. Gallium-68-DOTA-NOC PET/CT of Patients With Gastroenteropancreatic Neuroendocrine Tumors: A Prospective Single-Center Study. *American Journal of Roentgenology*, 197(5)**,** 1221-1228.

Nuyts, J. 2020. Using time-of-flight information for PET, PET/CT and PET/MRI reconstruction. *Nuovo Cimento della Societa Italiana di Fisica C*, 43(1).

Ozkan, Z. G., Kuyumcu, S., Uzum, A. K., Gecer, M. F., Ozel, S., Aral, F. & Adalet, I. 2015. Comparison of ^{68}Ga-DOTATATE PET-CT, ^{18}F-FDG PET-CT and ^{99m}Tc-(V)DMSA scintigraphy in the detection of recurrent or metastatic medullary thyroid carcinoma. *Nuclear Medicine Communications*, 36(3)**,** 242-250.

Palmer, M. R. & Brownell, G. L. 1992. Annihilation density distribution calculations for medically important positron emitters. *IEEE Transactions on Medical Imaging*, 11(3)**,** 373-378.

Palmer, M. R., Zhu, X. & Parker, J. A. 2005. Modeling and simulation of positron range effects for high resolution PET imaging. *IEEE Transactions on Nuclear Science*, 52(5 I)**,** 1391-1395.

Park, S. J., Rogers, W. L. & Clinthorne, N. H. 2007. Effects of Positron Range and Annihilation Photon Acolinearity on Image Resolution of a Compton PET. *IEEE Transactions on Nuclear Science*, 54(5)**,** 1543-1552.

Partridge, M., Spinelli, A., Ryder, W. & Hindorf, C. 2006. The effect of β+ energy on performance of a small animal PET camera. *Nuclear Instruments and Methods in Physics Research Section A: Accelerators, Spectrometers, Detectors and Associated Equipment*, 568(2)**,** 933-936.

Patel, Y. C. 1999. Somatostatin and Its Receptor Family. *Frontiers in Neuroendocrinology*, 20(3)**,** 157-198.

Pellegrini, P., Howell, N., Shepherd, R., Lengkeek, N., Oehlke, E., Katsifis, A. & Greguric, I. 2013. Synthesis and Radiolabelling of DOTA-Linked Glutamine Analogues with ^{67,68}Ga as Markers for Increased Glutamine Metabolism in Tumour Cells. *Molecules*, 18(6)**,** 7160.

Peng, H. & Levin, C. S. 2010. Recent Developments in PET Instrumentation. *Current Pharmaceutical Biotechnology*, 11(6)**,** 555-571.

Pepin, A., Daouk, J., Bailly, P., Hapdey, S. & Meyer, M. E. 2014. Management of respiratory motion in PET/computed tomography: the state of the art. *Nucl Med Commun*, 35(2), 113-22.

Persson, M., Madsen, J., Østergaard, S., Ploug, M. & Kjaer, A. 2012. ^{68}Ga-labeling and in vivo evaluation of a uPAR binding DOTA- and NODAGA-conjugated peptide for PET imaging of invasive cancers. *Nuclear Medicine and Biology*, 39(4), 560-569.

Phelps, M. E. 2006. *PET: physics, instrumentation, and scanners*, New York;Berlin;, Springer.

Pimpinella, M., Capogni, M., De Coste, V., Filippi, L., Spezi, E., Patterson, N., Mariotti, F., Ferrari, P., Chiaramida, P., Tapner, M., Fischer, A., Paulus, T., Pani, R., Iaccarino, G., Strigari, L. & Bagni, O. 2017. Phantom validation of quantitative Y-90 PET/CT-based dosimetry in liver radioembolization. *EJNMMI Research*, 7(1), 1-15.

Rahmim, A., Qi, J. & Sossi, V. 2013. Resolution modeling in PET imaging: Theory, practice, benefits, and pitfalls. *Medical Physics*, 40(6).

Rahmim, A., Tang, J., Lodge, M. A., Lashkari, S., Ay, M. R. & Bengel, F. M. Resolution Modeled PET Image Reconstruction Incorporating Space-Variance of Positron Range: Rubidium-82 Cardiac PET Imaging. IEEE Nuclear Science Symposium and Medical Imaging Conference, 2009. 2918-2925.

Rahmim, A., Tang, J., Lodge, M. A., Lashkari, S., Ay, M. R., Lautamaki, R., Tsui, B. M. & Bengel, F. M. 2008. Analytic system matrix resolution modeling in PET: an application to Rb-82 cardiac imaging. *Physics in Medicine and Biology*, 53(21), 5947-65.

Rapisarda, E., Bettinardi, V., Thielemans, K. & Gilardi, M. C. 2010. Image-based point spread function implementation in a fully 3D OSEM reconstruction algorithm for PET. *Physics in Medicine & Biology*, 55(14), 4131.

Reader, A. J., Julyan, P. J., Williams, H., Hastings, D. L. & Zweit, J. 2003. EM algorithm system modeling by image-space techniques for PET reconstruction. *IEEE Transactions on Nuclear Science*, 50(5), 1392-1397.

Reader, A. J., Létourneau, E. & Verhaeghe, J. Generalization of the image space reconstruction algorithm. IEEE Nuclear Science Symposium Conference Record, 23-29 Oct. 2011 2011. 4233-4238.

Reubi, J. C. 2004. Somatostatin and other Peptide receptors as tools for tumor diagnosis and treatment. *Neuroendocrinology*, 80 Suppl 1(51-56.

Robson, R. E., Brunger, M. J., Buckman, S. J., Garcia, G., Petrović, Z. L. & White, R. D. 2015. Positron kinetics in an idealized PET environment. *Scientific Reports*, 5(1)**,** 12674.

Roncali, E. & Cherry, S. R. 2011. Application of Silicon Photomultipliers to Positron Emission Tomography. *Annals of Biomedical Engineering*, 39(4)**,** 1358-1377.

Rusten, E., Rødal, J., Revheim, M. E., Skretting, A., Bruland, O. S. & Malinen, E. 2013. Quantitative dynamic ^{18}FDG-PET and tracer kinetic analysis of soft tissue sarcomas. *Acta oncologica (Stockholm, Sweden)*, 52(6)**,** 1160.

Saha, G. B. 2001. *Physics and radiobiology of nuclear medicine*, New York, Springer-Verlag.

Saha, G. B. 2013. Single Photon Emission Computed Tomography. *Physics and Radiobiology of Nuclear Medicine.* New York, NY: Springer New York.

Saha, G. B. 2015. *Basics of PET Imaging : Physics, Chemistry, and Regulations*, Cham, SWITZERLAND, Springer.

Saha, G. B. 2016. *Basics of PET Imaging : Physics, Chemistry, and Regulations*, Cham, Springer International Publishing.

Sanaat, A., Arabi, H., Reza Ay, M. & Zaidi, H. 2020. Novel preclinical PET geometrical concept using a monolithic scintillator crystal offering concurrent enhancement in spatial resolution and detection sensitivity: a simulation study. *Physics in Medicine & Biology*, 65(4)**,** 045013-045013.

Sanchez-Crespo, A. 2013. Comparison of Gallium-68 and Fluorine-18 imaging characteristics in positron emission tomography. *Applied Radiation and Isotopes*, 76(55-62.

Sanchez-Crespo, A., Andreo, P. & Larsson, S. A. 2004. Positron flight in human tissues and its influence on PET image spatial resolution. *Eur J Nucl Med Mol Imaging*, 31(1)**,** 44-51.

Santhanam, P. & Taïeb, D. 2014. Role of ^{18}F-FDOPA PET/CT imaging in endocrinology. *Clinical Endocrinology*, 81(6)**,** 789-798.

Sarrut, D., Bardiès, M., Boussion, N., Freud, N., Jan, S., Létang, J.-M., Loudos, G., Maigne, L., Marcatili, S., Mauxion, T., Papadimitroulas, P., Perrot, Y., Pietrzyk, U., Robert, C., Schaart, D. R., Visvikis, D. & Buvat, I. 2014. A review of the use and potential of the GATE Monte Carlo simulation code for radiation therapy and dosimetry applications. *Medical Physics*, 41(6)**,** 064301.

Schimmack, S., Svejda, B., Lawrence, B., Kidd, M. & Modlin, I. 2011. The diversity and commonalities of gastroenteropancreatic neuroendocrine tumors. *Langenbeck's Archives of Surgery*, 396(3)**,** 273-298.

Schneider, W., Bortfeld, T. & Schlegel, W. 2000. Correlation between CT numbers and tissue parameters needed for Monte Carlo simulations of clinical dose distributions. *Physics in Medicine and Biology*, 45(2)**,** 459-478.

Serra, C. & Andreone, A. 2016. Imaging of NETs. *In:* AMBROSINI, V. & FANTI, S. (eds.) *PET/CT in Neuroendocrine Tumors.* Cham: Springer International Publishing.

Sharma, P., Singh, H., Bal, C. & Kumar, R. 2014. PET/CT imaging of neuroendocrine tumors with (68)Gallium-labeled somatostatin analogues: An overview and single institutional experience from India. *Indian J Nucl Med*, 29(1)**,** 2-12.

Shastry, M., Kayani, I., Wild, D., Caplin, M., Visvikis, D., Gacinovic, S., Reubi, J. C. & Bomanji, J. B. 2010. Distribution pattern of 68Ga-DOTATATE in disease-free patients. *Nuclear Medicine Communications*, 31(12)**,** 1025-1032.

Shepp, L. A. & Vardi, Y. 1982. Maximum Likelihood Reconstruction for Emission Tomography. *IEEE Transactions on Medical Imaging*, 1(2)**,** 113-122.

Shetty, D., Lee, Y.-S. & Jeong, J. M. 2010. ^{68}Ga-labeled radiopharmaceuticals for positron emission tomography. *Nuclear Medicine and Molecular Imaging*, 44(4)**,** 233-240.

Singh, S., Poon, R., Wong, R. & Metser, U. 2018. [68]Ga PET Imaging in Patients With Neuroendocrine Tumors: A Systematic Review and Meta-analysis. *Clinical Nuclear Medicine*, 43(11)**,** 802-810.

Slomka, P. J., Pan, T. & Germano, G. 2016. Recent Advances and Future Progress in PET Instrumentation. *Seminars in Nuclear Medicine*, 46(1)**,** 5-19.

Soultanidis, G., Karakatsanis, N., Nikiforidis, G. & Loudos, G. 2011. Study of the effect of magnetic field in positron range using GATE simulation toolkit. *Journal of Physics: Conference Series*, 317(1)**,** 012021.

Soydal, N. C., Kucuk, I. O., Gecim, H. E., Bilgic, H. S. & Elhan, H. A. 2013. The prognostic value of quantitative parameters of ^{18}F-FDG PET/CT in the evaluation of response to internal radiation therapy with yttrium-90 in patients with liver metastases of colorectal cancer. *Nuclear Medicine Communications*, 34(5)**,** 501-506.

Sureau, F. C., Reader, A. J., Comtat, C., Leroy, C., Ribeiro, M.-J., Buvat, I. & Trébossen, R. 2008. Impact of image-space resolution modeling for studies with the high-resolution research tomograph. *Journal of nuclear medicine : official publication, Society of Nuclear Medicine*, 49(6)**,** 1000-1008.

Surti, S. & Karp, J. S. 2015. Advances in time-of-flight PET. *Physica Medica*, 32(1)**,** 12-22.

Titterington, D. M. 1987. On the Iterative Image Space Reconstruction Algorthm for ECT. *IEEE Transactions on Medical Imaging*, 6(1)**,** 52-56.

Tran, K., Khan, S., Taghizadehasl, M., Palazzo, F., Frilling, A., Todd, J. F. & Al-Nahhas, A. 2015. Gallium-68 Dotatate PET/CT is superior to other imaging modalities in the detection of medullary carcinoma of the thyroid in the presence of high serum calcitonin. *Hellenic Journal Of Nuclear Medicine*, 18(1)**,** 19-24.

Tsutsui, Y., Awamoto, S., Himuro, K., Umezu, Y., Baba, S. & Sasaki, M. 2017. Edge Artifacts in Point Spread Function-based PET Reconstruction in Relation to Object Size and Reconstruction Parameters. *Asia Oceania Journal of Nuclear Medicine & Biology*, 5(2)**,** 134-143.

Van Sluis, J., De Jong, J., Schaar, J., Noordzij, W., Van Snick, P., Dierckx, R., Borra, R., Willemsen, A. & Boellaard, R. 2019. Performance Characteristics of the Digital Biograph Vision PET/CT System. *Journal of Nuclear Medicine*, 60(7)**,** 1031-1036.

Vaquero, J. J. & Kinahan, P. 2015. Positron Emission Tomography: Current Challenges and Opportunities for Technological Advances in Clinical and Preclinical Imaging Systems. *Annual Review of Biomedical Engineering*, 17(1)**,** 385-414.

Vaska, P., Bolotnikov, A., Carini, G., Camarda, G., Pratte, J. F., Dilmanian, F. A., Park, S. J. & James, R. B. Studies of CZT for PET applications. IEEE Nuclear Science Symposium Conference Record, 2005 USA. 2799-2802.

Vázquez Canelas, L., Quintana Arnés, B., Montes Fuentes, C., Gutiérrez Palmero, M. J., Tamayo Alonso, P. & Blasco, J. M. Validation of the Monte Carlo Simulation of a Siemens Biograph mCT PET. 2016 Cham. Springer International Publishing, 227-231.

Velikyan, I. 2015. ^{68}Ga-Based Radiopharmaceuticals: Production and Application Relationship. *Molecules*, 20(7)**,** 12913.

Violet, J., Jackson, P., Ferdinandus, J., Sandhu, S., Akhurst, T., Iravani, A., Kong, G., Kumar, A. R., Thang, S. P., Eu, P., Scalzo, M., Murphy, D., Williams, S., Hicks, R. J. & Hofman, M. S. 2019. Dosimetry of ^{177}Lu-PSMA-617 in Metastatic Castration-Resistant Prostate Cancer: Correlations Between Pretherapeutic Imaging and Whole-Body Tumor Dosimetry with Treatment Outcomes. *Journal of Nuclear Medicine*, 60(4)**,** 517.

Visvikis, D., Cheze-Lerest, C., Costa, D., Bomanji, J., Gacinovic, S. & Ell, P. 2001. Influence of OSEM and segmented attenuation correction in the calculation of standardised uptake values for [^{18}F]FDG PET. *European Journal of Nuclear Medicine*, 28(9)**,** 1326-1335.

Walker, R. C., Smith, G. T., Liu, E., Moore, B., Clanton, J. & Stabin, M. 2013. Measured Human Dosimetry of ^{68}Ga-DOTATATE. *Journal of Nuclear Medicine,* 54(6)**,** 855.

Wang, T., Lei, Y., Dong, X., Higgins, K., Liu, T., Curran, W., Mao, H., Nye, J. & Yang, X. Attenuation correction for PET/MRI using MRI-based pseudo CT. SPIE Medical Imaging, 2020. SPIE.

Wang, W., Xu, Y., Schipper, M., Matuszak, M. M., Ritter, T., Cao, Y., Ten Haken, R. K. & Kong, F.-M. 2013. Effect of Normal Lung Definition on Lung Dosimetry and Lung Toxicity Prediction in Radiation Therapy Treatment Planning. *International Journal of Radiation Oncology, Biology, Physics,* 86(5)**,** 956-963.

Watson, P. F. & Petrie, A. 2010. Method agreement analysis: A review of correct methodology. *Theriogenology,* 73(9)**,** 1167-1179.

Watts, A., Singh, B., Shukla, J., Sharma, S. & Mittal, B. Physiological distribution of ^{68}Ga-DOTA-TATE in normal organs in disease-free NET patients: A semi-quantitative analysis. Journal of Nuclear Medicine, May 1 2014. 1956.

Weissgerber, T. L., Savic, M., Winham, S. J., Stanisavljevic, D., Garovic, V. D. & Milic, N. M. 2017. Data visualization, bar naked: A free tool for creating interactive graphics. *The Journal of Biological Chemistry,* 292(50)**,** 20592-20598.

Werner, R. A., Bluemel, C., Allen-Auerbach, M., Higuchi, T. & Herrmann, K. 2015. ^{68}Gallium- and ^{90}Yttrium-/ ^{177}Lutetium: "theranostic twins" for diagnosis and treatment of NETs. *Annals of Nuclear Medicine,* 29(1)**,** 1-7.

Wienhard, K., Dahlbom, M., Ericksson, L., Michel, C., Bruckbauer, T., Pietrzyk, U. & Heiss, W. D. 1994. The ECAT EXACT HR: Performance of a new high resolution positron scanner. *Journal of Computer Assisted Tomography,* 18(1)**,** 110-118.

Xu, M., Cutler, P. D. & Luk, W. K. 1996. Adaptive, segmented attenuation correction for whole-body PET imaging. *IEEE Transactions on Nuclear Science,* 43(1)**,** 331-336.

Xu, Q., Yuan, K. & Ye, D. 2011. Respiratory motion blur identification and reduction in ungated thoracic PET imaging. *Physics in Medicine and Biology,* 56(14)**,** 4481-4498.

Yalcin, S. 2015. Introduction to Neuroendocrine Tumours. *In:* YALCIN, S. & ÖBERG, K. (eds.) *Neuroendocrine Tumours: Diagnosis and Management.* Berlin, Heidelberg: Springer Berlin Heidelberg.

Yan, J., Schaefferkoetter, J., Conti, M. & Townsend, D. 2016. A method to assess image quality for Low-dose PET: analysis of SNR, CNR, bias and image noise. *Cancer Imaging*, 16(1)**,** 26.

Yang, B. Y., Jeong, J. M., Kim, Y. J., Choi, J. Y., Lee, Y.-S., Lee, D. S., Chung, J.-K. & Lee, M. C. 2010. Formulation of ^{68}Ga BAPEN kit for myocardial positron emission tomography imaging and biodistribution study. *Nuclear Medicine and Biology*, 37(2)**,** 149-155.

Yang, Y., Bec, J., Zhou, J., Zhang, M., Judenhofer, M. S., Bai, X., Di, K., Wu, Y., Rodriguez, M., Dokhale, P., Shah, K. S., Farrell, R., Qi, J. & Cherry, S. R. 2016. A Prototype High-Resolution Small-Animal PET Scanner Dedicated to Mouse Brain Imaging. *Journal of Nuclear Medicine*, 57(7)**,** 1130-1135.

Yao, J. C., Hassan, M., Phan, A., Dagohoy, C., Leary, C., Mares, J. E., Abdalla, E. K., Fleming, J. B., Vauthey, J.-N., Rashid, A. & Evans, D. B. 2008. One Hundred Years After "Carcinoid": Epidemiology of and Prognostic Factors for Neuroendocrine Tumors in 35,825 Cases in the United States. *Journal of Clinical Oncology*, 26(18)**,** 3063-3072.

Zaidi, H. & Alavi, A. 2007. Current Trends in PET and Combined (PET/CT and PET/MR) Systems Design. *PET Clinics*, 2(2)**,** 109-123.

Zeng, G. L. 2011. Gibbs artifact reduction by nonnegativity constraint. *Journal of Nuclear Medicine Technology*, 39(3)**,** 213-9.

Zheng, X., Deen, M. J. & Peng, H. 2014. Performance Characteristics of CZT Detectors for PET Imaging Applications. *ECS Transactions*, 61(35)**,** 7-13.

Ziegler, S., Jakoby, B., Braun, H., Paulus, D. & Quick, H. 2015. NEMA image quality phantom measurements and attenuation correction in integrated PET/MR hybrid imaging. *EJNMMI Physics*, 2(1)**,** 1-14.

APPENDICES

Appendix A: GATE main simulation code

```
#-------------------oooooOOOOO00000OOOOOooooo-------------------#
#
#     D E F I N E   Y O U R   S C A N N E R   A N D
#
#     Y O U R   C O M P L E T E   S I M U L A T I O N
#
#     F O R   I M A G I N G   A P P L I C A T I O N S
#
#-------------------oooooOOOOO00000OOOOOooooo-------------------#


#=====================================================
# VISUALISATION
#=====================================================
/vis/disable
/control/execute          Verbose.mac


#=====================================================
# GEOMETRY
#=====================================================
/gate/geometry/setMaterialDatabase    GateMaterials.db


#=====================================================
#   W O R L D
#=====================================================
/gate/world/geometry/setXLength      400. cm
/gate/world/geometry/setYLength      400. cm
/gate/world/geometry/setZLength      400. cm



#=====================================================
# VOXEL PHANTOM
#=====================================================

/control/execute voxelPhantomHU.mac


#=====================================================
# PHYSICS
#=====================================================
/gate/physics/addProcess ElectronIonisation
/gate/physics/processes/ElectronIonisation/setModel StandardModel e-
/gate/physics/processes/ElectronIonisation/setModel StandardModel e+

/gate/physics/addProcess Bremsstrahlung
```

```
/gate/physics/processes/Bremsstrahlung/setModel StandardModel e-
/gate/physics/processes/Bremsstrahlung/setModel StandardModel e+

/gate/physics/addProcess PositronAnnihilation

/gate/physics/addProcess MultipleScattering e+
/gate/physics/addProcess MultipleScattering e-

/gate/physics/processList Enabled
/gate/physics/processList Initialized


#=======================================================
# CUTS
#=======================================================
/gate/physics/Gamma/SetCutInRegion      world  1.0 mm
/gate/physics/Electron/SetCutInRegion    world  1.0 mm
/gate/physics/Positron/SetCutInRegion    world  1.0 mm
/gate/physics/SetMaxTrackLengthInRegion world 0 mm   #kill gamma
/gate/physics/ActivateSpecialCuts gamma          #kill gamma


#========
#Actor
#=========
/gate/actor/addActor ProductionAndStoppingActor  MyActor
/gate/actor/MyActor/save        Out1LesiWB09.hdr
/gate/actor/MyActor/attachTo     phantom
/gate/actor/MyActor/setResolution 201 201 612
/gate/actor/MyActor/stepHitType   post

#Particle filter

/gate/actor/MyActor/addFilter    particleFilter
/gate/actor/MyActor/particleFilter/addParticle e+


#======================================================
# INITIALISATION
#======================================================

/gate/run/initialize


#======================================================
#  VOXELISED SOURCE
#======================================================
/control/execute voxelPhantomSource.mac
#============== ==================================================
#  R A N D O M
#======================================================= ==============
```

```
/gate/random/setEngineName JamesRandom
/gate/random/setEngineSeed auto
/gate/random/verbose 1
#=================
#MEASUREMENT SETTINGS
#===================
/gate/application/setTimeSlice   500 ms
/gate/application/setTimeStart   0   ms
/gate/application/setTimeStop    500 ms
/gate/application/startDAQ
```

Appendix B: Simulation of emission distribution

/gate/source/addSource nema voxel

/gate/source/nema/reader/insert image

#This scales all image values directly into activities

/gate/source/nema/imageReader/translator/insert linear

/gate/source/nema/imageReader/linearTranslator/setScale 1. Bq

/gate/source/nema/imageReader/readFile Update0_lesi09.hdr

/gate/source/nema/setPosition -409 -409 -918 mm

#====================
#ForGa68 particle type
#====================
 #################### Mode 2: Histogram ####################

/gate/source/nema/gps/particle e+

/gate/source/nema/gps/energytype UserSpectrum

/gate/source/nema/gps/setSpectrumFile Ga68spectrum.txt

/gate/source/nema/setIntensity 190

#################### Mode 2: Histogram ####################

/gate/source/nema/setForcedUnstableFlag   true

/gate/source/nema/setForcedHalfLife   4098 s

/gate/source/nema/gps/angtype   iso

/gate/source/nema/dump   1

/gate/source/nema/attachTo phantom

/gate/source/list

Appendix C: Generating material and density database

#Generate materials from Hounsfield units

/gate/HounsfieldMaterialGenerator/SetMaterialTable   Schneider2000MaterialsTable.txt

/gate/HounsfieldMaterialGenerator/SetDensityTable   Schneider2000DensitiesTable.txt

/gate/HounsfieldMaterialGenerator/SetDensityTolerance   0.1 g/cm3

/gate/HounsfieldMaterialGenerator/SetOutputMaterialDatabaseFilename pat09-HUmaterials.db

/gate/HounsfieldMaterialGenerator/SetOutputHUMaterialFilename   pat09-HU2mat.txt

/gate/HounsfieldMaterialGenerator/Generate

/gate/world/daughters/name phantom

/gate/world/daughters/insert ImageRegularParametrisedVolume

/gate/phantom/geometry/setImage CtAllResample09.hdr

/gate/geometry/setMaterialDatabase pat09-HUmaterials.db

/gate/phantom/geometry/setRangeToMaterialFile pat09-HU2mat.txt

/gate/phantom/placement/setTranslation 0. 0. 0. mm

/gate/phantom/placement/setRotationAxis 1 0 0

/gate/phantom/placement/setRotationAngle 0 deg

/gate/phantom/attachPhantomSD

Appendix D: Schneider2000MaterialsTable to calibrate CT number (HU) to materials elements

```
[Elements]
Hydrogen  Carbon Nitrogen Oxygen Sodium Magnesium Phosphor Sulfur
Chlorine Argon Potassium Calcium
Titanium Copper Zinc  Silver Tin
[/Elements]
#
================================================================
=========
# HU     H     C     N     O    Na   Mg    P    S    Cl   Ar    K     Ca  Ti  Cu
Zn  Ag  Sn
#
================================================================
=========
 -1050   0     0   75.5 23.2   0    0    0    0    0   1.3   0     0   0    0   0
0   0      Air
  -950  10.3 10.5  3.1 74.9 0.2   0   0.2 0.3 0.3   0   0.2    0   0    0   0
0   0      Lung
  -120  11.6 68.1  0.2 19.8 0.1   0    0  0.1 0.1   0    0     0   0    0   0
0   0   AT_AG_SI1
  -82   11.3 56.7  0.9 30.8 0.1   0    0  0.1 0.1   0    0     0   0    0   0
0   0   AT_AG_SI2
  -52   11.0 45.8  1.5 41.1 0.1   0   0.1 0.2 0.2   0    0     0   0    0   0
0   0   AT_AG_SI3
  -22   10.8 35.6  2.2 50.9  0    0   0.1 0.2 0.2   0    0     0   0    0   0
0   0   AT_AG_SI4
   8    10.6 28.4  2.6 57.8  0    0   0.1 0.2 0.2   0   0.1    0   0    0   0
0   0   AT_AG_SI5
   19   10.3 13.4  3.0 72.3 0.2   0   0.2 0.2 0.2   0   0.2    0   0    0   0
0   0   SoftTissus
   80    9.4 20.7  6.2 62.2 0.6   0    0  0.6 0.3   0   0.0    0   0    0   0
0   0 ConnectiveTissue
  120    9.5 45.5  2.5 35.5 0.1   0   2.1 0.1 0.1   0   0.1   4.5  0    0   0
0   0  Marrow_Bone01
  200    8.9 42.3  2.7 36.3 0.1   0   3.0 0.1 0.1   0   0.1   6.4  0    0   0
0   0  Marrow_Bone02
  300    8.2 39.1  2.9 37.2 0.1   0   3.9 0.1 0.1   0   0.1   8.3  0    0   0
0   0  Marrow_Bone03
  400    7.6 36.1  3.0 38.0 0.1 0.1  4.7 0.2 0.1   0    0   10.1  0    0   0
0   0  Marrow_Bone04
  500    7.1 33.5  3.2 38.7 0.1 0.1  5.4 0.2    0 0    0   11.7  0    0   0
0   0  Marrow_Bone05
  600    6.6 31.0  3.3 39.4 0.1 0.1  6.1 0.2   0   0    0   13.2  0    0   0
0   0  Marrow_Bone06
  700    6.1 28.7  3.5 40.0 0.1 0.1  6.7 0.2   0   0    0   14.6  0    0   0
0   0  Marrow_Bone07
  800    5.6 26.5  3.6 40.5 0.1 0.2  7.3 0.3   0   0    0   15.9  0    0   0
0   0   Marrow_Bone08
```

```
 900     5.2 24.6  3.7 41.1 0.1 0.2  7.8 0.3  0    0    0   17.0 0    0   0
0   0  Marrow_Bone09
 1000    4.9 22.7  3.8 41.6 0.1 0.2  8.3 0.3  0    0    0   18.1 0    0   0
0   0  Marrow_Bone10
 1100    4.5 21.0  3.9 42.0 0.1 0.2  8.8 0.3  0    0    0   19.2 0    0   0
0   0  Marrow_Bone11
 1200    4.2 19.4  4.0 42.5 0.1 0.2  9.2 0.3  0    0    0   20.1 0    0   0
0   0  Marrow_Bone12
 1300    3.9 17.9  4.1 42.9 0.1 0.2  9.6 0.3  0    0    0   21.0 0    0   0
0   0  Marrow_Bone13
 1400    3.6 16.5  4.2 43.2 0.1 0.2 10.0 0.3  0    0    0   21.9 0    0   0
0   0  Marrow_Bone14
 1500    3.4 15.5  4.2 43.5 0.1 0.2 10.3 0.3  0    0    0   22.5 0    0   0
0   0  Marrow_Bone15
 1640    0   0     0    0    0   0   0    0    0    0    0    0   0    4
2  65  29  AmalgamTooth
 2300    0   0     0    0    0   0   0    0    0    0    0    0  100  0
0   0   0  MetallImplants
 3000    0   0     0    0    0   0   0    0    0    0    0    0  100  0
0   0   0  MetallImplants
```

Appendix E: Schneider2000DensitiesTable to correlate between CT number (HU) to mass density

```
# ==================
# HU  density g/cm3
# ==================
-1000 1.21e-3
-98   0.93
-97   0.930486
14    1.03
23    1.031
100   1.119900
101   1.076200
1600  1.964200
3000  2.8
```

Appendix F: Materials database generated from Appendix C

[Materials]
Material corresponding to H=[-1050;-950]
Air_0: d=1.21 mg/cm3; n=3;
+el: name=Nitrogen; f=0.755
+el: name=Oxygen; f=0.232
+el: name=Argon; f=0.013

Material corresponding to H=[-950;-852]
Lung_1: d=102.695 mg/cm3; n=9;
+el: name=Hydrogen; f=0.103
+el: name=Carbon; f=0.105
+el: name=Nitrogen; f=0.031
+el: name=Oxygen; f=0.749
+el: name=Sodium; f=0.002
+el: name=Phosphor; f=0.002
+el: name=Sulfur; f=0.003
+el: name=Chlorine; f=0.003
+el: name=Potassium; f=0.002

Material corresponding to H=[-852;-755]
Lung_2: d=202.695 mg/cm3; n=9;
+el: name=Hydrogen; f=0.103
+el: name=Carbon; f=0.105
+el: name=Nitrogen; f=0.031
+el: name=Oxygen; f=0.749
+el: name=Sodium; f=0.002
+el: name=Phosphor; f=0.002
+el: name=Sulfur; f=0.003
+el: name=Chlorine; f=0.003
+el: name=Potassium; f=0.002

Material corresponding to H=[-755;-658]
Lung_3: d=302.695 mg/cm3; n=9;
+el: name=Hydrogen; f=0.103
+el: name=Carbon; f=0.105
+el: name=Nitrogen; f=0.031
+el: name=Oxygen; f=0.749
+el: name=Sodium; f=0.002
+el: name=Phosphor; f=0.002
+el: name=Sulfur; f=0.003
+el: name=Chlorine; f=0.003
+el: name=Potassium; f=0.002

Material corresponding to H=[-658;-561]
Lung_4: d=402.695 mg/cm3; n=9;

+el: name=Hydrogen; f=0.103
+el: name=Carbon; f=0.105
+el: name=Nitrogen; f=0.031
+el: name=Oxygen; f=0.749
+el: name=Sodium; f=0.002
+el: name=Phosphor; f=0.002
+el: name=Sulfur; f=0.003
+el: name=Chlorine; f=0.003
+el: name=Potassium; f=0.002

Material corresponding to H=[-561;-464]
Lung_5: d=502.695 mg/cm3; n=9;
+el: name=Hydrogen; f=0.103
+el: name=Carbon; f=0.105
+el: name=Nitrogen; f=0.031
+el: name=Oxygen; f=0.749
+el: name=Sodium; f=0.002
+el: name=Phosphor; f=0.002
+el: name=Sulfur; f=0.003
+el: name=Chlorine; f=0.003
+el: name=Potassium; f=0.002

Material corresponding to H=[-464;-367]
Lung_6: d=602.695 mg/cm3; n=9;
+el: name=Hydrogen; f=0.103
+el: name=Carbon; f=0.105
+el: name=Nitrogen; f=0.031
+el: name=Oxygen; f=0.749
+el: name=Sodium; f=0.002
+el: name=Phosphor; f=0.002
+el: name=Sulfur; f=0.003
+el: name=Chlorine; f=0.003
+el: name=Potassium; f=0.002

Material corresponding to H=[-367;-270]
Lung_7: d=702.695 mg/cm3; n=9;
+el: name=Hydrogen; f=0.103
+el: name=Carbon; f=0.105
+el: name=Nitrogen; f=0.031
+el: name=Oxygen; f=0.749
+el: name=Sodium; f=0.002
+el: name=Phosphor; f=0.002
+el: name=Sulfur; f=0.003
+el: name=Chlorine; f=0.003
+el: name=Potassium; f=0.002

Material corresponding to H=[-270;-173]
Lung_8: d=802.695 mg/cm3; n=9;

+el: name=Hydrogen; f=0.103
+el: name=Carbon; f=0.105
+el: name=Nitrogen; f=0.031
+el: name=Oxygen; f=0.749
+el: name=Sodium; f=0.002
+el: name=Phosphor; f=0.002
+el: name=Sulfur; f=0.003
+el: name=Chlorine; f=0.003
+el: name=Potassium; f=0.002

Material corresponding to H=[-173;-120]
Lung_9: d=880.021 mg/cm3; n=9;
+el: name=Hydrogen; f=0.103
+el: name=Carbon; f=0.105
+el: name=Nitrogen; f=0.031
+el: name=Oxygen; f=0.749
+el: name=Sodium; f=0.002
+el: name=Phosphor; f=0.002
+el: name=Sulfur; f=0.003
+el: name=Chlorine; f=0.003
+el: name=Potassium; f=0.002

Material corresponding to H=[-120;-82]
AT_AG_SI1_10: d=926.911 mg/cm3; n=7;
+el: name=Hydrogen; f=0.116
+el: name=Carbon; f=0.681
+el: name=Nitrogen; f=0.002
+el: name=Oxygen; f=0.198
+el: name=Sodium; f=0.001
+el: name=Sulfur; f=0.001
+el: name=Chlorine; f=0.001

Material corresponding to H=[-82;-52]
AT_AG_SI2_11: d=957.382 mg/cm3; n=7;
+el: name=Hydrogen; f=0.113
+el: name=Carbon; f=0.567
+el: name=Nitrogen; f=0.009
+el: name=Oxygen; f=0.308
+el: name=Sodium; f=0.001
+el: name=Sulfur; f=0.001
+el: name=Chlorine; f=0.001

Material corresponding to H=[-52;-22]
AT_AG_SI3_12: d=984.277 mg/cm3; n=8;
+el: name=Hydrogen; f=0.11
+el: name=Carbon; f=0.458
+el: name=Nitrogen; f=0.015
+el: name=Oxygen; f=0.411

+el: name=Sodium; f=0.001
+el: name=Phosphor; f=0.001
+el: name=Sulfur; f=0.002
+el: name=Chlorine; f=0.002

Material corresponding to H=[-22;8]
AT_AG_SI4_13: d=1.01117 g/cm3 ; n=7;
+el: name=Hydrogen; f=0.108
+el: name=Carbon; f=0.356
+el: name=Nitrogen; f=0.022
+el: name=Oxygen; f=0.509
+el: name=Phosphor; f=0.001
+el: name=Sulfur; f=0.002
+el: name=Chlorine; f=0.002

Material corresponding to H=[8;19]
AT_AG_SI5_14: d=1.02955 g/cm3 ; n=8;
+el: name=Hydrogen; f=0.106
+el: name=Carbon; f=0.284
+el: name=Nitrogen; f=0.026
+el: name=Oxygen; f=0.578
+el: name=Phosphor; f=0.001
+el: name=Sulfur; f=0.002
+el: name=Chlorine; f=0.002
+el: name=Potassium; f=0.001

Material corresponding to H=[19;80]
SoftTissus_15: d=1.0616 g/cm3 ; n=9;
+el: name=Hydrogen; f=0.103
+el: name=Carbon; f=0.134
+el: name=Nitrogen; f=0.03
+el: name=Oxygen; f=0.723
+el: name=Sodium; f=0.002
+el: name=Phosphor; f=0.002
+el: name=Sulfur; f=0.002
+el: name=Chlorine; f=0.002
+el: name=Potassium; f=0.002

Material corresponding to H=[80;120]
ConnectiveTissue_16: d=1.1199 g/cm3 ; n=7;
+el: name=Hydrogen; f=0.094
+el: name=Carbon; f=0.207
+el: name=Nitrogen; f=0.062
+el: name=Oxygen; f=0.622
+el: name=Sodium; f=0.006
+el: name=Sulfur; f=0.006
+el: name=Chlorine; f=0.003

```
# Material corresponding to H=[ 120;200 ]
Marrow_Bone01_17: d=1.11115 g/cm3 ; n=10;
+el: name=Hydrogen; f=0.095
+el: name=Carbon; f=0.455
+el: name=Nitrogen; f=0.025
+el: name=Oxygen; f=0.355
+el: name=Sodium; f=0.001
+el: name=Phosphor; f=0.021
+el: name=Sulfur; f=0.001
+el: name=Chlorine; f=0.001
+el: name=Potassium; f=0.001
+el: name=Calcium; f=0.045

# Material corresponding to H=[ 200;300 ]
Marrow_Bone02_18: d=1.16447 g/cm3 ; n=10;
+el: name=Hydrogen; f=0.089
+el: name=Carbon; f=0.423
+el: name=Nitrogen; f=0.027
+el: name=Oxygen; f=0.363
+el: name=Sodium; f=0.001
+el: name=Phosphor; f=0.03
+el: name=Sulfur; f=0.001
+el: name=Chlorine; f=0.001
+el: name=Potassium; f=0.001
+el: name=Calcium; f=0.064

# Material corresponding to H=[ 300;400 ]
Marrow_Bone03_19: d=1.22371 g/cm3 ; n=10;
+el: name=Hydrogen; f=0.082
+el: name=Carbon; f=0.391
+el: name=Nitrogen; f=0.029
+el: name=Oxygen; f=0.372
+el: name=Sodium; f=0.001
+el: name=Phosphor; f=0.039
+el: name=Sulfur; f=0.001
+el: name=Chlorine; f=0.001
+el: name=Potassium; f=0.001
+el: name=Calcium; f=0.083

# Material corresponding to H=[ 400;500 ]
Marrow_Bone04_20: d=1.28295 g/cm3 ; n=10;
+el: name=Hydrogen; f=0.076
+el: name=Carbon; f=0.361
+el: name=Nitrogen; f=0.03
+el: name=Oxygen; f=0.38
+el: name=Sodium; f=0.001
+el: name=Magnesium; f=0.001
+el: name=Phosphor; f=0.047
```

+el: name=Sulfur; f=0.002
+el: name=Chlorine; f=0.001
+el: name=Calcium; f=0.101

Material corresponding to H=[500;600]
Marrow_Bone05_21: d=1.34219 g/cm3 ; n=9;
+el: name=Hydrogen; f=0.071
+el: name=Carbon; f=0.335
+el: name=Nitrogen; f=0.032
+el: name=Oxygen; f=0.387
+el: name=Sodium; f=0.001
+el: name=Magnesium; f=0.001
+el: name=Phosphor; f=0.054
+el: name=Sulfur; f=0.002
+el: name=Calcium; f=0.117

Material corresponding to H=[600;700]
Marrow_Bone06_22: d=1.40142 g/cm3 ; n=9;
+el: name=Hydrogen; f=0.066
+el: name=Carbon; f=0.31
+el: name=Nitrogen; f=0.033
+el: name=Oxygen; f=0.394
+el: name=Sodium; f=0.001
+el: name=Magnesium; f=0.001
+el: name=Phosphor; f=0.061
+el: name=Sulfur; f=0.002
+el: name=Calcium; f=0.132

Material corresponding to H=[700;800]
Marrow_Bone07_23: d=1.46066 g/cm3 ; n=9;
+el: name=Hydrogen; f=0.061
+el: name=Carbon; f=0.287
+el: name=Nitrogen; f=0.035
+el: name=Oxygen; f=0.4
+el: name=Sodium; f=0.001
+el: name=Magnesium; f=0.001
+el: name=Phosphor; f=0.067
+el: name=Sulfur; f=0.002
+el: name=Calcium; f=0.146

Material corresponding to H=[800;900]
Marrow_Bone08_24: d=1.5199 g/cm3 ; n=9;
+el: name=Hydrogen; f=0.056
+el: name=Carbon; f=0.265
+el: name=Nitrogen; f=0.036
+el: name=Oxygen; f=0.405
+el: name=Sodium; f=0.001
+el: name=Magnesium; f=0.002

+el: name=Phosphor; f=0.073
+el: name=Sulfur; f=0.003
+el: name=Calcium; f=0.159

Material corresponding to H=[900;1000]
Marrow_Bone09_25: d=1.57914 g/cm3 ; n=9;
+el: name=Hydrogen; f=0.052
+el: name=Carbon; f=0.246
+el: name=Nitrogen; f=0.037
+el: name=Oxygen; f=0.411
+el: name=Sodium; f=0.001
+el: name=Magnesium; f=0.002
+el: name=Phosphor; f=0.078
+el: name=Sulfur; f=0.003
+el: name=Calcium; f=0.17

Material corresponding to H=[1000;1100]
Marrow_Bone10_26: d=1.63838 g/cm3 ; n=9;
+el: name=Hydrogen; f=0.049
+el: name=Carbon; f=0.227
+el: name=Nitrogen; f=0.038
+el: name=Oxygen; f=0.416
+el: name=Sodium; f=0.001
+el: name=Magnesium; f=0.002
+el: name=Phosphor; f=0.083
+el: name=Sulfur; f=0.003
+el: name=Calcium; f=0.181

Material corresponding to H=[1100;1200]
Marrow_Bone11_27: d=1.69762 g/cm3 ; n=9;
+el: name=Hydrogen; f=0.045
+el: name=Carbon; f=0.21
+el: name=Nitrogen; f=0.039
+el: name=Oxygen; f=0.42
+el: name=Sodium; f=0.001
+el: name=Magnesium; f=0.002
+el: name=Phosphor; f=0.088
+el: name=Sulfur; f=0.003
+el: name=Calcium; f=0.192

Material corresponding to H=[1200;1300]
Marrow_Bone12_28: d=1.75686 g/cm3 ; n=9;
+el: name=Hydrogen; f=0.042
+el: name=Carbon; f=0.194
+el: name=Nitrogen; f=0.04
+el: name=Oxygen; f=0.425
+el: name=Sodium; f=0.001
+el: name=Magnesium; f=0.002

+el: name=Phosphor; f=0.092
+el: name=Sulfur; f=0.003
+el: name=Calcium; f=0.201

Material corresponding to H=[1300;1400]
Marrow_Bone13_29: d=1.8161 g/cm3 ; n=9;
+el: name=Hydrogen; f=0.039
+el: name=Carbon; f=0.179
+el: name=Nitrogen; f=0.041
+el: name=Oxygen; f=0.429
+el: name=Sodium; f=0.001
+el: name=Magnesium; f=0.002
+el: name=Phosphor; f=0.096
+el: name=Sulfur; f=0.003
+el: name=Calcium; f=0.21

Material corresponding to H=[1400;1500]
Marrow_Bone14_30: d=1.87534 g/cm3 ; n=9;
+el: name=Hydrogen; f=0.036
+el: name=Carbon; f=0.165
+el: name=Nitrogen; f=0.042
+el: name=Oxygen; f=0.432
+el: name=Sodium; f=0.001
+el: name=Magnesium; f=0.002
+el: name=Phosphor; f=0.1
+el: name=Sulfur; f=0.003
+el: name=Calcium; f=0.219

Material corresponding to H=[1500;1640]
Marrow_Bone15_31: d=1.94643 g/cm3 ; n=9;
+el: name=Hydrogen; f=0.034
+el: name=Carbon; f=0.155
+el: name=Nitrogen; f=0.042
+el: name=Oxygen; f=0.435
+el: name=Sodium; f=0.001
+el: name=Magnesium; f=0.002
+el: name=Phosphor; f=0.103
+el: name=Sulfur; f=0.003
+el: name=Calcium; f=0.225

Material corresponding to H=[1640;1807]
AmalgamTooth_32: d=2.03808 g/cm3 ; n=4;
+el: name=Copper; f=0.04
+el: name=Zinc; f=0.02
+el: name=Silver; f=0.65
+el: name=Tin; f=0.29

Material corresponding to H=[1807;1975]

AmalgamTooth_33: d=2.13808 g/cm3 ; n=4;
+el: name=Copper; f=0.04
+el: name=Zinc; f=0.02
+el: name=Silver; f=0.65
+el: name=Tin; f=0.29

Material corresponding to H=[1975;2142]
AmalgamTooth_34: d=2.23808 g/cm3 ; n=4;
+el: name=Copper; f=0.04
+el: name=Zinc; f=0.02
+el: name=Silver; f=0.65
+el: name=Tin; f=0.29

Material corresponding to H=[2142;2300]
AmalgamTooth_35: d=2.33509 g/cm3 ; n=4;
+el: name=Copper; f=0.04
+el: name=Zinc; f=0.02
+el: name=Silver; f=0.65
+el: name=Tin; f=0.29

Material corresponding to H=[2300;2467]
MetallImplants_36: d=2.4321 g/cm3 ; n=1;
+el: name=Titanium; f=1

Material corresponding to H=[2467;2635]
MetallImplants_37: d=2.5321 g/cm3 ; n=1;
+el: name=Titanium; f=1

Material corresponding to H=[2635;2802]
MetallImplants_38: d=2.6321 g/cm3 ; n=1;
+el: name=Titanium; f=1

Material corresponding to H=[2802;2970]
MetallImplants_39: d=2.7321 g/cm3 ; n=1;
+el: name=Titanium; f=1

Material corresponding to H=[2970;3000]
MetallImplants_40: d=2.79105 g/cm3 ; n=1;
+el: name=Titanium; f=1

Material corresponding to H=[3000;3001]
MetallImplants_41: d=2.8 g/cm3 ; n=1;
+el: name=Titanium; f=1

Appendix G: Attenuation segmentation based on CT number

```
-1050 -950 Air_0
-950 -852 Lung_1
-852 -755 Lung_2
-755 -658 Lung_3
-658 -561 Lung_4
-561 -464 Lung_5
-464 -367 Lung_6
-367 -270 Lung_7
-270 -173 Lung_8
-173 -120 Lung_9
-120 -82 AT_AG_SI1_10
-82 -52 AT_AG_SI2_11
-52 -22 AT_AG_SI3_12
-22 8 AT_AG_SI4_13
8 19 AT_AG_SI5_14
19 80 SoftTissus_15
80 120 ConnectiveTissue_16
120 200 Marrow_Bone01_17
200 300 Marrow_Bone02_18
300 400 Marrow_Bone03_19
400 500 Marrow_Bone04_20
500 600 Marrow_Bone05_21
600 700 Marrow_Bone06_22
700 800 Marrow_Bone07_23
800 900 Marrow_Bone08_24
900 1000 Marrow_Bone09_25
1000 1100 Marrow_Bone10_26
1100 1200 Marrow_Bone11_27
1200 1300 Marrow_Bone12_28
1300 1400 Marrow_Bone13_29
1400 1500 Marrow_Bone14_30
1500 1640 Marrow_Bone15_31
1640 1807 AmalgamTooth_32
1807 1975 AmalgamTooth_33
1975 2142 AmalgamTooth_34
2142 2300 AmalgamTooth_35
2300 2467 MetallImplants_36
2467 2635 MetallImplants_37
2635 2802 MetallImplants_38
2802 2970 MetallImplants_39
2970 3000 MetallImplants_40
3000 3001 MetallImplants_41
```

Appendix H: Post-Reconstruction PRC code

```matlab
function UpdatedImage =
UpdateRL_noisesuppress(currentEstimate,oldEstimate,PET_image,save);
%oldEstimate =  current GateOutput, CurrentEstimate header
%oldEstimate= Previous Updated Image, OldEstimate header
%PET_image = PET measured image header

%load currentEstimate
currentEst= load_untouch_nii(currentEstimate);
currentEstImage= double(currentEst.img);

%load oldEstimateBlurred
oldEst = load_untouch_nii(oldEstimate);
oldEstimateImg= double(oldEst.img);

%load Pet img
PET= load_untouch_nii(PET_image);
PetImg= double(PET.img);

%normalised Output
Out0N=(currentEstImage.*sum(PetImg(:)))./sum(currentEstImage(:));

%Correction Factor
Error0=PetImg./Out0N;
relax=sin(0.5*pi*(oldEstimateImg-
min(oldEstimateImg(:)))/(max(oldEstimateImg(:)-min(oldEstimateImg(:)))));
Update=oldEstimateImg.*(relax.*(Error0-1)+1); % Eq:16.13 in deconP6.jpg
Update(isnan(Update))=0;
Update(isinf(Update))=0;
UpdatedImage=Update;

if save %true or false
%save image as 'Update0.hdr'
ana = make_ana(UpdatedImage,[4.07 4.07 3],[],[8]);%phantom 4.07 4.07 2.03
save_untouch_nii(ana,'Update5_WB20_noAir800.hdr');

end
end
```

Appendix I: Ethics approval

THE UNIVERSITY OF
SYDNEY

Research Integrity & Ethics Administration
Human Research Ethics Committee

Friday, 24 November 2017

Dr Peter Kench

Medical Imaging and Radiation Sciences; Faculty of Health Sciences
peter.kench@sydney.edu.au

Dear Peter,

The University of Sydney Human Research Ethics Committee (HREC) has considered your application.

After consideration of your response to the comments raised your project has been approved. Approval is granted for a period of four years from **21/11/2017 to 21/11/2021**
Project title: Optimisation of PET image quality and quantification using positron range correction
Project no.:   2017/854
First Annual Report due: 21/11/2018
Authorised Personnel: Kench Peter; A Latiff Rukiah; Gillam John; Meikle Steven;

Documents Approved:

Date Uploaded	Version number	Document Name
13/11/2017	Version 1	consent for accessing your medical information
13/11/2017	Version 1	PET worksheet

<u>Condition/s of Approval</u>

- Research must be conducted according to the approved proposal.
- An annual progress report must be submitted to the Ethics Office on or before the anniversary of approval and on completion of the project.
- You must report as soon as practicable anything that might warrant review of ethical approval of the project including:
  - ➢ Serious or unexpected adverse events (which should be reported within 72 hours).

> ➢ Unforeseen events that might affect continued ethical acceptability of the project.

- Any changes to the proposal must be approved prior to their implementation (except where an amendment is undertaken to eliminate *immediate* risk to participants).

- Personnel working on this project must be sufficiently qualified by education, training and experience for their role, or adequately supervised. Changes to personnel must be reported and approved.

- Personnel must disclose any actual or potential conflicts of interest, including any financial or other interest or affiliation, as relevant to this project.

- Data and primary materials must be retained and stored in accordance with the relevant legislation and University guideline.

- Ethics approval is dependent upon ongoing compliance of the research with the *National Statement on Ethical Conduct in Human Research*, the *Australian Code for the Responsible Conduct of Research*, applicable legal requirements, and with University policies, procedures and governance requirements.
- The Ethics Office may conduct audits on approved projects.
- The Chief Investigator has ultimate responsibility for the conduct of the research and is responsible for ensuring all others involved will conduct the research in accordance with the above.

This letter constitutes ethical approval only.

Please contact the Ethics Office should you require further

information or clarification. Sincerely,

Associate Professor Stephen Assinder Chair

Human Research Ethics Committee (HREC 1)

The University of Sydney HRECs are constituted and operate in accordance with the National Health and Medical Research Council's (NHMRC) National Statement on Ethical Conduct in Human Research (2007) and the NHMRC's Australian Code for the Responsible Conduct of Research (2007).

Appendix J: Attenuation segmentation after CT number adjustment

```
-800 -702 Lung_0
-702 -605 Lung_1
-605 -508 Lung_2
-508 -411 Lung_3
-411 -314 Lung_4
-314 -217 Lung_5
-217 -120 Lung_6
-120 -120 Lung_7
-120 -82 AT_AG_SI1_8
-82 -52 AT_AG_SI2_9
-52 -22 AT_AG_SI3_10
-22 8 AT_AG_SI4_11
8 19 AT_AG_SI5_12
19 80 SoftTissus_13
80 120 ConnectiveTissue_14
120 200 Marrow_Bone01_15
200 300 Marrow_Bone02_16
300 400 Marrow_Bone03_17
400 500 Marrow_Bone04_18
500 600 Marrow_Bone05_19
600 700 Marrow_Bone06_20
700 800 Marrow_Bone07_21
800 900 Marrow_Bone08_22
900 1000 Marrow_Bone09_23
1000 1100 Marrow_Bone10_24
1100 1200 Marrow_Bone11_25
1200 1300 Marrow_Bone12_26
1300 1400 Marrow_Bone13_27
1400 1500 Marrow_Bone14_28
1500 1640 Marrow_Bone15_29
1640 1807 AmalgamTooth_30
1807 1975 AmalgamTooth_31
1975 2142 AmalgamTooth_32
2142 2300 AmalgamTooth_33
2300 2467 MetallImplants_34
2467 2635 MetallImplants_35
2635 2802 MetallImplants_36
2802 2970 MetallImplants_37
2970 3000 MetallImplants_38
3000 3499 MetallImplants_39
3499 3999 MetallImplants_40
3999 4000 MetallImplants_41
4000 4001 MetallImplants_42
```

Appendix K: Questionnaire for reader study

Patient ID:

Clinical History:

1. Overall Image quality (one answer only, place tick in the box)

Image Quality Description		PET_D	PET_E
Non-diagnostic			
Poor	(distinct artefacts, strong image noise)		
Satisfactory	(few artefacts, moderate image noise)		
Excellent	(no artefacts, low image noise)		

2. Are there obvious artefacts present in the following region/s (multiple answers allowed, place tick in the box)

Location	PET_D	PET_E
No obvious artefacts		
Liver		
Pancreas		
Peritoneum		
Bowel		
Bone		
Nodes		
Lung		
Other:		

3. Lesions. Comparison between PET_D and PET_E

Location	PET Study Preferred (circle one)			Reason for Preference (tick, multiple answers allowed)			
				More Lesions	Increased Contrast	Increased Sharpness	Artefact Free
Liver	D	E	NP				
Pancreas	D	E	NP				
Peritoneum	D	E	NP				
Bowel	D	E	NP				
Bone	D	E	NP				
Lymph Nodes	D	E	NP				
Lung	D	E	NP				
Other:	D	E	NP				

NP = no preference

4. My preferred PET Image
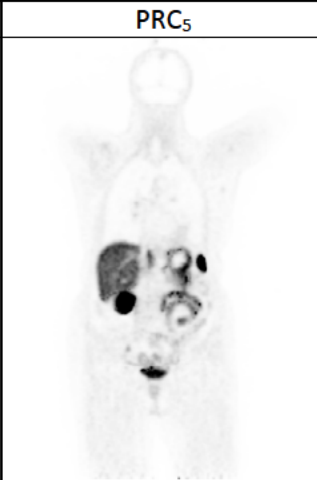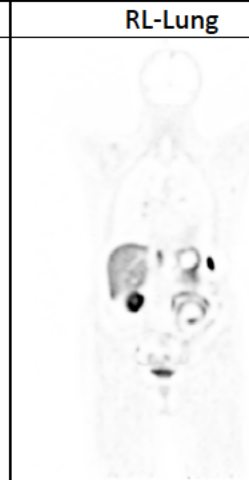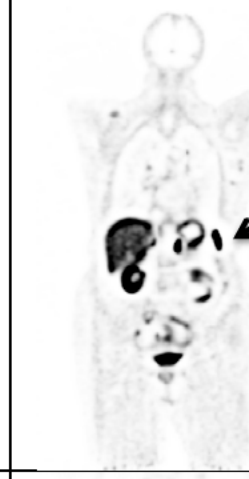
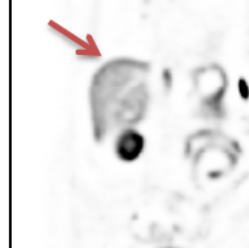| PET Study	(tick one)
PET_D	
PET_E	
No Preference	

5. Comments (optional response)

Appendix L: Demographic data

Patient's ID	Gender	Age	Weight	Injected Dose (MBq)
04	F	65	66.6	194.28
05	M	48	100.9	192.71
06	F	31	63	180.3
07	M	68	91	171.2
08	F	47	88	138
09	M	67	76.6	155
10	F	59	77.7	131.6
11	F	64	50.2	133
12	M	49	128	130.9
13	F	77	61.1	181
14	F	73	54.8	146.1
15	F	58	63.2	150
17	F	58	77.1	134
18	F	82	52.6	184.6
19	F	23	65	136
20	M	28	70.5	186.67

Appendix M: PET$_0$, PRC$_s$ and Richardson–Lucy deconvolution

eshold	PET$_0$	PRC$_5$	RL-Bone Kernel	RL-Water	RL-Lung
0%					
0%					
0%					

Figures above show the coronal view of PET_0, PRC_5 and Richardson-Lucy deconvolved images using ^{68}Ga bone, water and lung kernels, respectively. Images displayed at different percentage thresholding of the maximum voxel value. Black arrow shows the overcorrection of the PR effect in the soft tissue when the lung blurring kernel is used. Finally, images at the third row were magnified and red arrow indicate the Gibbs artefact at the lung/liver interface.